CONTROL OF A NINE-PHASE SYMMETRICAL PMSM WITH REDUCED RARE EARTH MATERIAL

MARKO SLUNJSKI

A thesis submitted in partial fulfilment of the requirements of Liverpool John Moores University for degree of Doctor of Philosophy

November 2020

ABSTRACT

The rising demand for high-power fault-tolerant applications such as wind generators and electric vehicles, alongside the desire to achieve better performance, have directed the interests of many research centres around the world towards electric drive configurations comprising AC machines with more than three stator phases. These so-called multiphase machines have become well recognized as an attractive alternative to the conventional three-phase machines and are used when the three-phase counterpart cannot provide a drive system with the desired performance.

The Thesis examines advanced control possibilities for multiphase surface-mounted permanent magnet synchronous machines (PMSMs). Although it is well-known that permanent magnet machines are today the first choice in many applications and that their market is anticipated to catch up with the induction machines market in the near future, the main drawbacks of this machine type are the relatively high capital costs, the security of magnet supply and the environmental costs associated with the rear-earth magnet materials used in the rotor construction. This has motivated researchers to investigate methods to reduce the amount of rare earth material used in the construction of these machines.

If the amount of permanent magnet material is reduced, this will inevitably result in a machine which produces lower electromagnetic tor que. On the other hand, the additional degrees of freedom, present in multiphase systems, can be exploited to inject, into the stator windings, harmonic current(s) to enhance the developed torque. This work analyses a new nine-phase symmetrical PMSM with two surface mounted magnet poles on the rotor with a shortened span. This simple design produces a highly non-sinusoidal back-electromotive force (back-EMF) comprising high third and fifth harmonic components. It is shown that these harmonic components can be utilised to boost the torque to near the value obtainable with full span magnets, provided a suitable control system is developed.

The developed control algorithm is based on the well-known vector space decomposition (VSD) and classic field-oriented control methods. To test the developed control algorithm, phase domain machine model is presented first, for both sinusoidal and non-sinusoidal back-EMF distributions. To transform variables from one reference frame to another, the VSD and rotational transformations are used. The optimal ratios between fundamental and other harmonic current components are derived using the maximal torque-per-Ampere (MTPA) theory. It is shown that, by using optimal current injection, the electromagnetic torque can be improved by 36% with third harmonic only, and, up to 45% with a combination of the fundamental, the third and the fifth harmonics. Simulation results are validated in finite element method software and afterwards verified experimentally using an experimental prototype.

Control of the PMSM is next expanded with position sensor fault-tolerant capability. For this purpose, the same EMF spectrum is used. When harmonic current elimination is performed in *x-y* subspace, remaining h^{th} harmonic order back-EMF can be efficiently used for position angle and speed estimation. For the estimation purpose, phase-locked-loop method is employed. With estimated position/speed, a new control algorithm is devised, which combines control in two auxiliary subspaces with the control of the first plane. The third harmonic is, in combination with the fifth, used for the torque boost prior to the fault, while afterwards, the fifth EMF harmonic enables position estimation for position-sensorless control. Hence, previously stated maximal torque improvement is preserved until position sensor fault is detected, while afterwards machine continues to operate in position-sensorless mode still with partial enhancement of the torque. Control is verified experimentally.

Finally, operation in the flux-weakening region is investigated. Because finding sets of multiple harmonic current references which maximize torque by taking into account voltage and current limits leads to a difficult problem to formulate, which is often impossible to solve analytically, the work presented here builds on (offline) numerical optimisation procedure. To obtain best performance, harmonics up to the (and including) fifth are considered. Limitation of voltage is achieved by comparing measured phase-to-phase voltage with maximal dc-link voltage, while thermal (RMS) constraint and inverter switch (peak) current constraint are taken into account by limiting the current. In such scenario, maximal reachable speed is much higher than the base speed, while respecting at the same time both machine and inverter constraints.

ACKNOWLEDGEMENTS

I would like to express my sincere gratitude to several people I came across during my research and education, to people who became my friends, my supervisors, my mentors and without exaggeration, my second family. Without them, being a person, a researcher that I am today, would not be possible.

Firstly, I would like to express my deepest gratitude to my supervisors, Dr Martin Jones and Prof Emil Levi. Without their exceptional mentoring and vast knowledge, endless patience for "one-minute" meetings and continuous support during my PhD studies, completion of this thesis would have not been possible. It was a privilege to study under your supervision and thank you for all the knowledge and experience that you shared with me.

Next, I would like to express my sincere appreciation to my dearest friend, Dr Obrad Đorđević, who was one of the most influential persons during the course of my PhD studies. Without hours that he spent with me in laboratory analysing all sorts of different problems that I came upon, many things would still be unclear to me and probably unsolved. All the discussions that we had in the office and laboratory have vastly influenced my research and often led me to the better solutions. Not to forgot, his friendship and always positive attitude have made my stay in Liverpool a very enjoyable experience which I will cherish for the rest of my life.

There are a few more people I would like to credit for being a true friends and exceptional colleagues during my stay in Liverpool. But first, I would like to thank Dr Milan Darijevic without whose unique ability to persuade people, my PhD studies would not have commenced. Many thanks also to my colleagues and friends, Dr Ivan Zoric (and his wife Vesna and kid Lazar), Dr Ivan Subotic, Dr Siratam Udomtamanupab, Dr Nandor Bodo (and his wife Andrea and kids Gabriella and Oliver), Dr Ahmad Abduallah and Mr Umar Khan. Sharing an office with some of them was a pleasure and I could only feel honoured to call them friends. During my stay in Liverpool, I was also lucky enough to spend some time with Dr Sandro Rubino, Dr Ignacio Gonzalez-Prieto, Prof Mario Duran, Miss Ornella Stiscia and Mr Andrea Cervone, who have given me an opportunity to work outside my thesis topic. I would like to also acknowledge Mr Steven Gotts for his help and constant support that he provided during my countless hours in laboratory.

Last but not least, I would like to thank my family for their endless love. The biggest influence on my development, as a researcher, and more importantly, as a person, definitely comes from my wife Helena. Thank you Helena, for every second spent with me in last eight years. Thank you for all moments of joy that you gave to me and for vast love and support that you had for me during my entire educational period. My mother, Mirjana, father, Tomislav and brother, Tomislav Jr., you know that any of these words wouldn't be possible without your help, your support, your patience, your knowledge, your experience and your endless love during my entire life.

CONTENTS

LIST OF PRINCIPAL ABBREVIATIONS

ac	*Alternating Current*
Back-EMF	*Back-Electromotive Force*
dc	*Direct Current*
FEM	*Finite Element Method*
FFT	*Fast Fourier Transformation*
FOC	*Field Oriented Control*
FW	*Flux-weakening*
MMF	*Magnetomotive Force*
MTPA	*Maximal Torque-Per-Ampere*
NdFeB	*Neodymium Iron Boron magnet material*
PLL	*Phase-Locked-Loop*
PM	*Permanent Magnet*
PMSM	*Permanent Magnet Synchronous Machine*
RMS	*Root Mean Square*
VSD	*Vector Space Decomposition*
VSI	*Voltage Source Inverter*

LIST OF PRINCIPAL SYMBOLS

^	*Over the label stands for estimated values.*
a	*Number of phases in a phase set.*
B_{roth}	*Maximal value of the h^{th} order spatial harmonic in the air-gap produced by PMs.*
$[C]$	*Decoupling transformation matrix (phase-variables to α-β variables).*
$[D]$	*Rotational transformation matrix (α-β to d-q reference frame).*
d/dt	*The first derivative of signal over time.*
e_h	*Back-EMF magnitude of the h^{th} harmonic in the FFT spectrum.*
$[e_{bEMF}]$	*Vector of the back-electromotive force voltages.*
$[f_{abcn}]$	*Voltage, current or flux linkage column matrix in phase-variables reference frame.*
$[f_{dq}]$	*Voltage, current or flux linkage column matrix in synchronous reference frame.*
$[f_{\alpha\beta}]$	*Voltage, current or flux linkage column matrix in α-β reference frame.*
f_{dq}	*Direct and quadrature voltage, current or flux components.*
f_{xy}	*x-y plane components of voltages, currents and flux.*
f_n	*Nominal value.*
g	*Power invariant/amplitude invariant coefficient.*
h	*Harmonic order.*
$[i_{abcn}]$	*Vector of the stator currents.*
i_{ch}	*Machine's characteristic current.*
i_d, i_q	*Flux- and torque-producing current components in rotating reference frame.*
i_{dqh}	*Flux- and torque-producing currents of the h^{th} harmonic component.*
$I_{max} = I_{VSI}$	*Maximal phase current peak value (inverter switches boundary).*
k_{1h}	*Current injection ratio between fundamental and h^{th} harmonic component.*
k_{dh}	*Distribution factor of the h^{th} order harmonic.*
k_I	*Gain for PI regulator integral component.*
k_P	*Gain for PI regulator proportional component.*
k_{ph}	*Pitch factor of the h^{th} order harmonic.*
$k_{VPI\text{-}Ih}$	*Resonant controller integral gain for the h^{th} order harmonic.*
$k_{VPI\text{-}Ph}$	*Resonant controller proportional gain for the h^{th} order harmonic.*
$k_{P\text{-}PLL}$, $k_{I\text{-}PLL}$	*Proportional and integral gains of the PLL PI controller.*
k_{wfh}	*Winding factor of the h^{th} order harmonic.*
k_{ws}	*Number of winding sets.*
l	*Rotor length.*

$[L_{ls}]$	*Leakage inductance matrix.*
L_d, L_q	*Stator winding self-inductance in d-q reference frame.*
$[M_{ss}]$	*Mutual inductance matrix between all phases in a machine.*
n	*Number of phases on stator.*
N_{ph}	*Number of the winding (coil) turns per phase.*
n_{max}	*Maximal speed in revolutions per minute (rpm).*
n_{mech}	*Mechanical rotor speed in rpm.*
q	*Number of slots per pole per phase.*
$[R_s]$	*Stator resistance matrix.*
R_{rot}	*Radius of the rotor.*
S	*Number of stator slots.*
T_{em}	*Electromagnetic torque.*
$T_{em1...h}$	*Sum of electromagnetic torques produced by different harmonic components.*
T_{em1h}	*Electromagnetic torque produced by fundamental and h^{th} harmonic component.*
$[v_{abcn}]$	*Vector of the stator voltages supplied to machine from power source/inverter.*
v_d, v_q	*Flux- and torque-producing voltage components in rotating reference frame.*
$V_{max} = V_{dc}$	*Maximum phase-to-phase peak voltage (limit imposed by the dc-bus voltage).*
y_{cp}	*Coil-pitch.*
$[\lambda_{abcn}]$	*Vector of the stator flux linkages in phase sets (total flux in the machine).*
$[\lambda_{m\text{-}abcn}]$	*Flux produced by permanent magnets.*
$\hat{\theta}_{el}$, $\hat{\omega}_{el}$	*Estimated position and speed in sensorless control.*
$\Delta\theta$	*Difference between measured (sensor) and estimated (PLL) angles (i.e. θ - θ_{est}).*
θ	*Angle measured by the position sensor in sensorless control.*
θ_{el}, θ_{mech}	*Rotor electrical/mechanical angle.*
θ_{fault}	*Angle measured by the position sensor, which is at the fault instant set to 0.*
θ_{phsh}	*Phase shift of the h^{th} harmonic in the FFT spectrum.*
$\theta_{est} = \theta_{PLL}$	*Position obtained using PLL controller.*
λ_{mh}	*Flux magnitude of the h^{th} harmonic in the FFT spectrum.*
τ_{pp}	*Pole-pitch.*
ω_{base}, n_{base}	*Base speed in radians per second (rad/s), rpm.*
ω_{el}, ω_{mech}	*Angular electrical/mechanical rotor speed in rad/s.*
ω_{PLL}	*Speed obtained using PLL controller.*
$\omega_{PLL\text{-}I}$	*Filtered speed obtained on the output of PLL controller used in closed-loop control.*

Chapter One

INTRODUCTION

1.1 Preliminary Remarks

The rapid development of industrial applications requires continuous improvement of different types of electrical drives. Three-phase machines are nowadays the most commonly used rotating electrical devices. They are routinely adopted for various purposes in different fields of human activity due to their low price, "*off-the-shelf*" availability and, because of high reliability, almost maintenance-free operation. On the other hand, the need to reduce costs and at the same time achieve better performances, as well as new safety regulations for more- and all-electrical vehicles, have directed the interests of many research centres around the world towards machine configurations with more than three stator phases. These, so-called, multiphase machines are therefore today well recognized as an attractive alternative to conventional three-phase machines and are used where, for one reason or another, three-phase machines cannot provide a drive system with the desired performance.

At the beginning of the electrical ac machines era, the number of machine phases was chosen to match with the three-phase grid, since induction machines were directly supplied from the mains. Later on, power electronic converters were introduced in order to allow easier speed and position control in industrial applications [Vaez-Zadeh (2018)]. Today, the power supply, control and motor are highly interconnected as shown in Fig. 1.1. The energy process of the motor system begins with the power supply, which provides electrical energy to the power converter. It is well-known that the most convenient way to supply a motor is to convert fixed dc power (from a battery or rectified electricity network) to a variable voltage and variable frequency power supply. The power converter in a low to medium power controlled motor system is usually an inverter, which receives the rectified power from a rectifier and inverts it to ac power. The motor, as the heart of the energy conversion system, converts electrical energy to mechanical. However, it may occasionally convert mechanical energy to electrical (i.e. in regenerative mode of operation). Finally, the control system is the information processing part which receives command signals from the user on one side and system signals (supply, power converter, motor) from the other side and generates driving signals for the power electronic switches of the inverter. The focus of this work is on the electrical machine (motor) and corresponding control system. In particular, this thesis is entirely related to the machines with permanent magnets (PMs) on rotor and with more than three phases on stator, i.e. multiphase permanent magnet synchronous machines (PMSMs).

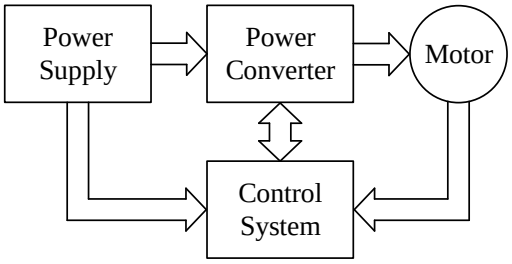

Figure 1.1 – A controlled (permanent magnet synchronous) motor system.

1.2 Machines with Permanent Magnets on Rotor

Permanent magnet synchronous machines emerged in the 1970s as the evolution of older machines at the crossroads of permanent magnet dc machines, line-start PM machines and power converter-supplied induction machines [Vaez-Zadeh (2018)]. Because they feature many advantages over other machine types, they have quickly become the main competitor to the widely used induction motors as the workhorse of today's industry. One of the main reasons for this is the fact that PMSMs usually work at an efficiency which is much higher than that of a standard induction motor of the same rating. Furthermore, the high efficiency of the motors compared to that of induction motors does not drop much at high speeds or under heavy loads; hence, this results in higher energy saving in PMSM case. Use of high energy PM materials results in high air-gap flux density with smaller motor size and weight, leading to compact motor design which increases power and torque density. These features open the door to a wide range of applications, from electric vehicles to aerospace systems, for which in addition to efficiency, weight and volume are critical. The higher torque density of the modern PMSM not only improves the steady-state operation of the machines, but also provides them with higher dynamic performances. This feature, in line with model simplicity and higher controllability of the motors, makes them the most appropriate option for high performance drive applications today. Based on that, the PMSM market is anticipated to capture the traditional market of variable speed induction motor drives in sectors such as paper and pulp, oil and gas, metals and mining, fans and pumps, chemical, plastic and cement, in order to save energy and improve quality and productivity [Vaez-Zadeh (2018)]. Applications in transport such as electric and hybrid vehicles, train propulsion systems and more/all-electric aircrafts that are suited for PMSM, must also be listed, because they are rapidly expanding markets today.

Four types of PM materials are used today in permanent magnet machine construction: neodymium iron boron (NdFeB), samarium-cobalt (SmCo), ferrite and aluminium nickel cobalt (AlNiCo). Among these, NdFeB dominates the electric motor magnet market due to linear demagnetization characteristic, high remanence/coercivity and the highest energy product. Consequently, this results in dominant position of PMSMs on the market with high power and torque density [Vaez-Zadeh (2018)].

NdFeB is mechanically strong and features good machinability. On the other hand, high quality means high market price. Furthermore, the main weakness of the material is the low Curie temperature. Based on these reasons, two main research areas are active today. The first one is related to the improvement of NdFeB thermal characteristic; if this is not achievable, the second one is related to finding similar materials which have good thermal resistance. A third (and probably most significant) drawback is the high transport price and price instability. China holds >85% of the worldwide rare-earth magnet share, and this continues to rise with every passing year [Benecki et al (2010)]. Final major drawback (which is rarely mentioned) is related to environmental impact of mining and rare earth

materials processing. Removal of these elements from the earth, using a mix of water and chemicals, in many cases causes extensive water and soil pollution.

The cost of PM material in the rotor can therefore be the major material cost in the PM synchronous machine. One example can be found in [Rahman (2013)], where material cost for electrical vehicle Prius 09 was investigated. It is shown in this work that permanent magnet material used in the rotor construction formed 64% and 81% of total machine material cost in 2005 and 2012, respectively. A similar investigation was published in [Widmer et al (2015)] as well, where it was shown that price of magnet material in interior PMSM is more than two times higher than combined price of steel and copper (a 30 kW traction motor was considered).

The stator of PM synchronous machine is not different from that of wound rotor synchronous or induction machines (some winding examples are given in Fig. 1.2). However, the main difference lies in the rotor configuration, which significantly influences motor performance (torque and power density, torque-speed characteristic, flux-weakening capability, etc.). There are two categories of PM synchronous machines when looking from the control point of view: motors with and without rotor saliency. In which category a motor is placed depends mostly on position of magnets on the rotor. The non-salient machines are with surface-mounted permanent magnets on rotor (Fig. 1.2a) (this is the type to be considered in this work), while machines with inset (Fig. 1.2b) and interior (Fig. 1.2c, d) permanent magnets are categorised as salient machines.

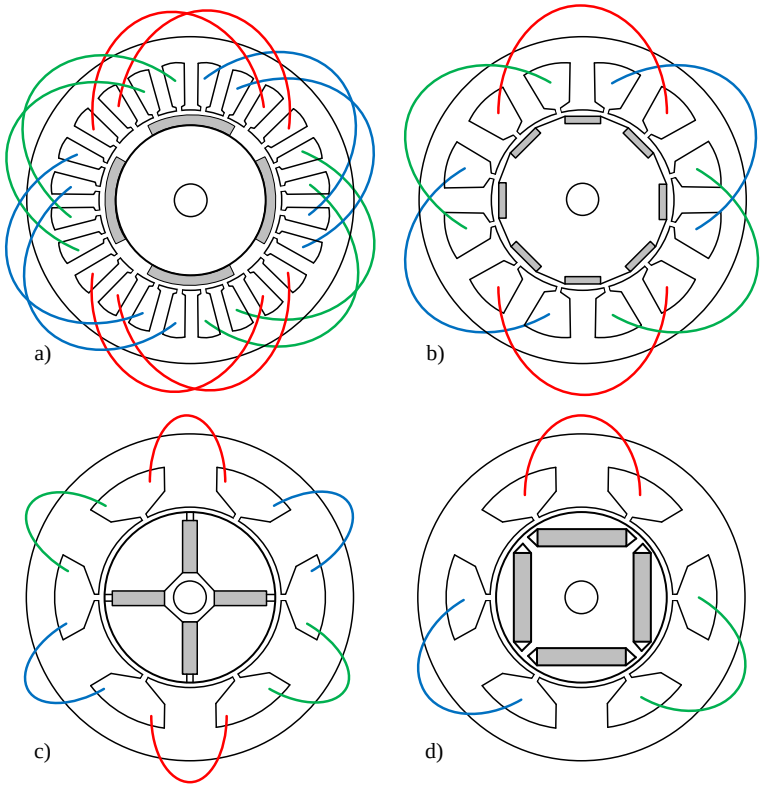

Figure 1.2 – Stator winding and rotor configurations: (a) overlapping-distributed stator with surface-mounted PM rotor, (b) overlapping-concentrated stator with inset PM rotor, (c) non-overlapping all teeth wound stator with radial PM rotor, (d) non-overlapping-alternate teeth wound stator with interior PM rotor.

In surface permanent magnet rotor case, magnetic air-gap is rather large. This is mostly related to magnet permeability, which is almost the same as permeability of air. Based on that, surface-mounted PM machines are characterised with almost the same reluctance in the magnet flux paths, i.e. machine is described with a single inductance. Inset magnet machines have magnet poles that are placed inside the rotor iron, but their external surface is not covered by iron. Finally, interior permanent magnet machines have PM poles totally buried inside the rotor iron, which results in uniform air-gap. However, the machine flux paths in the rotor are not uniform and one flux path through poles experiences much higher reluctance than the other. This provides extra torque which is known as reluctance torque and it also gives excellent opportunities in flux-weakening region (i.e. over-nominal speed operation).

1.3 Machines with More than Three Phases on Stator

Multiphase machines, machines with more than three phases on stator ($n > 3$), have long been recognized as an attractive alternative to conventional three-phase machines for applications where three-phase machines cannot easily achieve the desired performance requirements [Barrero and Duran (2016)]. Research into multiphase machines appeared in the late sixties of the last century [Ward and Härer (1969)]. In the last twenty years or so the interest has grown and significant contributions to this field have been made [Levi et al (2007), Levi (2008), Levi (2016)]. This surge in interest is due largely to the increasing demand for high-power (or high current), fault-tolerant drives in a growing number of applications. For example, electrical vehicles, electrical ship propulsion, railway traction, more-electric aircrafts, off-shore wind power generation, high-speed elevators and even aerospace applications are areas in which multiphase machines are finding a market. If compared with industries were PM machines are advantageous, it is easy to conclude that the two research areas overlap, thus making multiphase PM machines an excellent choice for applications such as electrical vehicles, trains, wind electricity generation, aircraft industry, etc.

The advantages of multiphase machines are nowadays generally well known. They are summarised as follows:

- Power splitting between more inverter legs, i.e. reducing the required current rating of the semiconductor components [Levi (2008), Barrero and Duran (2016)].
- Improved fault tolerance due to the ability to operate (albeit with reduced power) with some faulty phases (e.g. open circuited) [Levi (2016)].
- Lower torque ripple and torque pulsation [Ward and Härer (1969)].
- Additional degrees of freedom that can be used for control purposes that are not possible in standard three-phase machines [Levi (2016)]. Examples include:

- Electromagnetic torque enhancement, using harmonic current injection, and as well as fault-tolerant operation [e.g. Lyra and Lipo (2002), Semail et al (2004), Parsa (2005), Parsa and Toliyat (2007a)].
- Multi-motor multiphase drive systems with single VSI supply [Jones et al (2009), Mengoni et al (2012)].
- Capacitor voltage balancing in machines with multiple three-phase windings and multiple three-phase converters that are connected in series, giving an elevated dc-link voltage level [Che et al (2014)].
- Advantages in integrated on-board battery charger designs for electric vehicles [Subotic et al (2015), Subotic et al (2016)].

Multiphase machine types correspond to their three-phase predecessors and can be classified into two main groups: induction machines and synchronous machines. As already explained, synchronous machines are further classified on the basis of the rotor excitation type (permanent magnets or a field winding) and air-gap properties (with or without saliency). It is important to note that although each machine type has its advantages and drawbacks, this work will focus on multiphase synchronous permanent magnet machines with surface-mounted permanent magnets. Looking from the stator side, winding configuration of radial-field PM machine can be classified as overlapping (which can be distributed (Fig. 1.2a) or concentrated (Fig. 1.2b)) and non-overlapping (i.e. concentrated with all teeth wound stator (Fig. 1.2c) or alternate teeth wound stator (Fig. 1.2d)). Non-overlapping winding design is also known as fractional-slot concentrated winding. Alternate wound teeth are usually referred to as single-layer, while all teeth wound winding is better known as double-layer arrangement [El-Refaie et al (2008b)]. Taking into account the above given classification, the machine studied in this work has a winding arrangement that is classified as overlapping, symmetrically distributed as shown in Fig. 1.2a.

1.4 Research Aim and Objectives

As discussed earlier, there is a pressing need to develop PMSM machines constructed using a reduced amount of rare earth permanent magnet materials compared to the current solutions. This obviously will result in a machine with lower power density and torque capability when compared to a standard PMSM. To enhance the torque in such a machine, most of the authors use the properties of multiphase machines and specific rotor structures, either by adding magnetic material or shaping the magnets. In contrary, this work's aim is to demonstrate how the torque enhancement can be achieved by employing advanced control methods and by using a simple-to-manufacture rotor structure which significantly reduces the volume of PM material.

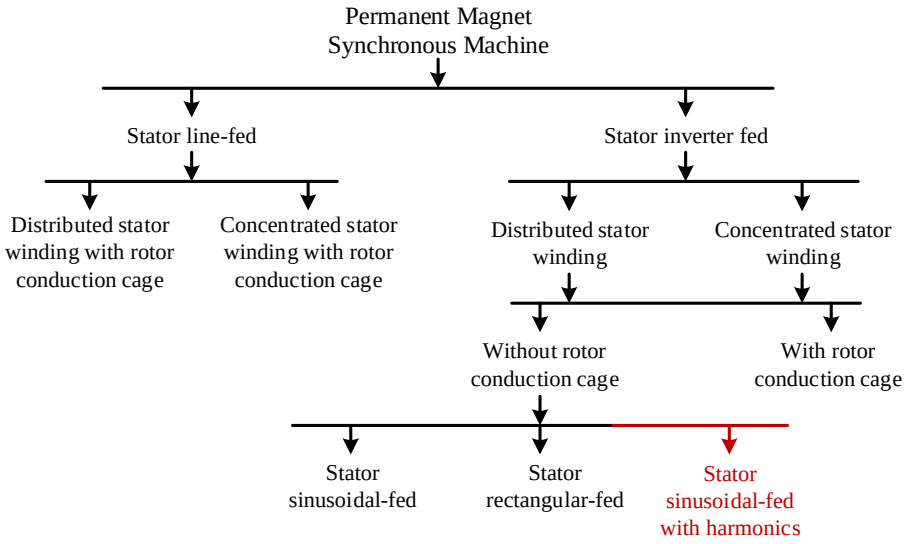

Figure 1.3 – Classification of permanent magnet synchronous motors.

To demonstrate this aim, this work will first explore modelling and vector control of a multiphase PMSM, designed with a triple three-phase stator winding. The relevant machine classification is shown in Fig. 1.3. The stator is equipped with 36 slots inside which a single-layer symmetrical (distributed) winding is arranged, so that there are 18 slots per pole (two slots per-phase-per-pole). Hence, a nine-phase winding is designed and mounted on the stator. However, the 2-pole rotor has been obtained by removing four poles from the original rotor, without conduction cage, i.e. magnet material on the rotor is reduced (by shortening the magnet span) which causes production of highly non-sinusoidal back-electromotive force (back-EMF) in the stator windings. Analysis of the back-EMF reveals a high third harmonic component, which is almost equal in magnitude to the fundamental. This harmonic has been used many times by researchers in the past to increase the torque density of multiphase machines. In addition to the approximately equal fundamental and third harmonic components, a significant fifth harmonic component with a magnitude equal to approximately half of the fundamental also exists.

The machine will be first tested under third harmonic current injection because it is believed that this will achieve significant torque improvement. The analysis will be afterwards extended to other low order odd EMF harmonic components lower than the machine phase number with the intention to maximize output torque. Next, it has been shown in the literature that the third EMF harmonic can be used for sensorless position estimation. Because the studied machine has more than one high magnitude odd EMF harmonic, a study will be conducted in that direction as well, with the intention to combine multiple harmonics for multiple purposes in the same control algorithm. In this context, the tolerance of the PMSM prototype to the position sensor fault will be investigated. Finally, because (as it will be shown) significant torque improvement using harmonic current injection can be achieved in constant torque region below base speed, it is believed that by injecting different combinations of optimal current harmonic references, improvement in constant power (flux-weakening) region can also be achieved. As

a result, after combining the above-mentioned studies, an advanced control algorithm for the proposed multiphase permanent magnet synchronous machines will be developed, which enables a machine with reduced magnetic material to have similar performance as a conventional machine with full magnet span. Furthermore, the developed control algorithms can also be applied to other machines with similar properties (i.e. EMF spectrum).

The stator of a multiphase machine with multiple three-phase windings is arranged either in symmetrical or asymmetrical winding configuration, i.e. with spatial displacement between first phases equal to $2\pi/n$ or π/n, respectively. In addition to the classification given in Fig. 1.3, the studied nine-phase machine can also be counted in a group of machines for which both winding configurations (symmetrical and asymmetrical) can be easily achieved by rearranging the voltage source inverter (VSI) supply leads in the machine's terminal box. In these machines, changing the stator winding configuration can be accomplished if both start (positive) and end (neutral) winding terminals are accessible for every phase winding; this winding type is known as open-ended. Multiphase machines used in research laboratories are usually with open-end winding because they are custom-made and commonly all $2n$ winding terminals are available in the machine's terminal box. In other words, the neutral point(s) of the machine are left to be formed according to the user requirements. The type of the machines where this is possible has never before been generalised; hence it will be here identified and the method for reconfiguration will be explained.

In the literature, many high-performance vector control methods have been investigated and derived for multiphase permanent magnet synchronous machines. They are much more convenient to implement than those for induction and wound rotor synchronous machines, because the dynamic model of a PMSM is much simpler. This is entirely related to the fact that electrical dynamics in the rotor are non-existent and control system design is entirely related to the stator winding equations. Generally formulated, vector control is a means by which the stator phase currents of ac machines are transformed into a current vector with two perpendicular components to control the torque and flux independently. By applying this method, features such as motor flux-weakening, current and voltage limitations, unity power factor, loss minimization operations, etc., can be achieved. It is because of these reasons that vector control is accepted as the most common control method in the industry [Vaez-Zadeh (2018)]. Additional reason for using vector control in this work is also related to the fact that once a suitable decoupled multiphase machine model has been developed (how this is done will be explained in detail in the following chapters), each harmonic can be controlled separately by using almost the same control approach. In another words, flux- and torque-producing currents can be for each harmonic controlled in a similar way. Hence, once implemented, the only difference between, for example torque enhancement and flux-weakening control, is how optimal current/torque references are calculated in the different operating regions.

To summarise, the project will explore modelling and control of a multiphase PM synchronous machine with shortened magnet poles. Based on the harmonic spectrum which is produced by specific rotor structure, the main aim relates to torque enhancement, sensorless control, and improvement of the machine's operation in the flux-weakening region by means of stator current harmonic injection. In order to meet this aim, the following project objectives are formulated:

- To investigate the design of the proposed machine using finite element method (FEM) software in-order to quantify the subsequent loss of torque capability due to the reduced magnet span, compared to a standard (benchmark) machine construction, and to utilise the developed model to determine the optimal rotor magnet span that will restore the developed torque to that of the benchmark machine under a suitable harmonic injection operating regime.
- To develop, using VSD machine modelling approach, appropriate models that will enable independent torque control using different harmonics present in the back-electromotive force developed in the machine. This technique will employ the additional degrees of freedom present in multiphase systems to control the selected harmonics.
- To develop a suitable control method, which, including the fundamental, employs third harmonic current component with the goal being to boost the developed torque towards that achievable by a machine with full magnet span (standard machine construction). The optimal injection ratio between the two harmonic components will also be investigated.
- To generalise harmonic current injection (and optimal injection ratio(s) calculation), that is, to include in torque enhancement study all meaningful harmonics from the back-EMF spectrum.
- To investigate position sensor fault-tolerant capability, i.e. to derive a control algorithm for the studied prototype which simultaneously uses different harmonics in different *x-y* subspaces for torque enhancement and sensorless position estimation.
- To develop a novel method to extend the operating speed range of the machine using selected harmonics present in the back-EMF, based again on the vector control principles, and to develop a technique (optimisation procedure) to calculate optimal current/torque references for each harmonic separately.
- To test the developed control algorithms by simulation, to verify them experimentally in the laboratory conditions, and to compare (where possible) the performances of the machine with a corresponding nine-phase machine having sinusoidal (near-sinusoidal) back-electromotive force. The latter machine is considered as benchmark.
- To investigate the possibility to change the stator winding configuration by rearrangement of the power supply connections in the terminal box of the machine.

Through completion of the above-mentioned objectives new contributions to the field are realised and these are summarised next.

1.5 Novelty and Originality

The original contributions of the thesis are presented in chapters 3-8. Research conducted within the scope of the thesis has led to the production of two IEEE conference papers and two IEEE journal papers. The literature survey, undertaken during research, demonstrates that a nine-phase PMSM of the type discussed here has never been investigated in the past. The main novelties presented in this thesis are in:

- **Machine modelling –** As the first step, the novel machine configuration was analysed in detail using FEM software and the results are reported in [Slunjski et al (2018)]. Different rotor configurations were tested, theoretically determined torque improvement was confirmed and optimal magnet span on the rotor has been found.

- **Optimal current injection control –** The work was then further extended by developing an enhanced field-oriented control (FOC) algorithm, with which theoretical and FEM results of the above-mentioned work were confirmed. Both simulation and experimental results are reported in [Slunjski et al (2019)]. The enhanced control algorithm of [Slunjski et al (2019)] takes into account only fundamental and the third harmonic and reports torque as ≈36% higher than the torque produced by the fundamental only. General analysis, taking into account all meaningful high-magnitude odd EMF harmonics lower than the machine phase number was performed in [Slunjski et al (2021)]. Optimal injection ratios were determined using maximal torque-per-Ampere (MTPA) approach for each EMF harmonic separately, and reported maximal achievable torque was ≈45% higher than the torque produced by the fundamental only. Reported percentage improvement is higher than in any published work so far.

- **Sensorless control –** In the same work ([Slunjski et al (2021)], and as an extension to the work reported in [Stiscia et al (2019)]), sensorless control was investigated. It has been shown for the first time that multiple harmonics in different subspaces can simultaneously be used for additional control purposes. To be specific, it was demonstrated that the third and the fifth harmonics can be used for torque improvement prior to a position sensor fault, while after a fault occurs, the fifth harmonic injection can instantaneously be switched off and reassigned for position estimation.

- **Flux-weakening operation –** Finally, the flux-weakening capability of the considered machine was investigated as well. Optimal torque/current references were obtained using optimisation tool, and general algorithm based on look-up tables was derived. Using multiple EMF harmonics

for this purpose has never been reported before. As shown with the aid of simulation results, when new approach which exploits different EMF harmonics is used, significantly higher speed in flux-weakening region can be achieved.

To summarise, published work in the above listed thesis outputs gives not only details of torque enhancement in multiphase permanent magnet synchronous machines (regardless of the EMF shape and the number of considered harmonics), but also leads and to the new knowledge in the areas of sensorless control and above-nominal (flux-weakening region) speed control.

Finally, it is important to note that work in this thesis also contributes to some extent to the knowledge in the field of machine design, not only from the rotor perspective (magnet shaping on rotor to produce different EMF(s) and corresponding spectra), but from stator perspective as well. As it turns out, the nine-phase machine can be classified in a category of machines for which both symmetrical and asymmetrical winding configurations can be achieved by only rearranging power supply leads in the machine terminal box. Detailed investigation and general reconfiguration algorithm are reported in [Slunjski et al 2020]. It is worth mentioning that, in parallel with the work described in this thesis which is related to the symmetrical machine winding configuration, a study of the asymmetrical nine-phase counterpart was also conducted; the results can be found in [Cervone et al (2019), Cervone et al (2020), Cervone et al (2021)].

1.6 Organization of the Thesis

The thesis is organised in 10 chapters and 2 appendices in the following manner. Chapter 2 provides a literature survey related to multiphase permanent magnet synchronous machines and their corresponding features such as torque improvement by stator current harmonic injection, sensorless control and flux-weakening control. At the beginning, multiphase machine modelling approaches are surveyed, including both phase-variable and synchronous reference frame models. To transform machine variables from one reference frame to another, decoupling transformation is needed; hence, a literature review relevant for vector space decomposition (VSD) and rotational transformation is provided. The literature concerning the vector control of multiphase machines is also briefly reviewed. After a detailed literature survey related to modelling and control of multiphase machines with sinusoidal back-electromotive force, the focus moves to machines with non-sinusoidal back-EMF distribution. An extensive literature survey related to the existing third harmonic (but also multi-harmonic) control implementations is provided next. A brief review of different sensorless control approaches (which afterwards focuses on EMF-based sensorless literature) is also given. In addition to torque enhancement and sensorless control, another objective of this work is related to control in the flux-weakening region, hence the corresponding existing literature is surveyed as well.

The mathematical modelling of a PM synchronous machine with (near) sinusoidal back-EMF distribution in the phase-variable and synchronous reference frames is given in chapter 3. The VSD transformation matrices and field-oriented control are commonly used to model and control PMSMs. To form these matrices, knowledge related to symmetrical and asymmetrical winding configurations is required. Hence, both cases are analysed and (as explained earlier), reconfiguration of the winding in composite odd phase number machines is explained. The derived nine-phase machine model in phase-variable form and the vector control algorithm in synchronous rotating reference frame are implemented in *Matlab*/*Simulink* environment for closed loop testing. The recorded results are presented at the end of the chapter. For validation purposes a finite element method software tool is also used.

Extensive finite element method analysis of the studied prototype with non-sinusoidal back-EMF is given in chapter 4. At the beginning of the chapter, the machine topology is presented in detail, electrical and design parameters are summarised, and the corresponding machine cross-section is given. Torque enhancement is analysed by injecting different current harmonics with order 1 to 5. It is shown that the prototype machine magnet span is not optimal; hence different rotor structures with shortened magnet span are analysed. The goal of this investigation is to find a magnet span, which, in combination with harmonic current injection, will produce the same electromagnetic torque as the benchmark machine with full (180°) magnet span. Finite element method analysis of benchmark configuration is therefore performed as well.

Chapter 5 deals with the modelling and control of the machine with the non-sinusoidal back electromotive force. An enhanced field-oriented control algorithm is derived, which considers only the third EMF harmonic component for torque boosting. Optimal injection ratio between fundamental and the third harmonic currents is also analysed and obtained using MTPA approach. Other low order odd EMF harmonics, although also capable of additional torque production, were in this chapter not used. Hence, a means for their elimination/mitigation must be investigated in order to avoid any additional losses. At the end of the chapter, simulation and experimental result are shown and comparison with FEM results from chapters 3 and 4 is given.

In chapter 6, the analysis of chapter 5 is further extended to include other EMF harmonics, resulting in a general approach for torque enhancement (and optimal injection ratio(s) calculation). It is shown that ≈45% higher torque can be produced than in the fundamental only case. A FEM analysis similar to the one in chapter 3 is also conducted.

Chapter 7 investigates sensorless position estimation control. The estimation method is based on the EMF, i.e. it extracts rotor position out of h^{th} harmonic machine model in a *x*-*y* subspace. For this purpose, the control algorithm derived in chapter 6 is further extended, so that in healthy mode both the third and the fifth harmonics are used for torque enhancement, while once sensor fault occurs, the utilisation of the fifth harmonic is instantaneously switched to position estimation (current for this

harmonic is set to zero). In this way, two non-fundamental harmonics in two different subspaces are used for two different control purposes simultaneously, which has not been done before.

Chapter 8 investigates the flux-weakening capability of the PMSM prototype. Optimal torque/current references are calculated using an off-line optimisation tool, saved in look-up tables and afterwards implemented in the control algorithm. As it will be shown, depending on the current/voltage limitations, the machine can achieve much higher speed than in normal operating mode with fundamental harmonic only.

Chapter 9 summarises the work done in the thesis and provides conclusions. In addition, possibilities for future work are discussed.

Chapter 10 provides a list of references used in the thesis.

The last part of the thesis consists of appendices, where a description of the experimental setup, including hardware and software, is given (Appendix A), and where publications resulting from the thesis are listed (Appendix B).

Chapter Two

LITERATURE REVIEW

2.1 Introduction

The aim of this chapter is to provide a survey of the literature relevant to this research and, following from that, an overview of the current state-of-the-art in the field. Probably the most important survey papers published in the last fifteen years on multiphase drives and their properties are those written by [Levi et al (2007), Levi (2008), Barrero and Duran (2016), Levi (2016)]. They provide a comprehensive overview of the developments in the field and demonstrate that the interest in multiphase machines has been steadily increasing for the past thirty years.

These developments are discussed in section 2.2, including also the reported advantages of multiphase machines and the applications where multiphase machines are used today. Five-phase, six-phase and dual three-phase machines are nowadays the most commonly investigated multiphase machines [Li et al (2017)]. Different modelling approaches, transformation techniques and control methods are also covered in this section. Recently, increased attention has been given to machines with a fractional-slot concentrated stator winding distribution, although it is well-known that a distributed winding is more often selected due to the near-sinusoidal magnetomotive force (MMF) and electromotive force (EMF) distribution. In section 2.3 a summary of the advantages and disadvantages for both winding types is provided. As mentioned in chapter 1, because one of the tasks of this thesis is to present a general algorithm for reconfiguration of composite odd phase number machines by only rearranging power supply leads in the machine's terminal box, a brief literature survey of the existing literature in this sub-area is given here.

Section 2.4 reviews electromagnetic torque enhancement using harmonic current injection and different machine topologies with non-sinusoidal back-EMFs. When analysing non-sinusoidal back-EMF, particular attention has been paid to the different rotor structures used in both internal and surface mounted permanent magnet machines. It is shown that the simple rotor structure proposed in this work has not been investigated before. Moreover, in previous research works the aim was to boost the electromagnetic torque beyond the original design parameters using harmonic current injection whereas the motivation here is to compensate the reduction in the developed torque due to the lessening of the magnetic material mass.

In section 2.5, sensorless control techniques are examined. After a brief overview of the field, the focus moves to consider EMF based sensorless techniques relevant to the work conducted in this thesis. In section 2.6, the literature related to machine operation in the flux-weakening region is given. The machine investigated in this thesis has surface-mounted permanent magnets, meaning that operation in the flux-weakening region is difficult to achieve [El-Refaie (2010)]. Nevertheless, it is believed that the specific harmonic spectrum produced by the considered rotor design can be used for additional improvement in this region; hence, a further investigation in this direction is also made.

2.2 Multiphase Machines

Three-phase machines are today the most commonly used rotating electrical devices for industrial applications. They are routinely adopted for various purposes in different fields of human activity due to their low price and wide availability and because of high reliability and almost maintenance-free operation [Levi et al (2007), Levi (2008)]. It is clear that this trend will continue in the future years with three-phase machines in the centre of electrical to mechanical (and vice versa) energy conversion process. As a consequence of rapid power electronic development, new methods for machine isolation from the grid were developed allowing usage of different ($n > 3$) number of phases in machines [Xu et al (2001), Zabaleta et al (2016a)]. When investigating multiphase machines, one can track the roots back to the late sixties of the 20th century [Ward and Härer (1969)]. Although multiphase machines have been a subject of investigation for quite some time [Levi et al (2007)], only in the last twenty years has a significant contribution to this field been made. In recent times, a complete technology overview can be found in journal papers written by [Levi et al (2007), Levi (2008), El-Refaie (2010), Barrero and Duran (2016), Duran and Barrero (2016), Levi (2016)].

As mentioned, the need for conventional three-phase machines is high, but a tendency to achieve better performances, as well as new safety regulations for more- and all-electrical vehicles, directed interests of many research centres around the world towards machine configurations with more than three stator phases. Because of this, multiphase machines have become well recognized as an attractive alternative to conventional three-phase machines and are used where, for one reason or another, three-phase machines cannot provide a drive system with the desired performance [Barrero and Duran (2016)]. Power splitting between inverter legs, i.e. reduction of the required power rating of a converter semiconductor components, reduction of torque pulsation in inverter fed machines, and power segmentation were one of the first reasons why multiphase machines gained so much interest [Lyra and Lipo (2001), Levi et al (2007), Levi (2008), Gautam (2011), Jung et al (2012), Barrero and Duran (2016)]. Reducing the stator current per-phase without increasing the voltage per-phase, lowering the dc-link current harmonics, increasing the torque per rms ampere for the same volume machine, and solving some of the control issues allowed some new applications which were at that time challenging using the existing power converter technologies [Lyra and Lipo (2002), Parsa (2005), Aslan and Semail (2014)].

Improved fault tolerance due to the ability to operate (albeit with reduced power) despite some faulty phases (e.g. open circuit) [Parsa and Toliyat (2004), Parsa and Toliyat (2007a), Levi (2016)] is another well-known advantage that multiphase machines have. Although fault tolerance is always highlighted in research papers as one of the main advantages that these machines possess [El-Refaie (2011)], when safety is not a priority, additional degrees of freedom can be used for other purposes. Essentially, having additional phases to control means also more degrees of freedom available

for further improvement in the drive systems [Xu et al (2001), Lyra and Lipo (2002), Parsa (2005), Levi et al (2007), Zahr et al (2016a)].

Other reported advantages of multiphase machines over conventional three-phase ones are higher reliability, improved acoustic (noise) characteristics, reduced stator copper losses [Ward and Härer (1969), Parsa (2005)], rotor harmonic current reduction [Xu et al (2001)], reduced torque pulsations [Nelson and Krause (1974), Klingshirn (1983)], and in some specific cases, lower manufacturing cost [Tessarolo (2010)] and higher efficiency [Apsley et al (2006)]. Multiphase machines are therefore today used in high-performance applications such as electrical power steering systems, servo motors and safety-critical direct-drive wind power offshore generators, where high torque and low torque ripple are expected but also fault tolerance capability is needed [Wang et al (2014), Li et al (2017)].

It is clear from the stated advantages that the application of machines with more than three stator phases is growing. This is not hard to understand because niche and specific areas where they were implemented fifteen years ago are now mainstream. For example, statements like "*electrical vehicles which will replace gas-driven vehicles are around the corner and replacement is assumed (scheduled) for year 2022*" [Miller and Howell (2013)] are numerous today, and they often name multiphase machines as a key technology. Multiphase machines are today researched for high-power drive applications such as high-speed elevators [Jung et al (2012)], electrical vehicles [Subotic et al (2015)] and more- and all-electrical aircrafts [Villani et al (2011), Cao et al (2012), Bojoi et al (2012)]. Marine applications, such as all-electrical ship propulsion [Parsa and Toliyat (2005a & 2005b), Nanoty and Chudasama (2011), Thongam et al (2013)], submarine propulsion [Arkkio et al (2002), Scuiller et al (2009)], naval generators to generate voltage for on-board power grid, and turbo-compressors [Gautam et al (2011)] are also very important examples. Other applications include railway and automotive traction [Parsa and Toliyat (2007a)], renewable energy production (i.e. offshore wind power generations) [Li et al (2014), Zabaleta et al (2016a)], and even aerospace applications [Bojoi et al (2016)]. It is important to note that in some of these listed areas, multiphase machines are not in test phase anymore but are already applied and used.

2.2.1 Modelling and Control

Although general tools for modelling machines with more than three-phases have been known since the middle of the twentieth century [White and Woodson (1959)], this remains an important research topic [Tessarolo (2009), Đorđević et al (2010), Levi (2011), Zoric et al (2017a)]. In general, to model a multiphase machine of any type, *n*-electric and *n*-magnetic equations must be written. This, so-called phase-variable approach has its advantages but, in many cases, a transformation is applied to simplify the model in order to enable the implementation of the machine's control algorithm. Commonly a

synchronous reference frame is used for control, and energy conversion is here governed by the control of direct and quadrature (*d*-*q*) stator current components. Although the governing equations for all machine types (in both phase-variable and synchronous reference frame) are well-known and stated at the beginning of almost every literature relevant for this area, transformation matrices (as it will be explained in the next subsection) can have different forms. That being said, they always depend on the machine (stator) design, so relation between transformation matrices and winding configuration on stator is explained here in detail. With focus on PM synchronous machine and possible winding arrangements, different magnetomotive force distribution and back-electromotive force shape (related to winding configuration on stator and magnet position on rotor) must then also be taken into consideration during modelling. Depending on the desired MMF distribution, windings can be either distributed (where all winding turns are arranged in several full-pitch or short-pitch coils) or concentrated (where all winding turns are wound in series to form one multi-turn coil around tooth) [Krause et al (2002), Pyrhonen et al (2008)]. More about this will follow in section 2.3.

Back-electromotive force shape is directly related to stator windings and permanent magnet shape, including also distribution/organisation around rotor [Pillay and Krishnan (1989a & 1989b)]. It can be (near-) sinusoidal, which is the case in most PM machines today with distributed windings, or non-sinusoidal which is the case in concentrated winding arrangements [Ferraris and Lazzari (1983), Lyra and Lipo (2001), Parsa and Toliyat (2003), Semail et al (2004), Parsa and Toliyat (2004), Parsa (2005), Parsa and Toliyat (2005a & 2005b), El-Refaie (2010), Bastos et al (2015)]. Modifications of EMF shape for specific torque boost purpose were lately also reported, using different magnet shaping techniques. A 20-slot 8-pole five-phase concentrated winding machine with winding factors of 0.588 and 0.951, for the fundamental and the third harmonic, respectively, was investigated in [Aslan and Semail (2014)]. A dual-harmonic interior magnet rotor was designed, by adding 16 small magnets, to improve the third harmonic flux. Similarly, by shaping the magnets to produce third harmonic flux, significant torque improvement with low torque ripple was reported in [Wang et al (2014)], for a five-phase surface-mounted PMSM. In [Zahr et al (2016b)] a fractional-slot concentrated winding five-phase machine with a dual-harmonic rotor was developed by introducing holes in the middle of the rotor pole pitch. An interior magnet dual-harmonic rotor with holes, similar to [Zahr et al (2016b)], was then designed in [Gong et al (2019)], the reason being investigation of a five-phase concentrated winding machine whose torque is produced equally by the first and the third harmonics of current and EMF. The machine is aimed at traction applications where field-weakening operation is of great importance. A five-phase 20-slot 8-pole dual-harmonic machine with surface magnets was investigated in [Scuiller et al (2017)] in order to reduce torque ripple. FEM analysis was used to select a suitable rotor leading to a two-thirds pole arc design. The resulting machine is capable of reducing the torque ripple by more than three times when compared to the equivalent three-phase machine. Magnet shaping with third harmonic flux within the same flux limit is another rotor topology

developed in [Zhu et al (2012), Wang et al (2017a)]. Related to this approach, the unequal stator tooth width, PM segmentation and Halbach array [Gu et al (2018), Wang et al (2018), Zhang et al (2019b)], respectively, are among the latest five-phase machine topologies aimed at boosting the torque using harmonic current injection.

During the machine modelling process, the corresponding electromotive force shape must be taken into consideration because of adjustments that are needed in control algorithm if standard (near-sinusoidal shape) is not present. This includes EMF induced current harmonic control or elimination. Controlled current harmonic injection (which will be discussed in more detail in section 2.4) is possible in multiphase machines using the additional degrees of freedom (i.e. additional subspaces) [Klingshirn (1983), Toliyat et al (1998)]. Regarding harmonic current elimination, PI or resonant controllers can be implemented in the mentioned subspaces [Yepes et al (2016), Yepes et al (2017)].

Regardless of the type of the machine and corresponding winding, multiphase machines can be classified into two distinct groups: machines with a prime number of phases, where spatial displacement between any two consecutive phases is always equal to $2\pi/n$ and there is a single isolated neutral point (i.e. 3, 5, 7, 11, …) [White and Woodson (1959), Levi (2011)], or machines with an even number or composite odd number of phases, which can be built with k_{ws} winding sets, each having a phases and where there may be a single or k_{ws} isolated neutral points (i.e. 6, 9, 12, …) [Nelson and Krause (1974), Levi et al (2007), Zabaleta et al (2016b)]. Moreover, if the winding sets are three-phase ones ($a = 3$), then the observed machine is a multiple three-phase winding machine ($n = a \cdot k_{ws}$). This type is particularly attractive since standard three-phase inverters can be used to supply the machine. Following from the above given classification, stator winding in a machine can be realised in two ways, i.e. sets can be designed in such a way that spatial displacement between first phases of the sets is equal to $2\pi/n$ or π/n, leading to symmetrical or asymmetrical distribution of magnetic axes in the cross-section of the machine. The number of isolated neutral points is also important in machine modelling. In addition to the already mentioned involvement in transformation matrix formation, some other machine properties are also directly related to it. One of them is fault tolerance. In multiphase machines which are constructed with multiple three-phase winding sets, if there is single isolated neutral point, only phase in which fault has occurred can be shut down, while in the case of multiple isolated neutral points this is not possible and often the whole three-phase sets must be excluded from machine operation (as explained in [Levi (2008), Zabaleta et al (2016a)]).

Control strategies for multiphase machines are mostly based on field oriented control and direct torque control [Xu et al (2002), Levi (2008)], but also new control algorithms, such as for example model predictive control, have recently emerged [Barrero et al (2009), Lim et al (2014)]. It is important to note that, although some new interesting solutions have been recently reported regarding direct torque control (e.g. [Karampuri et al (2014), Garcia-Entrambasaguas et al (2019)]), this control strategy will

not be further investigated here. As explained in chapter 1, the most common control strategy for (multiphase) machines is field-oriented control (FOC), since the only difference compared to three-phase drives is the number of current controllers. In other words, an *n*-phase drive (where *n* is odd) with a single neutral (the case in the machine studied in this thesis) needs to have (*n* - 1) independent current controllers to eliminate/control low-order harmonic current content. FOC is based on PI controllers that are used for flux- and torque-producing current control and on resonant regulators for current elimination in additional (not for other purposes used) *x-y* subspaces. How to set PI regulator parameters to obtain a satisfactory system response is in general well-known [Aström and Hägglund (1995), Peng et al (1996), O'Dwater (2003), Visioli (2003)], hence, it will not be further discussed. How to eliminate unwanted harmonic current content in drive systems by using resonant regulators can be found in [Yepes et al (2015), Yepes et al (2016), Yepes et al (2017), Zoric et al (2017a)]. Both approaches will be used through this research for different harmonic current controlling/eliminating purposes.

2.2.2 Machine Model Decoupling Methods

As explained in the previous subsection, multiphase machines can generally be modelled using *n* separate equations for electric and magnetic variables [Levi (2011)]. This model is termed the phase-variable model. It is extremely inconvenient for any practical use and hence transformations were invented with the aim to simplify the machine model. Two main transformations are predominantly used today. They are generally known as multiple *d-q* transformation (also called multi-stator approach) and vector space decomposition transformation. For machines where number of phases is equal to multiple of three ($n = a \cdot k_{ws}$), multiple *d-q* modelling approach that applies multiple three-phase transformations can be used. In these machines, *n*-dimensional domain can be divided into k_{ws} three-dimensional domains each of which can be modelled as a three-phase machine. Furthermore, each of these k_{ws} separate three-phase machine models can then be transformed to new reference frame with well-known trigonometric relationships (Clarke's (*abc* - $\alpha\beta$) and Park's ($\alpha\beta$ - *dq*) transformations) to form k_{ws} flux- and torque-producing subspaces and k_{ws} non-energy conversion subspaces (axes) [Zabaleta et al (2016b)]. Although the multiple *d-q* modelling approach is simple to use, which is mainly because of implementing technologies that are similar to the ones used in conventional three-phase machines, it leads to heavy cross-coupling between equations of different three-phase winding sets and does not offer clear insight into multiphase machine operation and harmonic mapping [Klingshirn (1983), Camillis et al (2001), Rubino et al (2020)]. Furthermore, multiple additional PI regulators are required for flux- and torque-producing current control [Zoric et al (2017a)], which increases complexity of control algorithms. All other transformation matrices for multiphase machines rely on the fact that initial set of equations can be rearranged in the form of the equations with (*n* - l)/2 (for odd or (*n*/2 - 1) for even phase number) mutually independent subspaces, while other remaining

component(s) represents zero sequences. In this way, control of multiphase machines becomes easier and examples can be found in [Semail et al (2003), Figueroa et al (2006)].

The vector space decomposition (VSD) modelling approach is an effective technique currently used to model electrical machines equipped with polyphase windings [Tessarolo (2009)]. It was introduced for a six-phase induction machine in [Zhao and Lipo (1994)] and it is based on the symmetrical component theory developed by [Fortescue (1918)]. Depending on the machine construction (symmetrical or asymmetrical), different ways of obtaining VSD matrices have been devised [Camillis et al (2001), Rockhill and Lipo (2009), Zoric et al (2017a)]. But, regardless of the winding configuration, the transformation always results in two torque- and flux-producing components and [(*n* - 3)]/2 (for odd *n*) other simple circuits, comprised of stator resistance and stator leakage inductance. In [Ryu et al (2004) and Rockhill and Lipo (2009)], a nine-phase PM synchronous machine model has been decomposed into orthogonal subspaces. It is shown that fundamental voltage and current components map into the *d*-*q* subspace. The remaining harmonics map into *x*-*y*-0 subspaces and can be used, for example, for fault-tolerant operation [Parsa and Toliyat (2004), Parsa and Toliyat (2007a)], harmonic elimination and harmonic injection [Parsa (2005), Yu et al (2014), Yepes et al (2015), Yepes et al (2016)], dc-bus voltage balancing [Che et al (2012), Che et al (2014)], etc. The main advantage of the VSD is that the control and analysis of the drive system become easier to perform. A number of generalised methods for matrix formation has been proposed in last decade [Tessarolo (2009), Rockhill and Lipo (2015), Subotic et al (2015), Zoric (2017a & 2017b)]. In [Subotic et al (2015)] VSD matrix formation for both symmetrical and asymmetrical induction nine-phase machine with single and multiple neutral isolated points was presented based on a study in [Levi (2011)]. Following from this work, a general (*n*-phase) algorithm to develop VSD matrix transformation applicable to any symmetrical or asymmetrical configuration with single or multiple neutral isolated points was later developed in [Zoric et al (2017b)]. In the case of a nine-phase PM synchronous machine with symmetrical winding configuration and a single isolated neutral point studied here, a similar approach for decoupling matrix formation is used. This approach will be detailed in chapter 3.

2.3 Machine Analysis from Winding Arrangement Perspective

Winding configuration of a radial-field PM machine can be classified as overlapping (which can be distributed or concentrated) and non-overlapping (i.e. concentrated with all teeth wound or alternate teeth wound). Non-overlapping winding design is also known as fractional-slot concentrated winding. Alternate wound teeth are usually referred to as single-layer, while all teeth wound winding is better known as double-layer arrangement [El-Refaie et al (2008b)]. In general, distributed overlapping winding mainly results in a more-sinusoidal magnetomotive force distribution and electromotive force waveform, so it is extensively used in PM machines. On the other hand, research on machines with

fractional-slot concentrated winding has, in the last decade, attained significant attention [Barrero and Duran (2016), Rezazadeh et al (2018), Sui et al (2019)]. A fractional-slot concentrated winding is employed when the slot pitch is lower than the pole pitch. If the required output waveform is trapezoidal with higher magnitude and less power rating, as for example in brushless dc (BLDC) motors, concentrated winding can be used. It has been shown in different research papers that such winding configurations can be advantageous over a conventional distributed one. In an attempt to observe and summarise the advantages and drawbacks of both winding configurations, a good starting point can be work presented in [El-Refaie (2010)]. Further recent and relevant data can be found in, for example, [Barrero and Duran (2016)].

The differences in performances of the fractional-slot concentrated winding (interior and surface PM) machine and the same machine with distributed windings have been established in recent literature [El-Refaie et al (2008a), El-Refaie (2010), Zheng et al (2013), Sui et al (2014), Reddy et al (2015)]. The machine performances (i.e. power density, torque ripple and field-weakening operation) for the two mentioned stator configurations have been investigated with different combinations of slots per pole per phase [El-Refaie et al (2008a), El-Refaie (2010)] and with different multilayer and multiphase machine configurations [El-Refaie et al (2008a), El-Refaie (2010), Alberti and Bianchi (2013)]. Studies using the same performance indices were later further expanded in [Pouramin et al (2017)]. Here, five different internal PM rotor topologies (V-type, double V-type, flat-type, double flat-type and spoke-type) in combination with both concentrated and distributed stator winding arrangements were analysed. A similar approach related to concentrated winding stator and customised rotor was also investigated in [Kang et al (2013), Aslan and Semail (2014), Zahr et al (2017)] but with a focus on harmonic current injection and flux-weakening region investigations. Because rotor losses are often stated as one of the main disadvantages of fractional-slot concentrated winding machines [Boglietti et al (2014)], impact of the number of phases and right slot-per-pole combination were studied in [Fornasiero et al (2012), Aslan et al (2014)]. In this study, a comparison was made for three-, five- and seven-phase machines with conclusion that higher phase number means lower spatial harmonic components (although higher than expected) and lower rotor losses.

Following from the cited works, it can be concluded that the interest in PM machines area with concentrated winding design is high. In the earlier days this was mainly because of lower winding cost in manufacturing process and more compact design when compared with conventional machines with distributed design [Magnussen et al (2004)]. In this paper, two three-phase different surface-mounted fractional-slot concentrated winding machines (with number of slots per pole per phase equal to $q = 0.5$ and $q = 0.36$) and machine with distributed winding design (with $q = 1$) were observed. Despite the fact that rotor characteristic and dimension of all three machines were equal, different results were acquired. It has been shown in this study that machines with concentrated windings have higher inductance (which is mainly related to higher slot leakage), superior thermal performance in constant power region (due to

lower winding losses), lower torque ripple and wider field-weakening operating region with better performances than machines with distributed windings. Nevertheless, the main advantage of distributed winding configuration, that is, the best utilisation of inverter rating in the base speed region, was once again also confirmed. But this was at that time of lesser importance because some interesting advantages of fractional-slot concentrated winding machines were highlighted, and many new areas of research were opened.

Based on this research, in the last ten years many studies have been conducted to further explore fractional-slot concentrated winding PM synchronous machines (both three-phase and multiphase cases). Advantages that this winding design offers are summarised in [El-Refaie (2010)], and are high-power density, high efficiency, short end-turns, high slot fill factor (particularly when coupled with segmented stator structures), low cogging torque and better field-weakening characteristics, as well as better fault-tolerant capability. In [Aslan and Semail (2014)] simplicity of manufacturing, maintenance and recycling were also added to the list. Although there are many advantages that fractional-slot concentrated winding design offers to designer, there are also some drawbacks that must be taken into consideration. Again, summarised in [El-Refaie (2010), Boglietti et al (2014), Rezazadeh et al (2018)], one must be aware that this winding arrangement causes significant rotor losses (including magnet losses, rotor core losses and sleeve losses in case of a conductive sleeve) and higher distortion of air gap flux density. This particularly applies in the high-speed region due to the lower (sub) and higher (super) order space harmonic inherent to such winding configuration, because they are not in synchronism with the rotor. Potentially higher parasitic effects (due to additional harmonic contents) like noise, unbalanced magnetic forces and torque ripple can also be present in this machine winding type.

Although fractional-slot concentrated winding multiphase machines are still under investigation, because of some important features that they have, they are today already employed in high-reliability applications such as off-shore wind energy conversion generators and electrical vehicles. When electrical vehicles are considered, a wide speed range and fault tolerance are required. This asks for good operational behaviour in the field-weakening region. In [Aslan and Semail (2014)] a concentrated winding machine with 20 slots and 8 poles (fractional number of slots per pole per phase) was investigated for hybrid automotive applications. The disadvantage of the winding arrangement related to low reluctance torque was compensated using a novel rotor structure. In [Cavagnino et al (2013)] a duplex three-phase surface PM generator integrated inside aircraft main gas turbine engine was studied from a safety (fault-tolerant) standpoint, while a similar investigation was made in [Zheng et al (2011)] for in-wheel motor. On the other hand, one of the main reasons why fractional-slot PM concentrated machines are used in wind energy conversion systems is good fault-tolerant capability. To achieve such capability, single-layer concentrated winding layouts were investigated in [Bianchi and Pre (2006)]. Based on that research, a similar machine configuration was later used to test a modular machine in [Li et al (2017)]. Because segments are separated physically and magnetically in modular machines,

faults would not propagate from one segment to another, i.e. possible fault interaction between phases is reduced. In this research, optimal slot/pole number combination for modular PM machines with different phase numbers is also identified.

As it can be concluded from this short literature survey related to machine winding design, concentrated fractional-slot arrangement is today an interesting choice in many cases (especially for machines with more than three phases), but distributed winding design is still advantageously used in (PM) machine production because of near-sinusoidal MMF/EMF distribution. For the machine in this thesis, a quasi-distributed winding is applied. This will result in a near-sinusoidal MMF distribution on stator side, but because magnets on rotor are arranged in a specific way (as explained in chapter 1), back-EMF shape in this machine will be non-sinusoidal, allowing further investigation of torque enhancement and flux-weakening (i.e. areas in which concentrated windings are dominant today).

2.3.1 Symmetrical/Asymmetrical Winding Reconfiguration

The nine-phase machine, investigated in this work, can be further classified as belonging to machine group with a composite odd phase number, for which winding configuration (symmetrical or asymmetrical) can easily be obtained by only rearranging voltage source inverter power supply cables at the machine's terminal box. Such a possibility was briefly mentioned in [Klingshirn (1983)] and restated in [Jung et al (2012)], but has never been explained in detail, generalised or experimentally verified. It therefore appears that this knowledge, common to electric machine designers, has so far by and large escaped the attention of the drive control community, and hence is covered in this thesis.

Asymmetrical and symmetrical configurations are rarely treated together for the same phase number, primarily since for each particular case it is known which topology is better. As stated in [Nelson and Krause (1974)], the required spacing between multiple winding sets for best performance is π/n for an even number of sets and $2\pi/n$ for an odd number of sets. A rare exception is [Patkar et al (2017)], where, to test derived symmetrical/asymmetrical structure control algorithms, two different six-phase induction machines (with different parameters and windings) were used. In real world applications, once when the phase number is selected, the preferred configuration (symmetrical or asymmetrical) is in essence known, hence the practical importance of the described work in this thesis primarily relates to the laboratory environment, where in most cases only a single machine is available.

2.4 Torque Enhancement in Machines with Non-Sinusoidal Back-EMF

In the past, considerable efforts have been devoted to designing rotating ac machines with distributed windings in order to create sinusoidal MMF and EMF. With the advent of solid-state

converters, the aim became to develop switching strategies such that the output voltage waveforms have low harmonic content, the objective being to produce a rotating field within the machine having a minimum of time harmonics. As a result, the iron core is effectively underutilized since only approximately one-third is near saturation. Probably the first work to consider machine designs that are better suited to the output waveforms of power electronic converters was published in 1984 [Lipo and Wang (1984)]. The paper describes design and analysis of an asymmetrical six-phase, salient-pole, synchronous machine with full-pitch concentrated windings having one slot per pole per phase. Each three-phase winding had an isolated neutral. The machine was tested as a generator supplying a resistive load through a rectifier. The paper reported that the machine is capable of supplying 15% more power than a conventional three-phase equivalent of the same size. Shortly after, the work reported in [Weh and Schroder (1985)] used a gate turn-off thyristor inverter producing almost square-wave current in conjunction with a 200 kW seven-phase synchronous reluctance machine, controlled in a similar way to a BLDC. The paper reported considerably higher torque production compared with a three-phase machine. Another interesting approach, referenced in many papers, considers torque enhancement through (third-) harmonic current injection. This approach was first used to increase the specific torque of five-phase induction and synchronous reluctance machines. It was shown that these machines are capable of producing more torque for the same amount of copper and iron as equivalent machines without it. Because high torque capability is essential for the electric machine drive system in the applications of emerging technologies in modern transportation, such as electrical vehicles and ship propulsion, and in wind power generation, a substantial amount of research works started to emerge.

A five-phase synchronous reluctance machine with concentrated windings was proposed in [Toliyat et al (1990)]. The machine (with third harmonic current equal to the 33% of fundamental) was capable of producing a 12% increase in torque per ampere, when compared to a three-phase equivalent. A number of papers then followed, which considered various aspects of the five-phase synchronous reluctance drive, such as mathematical modelling, parameter estimation, FEM modelling [Toliyat et al (1991a), Toliyat et al (1992), Toliyat et al (1998)] and field oriented control using a digital signal processing [Toliyat et al (2000), Shi et al (2001)]. A nine-phase synchronous reluctance machine was investigated in [Coates et al (2001)] under field-oriented control. Two types of current control techniques were investigated for torque improvement, one in the stator reference frame and the other in the *d-q* reference frame, and for this purpose, the third, the fifth and the seventh current harmonics were injected into the machine.

Induction machines with enhanced torque capabilities have also been the subject of research over the years [Toliyat et al (1991b), Toliyat et al (1991c), Toliyat and Lipo (1994), Xu et al (2001), Lyra and Lipo (2002), Duran et al (2008), Zheng et al (2008), Arahal et al (2009), Arahal and Duran (2009)]. The five-phase case is studied in [Toliyat et al (1991c), Toliyat and Lipo (1994), Xu et al (2001), Zheng et al (2008)]. The work in [Toliyat et al (1991b & 1991c)] contains a general theoretical analysis

of all relevant phase numbers, assuming a concentrated winding induction machine. Fourier analysis is used for investigation of the effects of different air-gap field spatial distribution harmonics (of order *h*) and time harmonics (of order *v*) in the supply. It is found that those MMFs that are produced by the same order of space and time harmonics rotate forward at synchronous speed. All others are rotating at speeds equal to *v/h* times synchronous speed, some in the forward direction and some backward. In asymmetrical nine-phase machine, for example, this means that the fifth and the seventh spatial harmonic, when interacting with the fifth and the seventh time harmonic, can produce average torque. In a symmetrical nine-phase machine (and single neutral), the additional torque can be produced using the third, fifth and the seventh harmonics of the current and winding function. In [Xu et al (2001)] a model of a five-phase induction machine including the third harmonic MMF is derived, and the corresponding transformation matrix which includes the third harmonic is given. A FOC scheme, including third harmonic injection, is designed and tested using simulations. As a result, 27% higher fundamental torque peak component was achieved. In [Mengoni et al (2015)] the maximum torque at any speed (even in the field-weakening region) is optimally found by injecting third harmonic current in a machine with classical integer-slot winding. As shown, the improvement of the torque can be up to 17% for a given RMS current. In [Zheng et al (2008)] a technique to improve the flux pattern within a five-phase induction machine is presented. The technique is developed through dual-plane vector control, with synchronised fluxes. The magnitude and rotating speed of the associated fluxes (fundamental and third harmonic) are independently controlled in each subspace. The resultant air-gap flux density is fully controlled, preventing iron saturation. A quasi-trapezoidal air-gap flux density distribution is achieved for better iron utilization and higher torque density. It is confirmed that, compared with sinusoidal fluxing, the quasi-trapezoidal flux pattern will not lead to an oversized power inverter when improving the machine's torque density. An asymmetrical six-phase induction machine with distributed windings is studied in [Lyra and Lipo (2001), Lyra and Lipo (2002)] and the third harmonic zero sequence current component is injected into the phase currents to increase the machine's torque density. It is shown that the increase in developed torque is due largely to the injection of the third harmonic, causing the fundamental air-gap peak flux density to reduce; thus, it is possible to increase the torque by increasing the fundamental flux component to re-establish the flux to its original value. This enables increasing the fundamental without saturating the machine. A nine-phase symmetrical induction machine with concentrated windings is considered in [Bastos et al (2015)] where a comprehensive approach for the derivation of equivalent circuits for steady state operation for both fundamental and third harmonic frequencies is given. The dynamic performance of the drive is verified using simulations. In [Arahal et al (2009)] a five-phase induction motor drive is studied with the aim to investigate variable third harmonic current injection, because constant current injection is not always optimal for the whole range of operation. Based on the similar optimisation idea, transient performances of the same multiphase machine were observed in [Arahal and Duran (2009)] and a dynamic PI regulator tuning algorithm was proposed.

Finally, torque enhancement in multiphase PMSMs has also been the subject of considerable research efforts. Works related to both surface mounted and interior magnet machines can be found in the literature. A five-phase PMSM with concentrated windings, such that the EMF is almost trapezoidal, is presented in [Parsa and Toliyat (2005a), Parsa et al (2005)]. The drive is supplied with combined sinusoidal plus third harmonic currents. The motor is able to produce the same torque as an equivalent BLDC; however, it overcomes the BLDC disadvantages such as torque ripple and complex control above the base speed region. The paper used FEM simulations to study flux density and calculate the steady state torque. Implementation of this, so called 5BPM, was afterwards applied to ship propulsion and the results are presented in [Parsa and Toliyat (2005b)], while in [Parsa et al (2005)] the operation of the same machine in the field-weakening region is analysed and a suitable control scheme is developed. Design considerations of a five-phase PMSM are given in [McCleer et al (1991)], where both radial and axial flux type machines are considered, and the authors claim that up to 27% improvement in torque per given volume of the machine is possible with additional current harmonic. Different improvement percentages were later reported in many other papers for a five-phase surface permanent magnet machines. In [Zhao and Yang (2011)], a 21% improvement was recorded with the same torque quality while for different adaptations of rotor investigated in [Wang et al (2014), Sadeghi et al (2014)] achieved improvement was in the range 9 - 17%, keeping the same RMS current value and small torque ripples. Torque enhancement through harmonics produced by magnet shaping was first investigated in [Li et al (2003)]. In this research, the optimal third harmonic component amplitude was not analysed. This problem was later investigated by [Zhu et al (2012)], while more recently, the work presented in [Wang et al (2017a), Wang et al (2017b)] looked at a five-phase permanent magnet machine, where the surface magnets are shaped to produce flux at fundamental and low order frequencies. It is shown that for optimal harmonic injection, the third harmonic component must be 1/6 of the fundamental and that in this case, torque improvement can be >30%. However, in addition to the third harmonic component, PM shape also adds the fifth and the seventh harmonic to the back-EMF. In a five-phase machine, those are non-torque producing harmonics (and they can cause undesirable effects such as localized saturation, additional iron losses, eddy currents losses in magnets etc.) and they need to be eliminated through resonant current control [Wang et al (2014), Yepes et al (2017)]. In [Sui et al (2017)] single- and dual-plane vector control strategy for five-phase PMSM was investigated and for dual-plane control, three different methods of current harmonic injection were compared. It can be concluded on the analysis given up to now that the problem of how to get more torque out of the same machine has been investigated many times during the last two decades. However, few papers focus on the evaluation of the machine losses due to the third harmonic current injection. Because of that reason, in [Fei and Zanasi (2011), Sui et al (2017)] a study was conducted with the purpose to further analyse this issue. In [Sui et al (2017)] three kinds of current injection methods for torque improvement were studied. Based on the principle of minimum copper loss and equal amplitude of currents, the post-fault control strategies were investigated with/without the third

harmonic component considered. It has been shown that in five-phase PM synchronous machine torque can be improved by injecting the third harmonic current but the choice between different third harmonic current injection methods depends entirely on the targeted application. Finally, as already mentioned in earlier sections, a low voltage five-phase interior PM synchronous machine is designed in [Aslan and Semail (2014)] for automotive applications. A new bi-harmonic rotor (created by adding extra radial magnets to the rotor) is designed, which produces the third harmonic EMF to link with the third harmonic MMF produced by the stator windings. In the base speed region, the machine operates using both the fundamental and third harmonic currents, producing 33% higher torque with the same volume machine. Above the base speed, the drive uses only the fundamental component effectively operating in a pseudo-field weakening mode. The principles related to the third harmonic current injection and bi-harmonic rotor structure presented in [Aslan and Semail (2014)] have led to further work of the same research group. For example, a surface PM five-phase machine torque optimisation was investigated in [Scuiller and Semail (2014)]. Further works include optimisation of control strategies for five-phase high-speed traction machines [Zahr et al (2016a)], investigation of maximum torque, power and speed with low armature reaction [Scuiller et al (2016)] and research about control under voltage and current limits (i.e. flux-weakening control) [Zahr et al (2017), Bermudez et al (2019), Zhang et al (2019a)]. In [Zahr et al (2016a)], FEM simulation shows how the torque/speed characteristics can be largely extended in constant power area for transient operations while in [Scuiller et al (2016)], a more general study has been achieved for investigated surface PMSM with low armature reaction showing potentials of such machines. Regarding research related to the flux-weakening region, a more detailed coverage is given in section 2.6.

Based on many research studies focusing on torque density improvement and the different increase percentages that have been reported, it is clear that the torque improvement in a machine depends mostly on the ratio between the magnitudes of the fundamental and the third harmonic components in back-EMF (PM flux). Mathematical models for the determination of the optimal third harmonic current injection were therefore investigated and derived in [Zhao and Yang (2011), Sui et al (2017), Gu et al (2018), Gong et al (2019)]. In [Sui et al (2017)], three different methods for optimal fundamental to third harmonic current ratio were studied based on PM flux magnitudes. The same amplitude constraint, the same RMS constraint and ratio of torque to losses methods were investigated and validated by FEM analysis. It should be noted that these are not the only techniques used in existing literature (there are also methods based on machine design properties and different optimisation procedures), but the same RMS constraint (calculated on maximal torque-per-Ampere principles) is the dominant one [Gong et al (2019)]. In [Gu et al (2018), Gong et al (2019)], a similar approach to the one in [Sui et al (2017)] was used, but this time equations for the optimal injection ratio were obtained by using back-EMF magnitudes instead of PM flux components. Going one step further, in [Wang et al (2015)], an investigation which studies relation between optimal injection ratio and stator

winding topologies/stator slot numbers was performed. For this purpose, a five-phase surface permanent magnet machines with the same rotor and with non-overlapping (10-slot/8-pole) winding and overlapping (40-slot/8-pole) winding was tested. It has been demonstrated that the machine stator slot number and different winding topologies can have significant influence on the optimal third harmonic current injection ratio. As shown, in 40-slot/8-pole configuration, produced third harmonic back-EMF component (22% of the fundamental) is much higher than the one in 10-slot/8-pole configuration (4%). Consequently, this means higher output torque in the machine with 40-slot/8-pole configuration.

With regard to interior permanent magnet multiphase machines, an interesting research is conducted in [Stumberger et al (2003)]. Regular three-phase stator windings of an interior permanent magnet synchronous motor were replaced with two sets of three-phase electrically isolated windings, and one set was shifted from the other by 30° in space. In this way, an asymmetrical six-phase stator winding was obtained. It was shown that improvement of the output torque with the third harmonic current injection is up to 42% if compared with original three-phase configuration, although this required use of the seventh inverter leg (since the third harmonic currents in an asymmetrical six-phase machine do not sum to zero). Beside work in [Stumberger et al (2003)] and some references given in previous paragraph, torque enhancement by harmonic current injection in an interior PMSM was reported in [Gautam et al (2011), Aslan et al (2012), Liu et al (2018) and Gong et al (2019)] as well, while research about enhancement of torque through magnet shaping can be found in, for example, [Wang et al (2012)].

Literature in this section has been so far categorized based on typical machine classification (i.e., synchronous reluctance, induction, PM synchronous). This was possible because most of the existing research works are mainly focused on the third (current/EMF) harmonic component. As stated in [Toliyat et al (1998), Levi (2008)], in an n phase machine (with n being an odd number) all high-magnitude odd low-order harmonics between 1 and n can be used to couple with the corresponding spatial MMF harmonics to produce additional torque. Although the third harmonic injection has been investigated many times to this day, other harmonic components higher than 3 and lower than machine phase number have been investigated to a far less extent. A brief summary is provided in what follows.

The 3^{rd}, 5^{th} and 7^{th} harmonic current injection to enhance torque of a nine-phase synchronous reluctance machine was investigated in [Coates et al (2001)]. Generalized *d-q* equations were derived, and it was shown that odd harmonics of the current can efficiently be used to enhance the output torque production. In [Abdel-Khalik et al (2010)], steady-state analysis of the 3^{rd}, 5^{th}, 7^{th} and 9^{th} harmonic current injection was conducted for an eleven-phase induction machine. It was shown that an increased number of injected harmonics increases the output torque and the maximum dynamic stability limit. The maximum achieved torque was 27.5% higher than with the fundamental only. The same machine was again investigated in [Abdel-Khalik et al (2011)] under open loop control. The target was to investigate the air-gap flux distribution under the applied sequence and harmonic injection to obtain an optimum

flux distribution using a generic algorithm that evaluates the optimal flux constants. Based on this concept, iron utilization was maximized giving more torque per ampere. Multi-harmonic torque enhancement was investigated in [Hu et al (2014), Hu et al (2017)] as well, considering the 5^{th} and 7^{th} harmonic currents. Here, a dual three-phase PMSM was studied using the same current amplitude constraint. It has been shown that the torque can be increased by 7.7-8.6% with negligible torque ripple. Another interesting research related to the multiple low-order harmonic utilisation in *n*-phase machines was presented in [Farshadnia et al (2018)]. Although this research is not entirely related to the machine control, it is worth mentioning because it presents a novel heuristic algorithm for symmetrical fractional-slot concentrated winding multiphase PMSM design, which maximizes the output average torque under the current harmonic injection. Likewise, research presented in [Gautam et al (2011)] deals with the modelling of a nine-phase internal PMSM considering the 3^{rd}, 5^{th} and 7^{th} harmonics. Cases with and without damper windings were studied for the clear understanding of advantages such as fault tolerance and torque ripple reduction. It is important to note that in the surveyed literature optimal injection ratios between fundamental and other injected harmonics were determined using optimisation tools [Hu et al (2014), Hu et al (2017)] or methods based on design machine properties, such as winding factor/flux density [Abdel-Khalik et al (2010), Abdel-Khalik et al (2011), Farshadnia et al (2018), Gautam et al (2011)].

2.5 Sensorless Control

To measure rotor's position and compute speed, typically an encoder or resolver is mounted on motor's shaft. These sensors need a special mechanical mounting and cabling, especially when the motor is far from the drive controller. Needless to say, with implementation of the position sensor overall cost of the drive is also increased. Because position sensor increases mounting and maintenance cost, i.e. reduces the reliability of the whole system [Batzel et al (2000), Lidozzi et al (2007)], in many applications today (such as for example smaller automotive and home applications [Betin et al (2014)]) position sensors are actually avoided and so called sensorless control strategies are implemented. Even if the position sensor is not completely removed from the drive system, the sensorless methods are sometimes still used as a backup to provide rotor position information in the case of position sensor failure [Betin et al (2014)]. This is of a major interest for safety critical applications such as for example more- and all-electrical aircrafts, and the electrical transportation applications in general. A mechanical position sensor is replaced by the corresponding position/speed estimator, which reconstructs the position information through electrical quantities measurements. Motor currents, voltages at motor's terminals and inverter dc-link voltage measurements are usually employed for this purpose.

Attempts to classify sensorless control solutions by considering specific aspect of PMSMs were reported in [Acarnley and Watson (2006), Garcia et al (2007), Boldea (2008), Briz and Degner (2011)].

Probably the most complete and up to date technology status classification nowadays can be found in [Ma and Zhang (2018)]. From this work a simple but complete classification of sensorless control techniques can be established. Two main categories of sensorless strategies exist: methods based on excitation signals at the fundamental motor frequency and methods based on motor saliency tracking. If the motor is operated using excitation signal at the fundamental frequency, estimation of the back-EMF or magnetic flux is used to extract the rotor position and speed. Normally, the back-EMF methods offer accurate position estimation when PMSM is operated in the middle and high-speed range, but zero-speed operation is not possible at no-load conditions (due to the low EMF harmonic magnitude). It should be mentioned that the minimum operating speed can approach zero if specific conditions are satisfied (such as highly accurate machine model, highly accurate measurements of voltages and currents, special compensation of the voltage source inverter effects, etc [Garcia et al (2007), Briz and Degner (2011)]). Needless to say, this is not always the case and certainly not easily applicable for the different real-world scenarios. A great amount of work was therefore completed trying to improve the low-speed performance of EMF based algorithms [Bolognani et al (2014)], or as an alternative, propose a so-called hybrid control methods [Fatu et al (2008)]. Large number of various state observer based methods, such as Luenberger observer, sliding mode observer, extended Kalman filter, I/f starting methods etc, have been studied for this purpose [Ma and Zhang (2018)]. Although hybrid combination of the two different methods for low- and high-speed ranges yields good results, there are still many problems that need to be solved or/and improved. Authors in [Ma and Zhang (2018)] give initial (starting) position estimation, parameter sensitivity, and FPGA implementation as some of the examples.

Methods based on saliency tracking are, on the other hand, sensorless control approaches that can work at standstill and at very low speeds. Fundamental frequency quantities are involved in the electromechanical energy conversion, while PMSM saliencies are exploited for the rotor position estimation. The category can be further divided into two groups: continuous high frequency injection and transient excitation methods (subcategories can be found in [Ma and Zhang (2018)]). Although the working performance of all high frequency injection methods is relatively good, in addition to the reduced efficiency at high speeds, signal injection could also cause extra losses, torque ripple and transient disturbances [Acarnley and Watson (2006)]. On the other hand, transient excitation methods require modification of the hardware and hence are, for example, not suitable for implementation in industrial applications. In general, saliency tracking based methods can work at zero speed and in low speed range but are highly dependent on the saliency information. Without the correct information of this parameter, interferences in control algorithm can easily occur [Acarnley and Watson (2006), Garcia et al (2007)].

While a considerable amount of work has been reported for three-phase systems, sensorless control of machines with more than three phases has been studied to a far less extent. In [Olivieri (2013)] the rotor position estimation with a Luenberger-like state observer for a five-phase PMSM was presented,

with the attention focused on the design criteria that can be used to extend the effective range of the sensorless strategy to operation under a faulty condition. In [Parsa and Toliyat (2007b), De Belie et at (2014)] similar problems were investigated for a five-phase interior permanent magnet motor where the position and speed information have been estimated using the position of the stator flux linkages and EMF harmonic components, respectively. In the latter case, estimation of the rotor position was performed by observing (from phase currents and phase voltages) the fundamental and the third harmonic orthogonal EMF components. Building on a technique from [De Belie et al (2014)], work in [Stiscia et al (2019)] investigated a novel sensorless control approach for a nine-phase non-sinusoidal back-EMF PM synchronous machine prototype studied in this work. It was shown that the third harmonic of the back-EMF can be successfully utilized for precise rotor position estimation. In both [De Belie et al (2014) and Stiscia et al (2019)] phase-locked loop control [Zhang et al (2016), Ilioudis (2017), Bierhoff (2017), Varatharajan et al (2018)] was used instead of usually implemented inverse trigonometrical functions (e.g. arctangent), since finding inverse of trigonometric functions can be computationally intensive.

Although EMF based sensorless control of a nine-phase PMSM in [Stiscia et al (2019)] showed that position estimation using the third harmonic is possible, the third EMF harmonic is not used there for the best possible outcome. As it will be shown in this work, the third harmonic (almost equal in magnitude to the fundamental), can be applied to significantly improve electromagnetic torque, by up to 36%.

2.6 Flux-Weakening Operation

In electrical vehicle applications, high-power density and fault-tolerant capability are commonly required properties for machine drives. In addition, a wide speed range capability is also required, often making the machine to operate above-nominal speed. It is well-known that a machine can operate in two operating regions, the first one being from zero up to rated speed/frequency (called constant flux or constant torque region) and the second one being above rated speed (known also as constant power or field- (flux-) weakening region). Because high-power density, fault tolerance and field-weakening operation must be achievable with low dc-bus voltage, multiphase PM machines are an interesting alternative [Scuiller and Semail (2014)]. The study of the field-weakening ability of multiphase machines can be considered as being equivalent to the study of dc-bus utilisation improvement [Scuiller et al (2016)] because the maximum voltage that can be supplied to the machine by the inverter is limited by dc-link voltage [Parsa et al (2005)]. This problem was (in case of multiphase machines) analysed in [Levi et al (2008)], where an analytical approach to determine the boundaries of the linear modulation region for multiphase inverter has been made. Because this study was mainly oriented to converter side, effects of back-EMF and inductances in machine were not examined. The approach and

its effectiveness were later demonstrated in [Casadei et al (2008), Casadei et al (2010), Mengoni et al (2015)] where this was applied to a seven-phase induction machine with field-weakening capability. It is shown that the proposed control approach is able to utilize the maximum torque capability of the motor at any speed.

Numerous researchers have investigated the flux-weakening operation for three-phase PM machines fed by a voltage source inverter. In [Schiferl and Lipo (1988)] surface PM synchronous three-phase machine with and without saliency was investigated to analytically determine the torque/speed characteristic in both below and above the nominal speed regions. For the same reason and using the machine with the same number of phases, in [Magnussen et al (2004)] the winding design influence on the flux-weakening ability was investigated. For that purpose, PM synchronous machines with concentrated fractional-slot design and distributed full pitch winding design were studied. A similar investigation was presented in [El-Refaie et al (2006)] where the focus was the development of a new technique for analysing a surface PM machines equipped with fractional-slot concentrated windings. It is important to note that, as already highlighted in section 2.3, one of the main disadvantages of surface PM machines is poor field-weakening capability. It is well-known that optimal flux-weakening for surface PM machines occurs when the characteristic current (i.e. magnitude ratio between the permanent magnet flux and the *d*-axis stator inductance) of the machine is equal to the rated machine current. If the flux-linkage is reduced, the torque capability of the machine is compromised and, as a result, the current tends to be significantly higher than the rated. Consequently, constant power is harder to maintain, i.e. flux-weakening operation for surface PM machines is severely limited [El-Refaie et al (2006), El-Refaie (2010)]. A key advantage of fractional-slot concentrated winding machines, as presented in [El-Refaie et al (2006)] is that they help achieve a wide speed range in constant power operation. As already explained, this is one of the reasons why fractional-slot concentrated winding PM machines are widely investigated today.

While there are many papers that address field-weakening operation of three-phase PM machines, there are few papers that deal with PM multiphase machines. The reasons, as stated in [Scuiller et al (2016)], are mainly because multiphase machines are not used to the same extent as three-phase machines and because they behave as several *d-q* circuit machines, thus making analytical computation of the *d-q* currents in flux-weakening region difficult to achieve. Furthermore, among the few papers that exist [e.g. Parsa et al (2005), Xuelei et al (2011)], most of them focus on the control side for a given machine and for a particular speed operating point. In [Parsa et al (2005)] the flux-weakening control method for a five-phase PM synchronous machine was proposed with a focus on the fundamental and third harmonic current commands. Equations to calculate flux- and torque-producing commands were determined analytically, and for this purpose stator resistance was neglected. Combining work in [Parsa et al (2005)] with the complex reference voltage vector limit calculation demonstrated in [Levi (2008)], extended field-weakening control strategies were proposed in [Casadei et al (2010)] and

later in [Xuelei et al (2011)]. Considered machines were five-phase permanent magnet [Xuelei et al (2011)] and seven-phase induction [Casadei et al (2010)]. Once again, in addition to the fundamental, the third harmonic currents were employed. By precisely determining the reference voltage vector limits, and harmonic current commands, improvements in the region above base speed were reported in both works. Nevertheless, it should be also noted that both works targeted specific multiphase machines, i.e. it is hard to apply the presented results to other multiphase machines types. In order to formulate a general technique, in [Lu et al (2012), Scuiller and Semail (2014)] a numerical approach was suggested and used to determine the current sharing among the *d*-*q* subspaces at a given speed and for a given dc voltage for an *n*-phase machine.

In [Aslan and Semail (2014)], an interesting approach for the flux-weakening operation of five-phase (concentrated winding) machine was introduced. A bi-harmonic rotor design was presented which produces a lower fundamental harmonic component amplitude of flux than the third harmonic flux component. A control strategy that combines these harmonics is developed in both speed-regions. In the low speed-region, current is distributed between fundamental and third harmonic, allowing high-torque density with classical third harmonic current injection. In the high-speed region (i.e. over nominal speed), only the fundamental current is used. Because control algorithm now uses only weakened fundamental flux component, lower current density in the machine slots is needed to keep constant power functionality, hence, better flux-weakening performance of surface PM synchronous machine can be achieved. Afterwards, work in [Scuiller et al (2016), Zahr et al (2017), Zhang et al (2019a)] extended the research in [Aslan and Semail (2014)] to consider open circuit faults and subsequently proposed fault-tolerant strategies which are beyond the scope of this work. Work in [Hassan (2018)] reported similar conclusions as the work in [Aslan and Semail (2014)]. As it turns out, investigated five-phase PMSM machine is in flux-weakening region achieving highest speed if only fundamental component is used, while third harmonic component (although used in MTPA region for torque boost) is controlled to zero. Optimal current references for flux-weakening (FW) control were here calculated analytically, by neglecting stator resistance. With such control, prototype machine can reach FW speed which is significantly higher than the base speed.

2.7 Summary

In this chapter, a review of the literature relevant to this research is presented. References are classified in a way that the main notions about multiphase machines (categorisation, design, modelling, model transformation and control) are presented first, followed by a review of works important to the work undertaken in this thesis (that is, winding distribution, torque enhancement using third- (and multiple) harmonic current injection(s), sensorless control and flux-weakening operations).

Chapter Three

MODELLING OF THE MULTIPHASE PMSMs

3.1 Introduction

In this chapter, multiphase machine modelling and control system are described. The main objective is to develop a generalised mathematical model of a machine with arbitrary phase number on the stator. The focus is placed on surface mounted permanent magnet synchronous machines. Two different modelling approaches are considered, that is, machine models in phase-variable (phase domain, *abcn*) and synchronous (rotating, *d-q*) reference frames are studied. The machine develops a (near-) sinusoidal back-EMF, hence ideal machine models are presented and tested in this chapter. In that way, the general machine modelling and control principles are explained, and a benchmark configuration (with two 180° magnets) is defined/analysed before moving on to the non-sinusoidal back-EMF distribution (and shortened magnet span) in the following chapters. A field oriented control method is developed and validated using the *Matlab*/*Simulink* environment. To further verify the results, a finite element method software tool is used.

The machine model in terms of phase-variables is first presented. In this process, n different equations for voltages, currents and flux linkages emerge. The mutual inductance between each phase and the other (n - 1) phases needs to be taken into consideration. Therefore, to simplify the model development, modelling process is divided into two sections, where one represents electrical part of the machine while the other deals with the magnetic equations. Analysis of the machine in phase-variable reference frame can be difficult to handle, so transformation matrices for decoupling are applied. Specifically, the vector space decomposition (VSD) transformation is used for this purpose. Matrices are presented for symmetrical and asymmetrical winding configurations with a single isolated neutral point and amplitude invariant scaling coefficient. After applying rotational transformation and system decoupling, flux- (d) and torque- (q) producing currents are obtained and the machine model in a rotating reference frame is further derived. Consequentially, this allows the modelling in phase-variables (which is more convenient here because of specific back-EMF) and control implementation in synchronous reference frame.

Finally, the composite odd phase number machine investigated here can be placed into a category of machines for which change of winding configuration can easily be achieved by simply rearranging the power supply leads in the machine's terminal box. Based on the provided literature review, it appears that this possibility has not been investigated in detail. This work has resulted in a journal publication [Slunjski et al 2020].

3.2 Phase-Variable Reference Frame Machine Modelling

When deriving machine model equations, a number of standard simplifying assumptions are usually postulated. In particular, it is assumed that all the individual phase windings are identical. Furthermore,

the winding is distributed across the circumference of the stator and it is designed in such a way that the MMF can be regarded as (near-) sinusoidal, i.e. all spatial harmonics except the fundamental and (in this thesis) small third are neglected. The reason why small third harmonic is modelled is related to the fact that when rotor with two 180° magnet poles is considered in the studied machine, this component is present in the back-EMF (more about this will be said at the end of the chapter where finite element analysis is given). Impact of slots is also neglected, i.e. the air-gap can be regarded as uniform. Temperature-related variations and frequency-related variations due to skin effect are neglected, so resistance on stator can be considered constant all the time and equal in all phase windings. The same can be also assumed for leakage inductances. Lastly, effects of saturation and losses in the ferromagnetic material due to hysteresis and eddy currents are neglected.

In a multiphase machine the number of phases n can be represented as product of winding sets k_{ws} and number of phases a per each winding set. Number of winding sets can be any integer larger or equal to 1, while number of phases per winding set is a prime number, which is equal to or larger than 3. This can be mathematically written as:

$$\begin{aligned} &n = k_{ws} \cdot a \\ &k_{ws} \geq 1; \quad a = 3,5,7... \end{aligned} \tag{3.1}$$

Distribution of phases around stator's circumference depends on the propagation angle between winding sets. This angle can be $2\pi/n$, in which case symmetrical winding configuration is implied, or π/n, which means that the winding configuration in a machine is asymmetrical. For the purpose of completeness, it must be noted that machines with a single winding set ($k_{ws} = 1$) also exist and are built with symmetrical winding configurations. Spatial angular position ($\theta_{j,i}$; generalised case) of the i^{th} ($i = 1, 2, 3, \ldots, a$) phase in j^{th} ($j = 1, 2, 3, \ldots, k_{ws}$) phase set, for a symmetrical and asymmetrical configuration can be defined as:

$$\theta_{j,i} = \begin{Bmatrix} \frac{2\pi}{n}\left(k_{ws}\left(i-1\right)+\left(j-1\right)\right), & sym. \\ \frac{\pi}{n}\left(2k_{ws}\left(i-1\right)+\left(j-1\right)\right), & asym. \end{Bmatrix} \tag{3.2}$$

Mathematical expression defined with (3.2) is illustrated in Fig. 3.1. In Fig. 3.2, a similar generalisation is shown, considering a winding distribution around stator circumference for machine configurations with multiple three-phase winding sets. Finally, following from the Fig. 3.2, a symmetrical and asymmetrical winding distribution possibilities in the studied machine are shown in Fig. 3.3. The stator windings are arranged as three three-phase sets (that is, $k_{ws} = 3$ and $a = 3$) and labelled as $a1$, $b1$, $c1$ for Set-1, $a2$, $b2$, $c2$ for Set-2 and $a3$, $b3$, $c3$ for Set-3. Such a nomenclature will be used throughout the thesis.

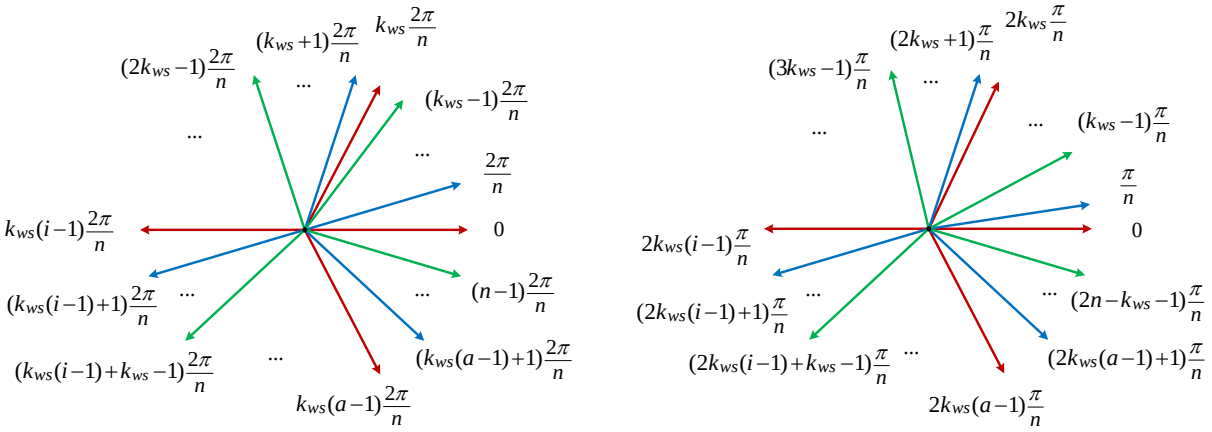

a) b)

Figure 3.1 – Arbitrary phase number machine winding distribution around stator circumference for: (a) symmetrical and (b) asymmetrical configuration.

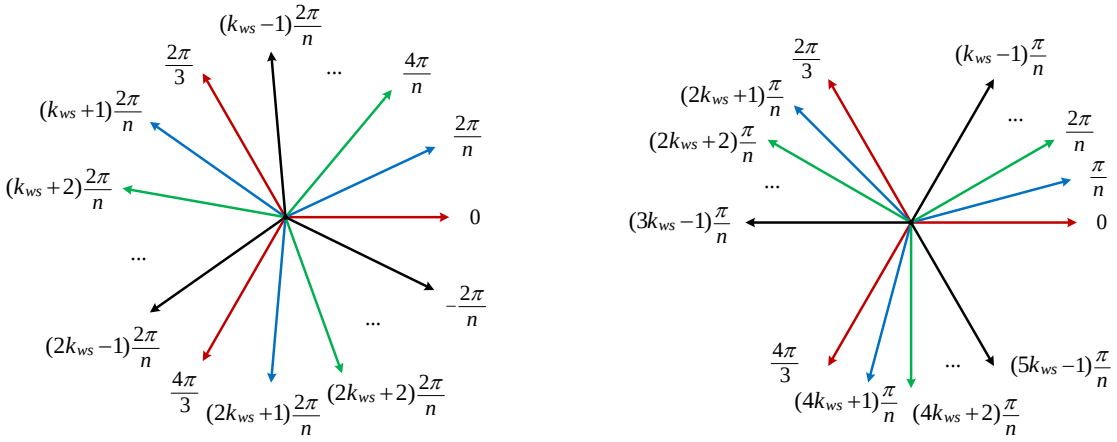

a) b)

Figure 3.2 – Multiple three-phase set ($k_{ws} \geq 1$, $a = 3$) winding distribution around stator circumference for: (a) symmetrical and (b) asymmetrical configuration.

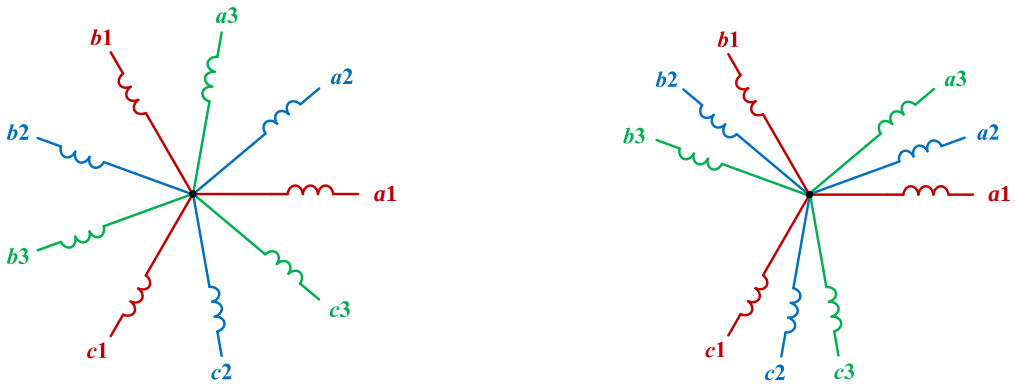

a) b)

Figure 3.3 – Nine-phase ($k_{ws} = 3$, $a = 3$) machine winding distribution around stator circumference for: (a) symmetrical and (b) asymmetrical configuration.

Application of Kirchhoff's law to the equivalent circuit of the multiphase machine shown in Fig. 3.4 results in:

$$\left[v_{abcn}\right]=\left[R_s\right]\cdot\left[i_{abcn}\right]+\frac{d}{dt}\left[\lambda_{abcn}\right] \tag{3.3}$$

$$\left[v_{abcn}\right]=\begin{bmatrix} v_{a1} \\ v_{a2} \\ \dots \end{bmatrix};\quad \left[i_{abcn}\right]=\begin{bmatrix} i_{a1} \\ i_{a2} \\ \dots \end{bmatrix};\quad \left[\lambda_{abcn}\right]=\begin{bmatrix} \lambda_{a1} \\ \lambda_{a2} \\ \dots \end{bmatrix}$$

where:

- $[v_{abcn}]$ stands for vector of the stator voltages,
- $[i_{abcn}]$ stands for stator winding current vector,
- $[\lambda_{abcn}]$ is the vector of the total stator flux linkages in phase sets, while
- $[R_s]$ represents stator phase winding resistance diagonal matrix.

It is important to note that (3.3) and all the other following equations are written using motor convention for positive power flow and a single isolated neutral point is assumed. As it is assumed that all individual phase windings are identical, $R_{a1} = R_{a2} = \dots = R_{ji} = R_s$ applies. Based on this and (3.3), electric equation can now be written for the nine-phase case as:

$$\begin{bmatrix} v_{a1} \\ v_{a2} \\ v_{a3} \\ v_{b1} \\ v_{b2} \\ v_{b3} \\ v_{c1} \\ v_{c2} \\ v_{c3} \end{bmatrix}=\begin{bmatrix} R_s & 0 & 0 & 0 & 0 & 0 & 0 & 0 & 0 \\ 0 & R_s & 0 & 0 & 0 & 0 & 0 & 0 & 0 \\ 0 & 0 & R_s & 0 & 0 & 0 & 0 & 0 & 0 \\ 0 & 0 & 0 & R_s & 0 & 0 & 0 & 0 & 0 \\ 0 & 0 & 0 & 0 & R_s & 0 & 0 & 0 & 0 \\ 0 & 0 & 0 & 0 & 0 & R_s & 0 & 0 & 0 \\ 0 & 0 & 0 & 0 & 0 & 0 & R_s & 0 & 0 \\ 0 & 0 & 0 & 0 & 0 & 0 & 0 & R_s & 0 \\ 0 & 0 & 0 & 0 & 0 & 0 & 0 & 0 & R_s \end{bmatrix}\cdot\begin{bmatrix} i_{a1} \\ i_{a2} \\ i_{a3} \\ i_{b1} \\ i_{b2} \\ i_{b3} \\ i_{c1} \\ i_{c2} \\ i_{c3} \end{bmatrix}+\frac{d}{dt}\begin{bmatrix} \lambda_{a1} \\ \lambda_{a2} \\ \lambda_{a3} \\ \lambda_{b1} \\ \lambda_{b2} \\ \lambda_{b3} \\ \lambda_{c1} \\ \lambda_{c2} \\ \lambda_{c3} \end{bmatrix} \tag{3.4}$$

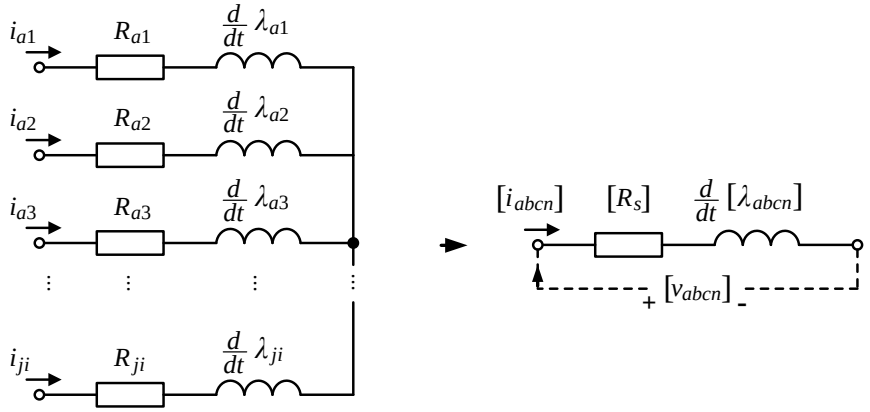

Figure 3.4 – Equivalent electrical circuit in phase domain for PMSM with single isolated neutral point.

Flux linkages are given with:

$$\left[\lambda_{abcn}\right]=\left[L_{ls}\right]\cdot\left[i_{abcn}\right]+\left[M_{ss}\right]\cdot\left[i_{abcn}\right]+\left[\lambda_{m-abcn}\right] \tag{3.5}$$

$$\left[\lambda_{m-abcn}\right]=\begin{bmatrix}\lambda_{m-a1}\\ \lambda_{m-a2}\\ \dots\end{bmatrix}$$

Here,

- $[M_{ss}]$ represents mutual inductance matrix between all phases in the machine,
- $[\lambda_{m\text{-}abcn}]$ represents flux produced by permanent magnets positioned on the rotor, while
- $[L_{ls}]$ stands for leakage inductance diagonal matrix.

Once again, because of the adopted assumptions, $L_{lsa1} = L_{lsa2} = \dots = L_{lsji} = L_{ls}$ applies.

In addition to the per-phase leakage inductances, $n \times n$ matrix containing mutual inductances between different phases must also be taken into consideration. In its general form, this matrix can be written as:

$$\left[M_{ss}\right]=\begin{bmatrix}M_{a1-a1} & M_{a1-a2} & M_{a1-a3} & M_{a1-b1} & M_{a1-b2} & \dots & M_{a1-i}\\ M_{a2-a1} & M_{a2-a2} & M_{a2-a3} & M_{a2-b1} & M_{a2-b2} & \dots & M_{a2-i}\\ M_{a3-a1} & M_{a3-a2} & M_{a3-a3} & M_{a3-b1} & M_{a3-b2} & \dots & M_{a3-i}\\ M_{b1-a1} & M_{b1-a2} & M_{b1-a3} & M_{b1-b1} & M_{b1-b2} & \dots & M_{b1-i}\\ M_{b2-a1} & M_{b2-a2} & M_{b2-b3} & M_{b2-b1} & M_{b2-b2} & \dots & M_{b2-i}\\ \dots & \dots & \dots & \dots & \dots & \dots & \dots\\ M_{j-a1} & M_{j-a2} & M_{j-a3} & M_{j-b1} & M_{j-b2} & \dots & M_{j-i}\end{bmatrix} \tag{3.6}$$

To define mutual inductance $M_{j\text{-}i}$ between any two arbitrary chosen phases, corresponding angular positions (θ_j and θ_i) in relation to the datum angle must be defined. The datum angle is usually taken as phase *a*1 angle, which is placed at 0° (i.e. $\theta_{a1} = 0°$). Arbitrary angle position of rotor in space θ_{el} must also be taken into account. Mutual inductances for every single phase in relation to other (n - 1) phases can be then calculated using:

$$M_{j-i}=M_I\cos(\theta_j-\theta_i)+M_A\cos(2\theta_{el}-\theta_j-\theta_i) \tag{3.7}$$

As it can be seen from the given equation, mutual inductance consists of two parts. Coefficient M_I in the equation stands for the isotropic, while M_A denotes the anisotropic mutual inductance component. If magnets in the machine are positioned on rotor's surface, anisotropic factor is equal to zero and machine is classified as isotropic (the case in this work), i.e. $M_{j\text{-}i} = M_I \cdot \cos(\theta_j - \theta_i)$.

By assuming permanent magnet flux in the air-gap to be constant and equal to λ_m and by assuming that this harmonic is shifted for θ_{phs} angle, influence of rotor magnets can be modelled as:

$$\lambda_{m-abcn} = \lambda_m \cdot \cos(1 \cdot (\theta_{el} - \theta_{ji}) + \theta_{phs}) \tag{3.8}$$

where θ_{ji} is an angle dependent on spatial phase distribution around circumference (symmetrical or asymmetrical; see (3.2)). It must be noted that this equation is valid in machine modelling only if sinusoidal back-EMF is assumed. If, in addition to the fundamental (now λ_{m1}, θ_{phs1}), the third harmonic (λ_{m3}, θ_{phs3}) also exists (as in the near-sinusoidal benchmark machine discussed further in this chapter), its influence must be included as well, and the new equations should be:

$$\lambda_{m-abcn} = \lambda_{m1} \cdot \cos(1 \cdot (\theta_{el} - \theta_{ji}) + \theta_{phs1}) + \lambda_{m3} \cdot \cos(3 \cdot (\theta_{el} - \theta_{ji}) + \theta_{phs3}) \tag{3.9}$$

Similar modification is also required in the mutual inductance matrix defined with (3.6)-(3.7), i.e. new matrix included in (3.5) should be $[M_{ss}] = [M_{ss1}] + [M_{ss3}]$.

For the nine-phase case the magnetic model becomes:

$$\begin{bmatrix} \lambda_{a1} \\ \lambda_{a2} \\ \lambda_{a3} \\ \lambda_{b1} \\ \lambda_{b2} \\ \lambda_{b3} \\ \lambda_{c1} \\ \lambda_{c2} \\ \lambda_{c3} \end{bmatrix} = \begin{bmatrix} L_{ls} & 0 & 0 & 0 & 0 & 0 & 0 & 0 & 0 \\ 0 & L_{ls} & 0 & 0 & 0 & 0 & 0 & 0 & 0 \\ 0 & 0 & L_{ls} & 0 & 0 & 0 & 0 & 0 & 0 \\ 0 & 0 & 0 & L_{ls} & 0 & 0 & 0 & 0 & 0 \\ 0 & 0 & 0 & 0 & L_{ls} & 0 & 0 & 0 & 0 \\ 0 & 0 & 0 & 0 & 0 & L_{ls} & 0 & 0 & 0 \\ 0 & 0 & 0 & 0 & 0 & 0 & L_{ls} & 0 & 0 \\ 0 & 0 & 0 & 0 & 0 & 0 & 0 & L_{ls} & 0 \\ 0 & 0 & 0 & 0 & 0 & 0 & 0 & 0 & L_{ls} \end{bmatrix} \cdot \begin{bmatrix} i_{a1} \\ i_{a2} \\ i_{a3} \\ i_{b1} \\ i_{b2} \\ i_{b3} \\ i_{c1} \\ i_{c2} \\ i_{c3} \end{bmatrix} + [M_{ss}] \cdot \begin{bmatrix} i_{a1} \\ i_{a2} \\ i_{a3} \\ i_{b1} \\ i_{b2} \\ i_{b3} \\ i_{c1} \\ i_{c2} \\ i_{c3} \end{bmatrix} + \begin{bmatrix} \lambda_{m-a1} \\ \lambda_{m-a2} \\ \lambda_{m-a3} \\ \lambda_{m-b1} \\ \lambda_{m-b2} \\ \lambda_{m-b3} \\ \lambda_{m-c1} \\ \lambda_{m-c2} \\ \lambda_{m-c3} \end{bmatrix} \tag{3.10}$$

Machine studied in this chapter is with surface permanent magnets on rotor, hence anisotropic part in equation (3.7) can be neglected. Isotropic constant can be obtained experimentally, by conducting machine parameter estimation tests. Taking this into account, mutual inductance matrix can be written as:

$$[M_{ss}] = \begin{bmatrix} M_{a1-a1} & M_{a1-a2} & M_{a1-a3} & M_{a1-b1} & M_{a1-b2} & M_{a1-b3} & M_{a1-c1} & M_{a1-c2} & M_{a1-c3} \\ M_{a2-a1} & M_{a2-a2} & M_{a2-a3} & M_{a2-b1} & M_{a2-b2} & M_{a2-b3} & M_{a2-c1} & M_{a2-c2} & M_{a2-c3} \\ M_{a3-a1} & M_{a3-a2} & M_{a3-a3} & M_{a3-b1} & M_{a3-b2} & M_{a3-b3} & M_{a3-c1} & M_{a3-c2} & M_{a3-c3} \\ M_{b1-a1} & M_{b1-a2} & M_{b1-a3} & M_{b1-b1} & M_{b1-b2} & M_{b1-b3} & M_{b1-c1} & M_{b1-c2} & M_{b1-c3} \\ M_{b2-a1} & M_{b2-a2} & M_{b2-a3} & M_{b2-b1} & M_{b2-b2} & M_{b2-b3} & M_{b2-c1} & M_{b2-c2} & M_{b2-c3} \\ M_{b3-a1} & M_{b3-a2} & M_{b3-a3} & M_{b3-b1} & M_{b3-b2} & M_{b3-b3} & M_{b3-c1} & M_{b3-c2} & M_{b3-c3} \\ M_{c1-a1} & M_{c1-a2} & M_{c1-a3} & M_{c1-b1} & M_{c1-b2} & M_{c1-b3} & M_{c1-c1} & M_{c1-c2} & M_{c1-c3} \\ M_{c2-a1} & M_{c2-a2} & M_{c2-a3} & M_{c2-b1} & M_{c2-b2} & M_{c2-b3} & M_{c2-c1} & M_{c2-c2} & M_{c2-c3} \\ M_{c3-a1} & M_{c3-a2} & M_{c3-a3} & M_{c3-b1} & M_{c3-b2} & M_{c3-b3} & M_{c3-c1} & M_{c3-c2} & M_{c3-c3} \end{bmatrix} \tag{3.11}$$

where $M_{j\text{-}i} = M_{I1} \cdot \cos(\theta_j - \theta_i) + M_{I3} \cdot \cos(3 \cdot (\theta_j - \theta_i))$.

It is easy to conclude from (3.3) and (3.5) that the common part for both electric and magnetic models is the total flux linkage λ_{abcn}. After performing a short mathematical manipulation to combine presented electric and magnetic expressions, final phase domain model form is acquired. In both equation (3.12) and in Fig. 3.5, the full multiphase machine model in phase variables can be seen:

$$\begin{aligned}&\left[i_{abcn}\right]=\left[L_{ss}\right]^{-1}\left(\int\left[v_{abcn}\right]-\left[R_s\right]\left[i_{abcn}\right]dt-\left[\lambda_{m-abcn}\right]\right)\\&\left[L_{ss}\right]=\left[M_{ss}\right]+\left[L_{ls}\right]\end{aligned} \tag{3.12}$$

From the concept of co-energy, general torque equation for any PM machine in terms of phase-variables can be defined, as it is shown in [Toliyat et al (1991a), Gautam et al (2011)], that is (capital T denotes matrix transposition):

$$T_{em}=\frac{\partial W_{co}}{\partial\theta_{el}};\quad T_{em}=\frac{P}{2}\cdot\left[i_{abcn}\right]^{\mathrm{T}}\cdot\frac{d\left[L_{ss}\right]}{d\theta_{el}}\cdot\left[i_{abcn}\right]+P\cdot\left[i_{abcn}\right]^{\mathrm{T}}\cdot\frac{d\left[\lambda_{m-abcn}\right]}{d\theta_{el}} \tag{3.13}$$

All equation terms in (3.13), except inductance matrix [L_{ss}], have been already defined. To derive this matrix, general inductance matrix form [L] must be defined. This matrix consists of stator [L_{ss}] and rotor [L_{rr}] self-inductance matrices and stator-to-rotor [L_{sr}] and rotor-to-stator [L_{rs}] mutual inductance matrices. Because studied PM synchronous machine's rotor is built without windings or bars, rotor self-inductance as well as both mutual inductance matrices can be neglected, resulting in:

$$\left[L\right]=\begin{bmatrix}\left[L_{ss}\right] & \left[L_{sr}\right]\\ \left[L_{rs}\right] & \left[L_{rr}\right]\end{bmatrix}\rightarrow\left[L\right]=\begin{bmatrix}\left[L_{ss}\right] & 0\\ 0 & 0\end{bmatrix}\rightarrow\left[L\right]=\left[L_{ss}\right]=\left[M_{ss}\right]+\left[L_{ls}\right] \tag{3.14}$$

By observing [L_{ss}] and based on equations (3.7) and (3.10), it can be seen that matrix components ([M_{ss}], [L_{ls}]) are not dependent on arbitrary electrical position θ_{el}, meaning that the entire first part of (3.13) can be omitted. Resulting simplified torque expression can be used to calculate torque in multiphase surface PMSMs modelled using phase-variables as:

$$T_{em}=P\cdot\left[i_{abcn}\right]^{\mathrm{T}}\cdot\frac{d\left[\lambda_{m-abcn}\right]}{d\theta_{el}} \tag{3.15}$$

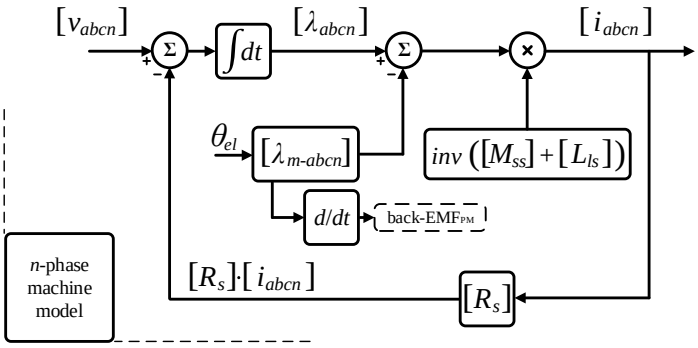

Figure 3.5 – Schematic representation of a PMSM model block diagram in phase-variable domain.

3.3 Vector Space Decomposition

It is clear from the previous section that multiphase machine modelling using phase-variables can be extremely complicated. This is mainly because of n different voltage, current and flux linkage equations that must be taken into consideration during calculations. To simplify the model, the equations are decoupled as explained in this section. Two approaches (called transformations) for multiphase machine decoupling are used today. The first, using a multiple *d-q* modelling method and the second a vector space decomposition (VSD) method. Multiple *d-q* (or multi-stator) modelling approach, applicable only to machines with multiple three-phase windings, has its advantages, such as for example independent control of each individual winding set [Nelson and Krause (1974)], but it leads to heavy cross-coupling between the equations of different three-phase winding sets and does not offer clear insight into machine operation and harmonic mapping [Zoric et al (2017a) and Zoric et al (2017b)]. Despite the aforementioned, it is a commonly used machine decoupling approach in industrial research centres because it uses well-known three-phase machine technologies.

The vector space decomposition modelling concept was first introduced for a six-phase machine in [Zhao and Lipo (1994)] and it is based on symmetrical component theory introduced in [Fortescue (1918)]. This method replaces n-original phase-variables with new sets of $n/2$ two-dimensional subspaces (if the phase number is an even number) or with $(n - 1)/2$ planes plus one single-dimensional quantity (if the number of phases is an odd number), i.e. multiple decoupled two-dimensional subspaces and (one or two) zero-sequence component(s) [Levi et al (2007)]. Fundamental components of the machine map into the so-called α-β subspace and are responsible for the electromechanical energy conversion (flux- and torque-production), while the remaining ($(n - 4)/2$ if n is even or $(n - 3)/2$ if n is odd) *R-L* circuits comprised of stator resistance and stator leakage inductance (also called *x-y* subspaces) are non-electromechanical energy producing where the non-zero-sequence harmonics map. In addition to the significant simplification, the main advantage of this technique is that the new two-dimensional subspaces are mutually perpendicular, so that there is no decoupling needed. Furthermore, after VSD transformation, it is relatively straightforward to implement any vector control strategy [Levi et al (2008)].

The form of the multiphase VSD transformation matrix, which is in real form the Clarke's transformation, for n-phase machines depends on phase propagation angle between winding sets, which can be arranged as symmetrical or asymmetrical. Furthermore, it also depends on the number of isolated neutral points, which in case of multiple three-phase winding set machines (the type being investigated in this work) can be single isolated neutral point or configuration with k_{ws} isolated neutral points. If the number of phases is an odd prime number, number of isolated neutral points is always one. Finally, the third component which must be taken into consideration when vector space decomposition matrix is derived is coefficient g. This coefficient stands in front of the decoupling matrix and is associated with

the powers of original machine and the new one obtained after the transformation. If coefficient g is equal to $2/n$, the total power is variant under transformation and so-called amplitude invariant transformation is performed. Alternatively, coefficient in front of the decoupling matrix can be equal to $\sqrt{2/n}$, in which case total powers of the original and new machine are kept the same in transformation, i.e. power-invariant transformation is performed.

The compact notation of Clarke's transformation, which is used to replace n phase variables with a new n component set in α-β domain, can be written as:

$$\left[f_{\alpha\beta}\right] = \left[C\right]\cdot\left[f_{abcn}\right] \tag{3.16}$$

Here, $[f_{\alpha\beta}]$ stands for voltage, current or flux linkage column matrices after transformation for stator (and rotor if applicable) variables in α-β reference frame, while $[f_{abcn}]$ represents corresponding column matrices in phase domain. The term in equation (3.16) denoted with $[C]$ stands for decoupling transformation matrix.

To derive decoupling VSD transformations applicable to nine-phase machines, one can start from [Zoric et al (2017a) and Zoric et al (2017b)], where generalisation of transformation is given. By using (3.1) and (3.2), arrays which contain the angles for the symmetrical and asymmetrical nine-phase configurations, respectively, can be obtained as:

$$\left[\theta_{sym}\right] = \frac{2\pi}{9}\left[0 \quad 1 \quad 2 \quad 3 \quad 4 \quad 5 \quad 6 \quad 7 \quad 8\right] \tag{3.17}$$

$$\left[\theta_{asym}\right] = \frac{\pi}{9}\left[0 \quad 1 \quad 2 \quad 6 \quad 7 \quad 8 \quad 12 \quad 13 \quad 14\right] \tag{3.18}$$

Substituting (3.17)-(3.18) into (3.19) [see Zoric et al (2017a) and Zoric et al (2017b)]:

$$\underset{9,1,sym}{\left[C_{VSD}\right]} = g\cdot\begin{bmatrix} \cos([\theta_{sym}]) \\ \sin([\theta_{sym}]) \\ \cos(2[\theta_{sym}]) \\ \sin(2[\theta_{sym}]) \\ \cos(4[\theta_{sym}]) \\ \sin(4[\theta_{sym}]) \\ \cos(3[\theta_{sym}]) \\ \sin(3[\theta_{sym}]) \\ \frac{1}{2}\cdot\cos(9[\theta_{sym}]) \end{bmatrix}; \qquad \underset{9,1,asym}{\left[C_{VSD}\right]} = g\cdot\begin{bmatrix} \cos([\theta_{asym}]) \\ \sin([\theta_{asym}]) \\ \cos(5[\theta_{asym}]) \\ \sin(5[\theta_{asym}]) \\ \cos(7[\theta_{asym}]) \\ \sin(7[\theta_{asym}]) \\ \cos(3[\theta_{asym}]) \\ \sin(3[\theta_{asym}]) \\ \frac{1}{2}\cdot\cos(9[\theta_{asym}]) \end{bmatrix} \tag{3.19}$$

and assuming power variant transformation ($g = 2/n$) leads to:

$$\underset{9,1,sym}{[C_{VSD}]} = \frac{2}{9}\cdot\begin{bmatrix}
1 & \cos\left(\frac{\pi}{9}\right) & \cos\left(\frac{2\pi}{9}\right) & \cos\left(\frac{3\pi}{9}\right) & \cos\left(\frac{4\pi}{9}\right) & \cos\left(\frac{5\pi}{9}\right) & \cos\left(\frac{6\pi}{9}\right) & \cos\left(\frac{7\pi}{9}\right) & \cos\left(\frac{8\pi}{9}\right) & \alpha \\
0 & \sin\left(\frac{\pi}{9}\right) & \sin\left(\frac{2\pi}{9}\right) & \sin\left(\frac{3\pi}{9}\right) & \sin\left(\frac{4\pi}{9}\right) & \sin\left(\frac{5\pi}{9}\right) & \sin\left(\frac{6\pi}{9}\right) & \sin\left(\frac{7\pi}{9}\right) & \sin\left(\frac{8\pi}{9}\right) & \beta \\
1 & \cos\left(2\frac{\pi}{9}\right) & \cos\left(2\frac{2\pi}{9}\right) & \cos\left(2\frac{3\pi}{9}\right) & \cos\left(2\frac{4\pi}{9}\right) & \cos\left(2\frac{5\pi}{9}\right) & \cos\left(2\frac{6\pi}{9}\right) & \cos\left(2\frac{7\pi}{9}\right) & \cos\left(2\frac{8\pi}{9}\right) & x_1 \\
0 & \sin\left(2\frac{\pi}{9}\right) & \sin\left(2\frac{2\pi}{9}\right) & \sin\left(2\frac{3\pi}{9}\right) & \sin\left(2\frac{4\pi}{9}\right) & \sin\left(2\frac{5\pi}{9}\right) & \sin\left(2\frac{6\pi}{9}\right) & \sin\left(2\frac{7\pi}{9}\right) & \sin\left(2\frac{8\pi}{9}\right) & y_1 \\
1 & \cos\left(4\frac{\pi}{9}\right) & \cos\left(4\frac{2\pi}{9}\right) & \cos\left(4\frac{3\pi}{9}\right) & \cos\left(4\frac{4\pi}{9}\right) & \cos\left(4\frac{5\pi}{9}\right) & \cos\left(4\frac{6\pi}{9}\right) & \cos\left(4\frac{7\pi}{9}\right) & \cos\left(4\frac{8\pi}{9}\right) & x_2 \\
0 & \sin\left(4\frac{\pi}{9}\right) & \sin\left(4\frac{2\pi}{9}\right) & \sin\left(4\frac{3\pi}{9}\right) & \sin\left(4\frac{4\pi}{9}\right) & \sin\left(4\frac{5\pi}{9}\right) & \sin\left(4\frac{6\pi}{9}\right) & \sin\left(4\frac{7\pi}{9}\right) & \sin\left(4\frac{8\pi}{9}\right) & y_2 \\
1 & \cos\left(3\frac{\pi}{9}\right) & \cos\left(3\frac{2\pi}{9}\right) & \cos\left(3\frac{3\pi}{9}\right) & \cos\left(3\frac{4\pi}{9}\right) & \cos\left(3\frac{5\pi}{9}\right) & \cos\left(3\frac{6\pi}{9}\right) & \cos\left(3\frac{7\pi}{9}\right) & \cos\left(3\frac{8\pi}{9}\right) & x_3 \\
0 & \sin\left(3\frac{\pi}{9}\right) & \sin\left(3\frac{2\pi}{9}\right) & \sin\left(3\frac{3\pi}{9}\right) & \sin\left(3\frac{4\pi}{9}\right) & \sin\left(3\frac{5\pi}{9}\right) & \sin\left(3\frac{6\pi}{9}\right) & \sin\left(3\frac{7\pi}{9}\right) & \sin\left(3\frac{8\pi}{9}\right) & y_3 \\
\frac{1}{2} & \frac{1}{2} & \frac{1}{2} & \frac{1}{2} & \frac{1}{2} & \frac{1}{2} & \frac{1}{2} & \frac{1}{2} & \frac{1}{2} & 0_+
\end{bmatrix} \tag{3.20}$$

$$\underset{9,1,asym}{[C_{VSD}]} = \frac{2}{9}\cdot\begin{bmatrix}
1 & \cos\left(\frac{\pi}{9}\right) & \cos\left(\frac{2\pi}{9}\right) & \cos\left(\frac{6\pi}{9}\right) & \cos\left(\frac{7\pi}{9}\right) & \cos\left(\frac{8\pi}{9}\right) & \cos\left(\frac{12\pi}{9}\right) & \cos\left(\frac{13\pi}{9}\right) & \cos\left(\frac{14\pi}{9}\right) & \alpha \\
0 & \sin\left(\frac{\pi}{9}\right) & \sin\left(\frac{2\pi}{9}\right) & \sin\left(\frac{6\pi}{9}\right) & \sin\left(\frac{7\pi}{9}\right) & \sin\left(\frac{8\pi}{9}\right) & \sin\left(\frac{12\pi}{9}\right) & \sin\left(\frac{13\pi}{9}\right) & \sin\left(\frac{14\pi}{9}\right) & \beta \\
1 & \cos\left(5\frac{\pi}{9}\right) & \cos\left(5\frac{2\pi}{9}\right) & \cos\left(5\frac{6\pi}{9}\right) & \cos\left(5\frac{7\pi}{9}\right) & \cos\left(5\frac{8\pi}{9}\right) & \cos\left(5\frac{12\pi}{9}\right) & \cos\left(5\frac{13\pi}{9}\right) & \cos\left(5\frac{14\pi}{9}\right) & x_1 \\
0 & \sin\left(5\frac{\pi}{9}\right) & \sin\left(5\frac{2\pi}{9}\right) & \sin\left(5\frac{6\pi}{9}\right) & \sin\left(5\frac{7\pi}{9}\right) & \sin\left(5\frac{8\pi}{9}\right) & \sin\left(5\frac{12\pi}{9}\right) & \sin\left(5\frac{13\pi}{9}\right) & \sin\left(5\frac{14\pi}{9}\right) & y_1 \\
1 & \cos\left(7\frac{\pi}{9}\right) & \cos\left(7\frac{2\pi}{9}\right) & \cos\left(7\frac{6\pi}{9}\right) & \cos\left(7\frac{7\pi}{9}\right) & \cos\left(7\frac{8\pi}{9}\right) & \cos\left(7\frac{12\pi}{9}\right) & \cos\left(7\frac{13\pi}{9}\right) & \cos\left(7\frac{14\pi}{9}\right) & x_2 \\
0 & \sin\left(7\frac{\pi}{9}\right) & \sin\left(7\frac{2\pi}{9}\right) & \sin\left(7\frac{6\pi}{9}\right) & \sin\left(7\frac{7\pi}{9}\right) & \sin\left(7\frac{8\pi}{9}\right) & \sin\left(7\frac{12\pi}{9}\right) & \sin\left(7\frac{13\pi}{9}\right) & \sin\left(7\frac{14\pi}{9}\right) & y_2 \\
1 & \cos\left(3\frac{\pi}{9}\right) & \cos\left(3\frac{2\pi}{9}\right) & \cos\left(3\frac{6\pi}{9}\right) & \cos\left(3\frac{7\pi}{9}\right) & \cos\left(3\frac{8\pi}{9}\right) & \cos\left(3\frac{12\pi}{9}\right) & \cos\left(3\frac{13\pi}{9}\right) & \cos\left(3\frac{14\pi}{9}\right) & x_3 \\
0 & \sin\left(3\frac{\pi}{9}\right) & \sin\left(3\frac{2\pi}{9}\right) & \sin\left(3\frac{6\pi}{9}\right) & \sin\left(3\frac{7\pi}{9}\right) & \sin\left(3\frac{8\pi}{9}\right) & \sin\left(3\frac{12\pi}{9}\right) & \sin\left(3\frac{13\pi}{9}\right) & \sin\left(3\frac{14\pi}{9}\right) & y_3 \\
\frac{1}{2} & -\frac{1}{2} & \frac{1}{2} & \frac{1}{2} & -\frac{1}{2} & \frac{1}{2} & \frac{1}{2} & -\frac{1}{2} & \frac{1}{2} & 0_+
\end{bmatrix} \tag{3.21}$$

Symmetrical version of the transformation (and corresponding inverse), that is, matrix given with (3.20), will be further used in this work to decouple the studied PMSM prototype.

Use of the (3.20)-(3.21) will not only decouple the machine into flux/torque producing and non-producing components, but will also uniquely map odd-order harmonics in the *x-y* subspaces. This means that each odd-order harmonic will be mapped only into a single subspace or zero-sequence. How odd low-order time harmonics are mapped into different subspaces in nine-phase symmetrical and asymmetrical multiphase machines with a single isolated neutral point, is explained in detail in [Yepes et al (2015), Yepes et al (2017), Zoric et al (2017a & 2017b)]. Following from mentioned studies and VSD matrices (3.20)-(3.21), graphical representation of harmonic mapping relevant for this work can be obtained, as shown in Fig. 3.6. Even harmonics are disregarded [Yepes et al (2015)].

Finally, it should be noted that in decoupled *α-β* model, stator windings are stationary, while rotor windings (if they exist) rotate together with the rotor. In order to dispense with time-varying inductance terms, it is necessary to perform another transformation, which is usually called rotational (Park's or *d-q*) transformation. Multiphase form [*D*] of this well-known matrix can be written as follows:

$$[f_{dq}] = [D]\cdot[f_{\alpha\beta}] \tag{3.22}$$

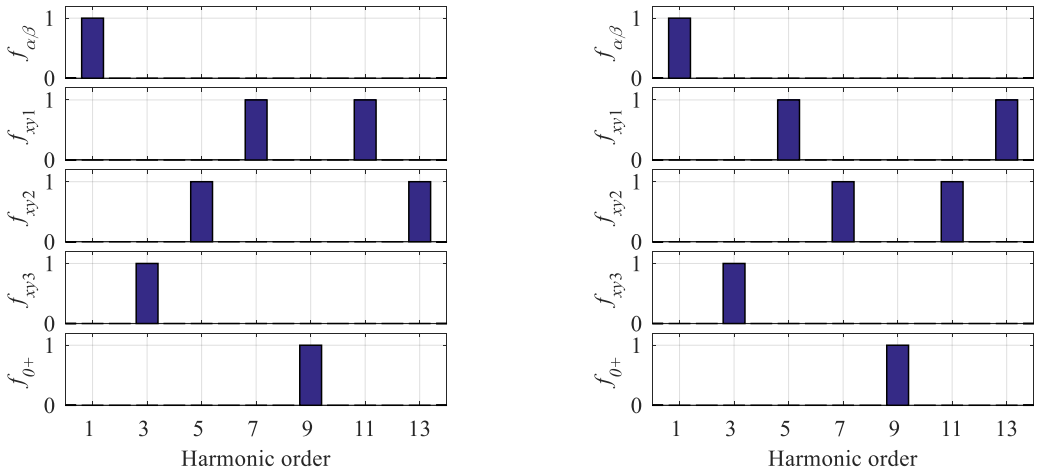

Figure 3.6 – Harmonic mapping using VSD transformation in case of the nine-phase machine: (a) symmetrical and (b) asymmetrical case.

$$[D] = \begin{bmatrix} \cos(\theta_{el}+\theta_{phs1}) & \sin(\theta_{el}+\theta_{phs1}) & 0 & \dots & 0 \\ -\sin(\theta_{el}+\theta_{phs1}) & \cos(\theta_{el}+\theta_{phs1}) & 0 & \dots & 0 \\ 0 & 0 & 1 & \dots & 0 \\ \dots & \dots & \dots & \dots & 0 \\ 0 & 0 & 0 & \dots & 1 \end{bmatrix} \tag{3.23}$$

Matrix equation is shown only for the stator winding, but the same concept is also applicable to rotor winding in an induction machine. The first two rows in (3.23) are responsible for flux- and torque-production, while the other subspaces do not participate in electromechanical energy conversion. Once again, this is the case only in this chapter. Modification of (3.23) to include additional terms to transform other harmonic components to a rotation reference frame will play an important role in controlling the shortened magnet span machine in chapter 5.

The inverse transformations (which is also important in control algorithm development), are as follows:

$$[f_{abcn}] = [C]^{-1} \cdot [f_{\alpha\beta}] \tag{3.24}$$

$$[f_{\alpha\beta}] = [D]^{-1} \cdot [f_{dq}] \tag{3.25}$$

$$[f_{abcn}] = [T]^{-1} \cdot [f_{dq}]; \quad [T] = [C][D] \tag{3.26}$$

3.4 Synchronous Reference Frame Machine Modelling

Upon application of the VSD and rotational transformations to the phase variable multiphase machine model, the following model (in which rotational reference frame is aligned with the rotor flux) is obtained [Levi (2011)]:

$$v_d = R_{sd} \cdot i_d + \frac{d\lambda_d}{dt} - \omega_{el}\lambda_q \tag{3.27}$$

$$v_q = R_{sq} \cdot i_q + \frac{d\lambda_q}{dt} + \omega_{el}\lambda_d \tag{3.28}$$

$$R_{sd} = R_{sq} = R_s \tag{3.29}$$

$$v_{xi} = R_s \cdot i_{xi} + \frac{d\lambda_{xi}}{dt}; \quad i = 1,2,3 \tag{3.30}$$

$$v_{yi} = R_s \cdot i_{yi} + \frac{d\lambda_{yi}}{dt}; \quad i = 1,2,3 \tag{3.31}$$

$$v_0 = R_s \cdot i_0 + \frac{d\lambda_0}{dt} \tag{3.32}$$

$$\lambda_d = L_d \cdot i_d + \lambda_m \tag{3.33}$$

$$\lambda_q = L_q \cdot i_q \tag{3.34}$$

$$\lambda_{xi} = L_{ls} \cdot i_{xi}; \quad i = 1,2,3 \tag{3.35}$$

$$\lambda_{yi} = L_{ls} \cdot i_{yi}; \quad i = 1,2,3 \tag{3.36}$$

$$\lambda_0 = L_{ls} \cdot i_0 \tag{3.37}$$

while torque equation in the *d*-*q* reference frame can be expressed as:

$$T_{em} = \frac{n}{2} \cdot P \cdot \left[\lambda_m \cdot i_q + (L_d - L_q) \cdot i_d i_q\right] \tag{3.38}$$

It is to be noted that the machine is considered star-connected and with single isolated neutral point.

In equations (3.27)-(3.37), v, i and λ denote voltage, current and flux linkages, while index l stands for leakage inductance. Variables L_d and L_q represent stator winding self-inductance along *d*- and *q*-axis. Generally speaking, indices *d* and *q* in any variable stand for the components along permanent magnet flux axis (d) and the torque current axis perpendicular to it (q). Number of pole pairs is denoted with P and amplitude invariant transformation is assumed. The resulting *d*-*q* equivalent circuits can be seen in Fig. 3.7.

Since a surface PMSM is considered, stator winding self-inductances are approximately equal ($L_d = L_q = L_s = L_{ls} + (n/2) \cdot M_l$) and (3.27), (3.28) and (3.38) can be further simplified as:

$$v_d = R_s \cdot i_d + L_s \frac{di_d}{dt} - \omega_{el} L_s i_q \tag{3.39}$$

$$v_q = R_s i_q + L_s \frac{di_q}{dt} + \omega_{el}(L_s i_d + \lambda_m) \tag{3.40}$$

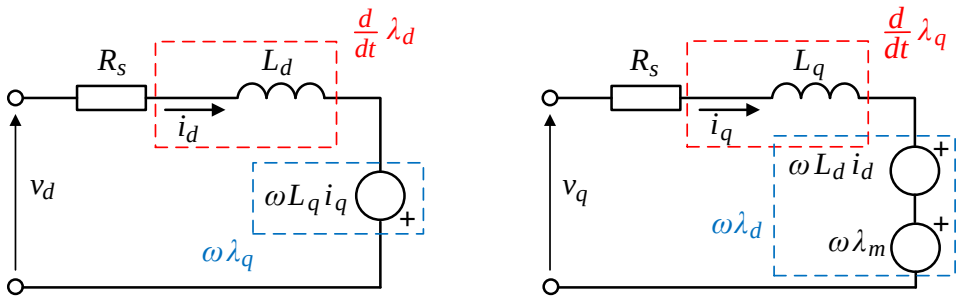

Figure 3.7 – Equivalent *d-q* electrical circuits for arbitrary phase number PM synchronous machine with single isolated neutral point in synchronous reference frame.

$$T_{em} = \frac{n}{2} \cdot P \cdot \lambda_m \cdot i_q \tag{3.41}$$

By comparing electromagnetic torque equations (3.38) and (3.41), one can see that because of equal stator self-inductances, torque is produced only by *q* component. Existence of only one (*q*) current component applies only when the machine is operating in the base speed region under MTPA control principles and flux-weakening control is not implemented, i.e. flux current component is constant and equal to zero.

Finally, to complete the simulation model, the equations representing the mechanical system must be formulated, which follow from the second Newton's law. In addition to the already presented equation for the electromagnetic torque (T_{em}), load torque (T_{load}), motor and load inertia coefficients ($J = J_M + J_L$), and friction torque (T_B; dependant on static, linear and parabolic speed contributions) must also be taken into consideration [Vaez-Zadeh (2018)]:

$$\begin{aligned} T_{em} &= T_{load} + J \cdot \frac{d\omega_{mech}}{dt} + T_B \\ &= T_{load} + \left(J_M + J_L\right) \cdot \frac{d\omega_{mech}}{dt} + T_{B0} + k_{B1} \cdot \omega_{mech} + k_{B2} \cdot \omega_{mech}^2 \end{aligned} \tag{3.42}$$

$$\omega_{el} = P \cdot \omega_{mech} \tag{3.43}$$

$$\theta_{el} = \int \omega_{el}\ dt \tag{3.44}$$

For ease of understanding, a block diagram of the mechanical subsystem defined with (3.42) is presented in Fig. 3.8.

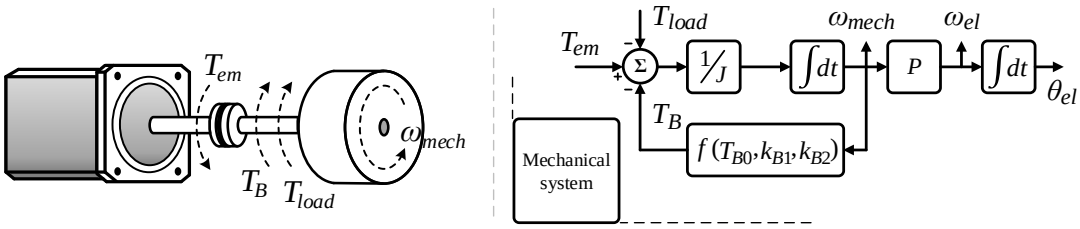

Figure 3.8 – Motor mechanical system and block scheme for electromagnetic torque, angular speed and angular position calculation.

3.5 Symmetrical/Asymmetrical Winding Reconfiguration

Asymmetrical and symmetrical winding configurations are rarely treated together for the same phase number, primarily since for each particular case it is known which topology is better. Nevertheless, machines where both winding configurations (symmetrical and asymmetrical) can be easily achieved by only rearranging the supply cables in the machine terminal box exist. For these machines, change of the winding configuration can be accomplished only if both (the start and the end) winding terminals are accessible for all phases; this winding type is known as open-ended. Multiphase machines used in research laboratories are usually with open-end winding because they are custom-made and commonly all $2n$ winding terminals are available in the machine's terminal box. In other words, the neutral point(s) of the machine are left to be formed according to the user requirements. The reconfigurations that lead from symmetrical (phase shift between phases equal to $2\pi/n$) to asymmetrical configuration (phase shift between consecutive sets equals π/n), and vice versa, are, as one of the objectives of this work, analysed first. Reconfigurations that lead to double-winding configurations (with 0° phase shift between the winding sets) are special reconfiguration cases and as such are discussed at the end of section.

Changing asymmetrical winding configuration to symmetrical and vice versa by only rearranging voltage source inverter supply leads in the machine's terminal box (and reconfiguring neutral point(s) connections) is possible only when the number of phases is a composite odd number equal to or higher than 9. Also, both the number of phases per set a and the number of winding sets k_{ws} must be odd numbers equal to or higher than 3. The number of isolated neutral points is not relevant and the machine can be with single or multiple isolated neutrals. Mathematical expression for stated principle can be defined with:

$$n \geq 9; \quad k_{ws} = 3,5,7...; \quad a = 3,5,7... \tag{3.45}$$

Based on the rule defined with (3.45), multiphase machines for which the reconfiguration is possible are given in Table 3.1. It must be noted that although mathematically correct, some of these configurations are not practical and are shown here just for the sake of completeness.

Table 3.1 – Machine configurations for which symmetrical/asymmetrical winding reconfiguration is possible.

$n \geq 9$	k_{ws} = **3**	k_{ws} = **5**	k_{ws} = **7**	k_{ws} = **9**	...
a = **3**	9	15	21	27	...
a = **5**	15	25	35	45	...
a = **7**	21	35	49	63	...
a = **9**	27	45	63	81	...
...	...	...	...	...	...

Before the algorithm for reconfiguration is derived, labelling system for winding sets and corresponding phases in them must be defined. Winding sets are denoted with 1, 2, 3, …, k_{ws} and each winding set can have a phases denoted with a, b, c, … (e.g. $a1$ represents the first phase in the first set,

*a*2 represents the first phase in the second set, etc.). Labelling always starts from phase *a*1 in Set-1, which is assumed to be placed at 0° angle. For a nine-phase machine case, stated phase annotation can be seen in Fig. 3.9a, where magnetic axes for asymmetrical winding configuration are shown. In addition to the phase labels (*a*1, *a*2, *a*3, etc.), phase sequential numbers (1, 2, 3, …, *n*) are also shown. They will play an important role in definition of the symmetrical to asymmetrical reconfiguration algorithm.

In Fig. 3.9b, a nine-phase voltage source inverter power supply leads and neutral point(s) connection leads (upper plot) and open-end winding machine terminal box (bottom plot) are shown. As can be seen, both start and end terminals of the machine's windings are accessible ($2 \cdot n = 18$). Starting winding terminals of every phase in the machine's terminal box are denoted with red underlined labels (*a*1, *a*2, …, *c*3), while corresponding end winding terminals are denoted with black underlined labels (*a*1, *a*2, …, *c*3). Similarly, VSI power supply leads are labelled with red *a*1, *a*2, …, *c*3 labels, while the leads used to form the neutral point(s) are denoted with black *a*1, *a*2, …, *c*3 labels. As already explained, the number of isolated neutral points is irrelevant and can be one or k_{ws}. For the time being, three neutral points are assumed.

From Fig. 3.9a one can see that if the magnetic axes of the second set (in blue) are rotated by 180°, i.e. inverted, a symmetrical machine configuration would be obtained. Therefore, the meaning of magnetic axis inversion should be explained first. This will be explained on inversion of the magnetic axis *a*1, as depicted in Fig. 3.10. In Fig. 3.10a the positive end of the inverter cable is connected to the start, red terminal, of the winding (while the end of the winding, black terminal, is forming a neutral point). This results in magnetic axis orientation as shown in Fig. 3.10a (red line; *a*1). If the voltage source power supply leads are rearranged as shown in Fig. 3.10b (if they are swapped), then new resulting magnetic axis is now oriented in the opposite direction (-*a*1). By observing the whole set for which the inversion should be done (in this case the second set), this means that the neutral point connection of this set should be reallocated from black to the red side, and the supply leads should be connected to the black terminals. In this way the magnetic axes of the second set (initially located at 20°, 140° and 260°, Fig. 3.9a), will be at 200°, 320° and 80°, respectively. For proper operation of the machine, phase delay of the reference for each phase must match with its magnetic axis angle. Only in this case, magnetic fluxes created by each set will be mutually aligned and will rotate together in the same direction. From Fig. 3.10, it may appear that software inversion, i.e. a multiplication of the reference by -1 for that phase, can have the same effect as the described hardware inversion. However, this would only mean that the initial position of the flux is changed for 180°. If all three sets are observed, and if the references of only one set are multiplied by -1, the flux generated by this set would not be aligned with the fluxes generated by the other two sets any more. This would result in a different current magnitude generated in that set. Hence, inversion of magnetic axes has to be done in hardware by moving the neutral point to the other side of the winding terminals.

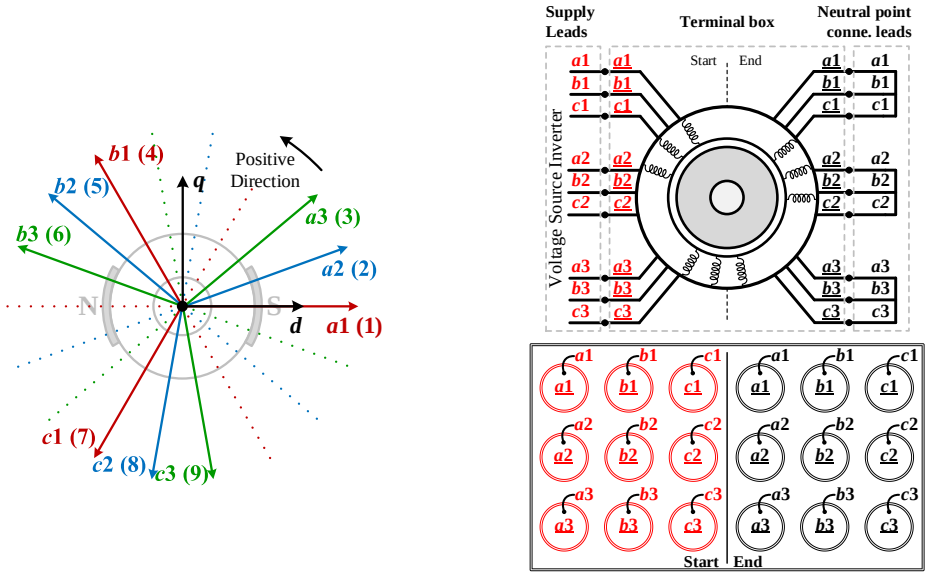

a) b)

Figure 3.9 – Example of a nine-phase (asymmetrical) winding with associated labelling: (a) magnetic axis diagram, and (b) nine-phase VSI power supply leads and the machine terminal box.

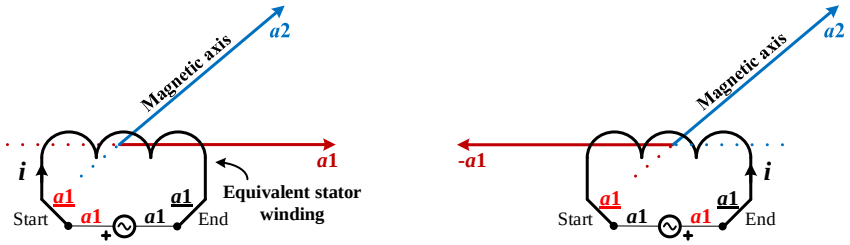

a) b)

Figure 3.10 – Depiction of magnetic axis inversion after rearrangement of supply leads in phase *a*1.

An example of a machine with nine phases, i.e. with the number of phase sets $k_{ws} = 3$ ($a = 3$), is shown in Fig. 3.11a. This figure illustrates how asymmetrical nine-phase machine can be easily reconfigured to be symmetrical. As already mentioned and as it is clear from Fig. 3.11a, the first (and every following odd number) winding set (Set-1, Set-3) should stay at the same angular position. Note that this is true for any other meaningful configuration even if $n > 9$. The second winding set, Set-2 (or in general case every even numbered set), must be inverted. In the shown case, start and end supply leads are swapped for the phases *a*2, *b*2, *c*2, i.e. rotational shift of magnetic axes for 180° is performed. In accordance with the labelling system, Set-2 of original asymmetrical configuration becomes Set-3, and Set-3 becomes Set-2 of the symmetrical configuration. Hence, the labels should be changed as indicated in Fig. 3.11a (upper plot, blue and red circle). Obtained new winding arrangement is with 40° spatial displacement between consecutive phases, which indeed represents symmetrical nine-phase machine ($2\pi/n$). How to rearrange VSI supply leads in the terminal box to perform this reconfiguration is shown in Fig. 3.11a, middle plots. Corresponding terminal boxes (mimic diagrams) are presented in Fig. 3.11a, bottom plots. Therefore, if the original machine is with an asymmetrical configuration and a symmetrical is needed, new mimic diagram should be placed over the old one and the power supply leads must be arranged in accordance with the new mimic diagram.

The opposite case, how to change a symmetrical configuration into an asymmetrical, is shown in Fig. 3.11b. In this case, the whole winding sets which contain phases identified with the following numbers:

$$m = \frac{n+1+i}{2} \tag{3.46}$$

should be inverted. In (3.46), i represents an integer even number smaller than or equal to the number of phase sets:

$$i = 2, 4, 6, \ldots \leq k_{ws} - 1 \tag{3.47}$$

For example, in nine-phase case (k_{ws} = 3), after applying (3.46)-(3.47), it is calculated that i = 2 and m = 6. The winding set which contains phase number 6 must be inverted. If phase diagram is observed, it is easy to conclude that this phase is in Set-3. Every phase in this set must now be inverted. By doing so, new spatial displacement is π/n, which means that asymmetrical configuration is achieved (Fig. 3.11b, upper plots). Supply lead rearrangement is similar to the one explained for asymmetrical to symmetrical winding reconfiguration and is given in Fig. 3.11b, middle. Mimic diagrams are given in Fig. 3.11b, bottom.

The same approach can be used for other configurations of Table 3.1. As an example, a simplified representation for the fifteen-phase case is shown in Fig. 3.12. Fifteen-phase winding can be arranged

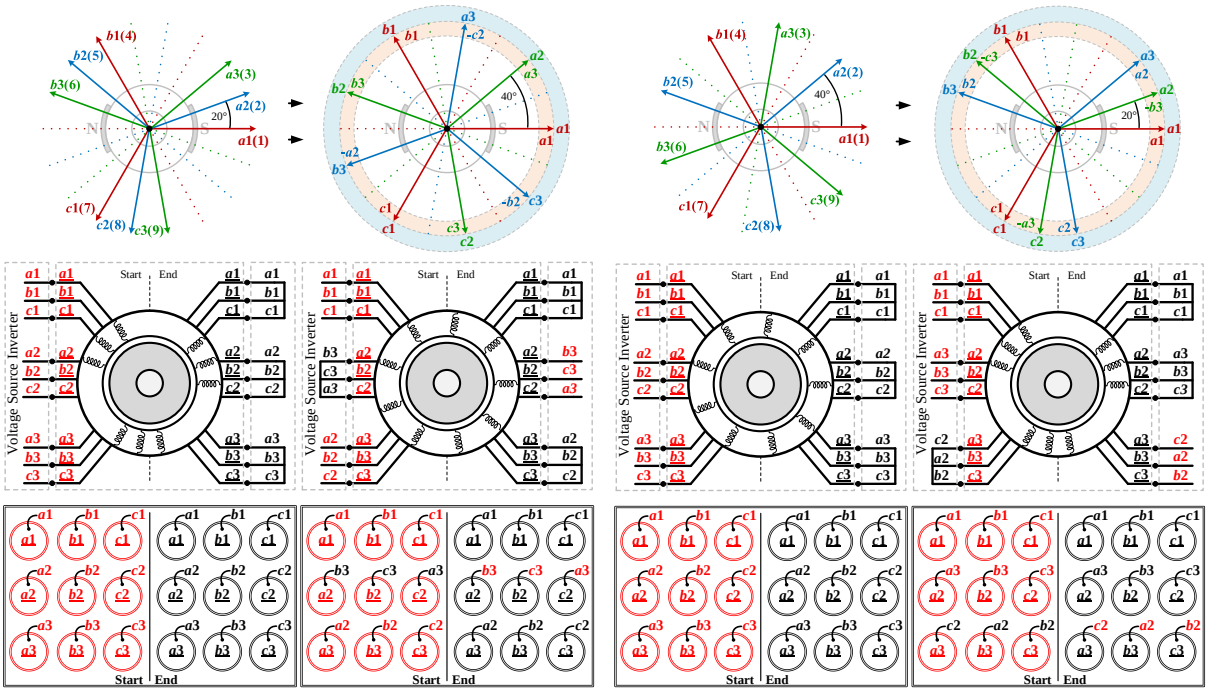

Figure 3.11 – Asymmetrical to symmetrical (a), and symmetrical to asymmetrical (b) winding reconfiguration: magnetic axis diagram (upper), VSI power supply leads rearrangement at the machine's terminal box (middle), and old and new mimic diagram (bottom plots).

in two different ways, with k_{ws} = 5, a = 3 or with k_{ws} = 3, a = 5. If the machine is asymmetrical with five three-phase winding sets (k_{ws} = 5), to achieve symmetrical configuration phases belonging to even sets (2nd and 4th) must be inverted. Following the same rule, if the fifteen-phase machine is with three-five-phase winding sets (k_{ws} = 3), the phases belonging to the 2nd set must be inverted. These cases are shown in Figs. 3.12a and b, respectively. As it can be seen from figures, in both cases new spatial displacement between consecutive phases is 24°. To achieve asymmetrical winding configuration out of a symmetrical fifteen-phase machine, two different possibilities are again available. If new required winding arrangement is with k_{ws} = 5, a = 3, using (3.46)-(3.47) it is easy to determine that the sets which contain phases numbered as 9 and 10 (i.e. Set-4 and Set-5) must be inverted. Following the same calculating principles, if winding arrangement is with k_{ws} = 3, a = 5, all phases in the set which contains phase number 9 (Set-4) must be inverted. Described rearrangements with new labels are shown in Figs. 3.12c and d, respectively. This time, new spatial displacement between consecutive winding sets is 12°.

As it can be concluded from Table 3.1, six-phase winding configuration is not in the group of the machines for which the winding reconfiguration can be achieved. Nevertheless, this is one of the most commonly used multiphase machine types; hence possible winding rearrangements are also briefly discussed here. Reconfiguration (that is, inversion of one three-phase set) in an asymmetrical six-phase machine will always result in another asymmetrical winding configuration, meaning that the winding type does not change (Fig. 3.13a). Therefore, for the asymmetrical six-phase case, the reconfiguration does not bring in anything new. On the other hand, reconfiguration of a symmetrical six-phase winding will result in a double-winding three-phase machine (with 0° shift between three-phase sets), as shown in Fig. 3.13b. The new configuration is obviously not asymmetrical (it is different from asymmetrical

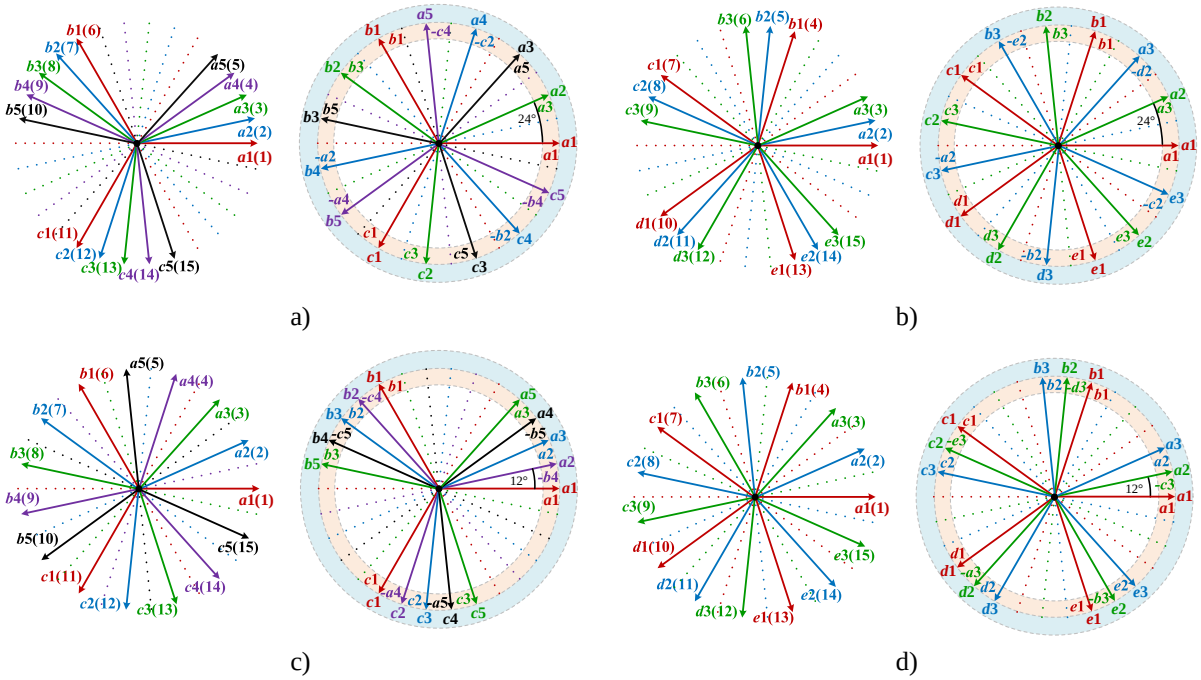

Figure 3.12 – Winding reconfiguration in a fifteen-phase machine. Asymmetrical to symmetrical for: (a) k_{ws} = 5, a = 3 and (b) k_{ws} = 3, a = 5; Symmetrical to asymmetrical for: (c) k_{ws} = 5, a = 3 and (d) k_{ws} = 3, a = 5.

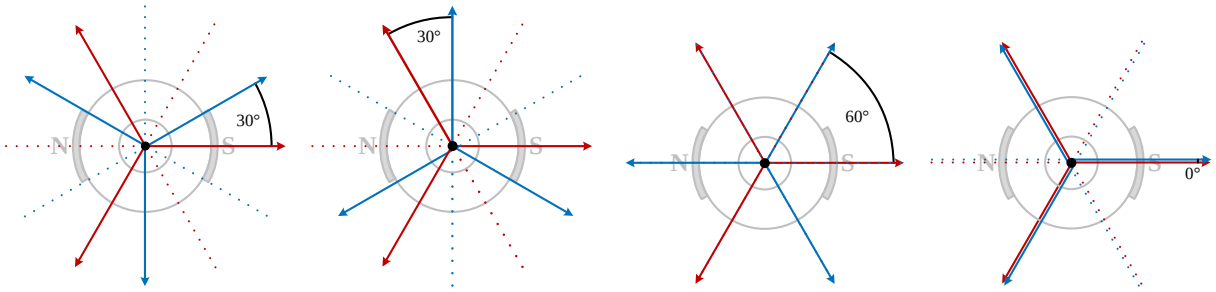

a) b)

Figure 3.13 – Winding reconfiguration in: (a) an asymmetrical, and (b) a symmetrical six-phase machine (blue set is inverted in both cases).

six-phase machines), but it can be useful in practice, e.g. [Zabaleta et al (2016a & b)]. Similarly, double-winding configuration can be also achieved in, for example, ten-phase symmetrical machine (new configuration is double-winding five-phase symmetrical), twelve-phase symmetrical machine (new configuration is double-winding six-phase asymmetrical), and so on.

In real world applications, once when the phase number is selected, the preferred configuration (symmetrical or asymmetrical) is in essence known. In general, the required spacing between multiple winding sets for best performance is π/n for an even number of sets and $2\pi/n$ for an odd number of sets. Nevertheless, as the multiphase machine prototypes for laboratories are commonly obtained by re-winding their three phase counterparts, one or the other configuration can be more suitable, depending on the envisaged research goal. Provided that the re-wound (multiphase) machine is with open end-windings, new control algorithms can be tested for both winding configurations using a single machine.

To validate theoretical considerations experimentally, two experimental setups, based on a nine-phase PMSM investigated in this work (see Appendix A) and on induction machine studied in [Zoric et al (2017a)], have been used. The recorded results (given here in Figs. 3.14 and 3.15) are published in [Slunjski et al (2020)], where a general algorithm for asymmetrical to symmetrical winding configuration change (and vice versa) can also be found. Harmonic mapping and parameter estimation tests were conducted, the goal being identification of differences caused by winding reconfiguration. Before testing induction machine, it was assumed that reconfiguration of winding will not cause any differences in machine parameters, and that therefore, the dynamics of the machine should not be different after reconfiguration (PI regulators are tuned using the same parameters). To validate these assumptions, parameter estimation tests and transient behaviour tests were performed. Corresponding results can be seen in Tables 3.2 and 3.3 and Fig. 3.14, respectively. By comparing the results given in tables, it is easy to conclude that change of the machine's configuration did not cause any relevant changes in the electrical parameters (which is expected because, with the change of position of supply leads, no physical changes of the machine structure have been done). Regarding transient testing, in both examined winding configurations speed was changed stepwise using FOC from 0 to 400 to 250 rpm and $T_{load} \approx 2$ Nm was kept constant. Based on the results one can see that in both cases transient performance

was the same (the same speed response, Fig. 3.14a). Also, after the reconfiguration, phase currents now have 40° displacement (Fig. 3.14b, bottom plot). Hence, it can be concluded that conversion of the asymmetrical into a symmetrical induction machine was successfully achieved.

Table 3.2 – Asymmetrical IM parameters.

Parameter	Value
Stator resistance (R_s)	5.42 Ω
Rotor resistance (R_r)	1.88 Ω
Stator leakage inductance (L_{ls})	23.7 mH
Rotor leakage inductance (L_{lr})	11.2 mH
Mutual inductance (L_m)	968 mH

Table 3.3 – Symmetrical IM parameters.

Parameter	Value
Stator resistance (R_s)	5.42 Ω
Rotor resistance (R_r)	1.84 Ω
Stator leakage inductance (L_{ls})	23.2 mH
Rotor leakage inductance (L_{lr})	10.9 mH
Mutual inductance (L_m)	987 mH

In the testing of the PMSM a simple FOC algorithm was again implemented (n_{ref} = 400 rpm, $T_{load} \approx$ 1.1 Nm). Fundamental current component was controlled for torque production, while the third current harmonic was not controlled (in essence, the third harmonic voltage generated by the PWM was zero on average in each switching period). In this way, the third EMF harmonic was inducing the third harmonic in the current, which was then analysed.

As can be seen in Fig. 3.15a, top, in symmetrical case each winding set phase currents have the same shape, i.e. the stator third harmonic is equally distributed. Hence,

$$i_{a1,3} + i_{b1,3} + i_{c1,3} + ... + i_{c3,3} = 0 \tag{3.48}$$

where

$$\begin{aligned} &i_{a1,3} = i_3 \cos(3\omega t - 0); \quad i_{b1,3} = i_3 \cos(3\omega t - 0); \quad i_{c1,3} = i_3 \cos(3\omega t - 0) \\ &i_{a2,3} = i_3 \cos(3\omega t - \frac{2\pi}{3}); \; i_{b2,3} = i_3 \cos(3\omega t - \frac{2\pi}{3}); \; i_{c2,3} = i_3 \cos(3\omega t - \frac{2\pi}{3}) \\ &i_{a3,3} = i_3 \cos(3\omega t - \frac{4\pi}{3}); \; i_{b3,3} = i_3 \cos(3\omega t - \frac{4\pi}{3}); \; i_{c3,3} = i_3 \cos(3\omega t - \frac{4\pi}{3}) \end{aligned} \tag{3.49}$$

is obviously satisfied. Because only fundamental and the third harmonic component are considered and other induced current harmonics with order higher than 3 are not of interest here, FFT analysis (Fig. 3.15a, bottom) is shown only for these two harmonics. On the other hand, current's third harmonic cannot have an equal distribution in an asymmetrical nine-phase machine, because the third harmonic stator currents would not sum to zero (if all have the same magnitudes i_3):

$$i_{a1,3} + i_{b1,3} + i_{c1,3} + ... + i_{c3,3} = i_3(3\sin(3\omega t) - 3\sqrt{3}\cos(3\omega t)) \neq 0 \tag{3.50}$$

$$\begin{aligned} &i_{a1,3} = i_3 \cos(3\omega t - 0); \quad i_{b1,3} = i_3 \cos(3\omega t - 0); \quad i_{c1,3} = i_3 \cos(3\omega t - 0) \\ &i_{a2,3} = i_3 \cos(3\omega t - \frac{\pi}{3}); \quad i_{b2,3} = i_3 \cos(3\omega t - \frac{\pi}{3}); \quad i_{c2,3} = i_3 \cos(3\omega t - \frac{\pi}{3}) \\ &i_{a3,3} = i_3 \cos(3\omega t - \frac{2\pi}{3}); \; i_{b3,3} = i_3 \cos(3\omega t - \frac{2\pi}{3}); \; i_{c3,3} = i_3 \cos(3\omega t - \frac{2\pi}{3}) \end{aligned} \tag{3.51}$$

As illustrated in Fig. 3.15b, top, the consequence of the inequality (3.50) is that the waveforms in the sets are obviously not of the same shape, i.e. the third harmonic currents attain different magnitudes in the different three-phase sets. Obtained different magnitudes of the third harmonics enable satisfaction of the condition $\Sigma_{i3} = 0$.

As a consequence, aspects such as, for example, torque enhancement using harmonic current injection, are not a straightforward task for an asymmetrical nine-phase machine because of the unequal current distribution. Hence, for control simplicity and in order to achieve higher torque, symmetrical configuration is preferred [Slunjski et al (2019)]. Although the work in [Slunjski et al (2019)] will be

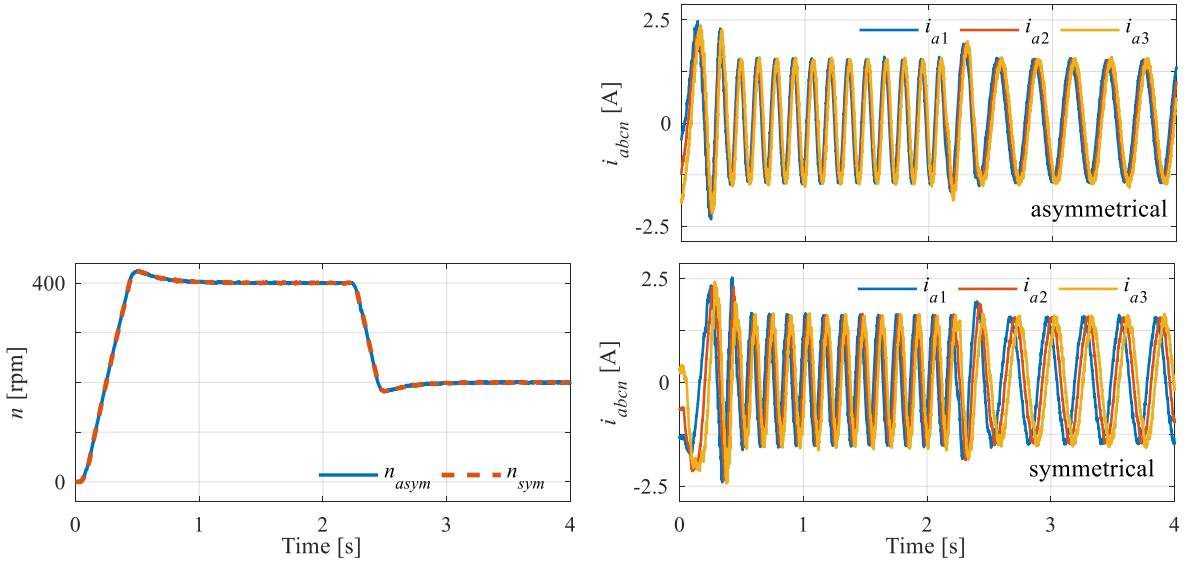

Figure 3.14 – Experimentally recorded mechanical speed (a) and phase currents ($a1$, $a2$, $a3$) (b) under applied sequence for both winding configurations – induction machine.

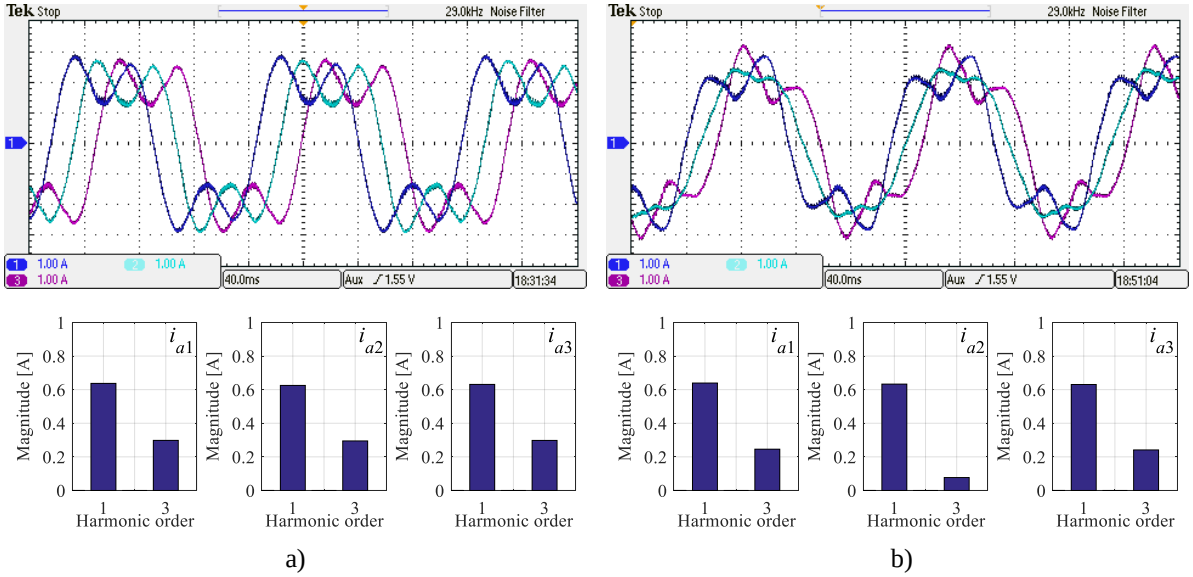

Figure 3.15 – Experimentally recorded phase currents (phases $a1$, $a2$, $a3$) and corresponding FFTs in: (a) symmetrical and (b) asymmetrical PM synchronous machine.

discussed in the chapters to follow, for the sake of completeness, it should be noted here that in both [Slunjski et al (2019)] and [Cervone et al (2019)], torque enhancement using the same machine was studied (for symmetrical/asymmetrical configurations, respectively). Reported torque improvement in [Slunjski et al (2019)] is ≈36%, while in [Cervone et al (2019)] it is only around 15%. This clearly shows how a symmetrical configuration (the one implemented in the real prototype used in this work), is preferable when harmonic injection for torque enhancement is studied.

3.6 Field Oriented Control (FOC)

Implementation of advanced and sophisticated control algorithms is today, from the cost perspective, negligible compared to the cost of the machine and converter production. The most commonly used control strategy for multiphase machines nowadays is the field oriented control technique. This method is based on multiple inner current control loops with a superimposed outer speed controller. It is an important motor control method, which turns the complicated and coupled motor model into a simple system similar to that of a separately excited dc drive, and then separately controls the flux- and torque-producing currents in the machine. The same control algorithm applied for three-phase machines can also be applied for multiphase machines with some modifications. The main difference is in the number of current controllers, i.e., an *n*-phase drive (where *n* is odd) with single neutral requires (*n* - 1) independent current controllers to control/reduce low-order harmonic current content. As explained in chapter 2, the FOC will be used further on in this work, so the basic concepts are introduced in this chapter. In this way, testing of the derived nine-phase PMSM benchmark model with near-sinusoidal back-EMF can be performed. Building on the basic FOC principles presented here, control algorithms for machines with non-sinusoidal EMF will be derived in the following chapters.

The block diagram of (fundamental current only) field oriented control strategy for multiphase machines can be seen in Fig. 3.16. With $i_d = 0$, produced torque is, in fact, a linear algebraic function of i_q current only. Therefore, an i_q control is essentially a torque control with just a constant coefficient in-between:

$$i_{q-ref} = T_{em} \cdot \frac{2}{n} \frac{1}{P \cdot \lambda_m} \tag{3.52}$$

Given equation is identical to the electromagnetic torque equation (3.38), with the only difference that it contains only torque-producing current part ($i_{d\text{-}ref} = 0$; surface PMs). Outputs of the stator *d-q* current PI regulators can be mathematically modelled as:

$$v_{d-reg} = R_s \cdot i_d + L_s \frac{di_d}{dt}; \qquad v_{q-reg} = R_s \cdot i_q + L_s \frac{di_q}{dt} \tag{3.53}$$

To acquire total stator voltage *d-q* references in the synchronous reference frame (as in (3.39), (3.40)) which are necessary for the coordinate transformation, decoupling voltages:

$$e_d = \omega_{el}\left(L_s \cdot i_d + \lambda_m\right); \qquad e_q = \omega_{el}\left(L_s \cdot i_q\right) \tag{3.54}$$

must be added to (3.53). Hence, the total stator voltage references are now equal to:

$$v_{d-ref} = v_{d-reg} - e_q; \qquad v_{q-ref} = v_{q-reg} + e_d \tag{3.55}$$

To achieve high-performance closed-loop control, proportional-integral (PI) regulators are usually used. Theory regarding k_P and k_I gains tuning for electric drives is today well-known, hence this will not be further discussed here. An anti-windup algorithm is usually implemented together with the PI controllers. A number of anti-windup techniques have been proposed in the literature. In this thesis, the technique presented in [Visioli (2003)] is used. The output value of the PI regulator is compared with high and low saturation limit. If the value is bigger than high saturation limit or lower than low saturation limit, integral component integrator is restarted by sending zero to its input. Otherwise, the output integral constant is set as an input of the corresponding integrator. In the rest of the thesis, whenever PI control is used, it is assumed that anti-windup given in Fig. 3.17 is implemented as well.

Complete near-sinusoidal PM synchronous machine model in phase-variable reference frame with an arbitrary phase number on stator and with accompanying field oriented control in synchronous reference frame, suitable for software implementation, is shown in Fig. 3.18. As mentioned earlier, this structure will be used in the following chapters to derive advanced control algorithms for the investigated nine-phase prototype.

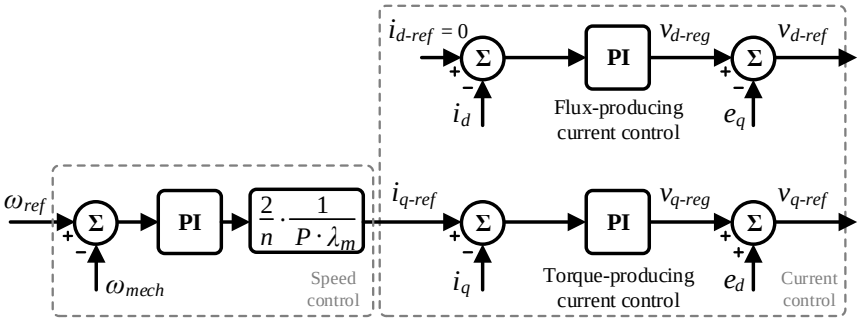

Figure 3.16 – Block diagram of field oriented control algorithm (speed and current control).

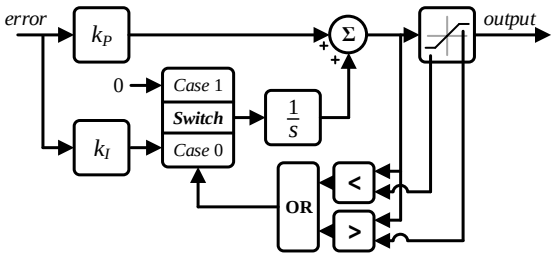

Figure 3.17 – Anti-windup algorithm block scheme.

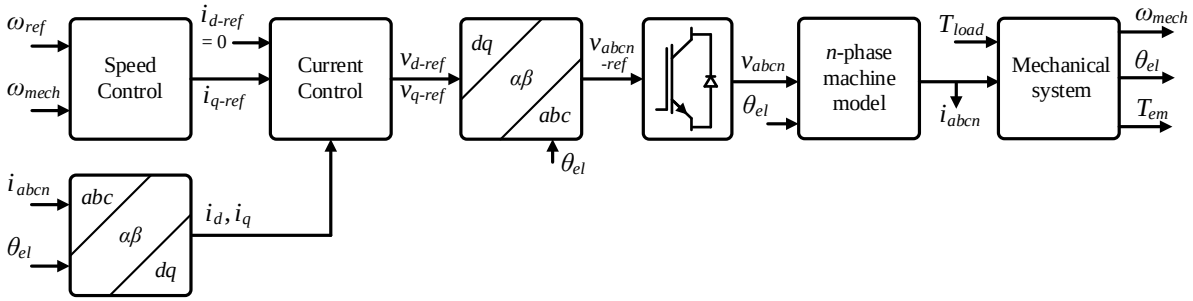

Figure 3.18 – Overview of the full model – field oriented control in synchronous reference frame and *n*-phase machine model in phase domain.

3.7 Simulation Results and Model Verification

The prototype machine is designed with two surface magnet poles, each spanning 45°. Such rotor configuration was obtained after removing 4 magnet poles from the original (six-pole) rotor. Stator of the machine was also re-wound (from three-phase to nine-phase and with different wire type), which means that comparison of the new prototype with the original machine is, although interesting, hard to achieve. A benchmark configuration was therefore chosen. Number of stator phases and their distribution around circumference is the same as in the studied prototype and design and electrical parameters (where possible) of the two machines are kept the same. The difference, however, between the two machines is in the magnet span. In the benchmark machine, each magnet span is 180° around rotor's circumference. Known design and electrical parameters which are used in 45° configuration (but are the same in benchmark machine), can be found listed in tables in chapter 4, section 4.2.

Different magnet span (i.e. different amount of magnetic material) in the case of the benchmark machine means different back-EMF and flux distribution (shape). Consequently, this also means different PM flux constants. To obtain these parameters, FEM model for prototype machine was first built and verified. Verification of this model is straightforward, because it can be directly compared with experimentally recorded back-EMF in the real machine under no-load generation mode. Once FEM modelling was verified for 45° configuration, the magnet span was increased to 180°, and the obtained back-EMF, recorded at 1500 rpm, can be seen in Fig. 3.19a. Corresponding harmonic spectrum is given in Fig. 3.19b. 81 FEM points were solved in total, but for clarity, every third one is shown. As is visible from the spectrum, for such magnet span, in addition to the fundamental a small third harmonic component also exists. By knowing that the back-EMF and permanent magnet flux are directly related though angular speed, λ_{m1} and λ_{m3} can be easily calculated. The values come out as λ_{m1} = 642 mWb and λ_{m3} = 27 mWb. It should be noted that the fundamental is placed at $\theta_{phs1} = 0°$, while the third harmonic is shifted for $\theta_{phs3} \approx 178°$ (recalculated out of FFT angles in Fig. 3.19b). Based on these parameters (and the ones from chapter 4, which are the same for both machines), the near-sinusoidal benchmark machine model is built in *Matlab*/*Simulink* environment.

Single periods of flux and back-EMF, obtained in no-load generating mode at 1500 rpm are given in Figs. 3.20a and b, respectively. Corresponding FFT harmonic spectrums are also given. As it can be seen, there is a high correspondence between these results and the ones obtained in Fig. 3.19 using finite element software. This confirms the validity of the modelling approach used for machines with near- (alternatively, non-) sinusoidal back-EMFs. Afterwards, the benchmark machine is tested in steady state, at 1500 rpm with a load of 3 Nm. The machine operates under field oriented control. The results are shown in Fig. 3.21, where FEM results are given in 3.21a plots, while (*Matlab*/*Simulink*) results can be seen in 3.21b plots. In addition to the speed (top plot) and torque (bottom plot), phase currents

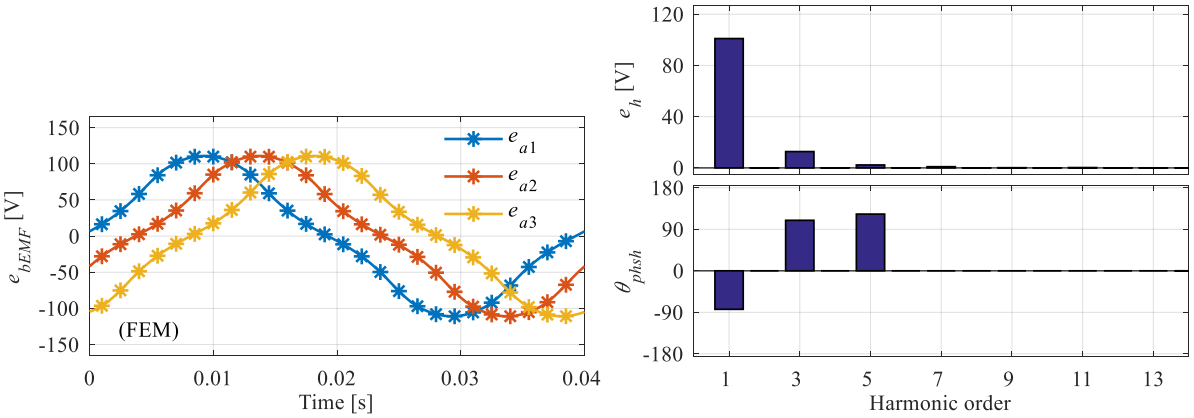

a) b)

Figure 3.19 – FEM results acquired in no-load generation mode: (a) back-EMF, and (b) corresponding FFT spectrum.

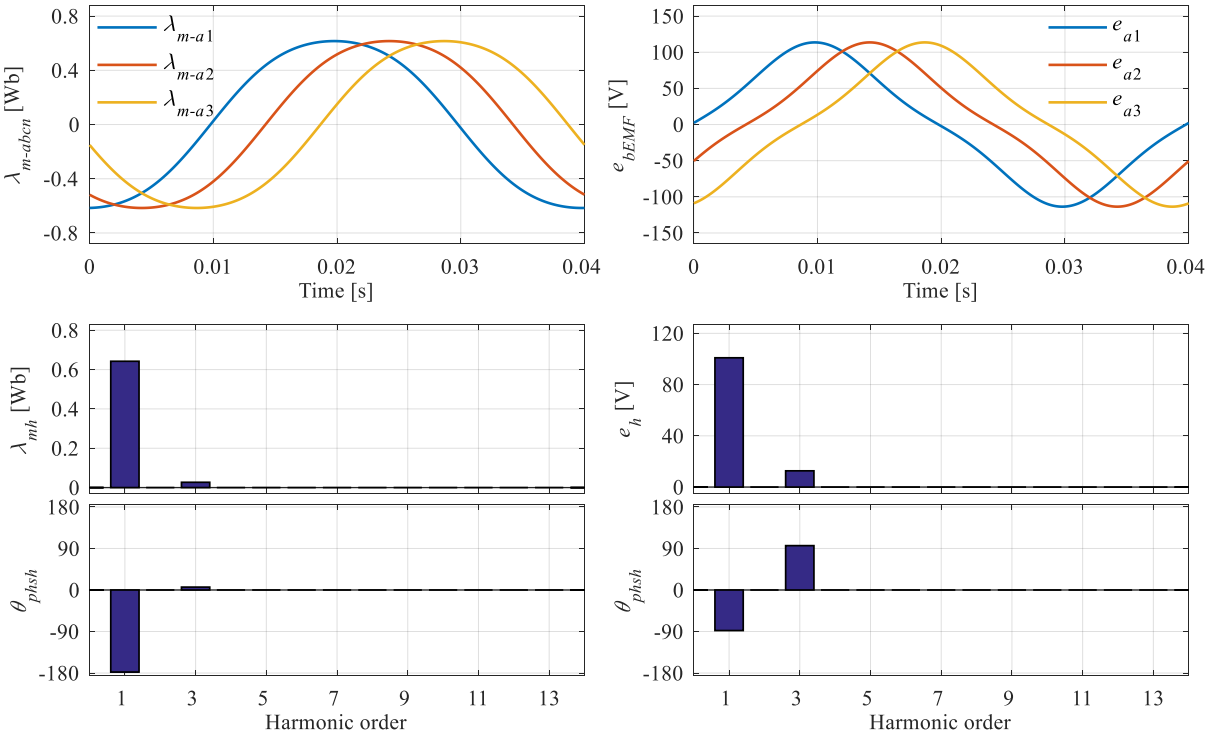

a) b)

Figure 3.20 – Simulation results acquired in *Matlab*/*Simulink*: (a) flux produced by PM and corresponding FFT analysis, and (b) derivative of flux produced by permanent magnets (i.e. back-EMF) and corresponding FFT.

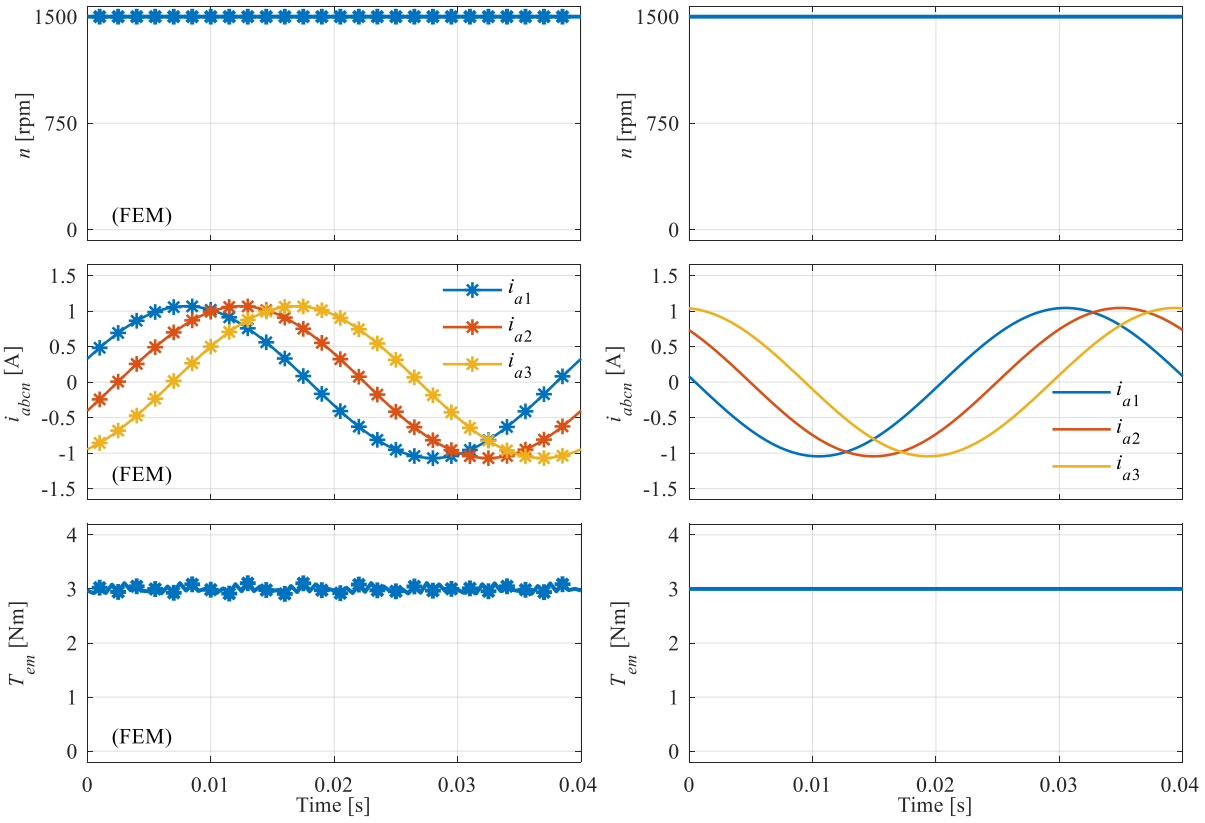

Figure 3.21 – Finite element method (a), and *Matlab*/*Simulink* environment (b) simulation results: mechanical speed (top), phase currents (middle), and electromagnetic torque (bottom).

(*a*1, *a*2, *a*3; middle) are also given. There is a high correspondence between Figs. 3.21a and 3.21b. The small difference is related to torque ripple in FEM results, which is coming from the simplifying assumptions made while developing the *Matlab*/*Simulink* model. To eliminate any effects caused by the small third harmonic (i.e. induced harmonic currents), additional controllers were implemented. The type of the controller used for this purpose will be explained in chapter 5, as it plays much more significant role in the work presented there.

3.8 Summary

In this chapter the complete modelling process for a permanent magnet synchronous multiphase machine with an arbitrary number of phases on stator and with (near-) sinusoidal MMF and back-EMF distributions has been presented. First, the machine model in phase-variable reference frame has been derived. Due to the high complexity of the resulting model, methods for machine model decoupling have also been presented. Vector space decomposition method was investigated for this purpose. To implement a VSD transformation, winding arrangement and the number of isolated neutral points must be defined. In general, machine can be configured to be symmetrical or asymmetrical and with single or multiple isolated neutral points. Since the intention is to use stator current harmonic injection to increase

the torque-per-Ampere, symmetrical winding with single isolated neutral point was chosen. Nevertheless, methods for winding reconfiguration in composite odd phase number machines (the category to which the studied machine belongs) only by rearranging power supply leads in the machine terminal box were also introduced. After decoupling the machine model, equations in the *d-q* reference frame are subsequently derived by using the rotational transformation.

The prototype machine was obtained by redesigning a three-phase machine. Because both stator and rotor have been changed, it is not possible to compare the results obtained with the new machine with the original one. Hence, a new benchmark configuration was chosen, in which the only difference when compared to the new prototype is the magnet span on rotor (180° and 45°, respectively). The benchmark machine model in the phase-variable reference frame with the control algorithm in the synchronous reference frame was tested in FEM and *Matlab*/*Simulink* environments. FOC has been used to evaluate the system performance. As shown, a high level of agreement between FEM results and the ones obtained in *Matlab*/*Simulink* environment was achieved. In the following chapter, prototype machine will be modelled and analysed in detail in FEM, and recorded results will be compared with the ones recorded in this chapter. In this way, the characteristics of the new rotor configuration (with shortened magnet span) will be investigated.

Chapter Four

ANALYSIS OF THE MACHINE WITH NON-SINUSOIDAL BACK-EMF

4.1 Introduction

A surface permanent magnet synchronous machine with a symmetrical nine-phase winding on stator and with different magnet spans on rotor is investigated in this chapter. For this purpose, a finite element method (FEM) software tool is used. The machine prototype (the one with 45° magnets) is first introduced (section 4.2), and corresponding back-EMF shape (i.e. FFT spectrum) recorded experimentally in the no-load generation mode is analysed. Cross-section of the machine and known electrical/design parameters are given as well. As explained in chapter 3, this is an important step because, based on design parameters, a FEM model can be built and verified using experimental data. A FEM model of the benchmark machine (the one with 180° magnet span used in chapter 3) is also built and analysed.

In section 4.3 both FEM models are tested under the sinusoidal phase current, with the same RMS value. The aim is to determine the derating in the torque production caused by the reduced magnet span. Although the torque produced with shortened magnets will be, as expected, significantly lower, the resulting back-EMF is characterised with highly non-sinusoidal shape. By performing analysis of the EMF, a third harmonic component, which is almost equal in magnitude to the fundamental, is revealed. The fifth and some seventh harmonic also exist. It has been shown in the chapter 2 that the low order odd harmonics, of the order below the machine phase number, can be used to increase the torque density of multiphase machines. The reduced magnet machine is here tested under different combinations of harmonic currents and a significant (up to 43% for FEM model) torque improvement is reported. It should be noted however that, when compared with the existing methods for torque improvement, the approach (i.e. reduction of the amount of magnet material, by reducing the magnet span, to produce high harmonic content in the back-EMF spectrum) is different. This stems from the fact that in the majority of PMSM related literature, to produce EMF spectrum with high low order harmonic content, magnets are either added to the rotor [e.g. Aslan and Semail (2014)] (hence increasing the price of the drive) or reshaped resulting in a difficult to manufacture machine [e.g. Wang et al (2018)].

As it will be shown in section 4.4, although significantly enhanced, the maximum achievable torque in the machine with 45° magnets is still lower than the torque produced by the machine with 180° magnets. Therefore, an additional study is conducted at the end of the chapter (section 4.5), where different (higher than 45°) magnet spans are analysed. As it is shown, to produce torque equal to the one of the benchmark machine, the rotor configuration needs to be with ≈75° magnets if, in addition to the fundamental, only the third harmonic is considered; on the other hand, ≈70° magnet span is required if all meaningful low order odd EMF harmonics are used for torque production. FEM analysis presented in this chapter was published in [Slunjski et al (2018) and Slunjski et al (2021)]. In [Slunjski et al (2018)] the analysis considered only the fundamental and the third harmonic, while [Slunjski et al (2021)] contains an extended study with the fifth (and seventh) harmonic included.

4.2 Prototype Machine Configuration

The cross-section of the studied machine is shown in Fig. 4.1a. The machine was obtained by rewinding a three-phase six-pole MOOG FAS T-2-M2-030 machine (180 V, 8.5 A, 1.73 kW, 3000 rpm, 150 Hz) and removing four NdFeB magnets from the rotor. Single-layer winding is distributed in 36 slots, number of slots per-pole-per-phase is equal to 2 and there is a single isolated neutral point; hence, regular winding is designed and mounted on stator. In places where four removed NdFeB magnets were, non-magnetic material was placed. Known electrical parameters of the nine-phase configuration are given in Table 4.1. Parameters were obtained experimentally by performing zero-sequence, single-phase and short-circuit tests, about which more can be found in [Stiscia (2019) - chapter 6]. Experimentally recorded back-EMF (phases *a*1, *a*2, *a*3; no-load generation mode), and corresponding (phase *a*1) FFT analysis are given in Figs. 4.2a and b, respectively. Based on Fig. 4.2, it is easy to conclude that harmonics with order 1 to 13 need to be taken further into consideration. The magnitudes are given in Table 4.2, where the given values are the average of all nine phase EMF (FFT) harmonic spectra.

Back-EMF magnitude of the h^{th} harmonic is related to the flux magnitude of the same order through the angular speed ω_{mech}, that is:

$$\lambda_{mh} = \frac{e_h}{h \cdot \omega_{mech}} \tag{4.1}$$

By knowing that the back-EMF signals were recorded at ≈1463.5 rpm (24.39 Hz), Table 4.2 can be further extended with the values of PM fluxes. Regarding harmonic angular shifts (which are given in the last column of the Table 4.2), the following simplification was adopted: fundamental is placed at 0° angle and all other harmonic angles are recalculated with respect to this datum value. As it can be noticed, the third harmonic is shifted for ≈180° (i.e. it is in counter phase) with regard to the fundamental. Although impact of two harmonics being in a counter phase is not further investigated as long as the machine is controlled using maximal torque-per-Ampere approach below base speed (chapters 5, 6, 7), it will play a significant role once machine enters flux-weakening region, hence further investigation regarding this will be performed in chapter 8.

Table 4.1 – Machine data and parameters.

Quantity/Value	R_s = 31.3 Ω L_{ls} = 84.7 mH	$L_{d1} = L_{q1}$ = 459.8 mH
		$L_{d3} = L_{q3}$ = 120.4 mH
		$L_{d5} = L_{q5}$ = 96.0 mH

Regarding stator and rotor dimensions and design parameters, the machine has 19.3 mm stator slot depth, 4.1 mm stator tooth width, 0.834 mm stator radial depth, 306 turns per phase (153 conductors in slot), 0.4/0.35 mm wire diameter (with/without insulation), 16.5 mm rotor shaft radius, 37 mm rotor external radius, 3 mm NdFeB (unsegmented) magnet thickness, 65.9 mm outer stator radius, 1 mm airgap and the length of 55 mm. All stated dimensions are approximate. Benchmark machine cross-section, with the same design parameters and with two 180° magnets, is shown in Fig. 4.1b.

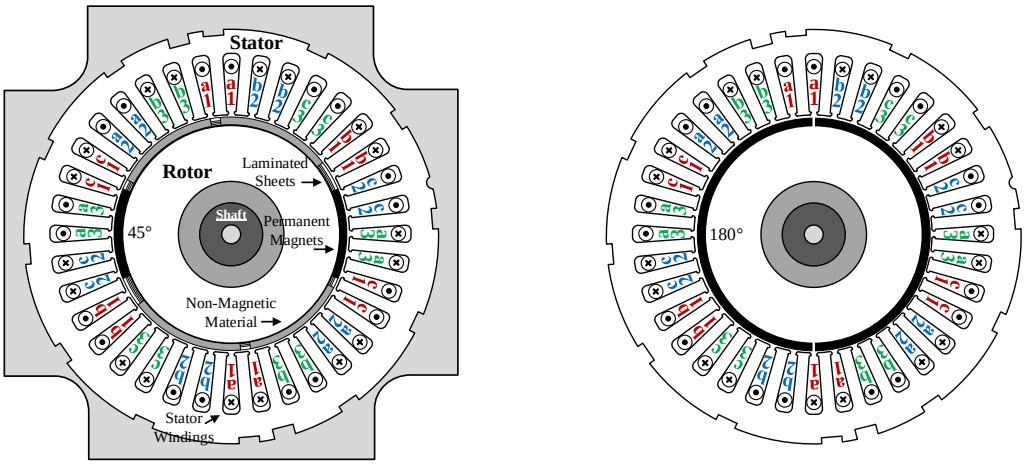

a) b)

Figure 4.1 – Cross-section of a nine-phase PM synchronous machine with equal stator and: (a) 45° magnet span, and (b) 180° magnet span on rotor.

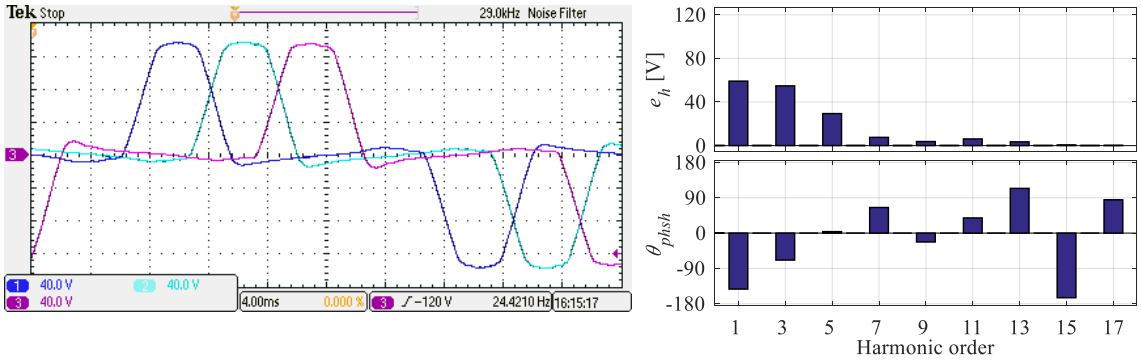

a) b)

Figure 4.2 – Experimental recorded non-sinusoidal back-EMF (a), and corresponding FFT (b) – no-load generation mode.

Table 4.2 – Back-EMF and flux harmonics (peak average values) recorded experimentally.

h	***e_h* [V]**	***λ_{mh}* [mWb]**	***θ_{phsh}* [°]**
1	59.13	385.83	0
3	54.81	119.22	177.25
5	29.37	38.33	-3.21
7	7.54	7.03	132.24
9	3.72	2.70	170.04
11	6.09	3.62	-33.37
13	3.42	1.72	142.45

4.3 FEM Analysis Considering Fundamental Current Only

By taking into account electrical and design parameters from the previous section, both non- (45°) and near- (180°) sinusoidal configurations have been constructed in FEM software. To verify models, machines were first tested in no-load generation mode (at 1500 rpm; 25 Hz). Recorded EMF results are given in Fig. 4.3 (upper plots), while corresponding FFT spectra can be seen in the same figure in the

bottom plots. Near-sinusoidal results are given on the left (a) side, while non-sinusoidal results can be seen on the right (b) side of the figure. In both cases, the first phase in each winding set (i.e. phases *a*1, *a*2, *a*3) is recorded, while FFT spectra are given for phase (*a*1). The results obtained for near-sinusoidal configuration (the ones already presented in chapter 3) are used in this chapter for benchmarking purposes. Furthermore, presentation of FEM steps with asterisks (as done in chapter 3) is in this chapter omitted because shown results are strictly related to the FEM; hence, there is no need to distinguish them from *Matlab*/*Simulink* simulation results. Each simulation is one period long, and during this time interval, 81 points are solved using finite element method.

As shown in Fig. 4.3a, in the near-sinusoidal case, the EMF is mostly produced by the fundamental component, but a small (12.6% of the fundamental) third harmonic component also exists. In the non-sinusoidal case (Fig. 4.3b), the back-EMF comprises almost equal fundamental and the third harmonic components (≈86.9%), with the fifth harmonic component approximately equal to the half of fundamental (≈48.5%), and with a small seventh harmonic component. If the shape is compared with the one shown in Fig. 4.2, a high correspondence can be seen. Small difference in harmonic magnitudes is caused by design parameter approximations and is also due to the fact that 2D version of FEM software is used (hence effects, such as, for example, magnet skewing on rotor, are not included in the simulation). Because prototype machine was manufactured overseas, not all machine properties (e.g., steel type, exact dimensions, exact NdFeB type, etc.) are known.

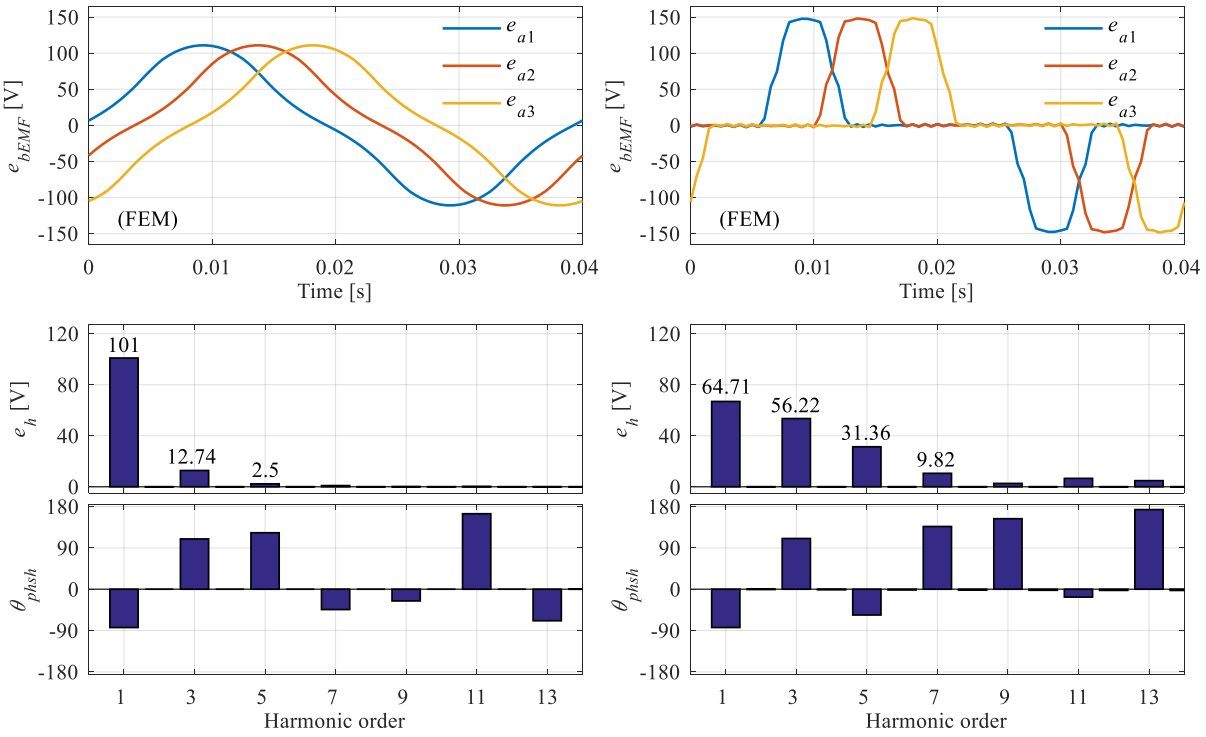

Figure 4.3 – Back-EMF and FFT obtained after FEM analysis of PMSM for: (a) near-sinusoidal, and (b) non-sinusoidal back-EMF configurations.

Under normal (sinusoidal current) operation, it is expected that the machine with 45° magnets will produce lower torque. To test the derating, both machines are analysed in motoring mode, applying sinusoidal currents with the same RMS. As before, mechanical speed is set to be 1500 rpm. The obtained FEM results for phase currents and electromagnetic torque are given in Fig. 4.4. It is clear from the figure that although applied currents in both test scenarios were equal ($1/\sqrt{2}$ A RMS and with symmetrical, 40° phase shift between them), the developed output torques are different. In the non-sinusoidal case (Fig. 4.4b), the electromagnetic torque is (on average) 1.68 Nm, which is a reduction of 42.5% compared to the torque developed by the near-sinusoidal machine (Fig. 4.4a), i.e. 2.92 Nm. To increase the output torque for non-sinusoidal back-EMF configuration, shape of the current is next altered, i.e. harmonic current injection is performed.

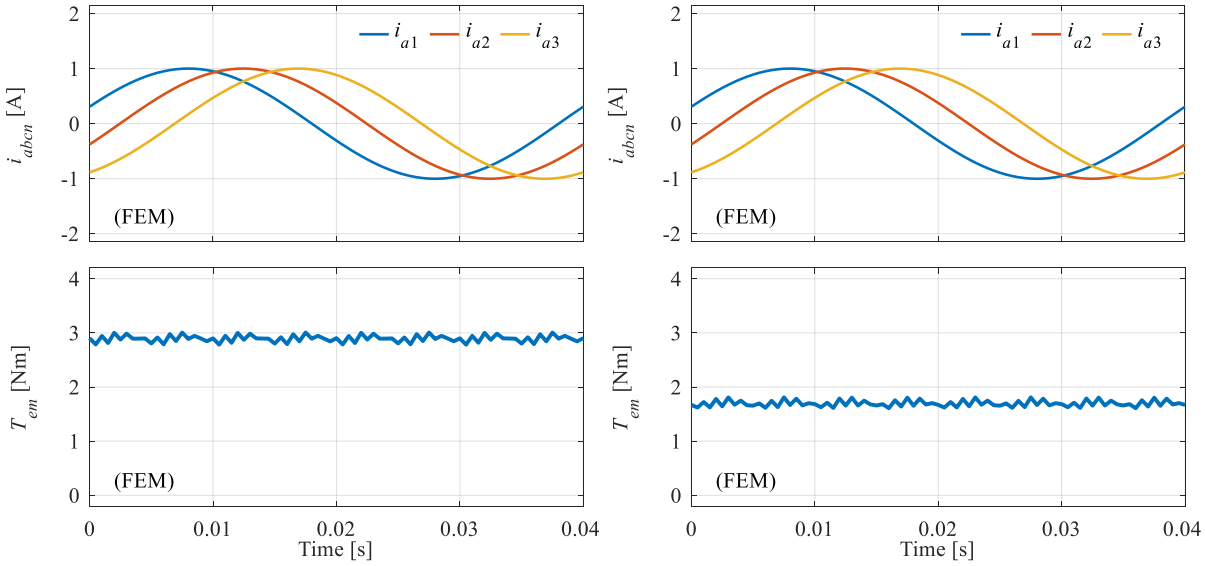

Figure 4.4 – Simulation results for phase currents and electromagnetic torque obtained by FEM for: (a) near-sinusoidal, and (b) non-sinusoidal case.

4.4 Torque Enhancement Analysis

Before continuing further, it should be noted that injection of current harmonics requires knowledge of optimal injection ratio between fundamental and other considered harmonic components. Subdivision of the current into the first and other harmonics (where appropriate) is one of the objectives investigated in chapter 5 (where optimal ratio between fundamental and the third harmonic is derived using MTPA approach), and in chapter 6 (where generalisation of this approach is given). For the time being, only a final equation from these chapters is used, showing how optimal injection ratio between fundamental and any other required harmonic can be calculated as a ratio between EMF/PM flux components:

$$k_{1h} = \frac{e_h}{e_1} = \frac{h \cdot \lambda_{mh}}{\lambda_{m1}} \tag{4.2}$$

By using (4.2) in combination with results from Fig. 4.3b, one can easily determine that for non-sinusoidal back-EMF FEM model, optimal injection coefficient relating fundamental and the third harmonic should be $k_{13} = 0.869$, i.e. $k_{15} = 0.485$ if, in addition to the fundamental, the fifth harmonic is used. For fundamental and the seventh harmonic, this ratio is $k_{17} = 0.152$.

Recorded phase currents and torques acquired under optimal current injection are shown in Fig. 4.5. Fundamental plus the third harmonic case is shown in Fig. 4.5a, while combination of the fundamental, the third and the fifth harmonic is shown in Fig. 4.5b. When coupled with the EMF, fundamental and the third harmonic currents are producing ≈2.24 Nm output torque. For the same phase current RMS value ($1/\sqrt{2}$ A), addition of the fifth harmonic causes increase in torque to ≈2.39 Nm. Because the contribution of the seventh injected harmonic compared to the contribution of combined third and fifth is relatively small (0.83%; $T_{em135} = 2.39$ Nm, $T_{\text{em1357}} = 2.41$ Nm) this harmonic is not further taken into consideration. It is important to note that although the phase current RMS was not changed in any of the above analysed cases, phase current peak value was increased with each additionally added current harmonic (this might not be the case in the other machines with different back-EMFs). Importance of this will be further discussed in chapter 8, where above-nominal speed operation is investigated.

Flux maps and corresponding isolines for above analysed cases (including the one from previous section where fundamental current only scenario was examined) are shown in Fig. 4.6. For FEM analysis two software tools were used: Finite Element Method Magnetics (FEMM 4.2) and Cedrat Flux2D 11.2. Graphical results in Fig. 4.6 were obtained in Flux2D software tool.

For the sake of completeness, it should be noted that the small third harmonic component, which exist in near-sinusoidal configuration, can also be employed for the torque production. By calculating the optimal ratio between two harmonics ($k_{13} = 0.126$) and under the same phase current RMS constraint, the final reachable output torque value comes as ≈2.99 Nm. A comparison of the developed torques can now be performed (Fig. 4.7). The highest torque is produced using 180° magnets, i.e. near-sinusoidal configuration with injected third current harmonic (2.99 Nm), while the lowest is produced with 45° magnets and fundamental current component only (1.68 Nm). The torque obtained with non-sinusoidal configuration and the third harmonic current injection (2.24 Nm) is ≈25% lower than the highest achievable torque, but is also ≈33% higher than the torque produced by the same non-sinusoidal configuration and fundamental current only. In the case of fifth (and similarly seventh) harmonic current contribution, achievable torque (2.39 Nm) is still ≈20% lower than the output torque in 180° configuration with the third harmonic current injection. Nevertheless, this is a significant ≈43% increase if compared with the torque produced in the same (non-sinusoidal) configuration working under fundamental current. It is important to note that although investigated prototype is not capable of reaching benchmark machine output torque, the magnets on rotor are spanning only 45°, i.e. 4 times less magnet material was used in the prototype machine's rotor construction.

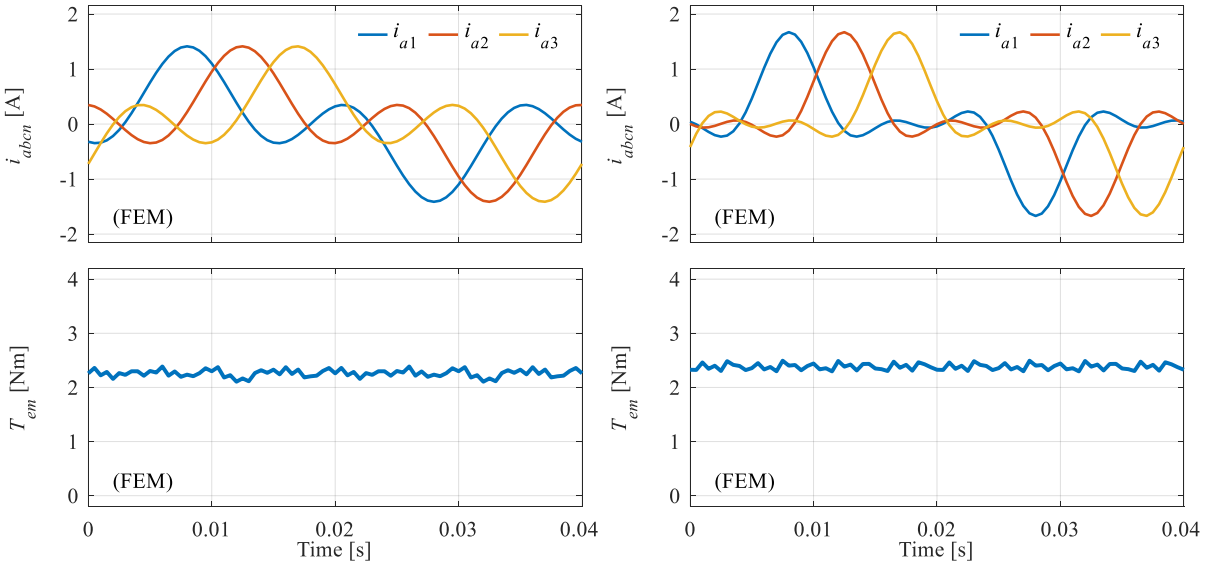

a) b)

Figure 4.5 – FEM results for phase currents and electromagnetic torque obtained in: (a) fundamental and third harmonic, and (b) fundamental, the third and the fifth harmonic case.

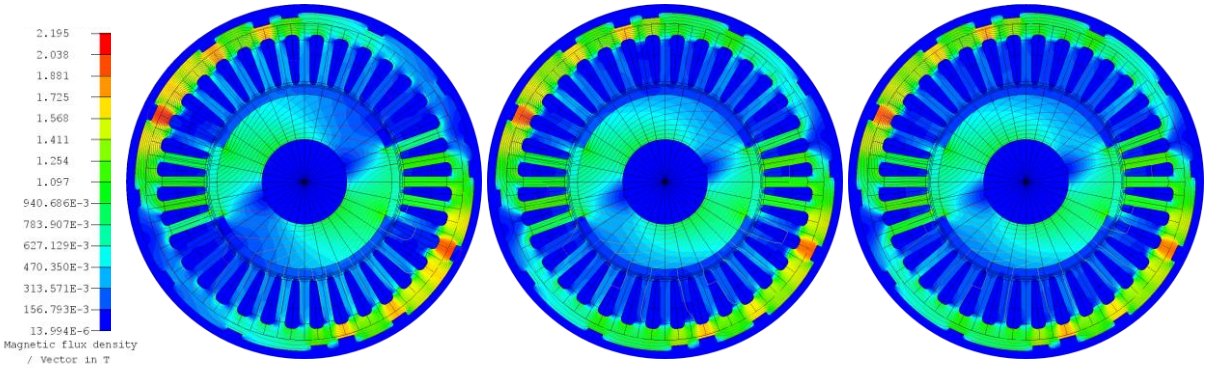

a) b) c)

Figure 4.6 – Flux map and corresponding isolines for: (a) fundamental current ($T_{em} \approx 1.68$ Nm), (b) the 1st and the 3rd harmonic currents ($T_{em} \approx 2.24$ Nm), and (c) the 1st, 3rd, 5th harmonic currents ($T_{em} \approx 2.39$ Nm).

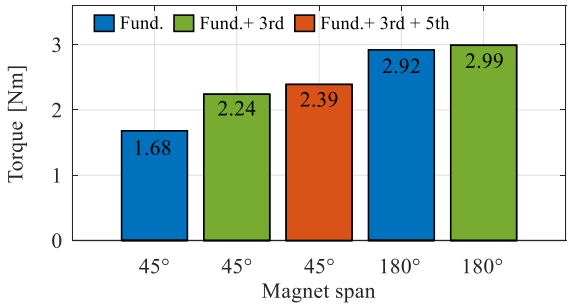

Figure 4.7 – Comparison of the electromagnetic torques produced with different magnet spans and the same phase current RMS.

For additional derating study between the two machine configurations, analysis of input/output powers (i.e. efficiency) is performed using *Matlab*/*Simulink* environment and taking into account only copper losses. Obtained results are summarised in Table 4.3. As can be seen from the table, the derating in terms of output power is relatively significant. However, the difference in achieved efficiency is

relatively small (76.7% for 180° case vs. 72.6% for 45° case). Low overall efficiency is caused by the winding stator resistance, which is, as shown in Table 4.1, very high.

Table 4.3 – Efficiency analysis of rotor configurations with 45° and 180° magnet spans at 1500 rpm.

Config. / Param.	T_{em} [Nm]	P_{in} [W]	P_{Cu} [W]	P_{out} [W]	η [%]
45° ***mag. span, fund. only***	1.68	407.7	143.8	263.9	64.7
45° ***mag. span, fund.*** **+ 3rd + 5th**	2.39	519.6	142.6	377.0	72.6
180° ***mag. span, fund. only***	2.92	602.2	143.5	458.7	76.2
180° ***mag. span, fund.*** **+ 3rd**	2.99	612.8	143.1	469.7	76.7

4.5 Investigation of Relation between Torque and Magnet Span around Rotor Circumference

The logical questions that arise from the previous section are: can the magnet material be reduced while at the same time the developed torque is preserved as close as possible to that of the near-sinusoidal machine configuration and, if so, how much is the magnetic span that will enable this in conjunction with suitable harmonic current injection strategy? In order to answer these questions, additional FEM analysis is conducted using different magnet circumferential spans. The obtained results are presented in Fig. 4.8.

In Fig. 4.8a, the fundamental, the third and the fifth EMF harmonic magnitudes are shown for magnet spans between 30°-80°, in 5° increments. The results were obtained in no-load generation mode. While for the observed span range the fundamental component is increasing (due to the increasing magnet material), the other two monitored harmonics are not following the same pattern. At first, both the third and the fifth EMF magnitudes increase, while afterwards, this trend reverses (finally reaching the values shown in the 180° case). Maximum third EMF harmonic magnitude is achieved when magnets span ≈60°. Regarding the fifth harmonic (whose magnitude after 75° starts to slightly oscillate), the maximum is achieved much earlier, i.e. at ≈40°.

If the 60° magnet span is used in combination with optimal harmonic current injection, an output torque equal to ≈2.72 Nm can be achieved. Compared to the maximal output torque in near-sinusoidal configuration (2.99 Nm; Fig. 4.7), the reduction is only around 9%. If around 70° magnet span is used, torque (≈2.90 Nm) nearly equal to that in the near-sinusoidal case can be produced. With further small magnet span increase to in between 70° and 75°, produced torque would precisely match the one produced by 180° configuration with injected third harmonic. At this point, the rotor has ≈2.4-2.6 times less magnet material, which is still a significant saving. By taking into account the above given results, Fig. 4.7 can be extended to that given in Fig. 4.8b.

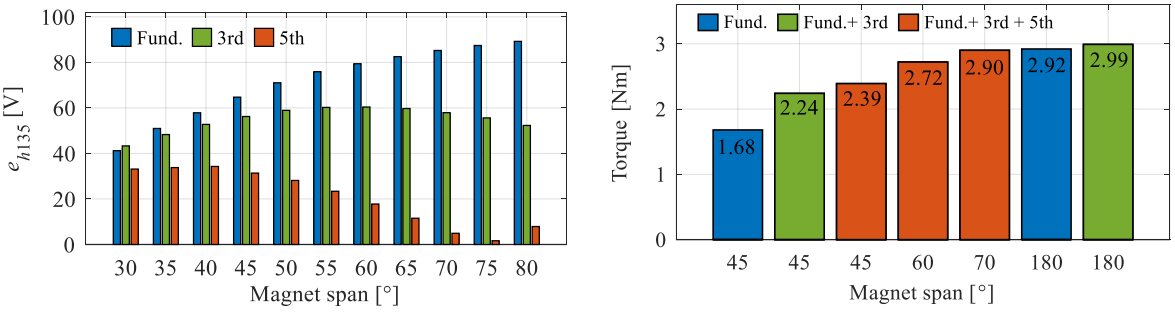

a) b)

Figure 4.8 – Comparison of 1st, 3rd and 5th EMF magnitudes for different magnet spans (a), and comparison of the electromagnetic torques (b).

4.6 Summary

In this chapter, a nine-phase PM synchronous machine with 36-slots on stator and with shortened two magnet poles on rotor was investigated. Details of the prototype configuration were first introduced and relevant (known) electrical/design parameters were given. Studied rotor structure gives rise to a highly non-sinusoidal back-EMF and, as a result, the third harmonic component almost equal to the fundamental is produced. High fifth and some seventh harmonic components also exist. A machine with near-sinusoidal back-EMF (first introduced in chapter 3) was used as a benchmark in order to compare the performance of the modified rotor structure. That is, an investigation related to the performance of the machine with reduced magnetic material, compared to a traditional rotor, was carried out. Although with reduced magnet span electromagnetic torque was, as expected, lower than the one produced by the near-sinusoidal configuration, it was shown that with proper injection of current harmonics, the derating can be reduced to only around 20%. However, such rotor configuration uses four times less magnet material.

What is the required magnet span which would, in combination with the third and the fifth harmonic current injection control (and the same phase current RMS) result in original (180° magnet span) torque value, was also investigated. As concluded, the required magnet span should be approximately ≈70-75°. In this case, the torque produced by benchmark machine with injected third current harmonic and in prototype machine with injected fundamental, the third and the fifth harmonics would be approximately the same. It is important to note that this is still ≈2.4-2.6 times less magnet material than in the benchmark case. Building on a specific rotor structure and corresponding EMF spectrum, in the chapters to follow advanced control algorithms for the studied machine prototype are developed.

Chapter Five

TORQUE ENHANCEMENT APPLYING THIRD HARMONIC CURRENT INJECTION

5.1 Introduction

This chapter deals with the modelling and vector control of the machine with non-sinusoidal back-EMF, which was introduced and studied using finite element method approach in chapter 4. It commences with a discussion related to a general approach for non-standard back electromotive force modelling in PM synchronous machines (section 5.2). This essentially means that the model with the near-sinusoidal back-EMF (which was originally derived in chapter 3) is in the following sections further modified to produce non-sinusoidal back-EMF similar to the one recorded in the real nine-phase prototype. To meet this goal, necessary modelling differences are highlighted. Building on the EMF spectrum achieved by shortening the magnets, a vector control algorithm capable of harmonic current injection to the stator is investigated (section 5.3). This is achieved by exploiting the additional degrees of freedom that multiphase machines possess.

Since the back-EMF spectrum contains a third harmonic component almost equal in magnitude to the fundamental, it is expected that the highest torque improvement contribution will result from this harmonic. Derived FOC algorithm from chapter 3, section 3.6 is therefore modified by implementing the required harmonic control. The optimal ratio between the fundamental and the third harmonic current components is investigated in detail using maximal torque-per-Ampere approach, and verified using winding factor approach. Other existing and, for the time being, non-torque producing back-EMF harmonics will induce harmonics in phase current spectrum, which - if left unattended - will produce additional losses. Vector proportional integral (VPI) controllers in α-β reference frame are therefore introduced for their elimination.

Finally, modified multiphase PM synchronous machine model controlled by the enhanced FOC is implemented in *Matlab*/*Simulink* environment, where it is tested under optimal third harmonic current injection (section 5.4). Obtained results are verified experimentally using the machine prototype. Results from this work are published in [Slunjski et al (2019)], and, in part, in [Slunjski et al (2021)] as well.

5.2 Modelling of the Machine with Highly Non-Sinusoidal Back-EMF

In chapter 3, a detailed multiphase PM synchronous machine model was derived. One of the assumptions which was stated at the beginning of the modelling process was that the MMF and the back-EMF are nearly sinusoidal. On the other hand, the proposed machine has a highly non-sinusoidal back-EMF. To model such a machine, the previously used approach must be further modified.

Electromotive force is in the PM synchronous machines produced entirely by the permanent magnets. To model machine's EMF which is produced by more than one harmonic, harmonic magnitudes and corresponding phase shift angles must be known. These values are for any machine

easily obtainable from no-load generation mode test (chapter 4). Thus, to reconstruct the back-EMF, the following equation can be used:

$$\begin{aligned} e_{bEMF} &= e_1 \cdot \sin(1 \cdot (\theta_{el} - \theta_n) + \theta_{phs1}) + e_3 \cdot \sin(3 \cdot (\theta_{el} - \theta_n) + \theta_{phs3}) \\ &+ e_5 \cdot \sin(5 \cdot (\theta_{el} - \theta_n) + \theta_{phs5}) + \ldots + e_h \cdot \sin(h \cdot (\theta_{el} - \theta_n) + \theta_{phsh}) \end{aligned} \tag{5.1}$$

In (5.1), e_1, e_3, …, e_h are the magnitudes of the 1, 3, …, h^{th} back-EMF harmonic in the FFT spectrum, while θ_{phs1}, θ_{phs3}, …, θ_{phsh} are corresponding harmonic angle shifts. θ_{el} is an arbitrary electrical position of rotor, while θ_n is an angle dependent on symmetrical (or asymmetrical) spatial phase distribution.

In this approach the EMF is given for one specific speed (i.e. the speed at which it was recorded). Hence, the magnitude of the back-EMF e_{bEMF} is not going to change with the speed variations. This can be solved if a flux approach is used instead of EMF, since, unlike EMF magnitudes, flux values are constants produced by permanent magnets and are not changeable with the speed variations. By knowing the speed at which the back-EMF was recorded, flux magnitudes can be for each harmonic easily calculated (see (4.1)).

With known flux constants and corresponding harmonic angles, flux linkage matrix $[\lambda_{m\text{-}abcn}]$, which includes h odd harmonic components, can be in nine-phase form written as:

$$\left[\lambda_{m-abcn}\right] = \lambda_{m1} \cdot \begin{bmatrix} \cos(1 \cdot (\theta_{el} - \theta_{a1}) + \theta_{phs1}) \\ \cos(1 \cdot (\theta_{el} - \theta_{a2}) + \theta_{phs1}) \\ \cos(1 \cdot (\theta_{el} - \theta_{a3}) + \theta_{phs1}) \\ \cos(1 \cdot (\theta_{el} - \theta_{b1}) + \theta_{phs1}) \\ \cos(1 \cdot (\theta_{el} - \theta_{b2}) + \theta_{phs1}) \\ \cos(1 \cdot (\theta_{el} - \theta_{b3}) + \theta_{phs1}) \\ \cos(1 \cdot (\theta_{el} - \theta_{c1}) + \theta_{phs1}) \\ \cos(1 \cdot (\theta_{el} - \theta_{c2}) + \theta_{phs1}) \\ \cos(1 \cdot (\theta_{el} - \theta_{c3}) + \theta_{phs1}) \end{bmatrix} + \ldots + \lambda_{mh} \cdot \begin{bmatrix} \cos(h \cdot (\theta_{el} - \theta_{a1}) + \theta_{phsh}) \\ \cos(h \cdot (\theta_{el} - \theta_{a2}) + \theta_{phsh}) \\ \cos(h \cdot (\theta_{el} - \theta_{a3}) + \theta_{phsh}) \\ \cos(h \cdot (\theta_{el} - \theta_{b1}) + \theta_{phsh}) \\ \cos(h \cdot (\theta_{el} - \theta_{b2}) + \theta_{phsh}) \\ \cos(h \cdot (\theta_{el} - \theta_{b3}) + \theta_{phsh}) \\ \cos(h \cdot (\theta_{el} - \theta_{c1}) + \theta_{phsh}) \\ \cos(h \cdot (\theta_{el} - \theta_{c2}) + \theta_{phsh}) \\ \cos(h \cdot (\theta_{el} - \theta_{c3}) + \theta_{phsh}) \end{bmatrix} \tag{5.2}$$

The matrix equation is obtained after extending the well-known $(\lambda_m \cdot \cos(\theta_{el} - \theta_n))$ equation for fundamental flux linkage modelling. A *n*-phase form can also be easily derived. As briefly noted in chapter 3, mutual inductance matrix must also be modified. In the case with *h* considered harmonics, this matrix has the following form:

$$\left[M_{ss}\right] = \left[M_{ss1}\right] + \left[M_{ss3}\right] + \ldots + \left[M_{ssh}\right] \tag{5.3}$$

Combined electric and magnetic PMSM model derived in chapter 3

$$\left[i_{abcn}\right] = \left(\left[M_{ss}\right] + \left[L_{ls}\right]\right)^{-1} \left(\int \left[v_{abcn}\right] - \left[R_s\right]\left[i_{abcn}\right] dt - \left[\lambda_{m-abcn}\right]\right) \tag{5.4}$$

can now be modified in a way that flux linkage [$\lambda_{m\text{-}abcn}$] and mutual inductance [M_{ss}] matrices ((5.2) and (5.3), respectively) are incorporated in (5.4). For validation purpose, the modified multiphase machine model was implemented in *Matlab*/*Simulink* environment. Flux produced by permanent magnets and corresponding back-EMF signals (where $e_{bEMF} = d\lambda_{m\text{-}abcn}/dt$) are recorded and are shown in Fig. 5.1. If the results are compared with the ones recorded for back-EMF analysed in chapter 4 (section 4.2), a high correspondence in signals can be seen, thus verifying the prototype machine modelling correctness and accuracy.

5.3 Control of the Machine with Highly Non-Sinusoidal Back-EMF

Implementation of the third harmonic current injection control requires modification of the basic FOC algorithm. As explained in chapter 3, this vector control strategy is derived and implemented in a synchronous reference frame. In the case when only fundamental harmonic component is considered, two current components (i_{d1} and i_{q1}) exist and must be controlled. Other current harmonic components in additional subspaces are then not of concern and are usually kept at zero using appropriate current control. If, in addition to the fundamental, the third harmonic current component is also to be controlled, additional two current components (further addressed as i_{d3} and i_{q3}) must also be taken into consideration. Total electromagnetic torque in the machine is then produced as the sum of two components, that is:

$$T_{em13} = T_{em1} + T_{em3} \tag{5.5}$$

To obtain torque-producing parts, adequate two machine models (related to the fundamental and the third harmonic) in synchronous reference frame must be separately considered. To perform MTPA control in such machine, flux-producing current component references are set (and controlled) to zero ($i_{d1} = 0$ and $i_{d3} = 0$). Fundamental torque-producing part T_{em1} can be obtained as explained in chapter 3, equations (3.39)-(3.41). Corresponding equivalent electric circuit was given in Fig. 3.7.

For the third harmonic electromagnetic torque-producing part (T_{em3}) calculation, a similar approach can be used. Equivalent circuit is given in Fig. 5.2. Apart from different modelling parameters, it must

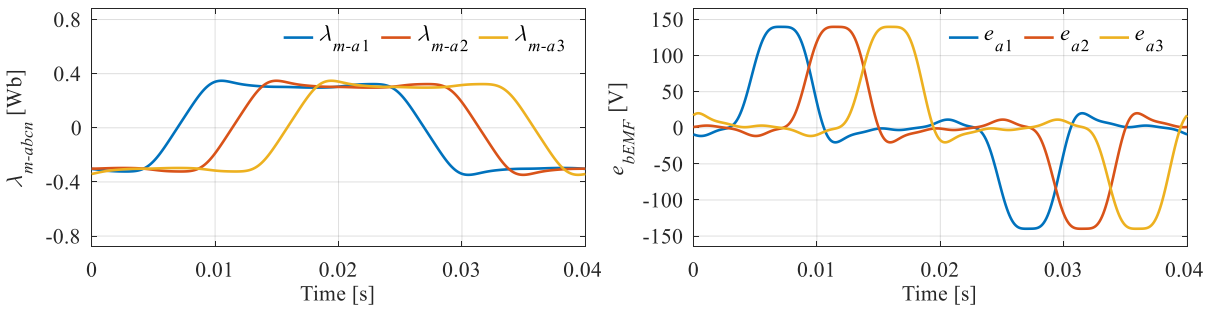

a) b)

Figure 5.1 – One period of flux linkage (a) and back-EMF (b) recorded in *Matlab*/*Simulink*.

be noted that frequency of the third harmonic is three times higher i.e. the electrical angular frequency is now three times the fundamental ($3\cdot\omega_{el}$):

$$v_{d3} = R_s \cdot i_{d3} + \frac{d\lambda_{d3}}{dt} - 3\omega_{el} \cdot \lambda_{q3} \tag{5.6}$$

$$v_{q3} = R_s \cdot i_{q3} + \frac{d\lambda_{q3}}{dt} + 3\omega_{el} \cdot \lambda_{d3} \tag{5.7}$$

$$\lambda_{d3} = L_{d3} \cdot i_{d3} + \lambda_{m3}; \qquad \lambda_{q3} = L_{q3} \cdot i_{q3} \tag{5.8}$$

$$T_{em3} = \frac{n}{2} \cdot P \cdot 3 \cdot \lambda_{m3} \cdot i_{q3} \tag{5.9}$$

From (3.41) and (5.9) it is obvious that produced electromagnetic torque T_{em13} depends entirely on the torque-producing currents i_{q1} and i_{q3} (as noted, i_{d1} and i_{d3} are controlled to 0; MTPA). For the ease of implementation, these currents can be replaced with their ratio, i.e. a constant k_{13}. After a short mathematical manipulation, relationship between fundamental torque-producing current i_{q1}, electromagnetic torque T_{em13} and ratio k_{13}, suitable for field-oriented control implementation can now be written as:

$$i_{q1} = \frac{2}{n \cdot P} \cdot \frac{T_{em13}}{\lambda_{m1} + 3 \cdot \lambda_{m3} \cdot k_{13}}; \qquad k_{13} = \frac{i_{q3}}{i_{q1}} \tag{5.10}$$

Following the same FOC theory as in chapter 3, PI controllers are once again used for flux- and torque-producing current components control/elimination. Outputs of the stator d_1-q_1 and d_3-q_3 PI regulators can be modelled as:

$$v_{d1-reg} = R_s \cdot i_{d1} + L_{s1}\frac{di_{d1}}{dt}; \qquad v_{q1-reg} = R_s \cdot i_{q1} + L_{s1}\frac{di_{q1}}{dt} \tag{5.11}$$

$$v_{d3-reg} = R_s \cdot i_{d3} + L_{s3}\frac{di_{d3}}{dt}; \qquad v_{q3-reg} = R_s \cdot i_{q3} + L_{s3}\frac{di_{q3}}{dt} \tag{5.12}$$

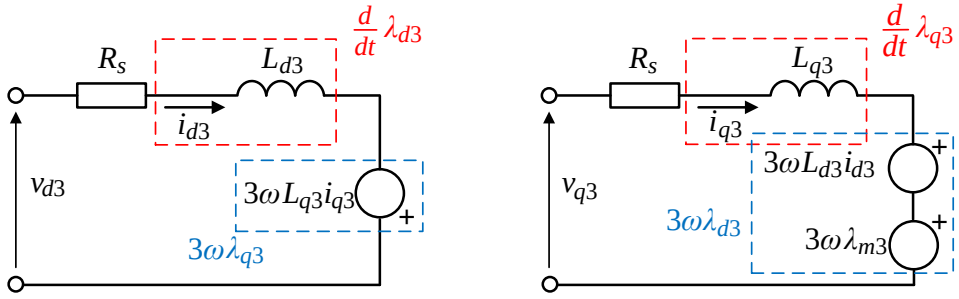

Figure 5.2 – Equivalent *d*-*q* electrical circuits for PMSM in synchronous reference frame – third harmonic component.

By adding the following decoupling voltages e_{d1}, e_{q1} and e_{d3}, e_{q3} to the output of the proportional-integral controllers,

$$e_{d1} = \omega_{el}\left(L_{s1} \cdot i_{d1} + \lambda_{m1}\right); \qquad e_{q1} = \omega_{el}\left(L_{s1} \cdot i_{q1}\right) \tag{5.13}$$

$$e_{d3} = 3\omega_{el}\left(L_{s3} \cdot i_{d3} + \lambda_{m3}\right); \qquad e_{q3} = 3\omega_{el}\left(L_{s3} \cdot i_{q3}\right) \tag{5.14}$$

total stator voltage references are acquired as:

$$v_{d1-ref} = v_{d1-reg} - e_{q1}; \qquad v_{q1-ref} = v_{q1-reg} + e_{d1} \tag{5.15}$$

$$v_{d3-ref} = v_{d3-reg} - e_{q3}; \qquad v_{q3-ref} = v_{q3-reg} + e_{d3} \tag{5.16}$$

To decouple the system and to obtain currents in the required synchronous reference frames for FOC algorithm implementation, vector space decomposition and rotational transformations have to be applied to the machine model. VSD matrix (3.20) remains unchanged when the third harmonic current injection takes place. However, part of the rotational transformation matrix responsible for i_{xy3} (where the third harmonic current maps after VSD), which will yield i_{dq3} after transformation, must be modified by adding the rotational transformation for this pair of rows. The complete rotational transformation matrix then becomes:

$$D = \begin{bmatrix} \cos(\theta_1) & \sin(\theta_1) & 0 & 0 & 0 & 0 & 0 & 0 & 0 \\ -\sin(\theta_1) & \cos(\theta_1) & 0 & 0 & 0 & 0 & 0 & 0 & 0 \\ 0 & 0 & 1 & 0 & 0 & 0 & 0 & 0 & 0 \\ 0 & 0 & 0 & 1 & 0 & 0 & 0 & 0 & 0 \\ 0 & 0 & 0 & 0 & 1 & 0 & 0 & 0 & 0 \\ 0 & 0 & 0 & 0 & 0 & 1 & 0 & 0 & 0 \\ 0 & 0 & 0 & 0 & 0 & 0 & \cos(\theta_3) & \sin(\theta_3) & 0 \\ 0 & 0 & 0 & 0 & 0 & 0 & -\sin(\theta_3) & \cos(\theta_3) & 0 \\ 0 & 0 & 0 & 0 & 0 & 0 & 0 & 0 & 1 \end{bmatrix} \tag{5.17}$$

where $\theta_h = h \cdot \theta_{el} + \theta_{phsh}$.

The corresponding field-oriented control algorithm for the symmetrical nine-phase permanent magnet synchronous machine, which includes the third harmonic current injection, is shown in Fig. 5.3. Although the control scheme is complete, there are still two segments (highlighted in blue in the figure) which must be further addressed. First, the value of the optimal third harmonic current injection coefficient (k_{13}) must be precisely determined, and second, the non-torque producing low order odd current harmonics induced by the back-EMF must be eliminated (in Fig. 5.3, "VPI resonant current controllers" block).

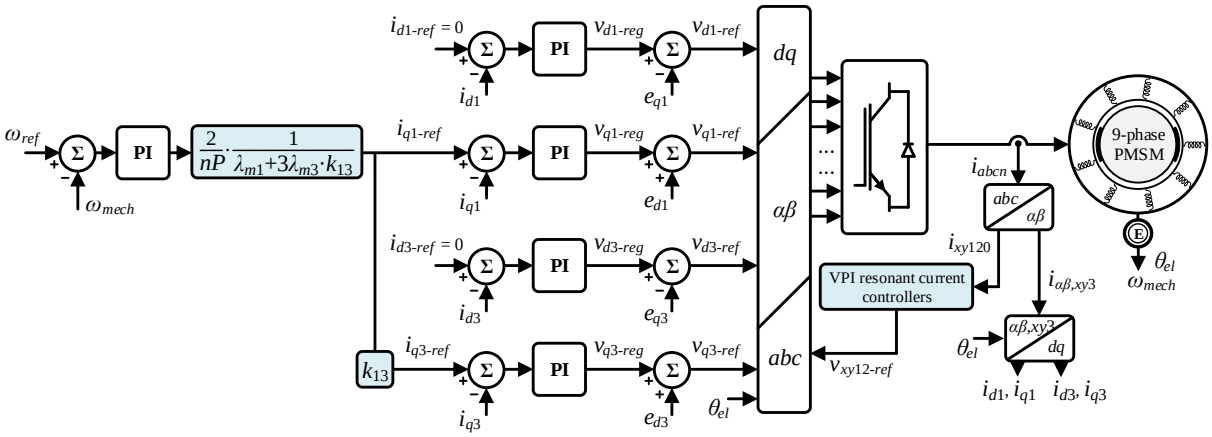

Figure 5.3 – Enhanced FOC algorithm for a surface PMSM with highly non-sinusoidal back-EMF.

5.3.1 Determination of the Optimal Third Harmonic Injection Ratio

The ratio between the fundamental and the third harmonic component plays an important role in the optimal third harmonic current injection, i.e. in electromagnetic torque improvement. As shown in the literature survey in chapter 2, there are several different methods nowadays used to calculate this ratio. To derive equation from which optimal ratio relevant for this work can be determined, MTPA approach, in combination with the constant phase current RMS constraint, is used. For additional validation, optimisation tool and winding factor approach (another two often reported methods) are also employed. It should be noted once more that, for the time being, only the fundamental and the third harmonic are taken into account. Generalisation on the MTPA approach for the optimal ratio calculation with arbitrary number of injected current harmonics will be discussed in the following chapter.

By neglecting the reluctance effect in the surface-mounted PMSM, it is possible to express the total produced electromagnetic torque, by combining (3.41), (5.5), (5.9), as a sum of the torques produced in the different rotating frames, i.e. as the sum of two torques produced in the two rotating frames associated with the first and the third harmonics:

$$T_{em13} = \frac{n}{2}\cdot P\cdot(i_{q1}\cdot\lambda_{m1} + 3\cdot i_{q3}\cdot\lambda_{m3}) \tag{5.18}$$

If (5.18) is further modified by taking into account:

$$k_{13} = \frac{i_{q3}}{i_{q1}}; \qquad I_{RMS} = \sqrt{\frac{i_{q1}^2 + i_{q3}^2}{2}} \tag{5.19}$$

where I_{RMS} is the root mean square value of the phase currents calculated using the fundamental and the third harmonic current peaks, electromagnetic torque as a function of the RMS current value and the harmonic injection ratio k_{13} can be obtained as:

$$T_{em13} = \frac{n}{2} \cdot P \cdot \left(\frac{\lambda_{m1} \cdot \sqrt{2} I_{RMS}}{\sqrt{1+k_{13}^2}} + \frac{3\lambda_{m3} \cdot \sqrt{2} I_{RMS} \cdot k_{13}}{\sqrt{1+k_{13}^2}} \right) \tag{5.20}$$

The classical MTPA control strategy can now be applied. With this method, the maximum electromagnetic torque value per given RMS current is calculated. For a given RMS value of the applied current I_{RMS}, the optimal value of the ratio between the fundamental and the third harmonic current (that is, $k_{13\text{-opt}}$) can be acquired after differentiating equation (5.20) with respect to k_{13}:

$$\frac{dT_{em13}}{dk_{13}} = \frac{n}{2} P \cdot \lambda_{m1} \sqrt{2} I_{RMS} \cdot \frac{-k_{13}}{\sqrt{(1+k_{13}^2)^3}} + \frac{n}{2} P \cdot 3\lambda_{m3} \sqrt{2} I_{RMS} \cdot \frac{1}{\sqrt{(1+k_{13}^2)^3}} = 0 \tag{5.21}$$

After some mathematical manipulation:

$$k_{13} = k_{13-opt} = \frac{3 \cdot \lambda_{m3}}{\lambda_{m1}} \tag{5.22}$$

By substituting (5.22) into (5.20), the maximum reachable torque under MTPA control strategy (produced by both PM flux components) for a given RMS current can be found as:

$$T_{em13} = \frac{n}{2} \cdot P \cdot \sqrt{2} I_{RMS} \cdot \frac{\dfrac{\lambda_{m1}^2 + 9\lambda_{m3}^2}{\lambda_{m1}}}{\sqrt{1+\left(\dfrac{3 \cdot \lambda_{m3}}{\lambda_{m1}}\right)^2}} \tag{5.23}$$

If the back-EMF harmonic magnitudes are used instead of the flux values (which is possible because relationship between back-EMF and flux for the h^{th} harmonic is governed by the angular frequency), a similar relation can be obtained:

$$\lambda_{mh} = \frac{e_h}{h \cdot \omega_{el}} \rightarrow T_{em13} = \frac{n}{2} \cdot P \cdot \sqrt{2} I_{RMS} \cdot \frac{1}{\omega_{el}} \frac{\dfrac{e_1^2 + e_3^2}{e_1}}{\sqrt{1+\left(\dfrac{e_3}{e_1}\right)^2}} \tag{5.24}$$

Finally, to be able to validate the torque improvement, value of the torque produced with both harmonics must be examined in relation with the value of the torque produced by the fundamental itself. This relation, denoted with H_{opt}, can be written as:

$$\begin{aligned} T_{em13} &= H_{opt} \cdot T_{em1} \\ H_{opt} &= \frac{T_{em13}}{T_{em1}(i_{q1} = \sqrt{2} \cdot I_{RMS}, i_{q3} = 0)} = \sqrt{1+\left(\frac{3 \cdot \lambda_{m3}}{\lambda_{m1}}\right)^2} = \sqrt{1+\left(\frac{e_3}{e_1}\right)^2} \end{aligned} \tag{5.25}$$

From (5.25), it is easy to conclude that optimal improvement of the torque by injecting the third harmonic current dependents on the ratio of the flux components $\lambda_{m3}/\lambda_{m1}$ (or in the back-EMF case, e_3/e_1 ratio). The larger this ratio is, the larger the gain H_{opt} with respect to the fundamental torque will be. By considering only one spatial harmonic of flux in the air gap (i.e. either fundamental or the third), flux component λ_{mh} produced by permanent magnets can be calculated as:

$$\lambda_{mh} = N_{ph} \cdot l \cdot R_{rot} \cdot k_{wfh} \cdot B_{roth} \cdot \int_0^{\pi/P \cdot h} \sin(h \cdot P \cdot \theta) \cdot d\theta = N_{ph} \cdot l \cdot R_{rot} \cdot k_{wfh} \cdot B_{roth} \cdot \frac{2}{P \cdot h} \tag{5.26}$$

Here, l stands for rotor length, R_{rot} is the radius of the rotor, N_{ph} is the number of wire turns per phase, while k_{wf} and B_{rot} are winding factor and the maximal value of spatial harmonic flux density in the air-gap generated by permanent magnets, respectively. For different harmonic order, components k_{wf} and B_{rot} have different values; hence subscript h is added in equations. Mechanical machine parameters l, R_{rot} and N_{ph} are, on the other hand, fixed and are therefore further accounted for through a single constant, that is, G:

$$\lambda_{mh} = G \cdot \frac{k_{wfh} \cdot B_{roth}}{P \cdot h}; \qquad G = 2 \cdot N_{ph} \cdot l \cdot R_{rot} \tag{5.27}$$

As noted in chapter 4, for prototype machine l = 55 mm, R_{rot} = 37 mm, N_{ph} = 306. After substituting (5.27) into (5.25), the new form of the equation is now:

$$H_{opt} = \sqrt{1 + \left(\frac{3 \cdot \lambda_{m3}}{\lambda_{m1}}\right)^2} = \sqrt{1 + \left(\frac{e_3}{e_1}\right)^2} = \sqrt{1 + \left(\frac{k_{wf3} \cdot B_{rot3}}{k_{wf1} \cdot B_{rot1}}\right)^2} \tag{5.28}$$

leading to:

$$\frac{3 \cdot \lambda_{m3}}{\lambda_{m1}} = \frac{e_3}{e_1} = \frac{k_{wf3} \cdot B_{rot3}}{k_{wf1} \cdot B_{rot1}} \tag{5.29}$$

Clearly, two additional (design) parameters appear here: the ratio of harmonic winding factors $(k_{wf3})/(k_{wf1})$ and the ratio of air-gap flux densities due to the rotor $(B_{rot3})/(B_{rot1})$. The ratio of winding factors depends on the winding configurations of the machine (i.e. the slot/pole combination and the type of winding), while the ratio of maximal values of the spatial harmonics in the air-gap generated by PMs is related to the magnetic properties of PMs and the rotor topology.

As previously established, investigated machine in this thesis is with 36 stator slots in which single-layer distributed winding is placed, and 2 rotor poles i.e. slot/pole combination is 36/2. Since each phase winding contains N_{ph} wire turns, the produced magnetic flux does not link all these turns ideally, but with a ratio of less than unity. This ratio is known as the winding factor k_{wfh} [Pyrhonen et al (2008)]. To calculate the total winding factor k_{wfh}, three components are necessary: a distribution factor k_{dh}, a pitch

factor k_{ph} and a skewing factor k_{sh} [Pyrhonen et al (2008)]. The winding factor component derived from the shifted voltage phasors in the case of a distributed winding is called the distribution factor. This factor is always $k_{dh} \leq 1$. If each coil is wound as a full-pitch winding (the case of the winding in machine investigated in this thesis), the coil-pitch is in principle the same as the pole-pitch. When the coil-pitch is shorter than the pole-pitch, the winding is called a short-pitch or chorded winding (employed usually in the machines with two-layer windings). The factor of this reduction is called the pitch factor k_{ph}. Finally, the skew factor k_{sh} reflects the fact that the winding is angularly twisted, which results in an angular spread and reduced EMF. For example, squirrel-cage induction motors have their rotor bars skewed by one slot-pitch in order to reduce the winding factor harmonics introduced by the slotting of the stator. Following from the above said, skew factor is not of further interest here ($k_{sh} = 1$). The total winding factor is therefore calculated as:

$$k_{wfh} = k_{dh} \cdot k_{ph} \cdot \cancel{k_{sh}} = k_{dh} \cdot k_{ph} \tag{5.30}$$

Equations to calculate the distribution factor k_{dh} and the pitch factor k_{ph} are generally well-known. How to derive them for different machine types can be, for example, found in [Pyrhonen et al (2008), Scuiller et al (2010)]. In a PMSM case, final forms of equations are given next, in a general form for an *n*-phase system with distributed winding. They can, in addition to the fundamental, be used to calculate k_{dh}, k_{ph} for the other low order odd harmonic components as well:

$$k_{dh} = \frac{\sin\left(h \cdot \frac{1}{n} \cdot \frac{\pi}{2}\right)}{q \cdot \sin\left(h \cdot \frac{1}{n \cdot q} \cdot \frac{\pi}{2}\right)}; \qquad k_{ph} = \sin\left(h \cdot \frac{y_{cp}}{\tau_{pp}} \cdot \frac{\pi}{2}\right) \tag{5.31}$$

In (5.31), q stands for number of slots-per-pole-per-phase, while y_{cp} and τ_{pp} are coil-pitch and pole-pitch, respectively. Peripheral distance between identical points of two adjacent poles is the pole-pitch, while the distance between two coil-sides of the same coil (measured in terms of teeth or slots) is called coil-pitch (or coil-span). To determine these values, necessary for the distribution and the pitch factor calculation, the following equations are used:

$$q = \frac{S}{2P \cdot n}; \quad \tau_{pp} = \frac{S}{2P}; \quad y_{cp} \lneq \tau_{pp} \quad \begin{cases} y_{cp} = \tau_{pp} \rightarrow full - pitch \\ y_{cp} < \tau_{pp} \rightarrow short - pitch \end{cases} \tag{5.32}$$

In (5.32), P stands for the number of pole pairs, while S represents number of stator slots.

Using the nine-phase PMSM stator winding diagram, which corresponds to the real prototype (Fig. 5.4), graphical representation of the coefficients defined with (5.32) can be shown as well. From the given figure, it is easy to conclude that the number of slots-per-pole-per-phase is equal to $q = 2$, and

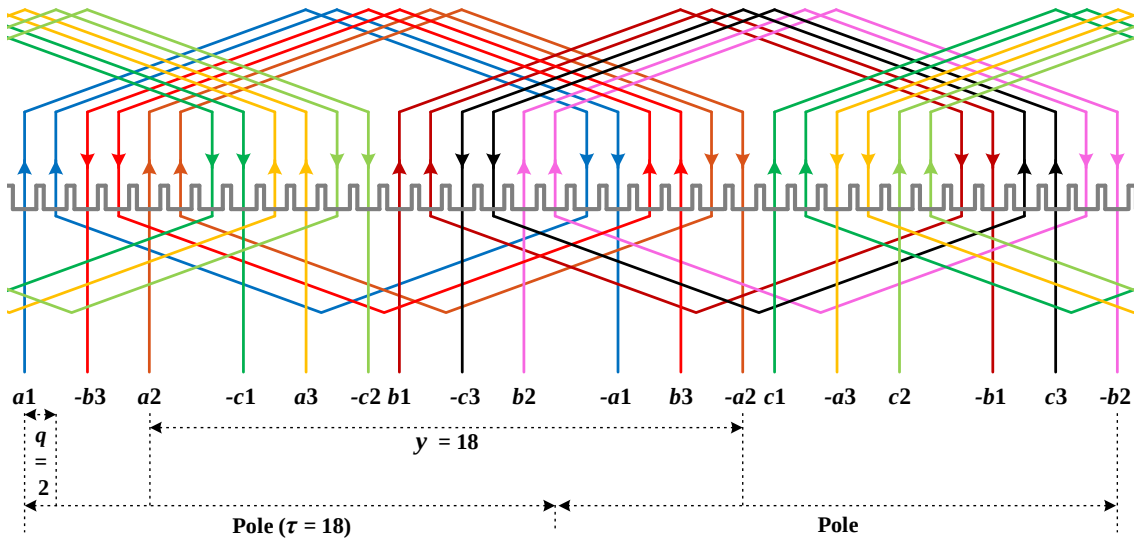

Figure 5.4 – Winding diagram of a symmetrical nine-phase, two-pole PM synchronous machine.

that coil-pitch is equal to pole-pitch $y_{cp} = \tau_{pp}$ (full-pitch winding). With obtained parameters, distribution and pitch factors can be for the two studied harmonic components computed as:

$$k_{d1} = \frac{\sin\left(1 \cdot \frac{1}{9} \cdot \frac{\pi}{2}\right)}{2 \cdot \sin\left(1 \cdot \frac{1}{9 \cdot 2} \cdot \frac{\pi}{2}\right)} = 0.9962; \qquad k_{p1} = \sin\left(3 \cdot \frac{18}{18} \cdot \frac{\pi}{2}\right) = 1$$

$$k_{d3} = \frac{\sin\left(3 \cdot \frac{1}{9} \cdot \frac{\pi}{2}\right)}{2 \cdot \sin\left(3 \cdot \frac{1}{9 \cdot 2} \cdot \frac{\pi}{2}\right)} = 0.9659; \qquad k_{p1} = \sin\left(3 \cdot \frac{18}{18} \cdot \frac{\pi}{2}\right) = 1 \tag{5.33}$$

Following from (5.30) and (5.33), the ratio between two winding factors can be calculated as:

$$\left.\begin{aligned} k_{wf1} &= k_{d1} \cdot k_{p1} = 0.9962 \\ k_{wf3} &= k_{d3} \cdot k_{p3} = 0.9659 \end{aligned}\right\} \qquad \frac{k_{wf3}}{k_{wf1}} = 0.9696 \tag{5.34}$$

In addition to the winding factors, the knowledge of ratio $(B_{rot3})/(B_{rot1})$ is also required. This ratio depends mainly on the rotor geometry and magnet arrangement. Surface PMSM in this work is with two magnet poles, each spanning 45° around rotors circumference. Air-gap flux densities due to such rotor can be approximately estimated as shown in Fig. 5.5a. For validation purpose, air-gap flux density obtained in FEM is also given. By performing FFT analysis of the FEM signal, magnitudes of spatial harmonics in the air-gap generated by PMs are obtained as illustrated in Fig. 5.5b.

Based on the first two odd order magnitudes, $(B_{rot3})/(B_{rot1})$ ratio needed for torque improvement analysis is determined as:

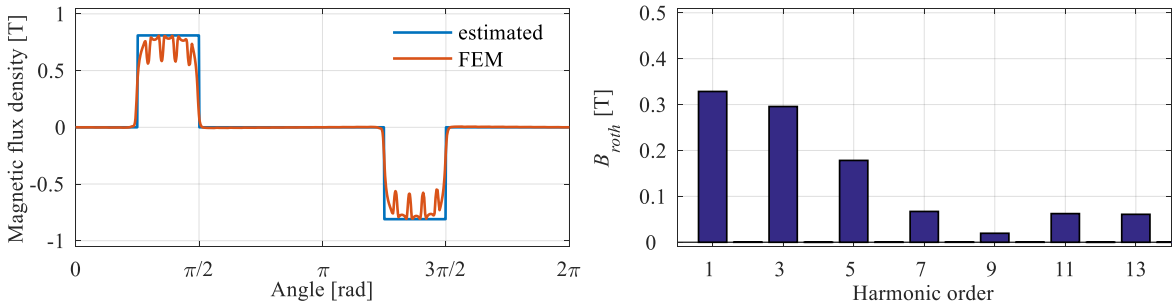

a) b)

Figure 5.5 – Air-gap flux densities produced by rotor: estimated/FEM traces (a), and FEM FFT spectrum (b).

$$\frac{B_{rot3}}{B_{rot1}} = 0.9562 \tag{5.35}$$

With (5.35) all required equations/parameters are now obtained. Hence optimal third harmonic current coefficient can be fully analysed (see Table 5.1). For FEM model, improvement of the output torque is in the range between ≈32.5-32.7%, and to achieve such torque, optimal third harmonic current injection ratio must be $k_{13\text{-}opt} = 0.87$. This is a confirmation of the result already used in chapter 4. A similar conclusion can be made for the real prototype as well. As shown in the table, maximum achievable torque improvement with the third harmonic current injection for this case is even higher, i.e. it is ≈36.4%. To achieve such an improvement, the optimal torque improvement ratio must be $k_{13\text{-}opt} = 0.927$. This ratio is used in the rest of the chapter for control algorithm implementation and validation purposes. Please note that the obtained improvement is only for the investigated machine and therefore might not be the same for the other PMSM configurations with different back-EMF harmonic magnitudes and angles.

Table 5.1 – The optimal third harmonic current injection ratio analysis.

\\\\	e_1, e_3 [V]	k_{wf1}, k_{wf3}	B_{rot1}, B_{rot3} [T]
FEM model	$e_1 = 64.71$ $e_3 = 56.22$	$k_{wf1} = 0.9962$ $k_{wf3} = 0.9659$	$B_{rot1} = 0.3285$ $B_{rot3} = 0.2956$
	$\frac{e_3}{e_1} = k_{13} = \mathbf{0.8688}$	$\frac{k_{wf3}}{k_{wf1}}\frac{B_{rot3}}{B_{rot1}} = k_{13} = \mathbf{0.8725}$	
	$\sqrt{1+\left(\frac{e_3}{e_1}\right)^2} = 1.3250$	$\sqrt{1+\left(\frac{k_{wf3}}{k_{wf1}}\frac{B_{rot3}}{B_{rot1}}\right)^2} = 1.327$	
	$\frac{T_{em13} - T_{em1}}{T_{em1}} = \mathbf{32.5\%}$	$\frac{T_{em13} - T_{em1}}{T_{em1}} = \mathbf{32.7\%}$	
Real machine prototype	$e_1 = 59.13$ $e_3 = 54.81$	$k_{wf1} = 0.9962$ $k_{wf3} = 0.9659$	$B_{rot1} = 0.3102$ $B_{rot3} = 0.2966$
	$\frac{e_3}{e_1} = k_{13} = \mathbf{0.9269}$	$\frac{k_{wf3}}{k_{wf1}}\frac{B_{rot3}}{B_{rot1}} = k_{13} = \mathbf{0.9271}$	
	$\sqrt{1+\left(\frac{e_3}{e_1}\right)^2} = 1.364$	$\sqrt{1+\left(\frac{k_{wf3}}{k_{wf1}}\frac{B_{rot3}}{B_{rot1}}\right)^2} = 1.364$	
	$\frac{T_{em13} - T_{em1}}{T_{em1}} = \mathbf{36.4\%}$	$\frac{T_{em13} - T_{em1}}{T_{em1}} = \mathbf{36.4\%}$	

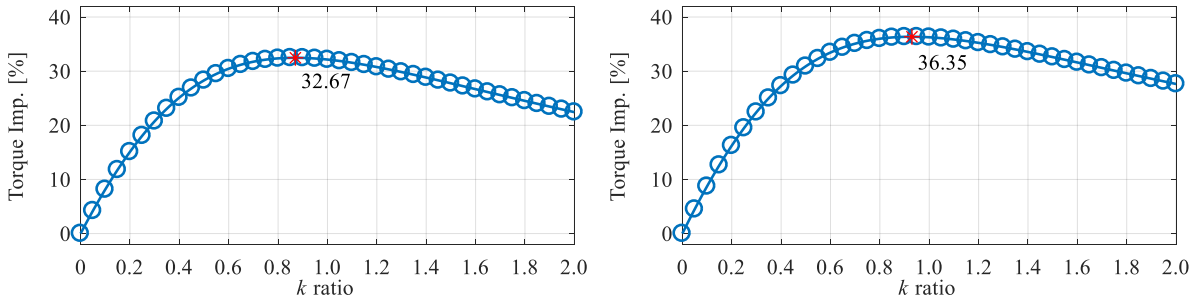

a) b)

Figure 5.6 – Optimal third harmonic current injection ratio determination using optimisation procedure under the same RMS current constraint: FEM (a) and real prototype (b).

Finally, the optimisation procedure (function *fmincon* offered by Matlab Toolbox) can be used for the same purpose. Although detail study of this procedure will be given in chapter 8, where it is used to determine optimal flux-weakening current references, the same procedure can be used for optimal ratio calculation as well. In its steps, the function solves the machine model maximising at the same time torque (5.20) for the given k_{13} step and I_{RMS} constraints. Results are shown in Fig. 5.6.

5.3.2 Low Order Harmonic Elimination

As it was explained at the beginning of the chapter, elimination of the non-torque producing low order harmonics induced by non-sinusoidal back-EMF (but also non-ideal machine construction, inverter dead time, etc.) is a necessary step in control algorithm design. For this purpose, resonant controllers are employed in this thesis. To be more specific, vector proportional integral (VPI) resonant type is used, for which transfer function can be written as:

$$G_{VPIh}(s) = \frac{s^2 \cdot k_{VPI-Ph} + s \cdot k_{VPI-Ih}}{s^2 + h^2 \cdot \omega_{fund}^2} \tag{5.36}$$

In (5.36), ω_{fund} is the fundamental angular harmonic frequency and $k_{VPI\text{-}Ph}$ and $k_{VPI\text{-}Ih}$ are proportional and integral regulator constants, respectively. At the fundamental frequency, $h \cdot \omega_{fund}$ is equal to the machine's electrical angular frequency (and speed) ω_{el}. As shown in [Yepes et al (2015), Yepes et al (2016)], to get a fast enough controller response, while at the same time avoiding influence of the switching noise in the controller performance, tuning must be performed by respecting:

$$\frac{k_{VPI-Ih}}{k_{VPI-Ph}} = \frac{R_s}{L_{ls}}; \qquad k_{VPI-Bh} = \frac{k_{VPI-Ph}}{L_{ls}} \tag{5.37}$$

Constant $k_{VPI\text{-}Bh}$ stands for the regulator bandwidth. Final transfer function of the tuned VPI controller, employing (5.37), can be written as:

$$G_{VPIh}(s) = k_{VPI-Bh} \cdot \frac{s^2 \cdot L_{ls} + s \cdot R_s}{s^2 + h^2 \cdot \omega_{fund}^2} \tag{5.38}$$

Implementation of the VPI regulator is completed by means of two integrators, as can be seen in Fig. 5.7a. Usually stated advantage of VPI over PI regulators [Yepes et al (2015), Yepes et al (2016)] is a possibility to use multiple VPI controllers in parallel. By utilizing such implementation, it is possible to eliminate all unwanted harmonics in each of the controlled *x-y* planes. Parallel connection of VPI resonant controllers can be achieved as shown in Fig. 5.7b. Here h_1, h_2, …, h_i denotes harmonics mapped in the same subspace, which must be eliminated for the system to work without harmonic losses.

In order to demonstrate the effectiveness of the VPI current controllers, simulation testing was performed, and results are given in Fig. 5.8. The machine was tested at 1500 rpm under FOC and with implemented third harmonic current injection. The fundamental and third harmonic component are controlled by PI type regulators and the ratio between them is set in accordance with the optimal k_{13}

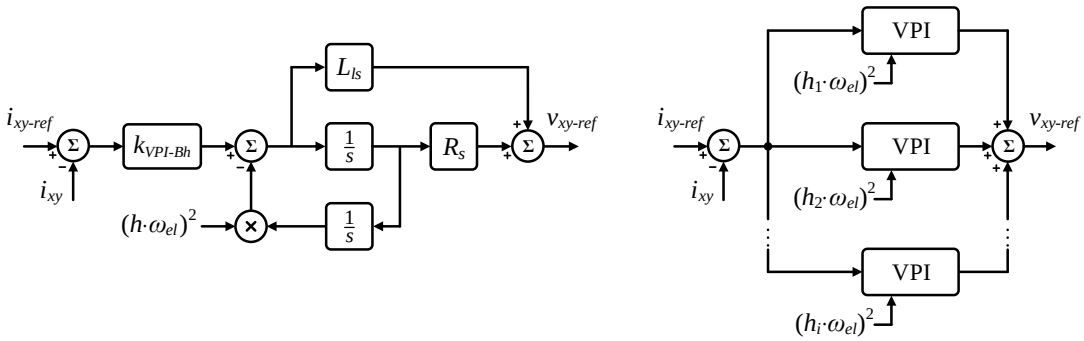

a) b)

Figure 5.7 – Block scheme of VPI resonant controller: single (a) and parallel (b) VPI connection.

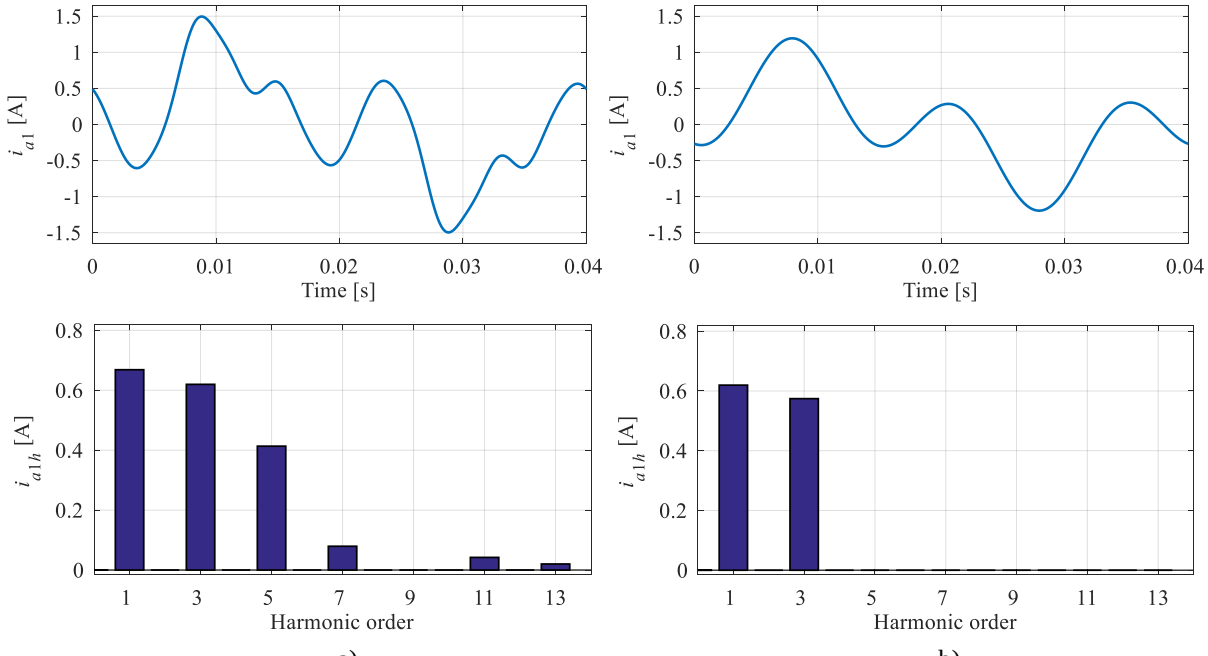

a) b)

Figure 5.8 – Phase currents with the harmonic (VPI) control switched off (a), and on (b).

value. In the first testing scenario harmonic elimination was turned off. One period of the phase current (phase $a1$) with the corresponding FFT spectrum is shown in the left plots of Fig. 5.8. It can be seen that, in addition to the fundamental and the third (which are contributing to the torque production), significant 5^{th}, 7^{th}, 11^{th} and 13^{th} harmonic components also exist. These harmonics, as explained in chapter 3, map into x_1-y_1 (7^{th} and 11^{th}) and x_2-y_2 (5^{th} and 13^{th}) subspaces. Therefore, for their elimination, a parallel resonant controller structure (shown in Fig. 5.7b) must be applied.

The same testing scenario was then repeated, this time with active VPI controllers. Phase current and its spectrum are given in the right plots of Fig. 5.8. The spectrum shows that the shape of the current is improved, i.e. that the loss-producing low order odd harmonics are successfully eliminated. It should be noted that, in the rest of the thesis, whenever harmonic elimination in α-β domain is addressed, one of the VPI controllers' schemes (single or parallel) from Fig. 5.7 is assumed for this purpose.

5.4 PMSM Model Testing and Experimental Verification

Simulation and experimental results are shown and analysed in this section. After testing derived multiphase PMSM model in *Matlab*/*Simulink* environment, results were experimentally validated in the experimental rig with the prototype machine. The enhanced FOC algorithm derived earlier in this chapter was used. A detail description of the experimental setup can be found in Appendix A.

The machine is first tested using the fundamental current only (labelled as the 1^{st} region in figures), followed by both the fundamental and the third current harmonic with optimal injection ratio k_{13} (further called 1^{st} + 3^{rd} region). Special focus is placed on the phase current shape and torque-producing currents i_{q1} and i_{q3}. When changing the region, i_{q1} is recalculated to a new value, while at the same time i_{q3} should compensate fundamental current change (and vice versa), so that the requested torque reference is always met. To test the FOC algorithm, two approaches are used (Method I and Method II). Both methods are based on equation (5.20), which shows that the electromagnetic torque and the phase current RMS value are proportional.

To demonstrate the approaches, Fig. 5.9 and Table 5.2 are given. The data in the table are calculated using the real machine parameters, i.e. λ_{m1} = 385.83 mWb, λ_{m3} = 119.22 mWb, P = 1, $k_{13\text{-}opt}$ = 0.93. It can be seen from Fig. 5.9a that Method I sets the electromagnetic torque to constant 1 Nm during the first 0.2 seconds (1^{st} region) and to 1.36 Nm from 0.2s onwards (1^{st} + 3^{rd} region). The boost of ≈36% directly follows from the analysis conducted earlier. For 1 Nm of torque, the torque-producing currents are i_{q1} = 0.58 A, i_{q3} = 0 A ($I_{RMS} = i_{q1}/\sqrt{2}$ = 0.41 A), while for the boosted torque (1.36 Nm), the required currents are i_{q1} = 0.42 A, i_{q3} = 0.39 A resulting in phase current RMS = $\sqrt{(i_{q1}^2 + i_{q3}^2)/2}$ = 0.41 A, i.e. in both regions practically the same I_{RMS} value is needed. Note that if the fundamental current (i_{q1}) alone is used to create the boosted torque (1.36 Nm), the require RMS would have been 0.56 A.

In the second method (Method II), the electromagnetic torque value is set to be constant in both regions (Fig. 5.9b). To achieve 1 Nm of torque in the 1st region, torque-producing currents must be, once again, i_{q1} = 0.58 A, i_{q3} = 0 A (I_{RMS} = 0.41 A). On the other hand, to maintain the same torque in 1st + 3rd region, the fundamental and the third harmonic currents must be i_{q1} = 0.31 A, i_{q3} = 0.29 A. Calculated I_{RMS} value is now $\sqrt{(i_{q1}^2 + i_{q3}^2)/2}$ = 0.3 A. It is easy to conclude that, to maintain the same electromagnetic torque value in the second region, a lower phase current RMS value is needed. This will have significant influence on powers, that is, the input power and power losses, as it will be shown in the rest of this section.

Although slightly different, both methods are validating the same (in this case 36%) electromagnetic torque improvement. Furthermore, both methods are simulated by setting the load torque to the desired value. On the other hand, achieving torque variation in the experimental setup is not a straightforward task. For this to be possible, one would need a continuously variable resistor for connection to the dc generator armature, which is in this work used for loading purposes. Because this is not available, Method II is chosen as the testing method further on. From the point of view of verifying the results, the selected approach simply comes down to the expectation that the relative reduction in the current RMS will be similar/the same as the corresponding relative torque increase.

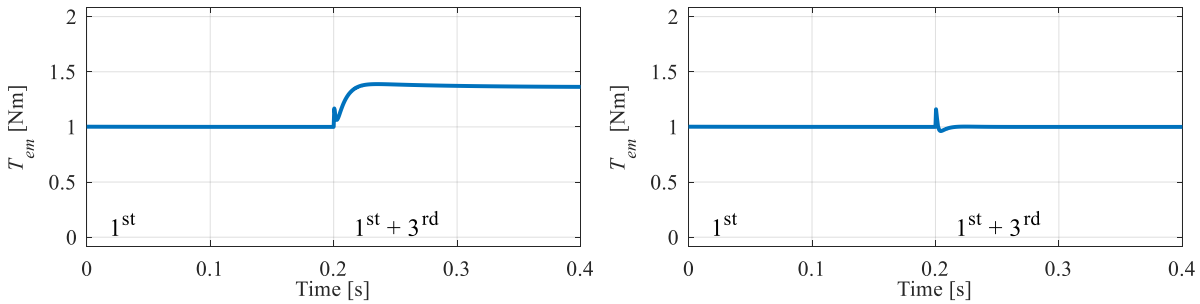

Figure 5.9 – Electromagnetic torque in: (a) Method I, and (b) Method II approaches obtained in simulations.

Table 5.2 – Analysis of the methods proposed for the machine testing.

\\\\\\\\\	**1st region**	**1st + 3rd region**
Method I	T_{em} = 1 [Nm]	T_{em} = 1.36 [Nm]
	i_{q1} = 0.58 [A] i_{q3} = 0 [A]	i_{q1} = 0.42 [A] i_{q3} = 0.39 [A]
	$\sqrt{(i_{q1}^2 + i_{q3}^2)/2}$ = 0.41 [A]	$\sqrt{(i_{q1}^2 + i_{q3}^2)/2}$ = 0.41 [A]
Method II	T_{em} = 1 [Nm]	T_{em} = 1 [Nm]
	i_{q1} = 0.58 [A] i_{q3} = 0 [A]	i_{q1} = 0.31 [A] i_{q3} = 0.29 [A]
	$\sqrt{(i_{q1}^2 + i_{q3}^2)/2}$ = 0.41 [A]	$\sqrt{(i_{q1}^2 + i_{q3}^2)/2}$ = 0.30 [A]

In the rest of the section, figures showing simulation results from *Matlab*/*Simulink* environment and experimental results from experimental setup are shown. The load torque is maintained constant (≈2 Nm) using a fixed value resistor connected to the dc machine terminals while holding a constant speed reference, as shown in Fig. 5.10. In the simulation case, the speed trace is a straight line without any oscillations (including the region change), while on the other hand, a small disturbance can be seen in the experimental trace (Fig. 5.10b). This is a consequence of the step change in the third harmonic current injection ratio.

In Fig. 5.11 and Fig. 5.12 simulation and experimental phase current waveforms are shown, respectively. The plots show the full sequence which is 4 s long and zoomed traces around the transient (1.9 - 2.1 s). Only waveforms for first phase in each phase set (i.e. phases *a*1, *a*2, *a*3) are shown. Regarding the simulation results (Fig. 5.11), phase current is in the 1st region having sinusoidal shape with peak value of ≈1.16 A. In the 1st + 3rd region, after optimal current injection takes place (k_{13} = 0.93), slight increase in peak can be noted. The shape is, as expected, following the shape of the machine's back-EMF. Comparing Fig. 5.11 and Fig. 5.12 shows good agreement between the simulation and experimental results, although the transient time is a little longer in the experiment. Small difference in results comes from the fact that windings in the real machine prototype are not entirely symmetrical (equal), as assumed in simulation model.

By analysing only one period of the recorded phase current waveforms, RMS value can be calculated. Results are summarised in Tables 5.3a and 5.3b. It can be concluded that the phase current RMS results are in both simulation and experiment almost the same. Furthermore, it is also important to note that, in the 1st + 3rd region, phase current RMS values (0.60 A and 0.58 A for simulation and experiment, respectively) are lower than the ones calculated in the 1st region (0.81 A and 0.79 A), meaning lower power losses, i.e. lower input power on the input terminals of the machine (output power P_{out} is constant because speed and electromagnetic torque are not changed during entire sequence time). If the difference in the RMS current is calculated as percentage, as expected, 1st region value is ≈36% higher than the one calculated in the 1st + 3rd region case. Please note that this is valid for the investigated machine back-EMF and corresponding injected current, i.e., different back-EMF magnitudes at different phase shift angles might result in different phase current RMS value reduction (torque improvement).

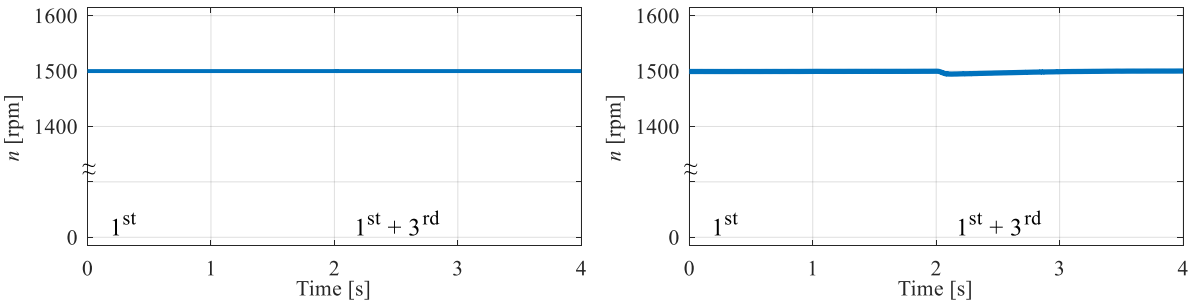

Figure 5.10 – Rotational speed results: (a) simulation, and (b) experiment.

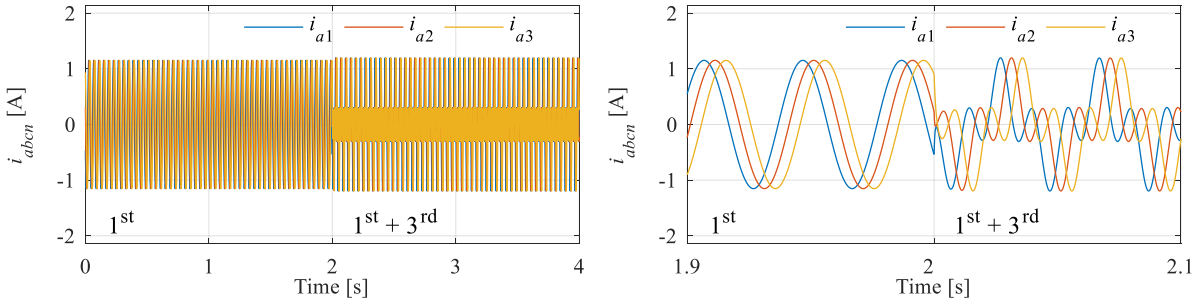

a) b)

Figure 5.11 – Phase current results: (a) full sequence, and (b) magnified traces around transient initiation instant.

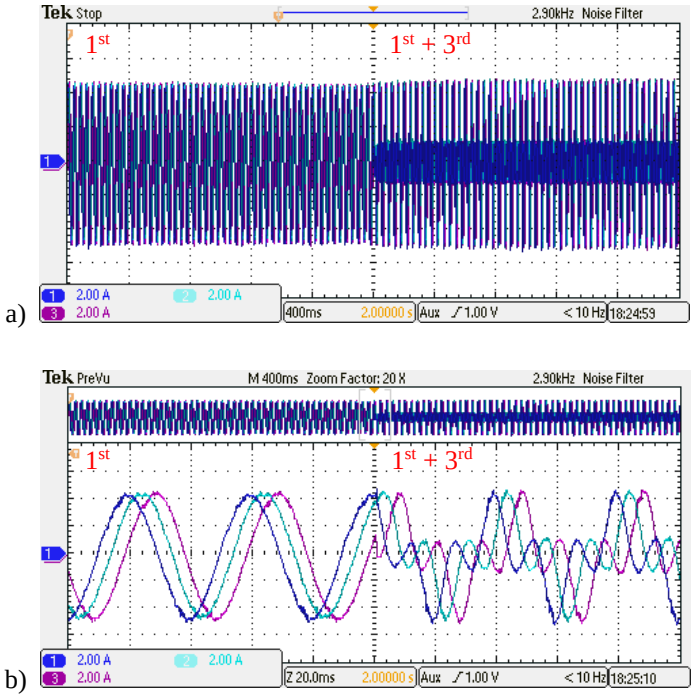

a)

b)

Figure 5.12 – Experimentally recorded phase currents (1 A on oscilloscope = 1/4 A of real current – 4 wire turns were used for higher precision): (a) full sequence, and (b) magnified traces around transient initiation instant.

Table 5.3a – Simulation phase current RMS.

Region / Time [s]	RMS value [A]
1st / 0 - 2	0.8144
1st + 3rd / 2 - 4	0.5970

Table 5.3b – Experimental phase current RMS.

Region / Time [s]	RMS value [A]
1st / 0 - 2	0.7946
1st + 3rd / 2 - 4	0.5816

Figs. 5.13a and b show the phase voltage (filtered: 2.9 kHz) simulation and experimental results - similar conclusion as in the phase current case can be made. Two intervals around transition instants (the same as in Fig. 5.11b) are again shown. Non-sinusoidal shape of phase voltage is directly related to the non-sinusoidal back-EMF to which additional voltages from controllers are added to zero or to control (as applicable) induced current harmonic components.

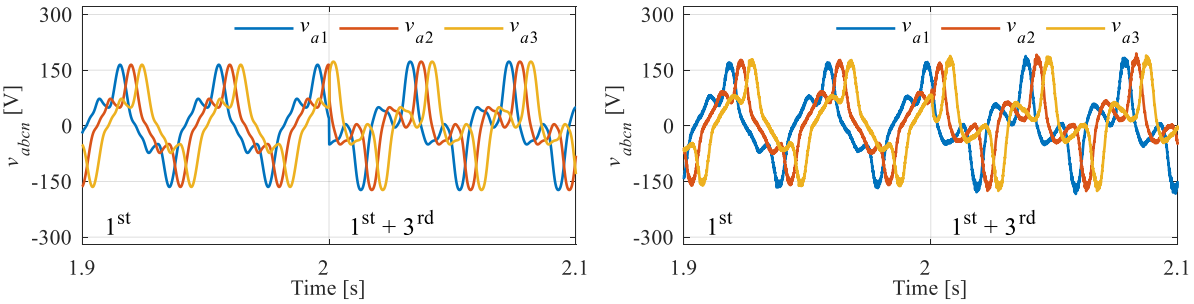

a) b)

Figure 5.13 – Phase voltage results: (a) simulation, and (b) experimental.

Power analysis results, which are closely related to the phase current RMS reduction, are given for the simulation and experiment in Figs. 5.14a and b, respectively. In simulation input power is calculated as:

$$P_{in} = v_{a1}(t) \cdot i_{a1}(t) + v_{a2}(t) \cdot i_{a2}(t) + ... + v_{c3}(t) \cdot i_{c3}(t) \tag{5.39}$$

while copper losses are computed as:

$$P_{Cu} = P_{in} - P_{out} = P_{in} - T_{em} \cdot \omega_{mech} \tag{5.40}$$

To obtain the traces in Fig. 5.14b, the voltage and current of the first phase in each three-phase set were measured using current and voltage probes and two synchronised oscilloscopes. The values were then imported into *Matlab* for post-processing. It is assumed that power per-phase in each three-phase set is the same. To get the stator winding losses, RMS of the measured current in the first phase of each three-phase set is calculated using *Matlab*. It is assumed that the same value applies to all three phases; likewise the stator resistance is considered to be the same for all phases.

In the simulation case (Fig. 5.14a), copper losses were reduced from P_{Cu1} = 190 W to P_{Cu13} = 102 W (ΔP_{Cu} ≈88 W), while in the experiment (Fig. 5.14b) this reduction is from P_{Cu1} = 178 W to P_{Cu13} = 94 W (ΔP_{Cu} ≈84 W). Reduction of the power losses in both simulation and experiments is directly related to the lower phase current RMS value shown in Tables 5.3a and 5.3b. Because only copper losses were modelled in the machine model (mechanical and iron losses were neglected in accordance with modelling assumptions), total losses are in fact equal to calculated copper losses ($P_{in} = P_{out} + P_{Cu}$). Input power calculated in the simulation case (Fig. 5.14a) is P_{in1} = 505 W for the 1st region, i.e. P_{in13} = 417 W for the 1st + 3rd region (ΔP_{in} ≈88 W). On the other hand, this power is in the experiment slightly higher, because mechanical and iron losses exist. Nevertheless, the impact of these losses is not significant. If difference between input powers in two regions is once again calculated, now using P_{in1} = 514 W and P_{in13} = 429 W recorded experimentally in the 1st and 1st + 3rd regions, respectively, a good agreement between simulation (ΔP_{in} ≈88 W) and experimental (ΔP_{in} ≈85 W) results can be noted. Finally, by re-

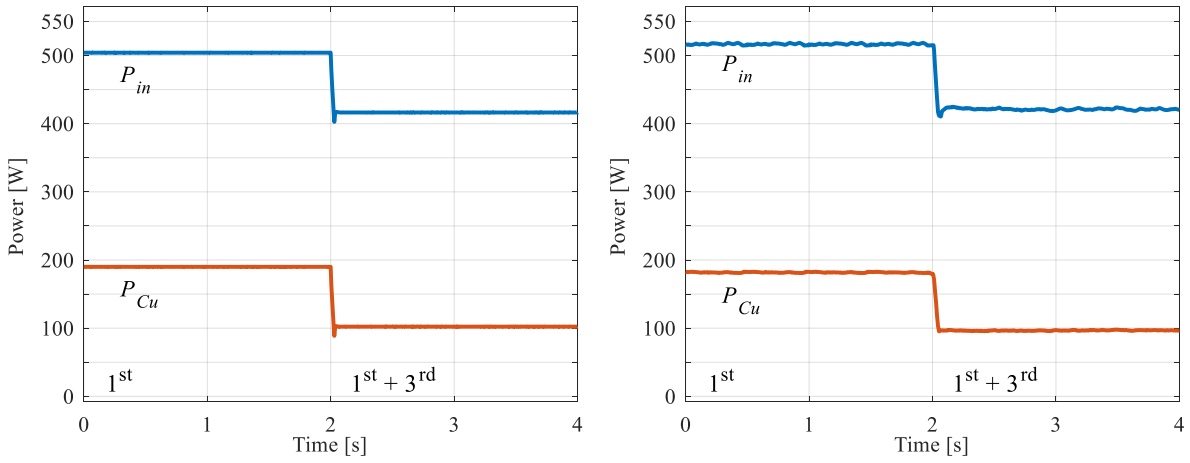

Figure 5.14 – Input power and stator winding losses results: (a) simulation, and (b) experiment.

calculating experimental copper loss power reduction, electromagnetic torque improvement can be once again confirmed. The difference between observed powers without (the 1st region) and with (the 1st + 3rd region) the third harmonic current injection is $\sqrt{P_{Cu1} / P_{Cu13}} = I_{RMS1}/I_{RMS13} = 1.364$ (≈36%).

Simulation and experimental results, showing the current mapping after vector space decomposition transformation, can be seen in Figs. 5.15a and b, respectively. As expected, in the region where $k_{13} = 0$, torque is entirely produced by the fundamental component only, while other harmonic components are suppressed by the resonant controllers. In the region where $k_{13} = 0.93$, torque is produced with both (lower) fundamental and (increased) third harmonic components, which are adequately set by the PI controllers. Similar results are obtained using the experimental rig. Here, currents are characterised with some noise. Both simulation and experimental results are shown around transient initiation points (that is, 1.9 - 2.1 s).

Flux- and torque-producing currents in synchronous domain can be seen in Fig. 5.16. Flux-producing currents i_{d1} and i_{d3} are set and controlled to 0 (MTPA control). Regarding torque-producing currents, in both simulation and experiment high correspondence in results can be noted. The only difference is related to the unavoidable noise in the experiment. In the region before the coefficient change, only fundamental torque-producing current component i_{q1} is used for electromagnetic torque production. Recorded peak current value is approximately $i_{q1} = 1.16$ A ($I_{RMS} = 0.81$ A). As expected, after the third harmonic current injection ratio is changed to its optimal value i.e. $k_{13} = 0.93$, fundamental current value decreases to $i_{q1} = 0.62$ A, while at the same time there is an increase in the third harmonic current i_{q3} from $i_{q3} = 0$ A to $i_{q3} = 0.58$ A ($I_{RMS} = \sqrt{(i_{q1}^2 + i_{q3}^2)/2} = 0.60$ A). Experimental results are approximately the same as the simulation results, i.e. before harmonic current injection $i_{q1} = 1.12$ A, $i_{q3} = 0$ A ($I_{RMS} = 0.79$ A), while after change, $i_{q1} = 0.604$ A, $i_{q3} = 0.564$ A ($I_{RMS} = 0.58$ A).

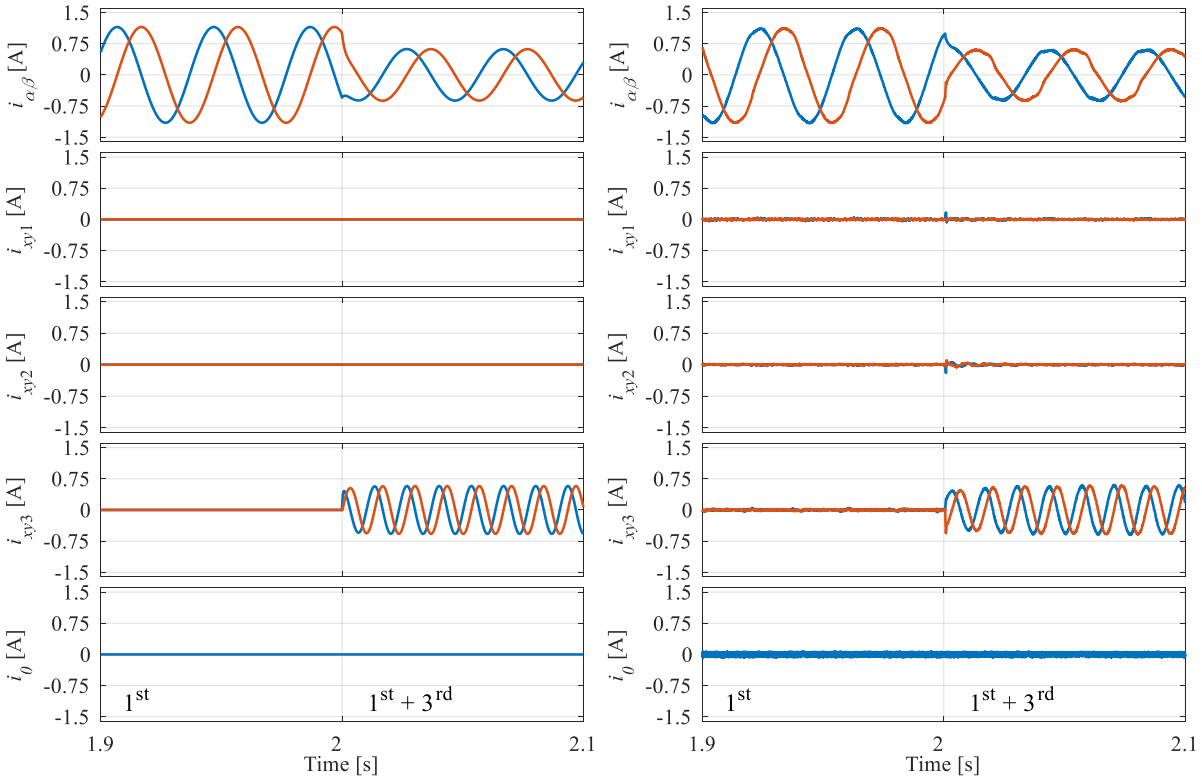

a) b)

Figure 5.15 – Current mapping results after system decoupling using vector space decomposition: (a) simulation, and (b) experiment.

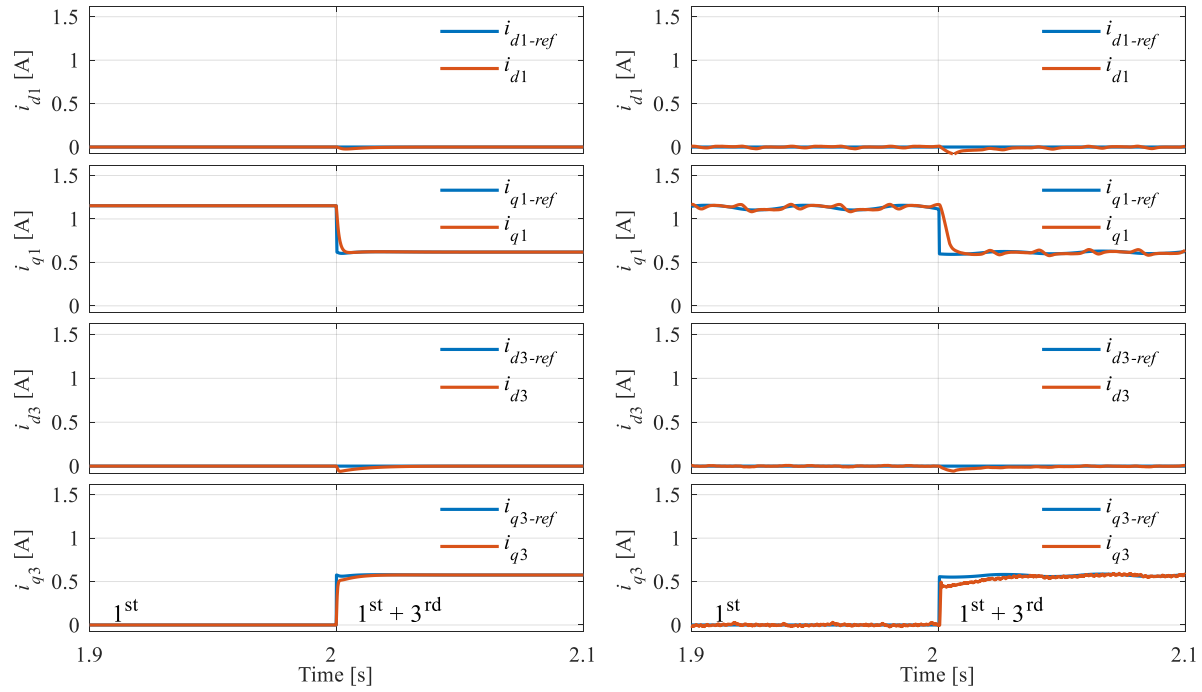

a) b)

Figure 5.16 – Flux- and torque-producing currents results recorded after applying rotational transformation: (a) simulation, and (b) experiment.

5.5 Summary

At the beginning of this chapter modelling approach for multiphase machines with highly non-sinusoidal back-EMF is given. It has been shown how to, based on the recorded back-EMF (from no-load generation mode test), modify near-sinusoidal back-EMF machine model to get the same electromotive force as in the real machine prototype. For this purpose, flux harmonic components and corresponding harmonic angles were used.

The third harmonic current component was used for torque density improvement, while other low order harmonics, although also capable of additional torque enhancement (as it will be shown in the following chapter), were mitigated. For this purpose, PI and VPI resonant controllers were used, respectively. Third harmonic current injection ratio between fundamental and the third harmonic currents plays an important role in the current injection techniques. Extensive analysis was therefore conducted, with the goal being to calculate its optimal value. MTPA and winding factor approaches were used for this purpose. Brief comparison with the results obtained by optimisation procedure was also given for verification purposes.

By implementing the optimal third harmonic current injection method to improve torque and by eliminating non-torque producing harmonic content with VPI resonant controller, enhanced, high-performance FOC algorithm, suitable for control of the machine with highly non-sinusoidal back-EMF investigated in this work, was derived. By testing the multiphase PMSM model in *Matlab*/*Simulink* environment, expected 36% torque improvement was confirmed. The same testing scenario was afterwards applied for the real machine prototype and experimental results similar to the ones obtained using the simulation model in *Matlab*/*Simulink* were recorded. Based on the high degree of agreement between experimental and simulation results, it can be concluded that the FOC algorithm was validated. Note that the above stated improvement is directly related to the specific back-EMF (harmonic magnitudes and angle shifts), i.e. by applying the same control principles, improvements in some other multiphase PMSM configurations might not be the same. The FOC algorithm will be further modified in the next chapter for torque enhancement using all possible low order odd harmonics between 1 and n and validation will apply again to the considered nine-phase surface PMSM.

Chapter Six

GENERAL HARMONIC CURRENT INJECTION ANALYSIS

6.1 Introduction

In chapter 5, the third back-EMF harmonic was studied for torque improvement. It has been shown that, by applying a right amount of the harmonic current, output torque of the nine-phase surface PMSM can be improved for additional ≈36%. Although existing in the EMF spectrum, other high-magnitude odd harmonic components were not considered for either torque enhancement or any other additional purposes, i.e. they were eliminated using VPI resonant controllers. This might not be the best approach in multiphase machines, because output torque can be enhanced (without additional losses) using these components as well, as long as the order of the harmonic does not exceed the number of machine's phases ($h < n$; [Toliyat et al (1998)]). In the EMF FFT spectrum of the studied machine prototype, in addition to the high third harmonic, significant fifth (49.8% of the fundamental) and some seventh harmonics (12.8% of the fundamental) also exist. The analysis of chapter 5 is therefore here further extended and a general vector control algorithm which employs all possible (meaningful) high-magnitude low-order odd EMF harmonics for torque boost is derived.

The chapter commences by giving the machine models for the fifth and the seventh harmonics in synchronous reference frame (section 6.2). Next, a generalised FOC algorithm for multiphase PMSMs is derived, which in addition to the fundamental and third, employs the fifth and seventh harmonics for the torque improvement as well. To determine the optimal current injection ratios an optimisation procedure and the maximal torque-per-Ampere method are employed in section 6.3. How various injection ratios interact is also investigated. Detailed analysis of the level of torque improvement and a comparison with the FEM results from chapter 4 is given in section 6.4. The developed FOC algorithm is validated using simulation studies and further verified using an experimental setup. The key findings of this chapter can be found in [Slunjski et al (2021)].

6.2 FOC Applying the Fifth and the Seventh Harmonic Currents

To derive a FOC method which considers all possible odd harmonics in addition to the already presented fundamental and the third, the fifth and the seventh harmonic synchronous reference frame machine models must be taken into consideration. Although harmonics higher than the ninth, i.e. the 11^{th} and 13^{th} harmonics, could also be considered for the same purpose (as shown in [Hu et al (2017)] where the seventh harmonic was studied in a six-phase machine for additional 9% torque enhancement purpose), such a special case is not the objective of the study here. Because this can lead to, for example, additional torque ripple, only harmonics lower than the machine phase number ($h < n$) are of interest in this chapter/thesis.

As explained in chapter 5, at the beginning of the analysis all flux-producing current references must be set (and afterwards controlled) to zero ($i_{d1} = 0$, $i_{d3} = 0$, $i_{d5} = 0$ and $i_{d7} = 0$). Total electromagnetic

torque T_{em1357} is therefore produced as the sum of the torque-producing components T_{em1}, T_{em3}, T_{em5}, T_{em7} (i.e. equivalent currents i_{q1}, i_{q3}, i_{q5}, i_{q7},) as:

$$T_{em1357} = T_{em1} + T_{em3} + T_{em5} + T_{em7} \tag{6.1}$$

Fundamental and the third harmonic torque-producing parts T_{em1} and T_{em3} were presented in detail in section 5.3, and so are not discussed here. To derive T_{em5} and T_{em7}, the adequate equivalent machine models in synchronous reference frame must be considered (Figs. 6.1 top and bottom, respectively). The fifth harmonic model equations for T_{em5} torque producing part calculation can be given as:

$$v_{d5} = R_s \cdot i_{d5} + \frac{d\lambda_{d5}}{dt} + 5\omega_{el} \cdot \lambda_{q5} \tag{6.2}$$

$$v_{q5} = R_s \cdot i_{q5} + \frac{d\lambda_{q5}}{dt} - 5\omega_{el} \cdot \lambda_{d5} \tag{6.3}$$

$$\lambda_{d5} = L_{d5} \cdot i_{d5} + \lambda_{m5}; \qquad \lambda_{q5} = L_{q5} \cdot i_{q5} \tag{6.4}$$

$$T_{em5} = \frac{n}{2} \cdot P \cdot 5 \cdot \lambda_{m5} \cdot i_{q5} \tag{6.5}$$

Following the same principles, electromagnetic torque component T_{em7} for the seventh harmonic can be described with:

$$v_{d7} = R_s \cdot i_{d7} + \frac{d\lambda_{d7}}{dt} + 7\omega_{el} \cdot \lambda_{q7} \tag{6.6}$$

$$v_{q7} = R_s \cdot i_{q7} + \frac{d\lambda_{q7}}{dt} - 7\omega_{el} \cdot \lambda_{d7} \tag{6.7}$$

$$\lambda_{d7} = L_{d7} \cdot i_{d7} + \lambda_{m7}; \qquad \lambda_{q7} = L_{q7} \cdot i_{q7} \tag{6.8}$$

$$T_{em7} = \frac{n}{2} \cdot P \cdot 7 \cdot \lambda_{m7} \cdot i_{q7} \tag{6.9}$$

To control flux- and torque-producing currents, PI current controllers can be applied once again. Outputs of the stator voltages d_5-q_5 and d_7-q_7 for both current PI regulators can be mathematically modelled as:

$$v_{d5-reg} = R_s \cdot i_{d5} + L_{s5} \frac{di_{d5}}{dt}; \qquad v_{q5-reg} = R_s \cdot i_{q5} + L_{s5} \frac{di_{q5}}{dt} \tag{6.10}$$

$$v_{d7-reg} = R_s \cdot i_{d7} + L_{s7} \frac{di_{d7}}{dt}; \qquad v_{q7-reg} = R_s \cdot i_{q7} + L_{s7} \frac{di_{q7}}{dt} \tag{6.11}$$

By adding the decoupling voltages e_{d5}, e_{q5} and e_{d7}, e_{q7} to the outputs of the PI controllers:

$$e_{d5} = -5\omega_{el}\left(L_{s5}\cdot i_{d5} + \lambda_{m5}\right); \qquad e_{q5} = 5\omega_{el}\left(L_{s5}\cdot i_{q5}\right) \tag{6.12}$$

$$e_{d7} = -7\omega_{el}\left(L_{s7}\cdot i_{d7} + \lambda_{m7}\right); \qquad e_{q7} = 7\omega_{el}\left(L_{s7}\cdot i_{q7}\right) \tag{6.13}$$

total stator voltage references similar to (6.2)-(6.3) and (6.6)-(6.7) are acquired.

To decouple the system and to obtain currents in the required synchronous reference frames for FOC implementation, VSD and rotational transformations have to be applied to the machine models. VSD matrix (first presented in section 3.3) remains unchanged when the harmonic current injection takes place. However, parts of the rotational matrix responsible for i_{xy1}, i_{xy2}, i_{xy3}, (where the 7th, the 5th and the 3rd current harmonics map after VSD, respectively), which will yield i_{dq7}, i_{dq5}, i_{dq3} after transformation, must be modified by adding the rotational transformations for these pairs of rows. The complete (nine-phase) rotational transformation matrix, which takes into account transformation of all possible low-order odd harmonics lower than the machine phase number, can be written as:

$$D = \begin{bmatrix} \cos(\theta_1) & \sin(\theta_1) & 0 & 0 & 0 & 0 & 0 & 0 & 0 \\ -\sin(\theta_1) & \cos(\theta_1) & 0 & 0 & 0 & 0 & 0 & 0 & 0 \\ 0 & 0 & \cos(\theta_7) & -\sin(\theta_7) & 0 & 0 & 0 & 0 & 0 \\ 0 & 0 & \sin(\theta_7) & \cos(\theta_7) & 0 & 0 & 0 & 0 & 0 \\ 0 & 0 & 0 & 0 & \cos(\theta_5) & -\sin(\theta_5) & 0 & 0 & 0 \\ 0 & 0 & 0 & 0 & \sin(\theta_5) & \cos(\theta_5) & 0 & 0 & 0 \\ 0 & 0 & 0 & 0 & 0 & 0 & \cos(\theta_3) & \sin(\theta_3) & 0 \\ 0 & 0 & 0 & 0 & 0 & 0 & -\sin(\theta_3) & \cos(\theta_3) & 0 \\ 0 & 0 & 0 & 0 & 0 & 0 & 0 & 0 & 1 \end{bmatrix} \tag{6.14}$$

where $\theta_h = h\cdot\theta_{el} + \theta_{phsh}$.

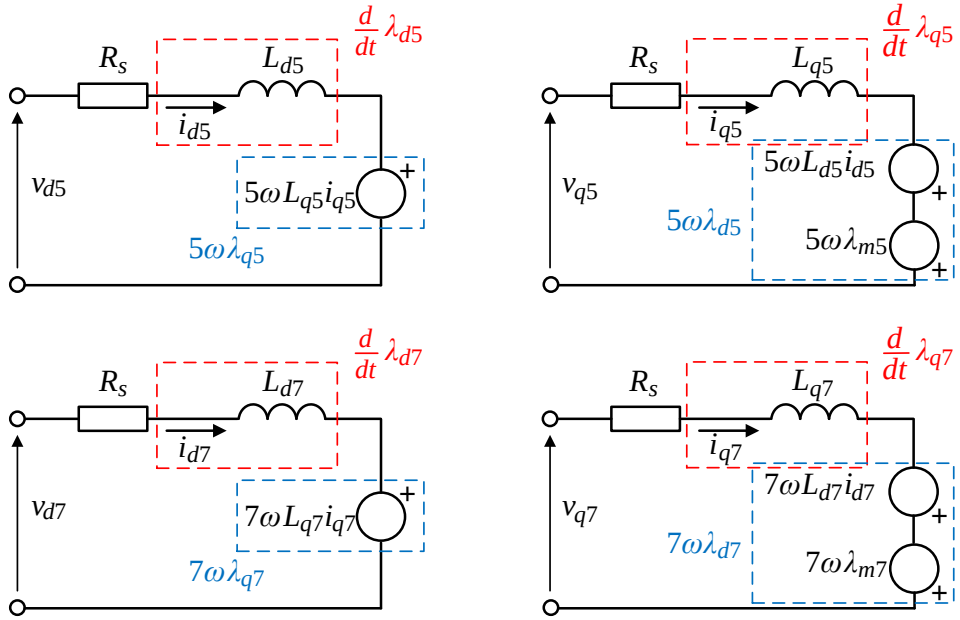

Figure 6.1 – Equivalent *d-q* electrical circuits for a PMSM in respective synchronous reference frames: the fifth (upper) and the seventh (bottom) harmonic.

Although similar, the equivalent circuits in Fig. 6.1 and the corresponding model equations (6.2)-(6.13) for the fifth and the seventh harmonics are slightly different from models presented in earlier chapters for the fundamental and the third harmonics. The difference comes from the fact that both the fifth and the seventh harmonic are rotating in the opposite (anti-synchronous) direction (hence the opposite distribution of the minus and plus signs in the voltage equations). In this case the only way to obtain constant *x-y* voltage references on the output of the PI controller is to perform a rotation in the anti-synchronous direction using the inverse Park's transformation first, following by the rotational transformation implemented after PI current controllers [Che et al (2014), Gonzales-Prieto et al (2016)]. Illustration of the stated transformation process can be seen in Fig. 6.2. In this way, the control algorithm in the synchronous domain is still the same but with rearranged rotational transformations.

The inverse of the transformation defined with (6.14) is:

$$D^{-1}=\begin{bmatrix} \cos(\theta_1) & -\sin(\theta_1) & 0 & 0 & 0 & 0 & 0 & 0 & 0 \\ \sin(\theta_1) & \cos(\theta_1) & 0 & 0 & 0 & 0 & 0 & 0 & 0 \\ 0 & 0 & \cos(\theta_7) & \sin(\theta_7) & 0 & 0 & 0 & 0 & 0 \\ 0 & 0 & -\sin(\theta_7) & \cos(\theta_7) & 0 & 0 & 0 & 0 & 0 \\ 0 & 0 & 0 & 0 & \cos(\theta_5) & \sin(\theta_5) & 0 & 0 & 0 \\ 0 & 0 & 0 & 0 & -\sin(\theta_5) & \cos(\theta_5) & 0 & 0 & 0 \\ 0 & 0 & 0 & 0 & 0 & 0 & \cos(\theta_3) & -\sin(\theta_3) & 0 \\ 0 & 0 & 0 & 0 & 0 & 0 & \sin(\theta_3) & \cos(\theta_3) & 0 \\ 0 & 0 & 0 & 0 & 0 & 0 & 0 & 0 & 1 \end{bmatrix} \quad (6.15)$$

6.2.1 Generalisation of the FOC Method

Following from the synchronous domain machine models and equations needed for 1st - 7th current harmonic injection control implementation, it can be concluded that general form of the required equations can be easily formulated by knowing the corresponding h^{th} order harmonic parameters. This includes synchronous reference frame flux inductances (λ_{dh}, λ_{qh}, λ_{mh}), stator winding self-inductance (L_{dh}, L_{qh}), stator resistance (R_s), and machine's angular speed ω_{el} (which for h^{th} harmonic order must be set to $h \cdot \omega_{el}$). By knowing these parameters and with *d-q* reference frame currents i_{dh} and i_{qh} at the input, output voltages v_{dh} and v_{qh} in stated reference frames can be calculated. General case of a synchronous reference

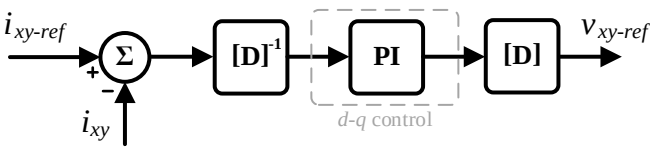

Figure 6.2 – Rotational transformation order in the case when current harmonic is rotating in the anti-synchronous direction.

frame machine model for the h^{th} harmonic order can be written as shown next. In some systems specific harmonics might rotate in anti-synchronous direction. This causes different sign in front of the rotational speed, hence ± notation is used here. For the sake of completeness, generalised electrical circuit is illustrated in Fig. 6.3.

$$v_{dh} = R_s \cdot i_{dh} + \frac{d\lambda_{dh}}{dt} \mp h\omega_{el} \cdot \lambda_{qh}; \qquad v_{qh} = R_s \cdot i_{qh} + \frac{d\lambda_{qh}}{dt} \pm h\omega_{el} \cdot \lambda_{dh} \tag{6.16}$$

$$\lambda_{dh} = L_{dh} \cdot i_{dh} + \lambda_{mh}; \qquad \lambda_{qh} = L_{qh} \cdot i_{qh} \tag{6.17}$$

$$T_{emh} = \frac{n}{2} \cdot P \cdot h \cdot \lambda_{mh} \cdot i_{qh} \tag{6.18}$$

By knowing in which subspace a harmonic is mapped, basic rotational transformation matrix, given in section 3.3, can be for the h^{th} order component transformation modified by adding the rotational transformation for the corresponding pair of rows as:

$$\begin{bmatrix} \dots \\ i_{dh} \\ i_{qh} \\ \dots \end{bmatrix} = \begin{bmatrix} \dots & \dots & \dots & \dots \\ \dots & \cos(h\theta + \theta_{phsh}) & \pm\sin(h\theta + \theta_{phsh}) & \dots \\ \dots & \mp\sin(h\theta + \theta_{phsh}) & \cos(h\theta + \theta_{phsh}) & \dots \\ \dots & \dots & \dots & \dots \end{bmatrix} \begin{bmatrix} \dots \\ i_{xj} \\ i_{yj} \\ \dots \end{bmatrix} \tag{6.19}$$

In (6.19), subscript *j* represents auxiliary subspace in which the harmonic is mapped.

Regardless of whether only one additional harmonic component with specific magnitude (e.g. only the third or the fifth) is needed, or more than one (e.g. combination of the third plus the fifth) are required, the optimal ratio of the fundamental torque-producing current i_{q1} and torque-producing currents of the other required harmonics $i_{q3}, i_{q5}, \dots, i_{qh}$ must be calculated. As before, this ratio can be represented with constants k_{13}, k_{15}, …, k_{1h} as:

$$k_{13} = \frac{i_{q3}}{i_{q1}}; \quad k_{15} = \frac{i_{q5}}{i_{q1}}; \quad \dots, k_{1h} = \frac{i_{qh}}{i_{q1}} \tag{6.20}$$

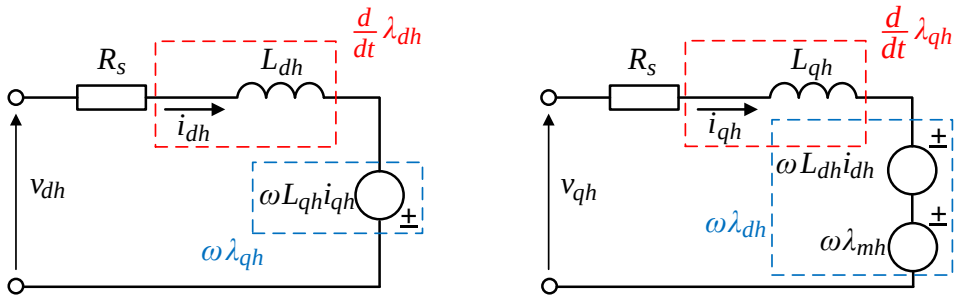

Figure 6.3 – Equivalent *d-q* electrical circuits for a PM synchronous machine in respective synchronous reference frame: h^{th} order harmonic component.

Determination of the optimal current ratios in the case of multiple injected harmonics will be considered later. For the time being, only equivalences presented in (6.20) are needed to complete the generalised field-oriented control algorithm for current harmonic injection. The number of torque-producing parts in the total output torque $T_{em1\ldots h}$ depends on the number of the required current harmonic injections. Relation between fundamental torque producing current i_{q1}, total electromagnetic torque $T_{em1\ldots h}$ and defined ratios k_{13}, k_{15}, …, k_{1h} suitable for FOC implementation for the general case is:

$$\begin{aligned} T_{em1\ldots h} &= \frac{n}{2} P \cdot \left(\lambda_{m1} \cdot i_{q1} + 3\lambda_{m3} \cdot i_{q3} + \ldots + h\lambda_{mh} \cdot i_{qh} \right) \\ T_{em1\ldots h} &= \frac{n}{2} P \cdot \left(\lambda_{m1} \cdot i_{q1} + 3\lambda_{m3} \cdot k_{13} \cdot i_{q1} + \ldots + h\lambda_{mh} \cdot k_{1h} \cdot i_{q1} \right) \end{aligned} \tag{6.21}$$

$$i_{q1} = \frac{2}{n \cdot P} \cdot \frac{T_{em1\ldots h}}{\lambda_{m1} + 3 \cdot \lambda_{m3} \cdot k_{13} + \ldots + h \cdot \lambda_{mh} \cdot k_{1h}} \tag{6.22}$$

A diagram of the generalised FOC algorithm can be seen in Fig. 6.4.

6.3 Optimal Current Injection Ratio Analysis

It was shown in chapter 5 how to determine optimal current injection ratio in the case when, in addition to the fundamental, a single additional harmonic is considered. Building on the given technique, a study related to the additionally added harmonics (e.g. the fifth, the seventh), i.e. how they interact with already implemented harmonics (e.g. the third) is conducted. To start with, for multiple optimal ratio determination, a simple iterative procedure is used. For this technique, an objective function which relates output torque, phase current RMS value and injection ratios must be derived.

Disregarding for the moment the seventh harmonic component, the relation between electromagnetic torque T_{em135} and two harmonic current injection ratios k_{13} and k_{15} can be obtained after short mathematical manipulation as:

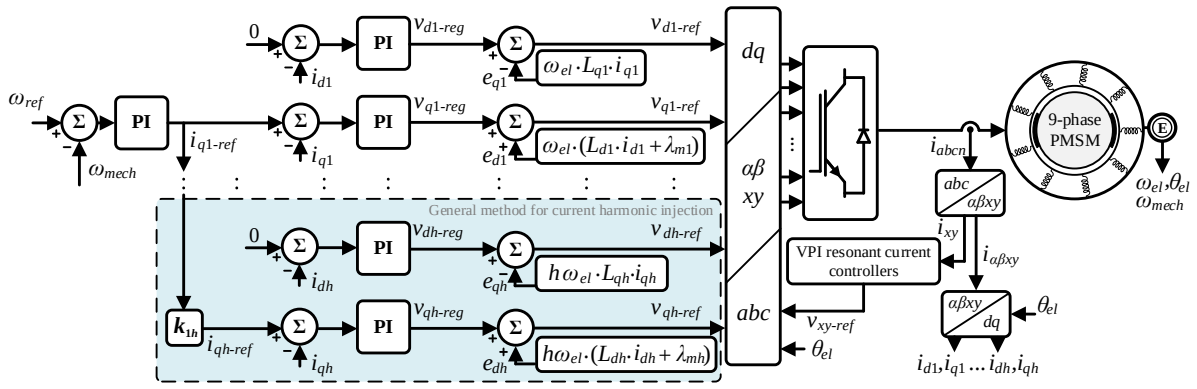

Figure 6.4 – Schematic representation of the FOC algorithm modified for general harmonic current injection and low-order harmonic elimination.

$$T_{em135} = \frac{n \cdot P}{2} \cdot \left(\lambda_{m1} \cdot i_{q1} + 3\lambda_{m3} \cdot i_{q3} + 5\lambda_{m5} \cdot i_{q5} \right)$$
$$k_{13} = \frac{i_{q3}}{i_{q1}}; \quad k_{15} = \frac{i_{q5}}{i_{q1}}; \quad \rightarrow T_{em135} = \frac{n \cdot P}{2} \cdot \left(\lambda_{m1} + 3\lambda_{m3} \cdot k_{13} + 5\lambda_{m5} \cdot k_{15} \right) \cdot i_{q1} \tag{6.23}$$

$$I_{RMS} = \sqrt{\frac{i_{q1}^2 + i_{q3}^2 + i_{q5}^2}{2}}; \quad \rightarrow i_{q1} = \frac{\sqrt{2} I_{RMS}}{\sqrt{1 + k_{13}^2 + k_{15}^2}} \tag{6.24}$$

$$T_{em135} = \frac{n \cdot P}{2} \cdot \frac{(\lambda_{m1} + 3 \cdot \lambda_{m3} \cdot k_{13} + 5 \cdot \lambda_{m5} \cdot k_{15}) \cdot \sqrt{2} I_{RMS}}{\sqrt{1 + k_{13}^2 + k_{15}^2}} \tag{6.25}$$

Phase current RMS value I_{RMS} is for the simplicity in this analysis assumed to be $1/\sqrt{2}$ A. Apart from I_{RMS} and constants n, P, λ_{m1}, λ_{m3}, λ_{m5}, final objective function presented in (6.25) depends on three variables; hence the system can be regarded as three-dimensional. By solving this three-dimensional function (for k_{13}, k_{15} and both in [0-2] interval), the plot presented in Fig. 6.5 is obtained. Corresponding results are summarised in Table 6.1 (red part). It can be seen in Table 6.1 that the maximal reachable torque achieved with two injected harmonics is T_{em135} = 2.52 Nm. To achieve such an electromagnetic torque, calculated optimal harmonic injection ratios must be k_{13} = 0.927 and k_{15} = 0.497. If compared with the results obtained using the third harmonic current injection from chapter 5, it can be concluded that the value of the injection ratio k_{13} has stayed unchanged. To validate the results, the finite element method study from chapter 4 is used. Recorded electromagnetic torque results can be found in the last column of the Table 6.1 (blue section). The finite element method results are in good agreement with the optimisation results. Small differences that can be seen are, as explained in chapter 4, related to the approximation of some design and electrical machine parameters needed to build the finite element method model.

By including the seventh harmonic into the maximal achievable torque calculation, the objective function is now:

$$T_{em1357} = \frac{n \cdot P}{2} \cdot \left(\lambda_{m1} \cdot i_{q1} + 3\lambda_{m3} \cdot i_{q3} + 5\lambda_{m5} \cdot i_{q5} + 7\lambda_{m7} \cdot i_{q7} \right)$$

$$k_{13} = \frac{i_{q3}}{i_{q1}}; \quad k_{15} = \frac{i_{q5}}{i_{q1}}; \quad k_{17} = \frac{i_{q7}}{i_{q1}}; \tag{6.26}$$

$$\rightarrow T_{em1357} = \frac{n \cdot P}{2} \cdot \left(\lambda_{m1} + 3\lambda_{m3} \cdot k_{13} + 5\lambda_{m5} \cdot k_{15} + 7\lambda_{m7} \cdot k_{17} \right) \cdot i_{q1}$$

$$I_{RMS} = \sqrt{\frac{i_{q1}^2 + i_{q3}^2 + i_{q5}^2 + i_{q7}^2}{2}}; \quad \rightarrow i_{q1} = \frac{\sqrt{2} I_{RMS}}{\sqrt{1 + k_{13}^2 + k_{15}^2 + k_{17}^2}} \tag{6.27}$$

$$T_{em1357} = \frac{n \cdot P}{2} \cdot \frac{(\lambda_{m1} + 3 \cdot \lambda_{m3} \cdot k_{13} + 5 \cdot \lambda_{m15} \cdot k_{15} + 7 \cdot \lambda_{m7} \cdot k_{17}) \cdot \sqrt{2} I_{RMS}}{\sqrt{1 + k_{13}^2 + k_{15}^2 + k_{17}^2}} \tag{6.28}$$

Obtained results are summarised in Table 6.2. Because the system is now dependant on four variables (k_{13}, k_{15}, k_{17}, T_{em1357}), corresponding plot cannot be produced. A comparison of the optimised coefficients, i.e. recorded torque values, with the ones previously recorded in FEM, leads to the conclusion that the two methods are in good agreement.

Table 6.1 – Optimal injection ratio calculation for the 1st, 3rd and 5th harmonics.

Harmonics	Ratio	Torque [Nm]	FEM Torque [Nm]
1st	$k_1 = 1$	1.74	1.68
1st + 3rd	$k_{13} = 0.927$	2.38	2.24
1st, 3rd + 5th	$k_{15} = 0.497$	2.52	2.39

Table 6.2 – Optimal injection ratio calculation for the 1st, 3rd, 5th and 7th harmonics.

Harmonics	Ratio	Torque [Nm]	FEM Torque [Nm]
1st	$k_1 = 1$	1.74	1.68
1st + 3rd	$k_{13} = 0.927$	2.38	2.24
1st, 3rd + 5th	$k_{15} = 0.497$	2.52	2.39
1st, 3rd, 5th + 7th	$k_{17} = 0.128$	2.53	2.41

Based on the results presented in Tables 6.1 and 6.2, several conclusions can be made. Complexity of the system that needs to be solved grows by one extra dimension with every addition of another harmonic. However, regardless of the dimension, the optimal third harmonic current injection ratio remains the same as in chapter 5, as shown in Table 6.1 and in Table 6.2. Furthermore, by comparing the results acquired for k_{15} ratio in Table 6.1 and in Table 6.2, it can be concluded that the optimal ratio for the fifth harmonic did not change either. This leads to the conclusion that optimal ratios can be calculated separately by solving less complex two-dimensional functions for each new harmonic in relation to the fundamental. Corresponding two-dimensional functions can be defined as:

$$T_{em13} = \frac{n \cdot P}{2} \cdot \frac{(\lambda_{m1} + 3 \cdot \lambda_{m3} \cdot k_{13}) \cdot \sqrt{2} I_{RMS}}{\sqrt{1 + k_{13}^2}} \rightarrow \textit{for } 1^{st} + 3^{rd} \tag{6.29}$$

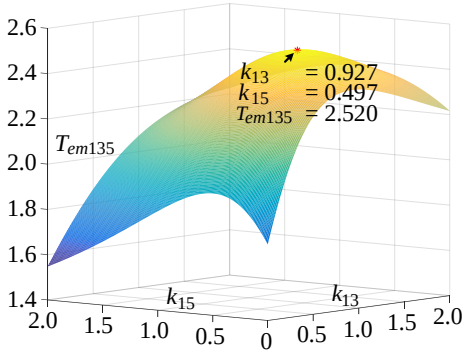

Figure 6.5 – Objective function optimisation for optimal third and fifth harmonic current ratios determination.

$$T_{em15} = \frac{n \cdot P}{2} \cdot \frac{(\lambda_{m1} + 5 \cdot \lambda_{m5} \cdot k_{15}) \cdot \sqrt{2} I_{RMS}}{\sqrt{1 + k_{15}^2}} \rightarrow for\ 1^{st} + 5^{th} \tag{6.30}$$

$$T_{em17} = \frac{n \cdot P}{2} \cdot \frac{(\lambda_{m1} + 7 \cdot \lambda_{m7} \cdot k_{17}) \cdot \sqrt{2} I_{RMS}}{\sqrt{1 + k_{17}^2}} \rightarrow for\ 1^{st} + 7^{th} \tag{6.31}$$

For validation purpose, Fig. 6.6 is given. It is visible that the same values of coefficients are obtained by solving two-dimensional systems, as before when a single multi-dimensional system was optimised. Although being easier to execute, the 2D method does not provide final achievable torque value immediately. Nevertheless, by using the optimal ratios from 2D analysis and I_{RMS}, the maximal electromagnetic torque can be calculated as:

$$T_{em1...h} = \frac{n \cdot P}{2} \left(\lambda_{m1} + \sum_1^l \boldsymbol{h}(l) \lambda_{m\boldsymbol{h}(l)} k_{1\boldsymbol{h}(l)} \right) \cdot \frac{\sqrt{2} I_{RMS}}{\sqrt{1 + \sum_1^l k_{1\boldsymbol{h}(l)}^2}} \tag{6.32}$$

where $\boldsymbol{h}$ = [3, 5, …, n - 2] and l = [(n-3)/2]. Finally, by testing the MTPA theory for multi-dimensional injection ratio(s) calculations (derived originally in chapter 5 for the third harmonic):

$$k_{13} = \frac{3 \cdot \lambda_{m3}}{\lambda_{m1}} = \frac{e_3}{e_1} = \frac{k_{wf3} \cdot B_{rot3}}{k_{wf1} \cdot B_{rot1}} = 0.9270 \tag{6.33}$$

$$k_{15} = \frac{5 \cdot \lambda_{m5}}{\lambda_{m1}} = \frac{e_5}{e_1} = \frac{k_{wf5} \cdot B_{rot5}}{k_{wf1} \cdot B_{rot1}} = 0.4967 \tag{6.34}$$

$$k_{17} = \frac{7 \cdot \lambda_{m7}}{\lambda_{m1}} = \frac{e_7}{e_1} = \frac{k_{wf7} \cdot B_{rot7}}{k_{wf1} \cdot B_{rot1}} = 0.1275 \tag{6.35}$$

optimal injection values for the studied PMSM can be once again confirmed. Calculated results using MTPA theory are identical to the ones obtained in previously performed analysis. Hence generalised form for optimal h^{th} order current harmonic injection ratio calculation can be defined as:

$$k_{1h} = \frac{h \cdot \lambda_{mh}}{\lambda_{m1}} = \frac{e_h}{e_1} = \frac{k_{wfh} \cdot B_{roth}}{k_{wf1} \cdot B_{rot1}} \tag{6.36}$$

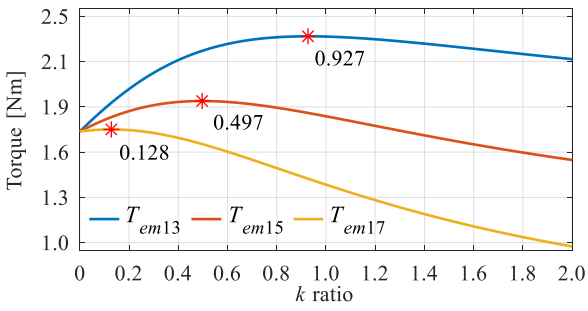

Figure 6.6 – Torque versus injection ratio with a single harmonic injection (added indices in torque symbols specify which harmonics are injected).

6.4 Electromagnetic Torque Analysis

Results of the previous section are summarised in Table 6.3. As expected, electromagnetic torque improvement with the third harmonic under the optimal current injection ratio is ≈36% (increase from 1.74 Nm to 2.38 Nm). By applying the additional fifth harmonic control, maximal reachable torque is now 2.52 Nm. This is 44.83% improvement with the respect to the torque produced by the fundamental harmonic only, i.e. additional 6.33% improvement is achieved with the respect to the third harmonic current injection. Finally, after the seventh harmonic is employed for the torque production as well, maximal reachable torque value becomes 2.53 Nm. Presented in percentages, final reachable torque produced after applying all the possible harmonics (and respecting $h < n$) is 45.40% higher than the torque produced with the fundamental only. If compared with the improvement reachable with combined third and fifth harmonics, the new value is only around 0.4% higher. For this reason, improvement of this harmonic is not implemented, and resonant controller is used for induced current elimination together with the eleventh harmonic which maps into the same subspace. Note that the similar results were reported in section 4.4, where FEM analysis was performed.

Table 6.3 – Electromagnetic torque improvement analysis – results of the optimisation procedure.

Harmonics	**Torque [Nm]**	**Imp. from only 1st**	**Imp. from 1st and 3rd**	**Imp. from 1st, 3rd and 5th**
1st	1.74	///////	///////	///////
1st + 3rd	2.38	36.21%	///////	///////
1st, 3rd + 5th	2.52	44.83%	6.33%	///////
1st, 3rd, 5th + 7th	2.53	45.40%	6.75%	0.4%

6.5 PMSM Model Testing and Experimental Verification

Simulation results acquired in *Matlab*/*Simulink* environment and afterwards verified using experimental prototype are summarised next. The same testing scenario (Method II), presented originally in chapter 5, is used. The electromagnetic torque of the machine is kept constant (≈2 Nm) during the entire sequence. Recorded sequence has three regions and it is in total 6 seconds long. In the first 2 seconds (further on the 1st region) only fundamental current harmonic component is used for the electromagnetic torque production ($k_{13} = 0$, $k_{15} = 0$). In the following 2 seconds (the 1st + 3rd region), injection ratio k_{13} is changed to its optimal value, i.e. $k_{13} = 0.93$ ($k_{15} = 0$). Finally, in the last 2 seconds (the 1st, 3rd + 5th region), in addition to the third, the fifth harmonic current injection is also employed for the torque boost. Injection ratio k_{15} is in this case set to its optimal value $k_{15} = 0.5$. For the duration of the first and second regions, the fifth harmonic current is kept at 0 using PI regulators, rather than VPI controller as before. The sequence was chosen so that a comparison with the results from chapter 5 can easily be performed. In addition to the torque, the speed is also kept constant for the entire duration of the sequence (Fig. 6.7).

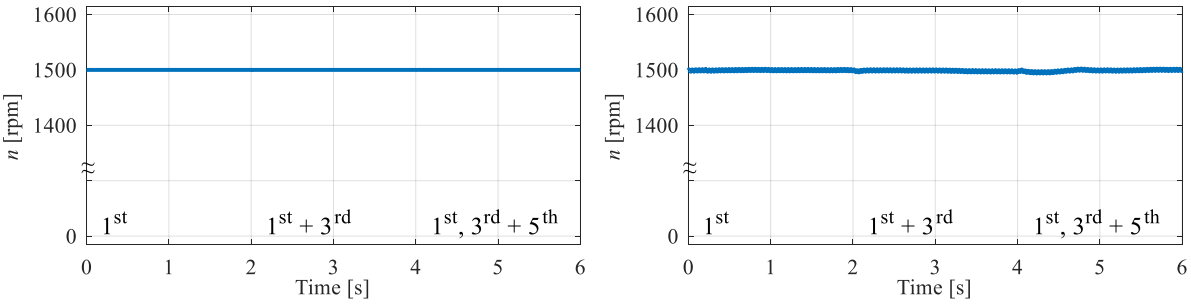

Figure 6.7 – Mechanical speed results recorded in: (a) simulation, and (b) experiment.

Phase current simulation and experimental results can be seen in Figs. 6.8 and 6.9, respectively. As in the previous chapter, only the first phase in each phase set is shown. The entire sequence is shown first (upper plots), followed by the enlarged portions around transition points (bottom plots). These portions are 0.2 s long (1.9 - 2.1 s for the 1^{st} and the $1^{st} + 3^{rd}$, i.e. 3.9 – 4.1 s for the $1^{st} + 3^{rd}$ and 1^{st}, $3^{rd} + 5^{th}$ transition). As expected, currents are following the shape of the back-EMF. This correspondence is more visible each time an additional current harmonic is injected. Note that stator phase windings are not entirely identical (as assumed in the simulation model), hence small deviations between simulation and experiment exist. Although phase current peak value increases when the fifth harmonic is injected, phase current RMS value is on the contrary decreased. This, in addition to the figures, can be concluded based on the results presented in Tables 6.4a and 6.4b, where a detailed analysis of the phase current RMS in different regions is performed. During RMS analysis, multiple periods in each region were used, and the presented results are obtained as an average.

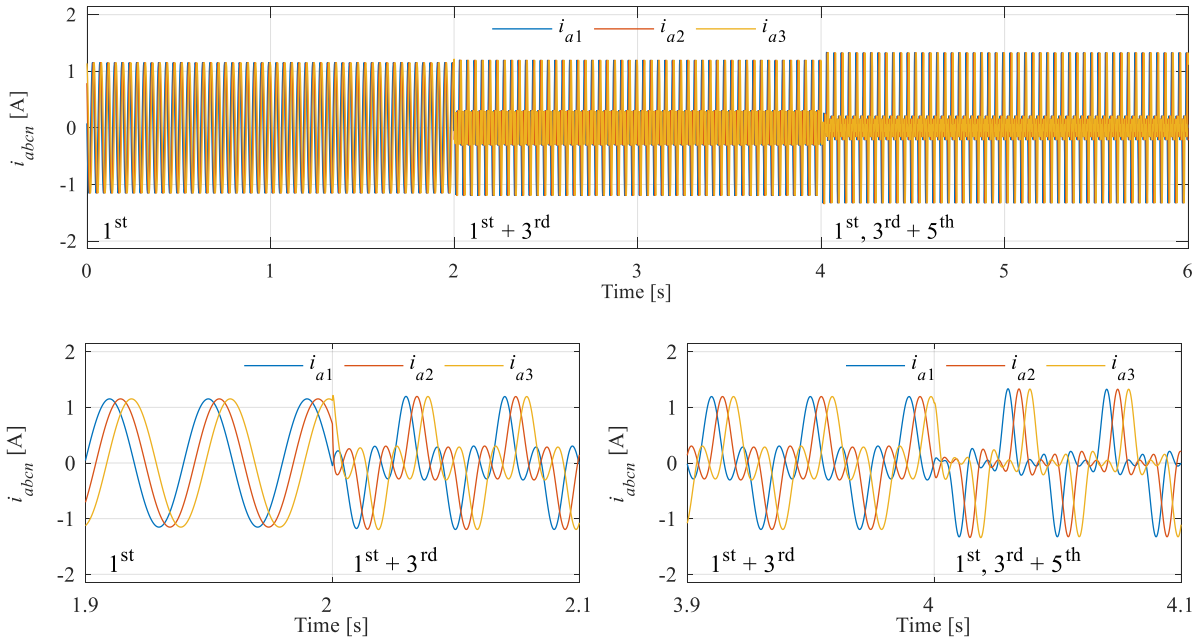

Figure 6.8 – Phase current (phases *a*1, *a*2, *a*3) results recorded using simulation model: full sequence (top) and transient point periods (bottom).

By comparing the Tables 6.4a and 6.4b, it is easy to conclude that the phase current RMS values are almost the same in all three analysed regions. If in addition to the fundamental, the third harmonic current is injected, phase current RMS values are 0.597 A and 0.599 A in simulation and experiment, respectively. As concluded in chapter 5, these values are lower than the ones calculated in the 1st region (here 0.814 A and 0.817 A), meaning less copper losses and therefore lower input power. If difference in RMS current is calculated as percentage, as expected, 1st region value is ≈36% higher. In the 1st, 3rd + 5th region, average phase current RMS values are 0.562 A and 0.565 A. As visible from the tables, 1st region RMS values are approximately 45% higher than values in final region. Furthermore, 1st + 3rd region current RMS value is ≈6% higher than the value recorded in 1st, 3rd + 5th region. Both simulation and experimental results are in good agreement with the electromagnetic torque improvement results calculated mathematically and summarised in Tables 6.2 and 6.3.

Table 6.4a – Simulation phase current RMS.

Region / Time [s]	**RMS value [A]**		
1st / 0 - 2	0.8143	≈36.4%	≈44.9%
1st + 3rd / 2 - 4	0.5968	≈6.2%	
1st, 3rd + 5th / 4 - 6	0.5618		

Table 6.4b – Experimental phase current RMS.

Region / Time [s]	**RMS value [A]**		
1st / 0 - 2	0.8167	≈36.2%	≈44.5%
1st + 3rd / 2 - 4	0.5995	≈6.1%	
1st, 3rd + 5th / 4 - 6	0.5650		

Oscilloscope screenshots of phase current transients are shown in Fig. 6.10. Only transition from the 1st + 3rd to the 1st, 3rd + 5th region (Fig. 6.10a) is shown, because 1st to 1st + 3rd case was already given in chapter 5. Fig. 6.10b shows the transient between the 1st and the 1st, 3rd + 5th regions. 2.90 kHz noise filter was applied while taking the screenshots.

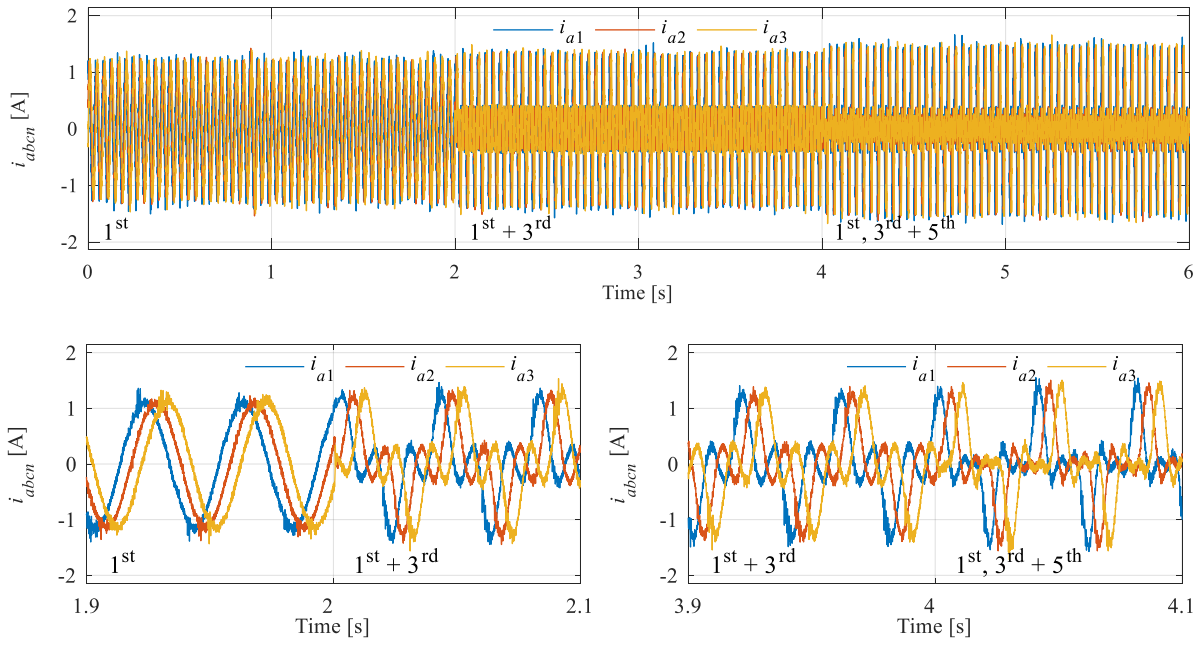

Figure 6.9 – Phase current (phases *a*1, *a*2, *a*3) results recorded using experimental setup: full sequence (top) and portions of the waveforms around transitions instants (bottom).

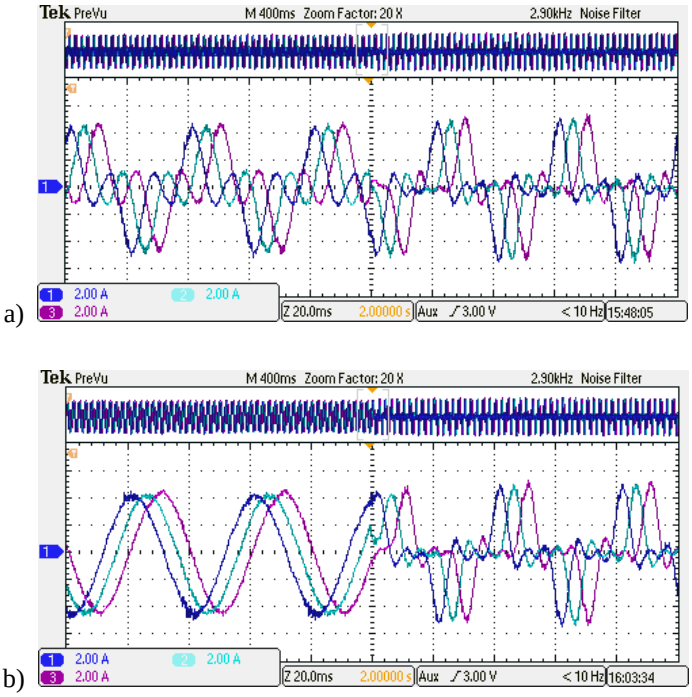

Figure 6.10 – Oscilloscope screenshots of experimentally recorded phase current (1 A on oscilloscope = 1/4 A of the real current – 4 wire turns were used for higher precision) transients for: (a) 1st + 3rd to 1st, 3rd + 5th, and (b) 1st to 1st, 3rd + 5th testing scenarios.

Filtered phase voltage waveforms (2.9 kHz filter) can be seen in Figs. 6.11 and 6.12. A good agreement between the results obtained in simulation (Fig. 6.11) and the ones from experiments (Fig. 6.12) can be noted. Non-sinusoidal shape is in both cases directly related to non-sinusoidal back-EMF and additional voltages from controllers added to zero or to control (as applicable) induced current components. In addition to the filtered traces, unfiltered case and harmonic spectrum analysis performed on experimentally recorded voltages (phase *a*1) for different regions can also be seen in Fig. 6.12.

As shown in Fig. 6.13, input power of the machine is decreased at two instants in time, i.e. each time after a current harmonic is injected. This can be directly related to the reduced phase current RMS value, i.e. lower winding losses in the machine after harmonic current injection. Copper losses recorded with the injected third and fifth harmonic currents are ≈100 W lower than in the case when only the fundamental harmonic component is used. This once again confirms the electromagnetic torque improvement analysis because ratio between these losses is $\sqrt{P_{Cu1} / P_{Cu135}} = I_{RMS1}/I_{RMS135} = 1.451$ (≈45%). As noted, mechanical and iron losses are not considered in the simulation model (consequently $P_{in} = P_{out} + P_{Cu}$). Existence of these losses is directly visible from recorded input power values, which are in experimental case slightly higher (Fig. 6.13b).

Current mapping after VSD can be seen in Fig. 6.14. In the first interval (0 - 2 s), only fundamental is used for torque production; hence only α-β currents exist. Other harmonic components are controlled to zero. In the second region (2 - 4 s), the third harmonic current injection is also employed for torque

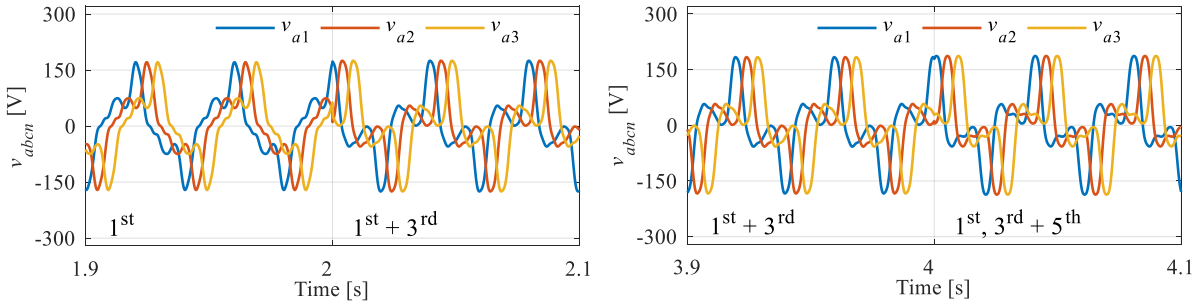

Figure 6.11 – Phase voltage (phases *a*1, *a*2, *a*3) results obtained using the simulation model.

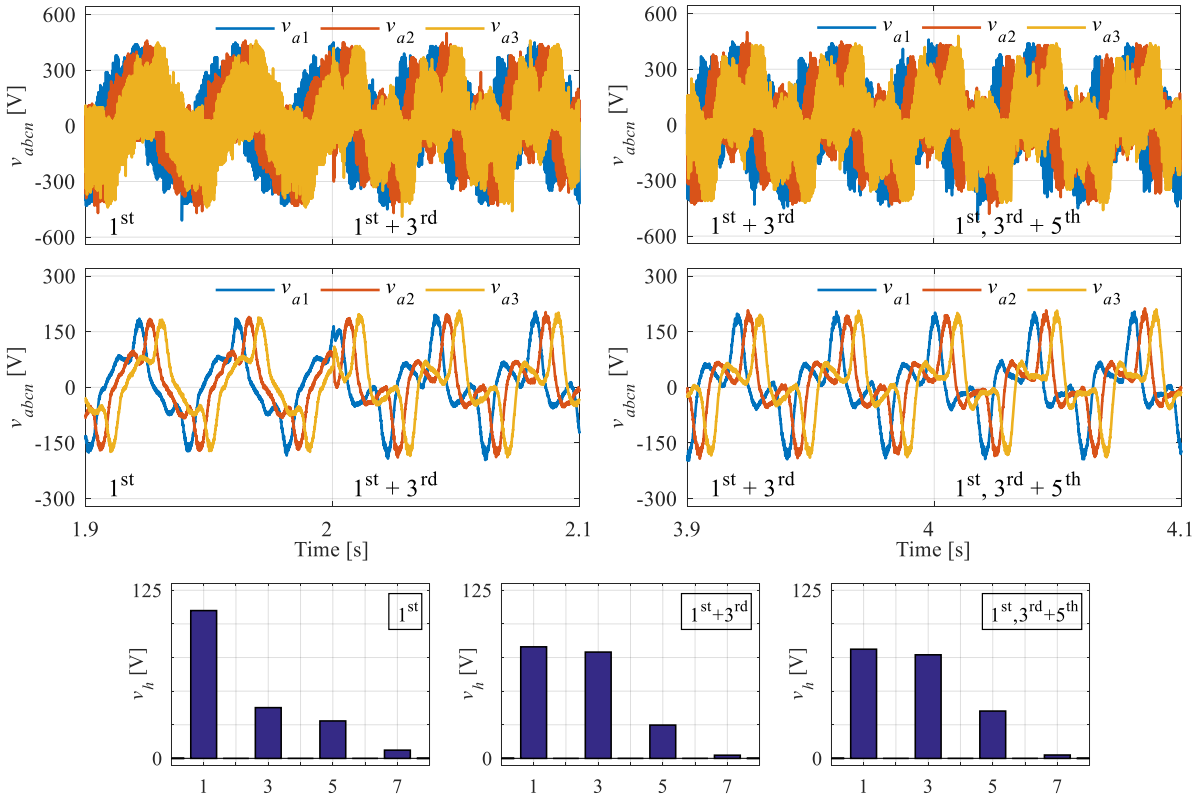

Figure 6.12 – Phase voltage (phases *a*1, *a*2, *a*3) results recorded using experimental setup (top - not filtered; bottom - filtered with 2.9 kHz filter) and corresponding FFT harmonic spectra (phase *a*1).

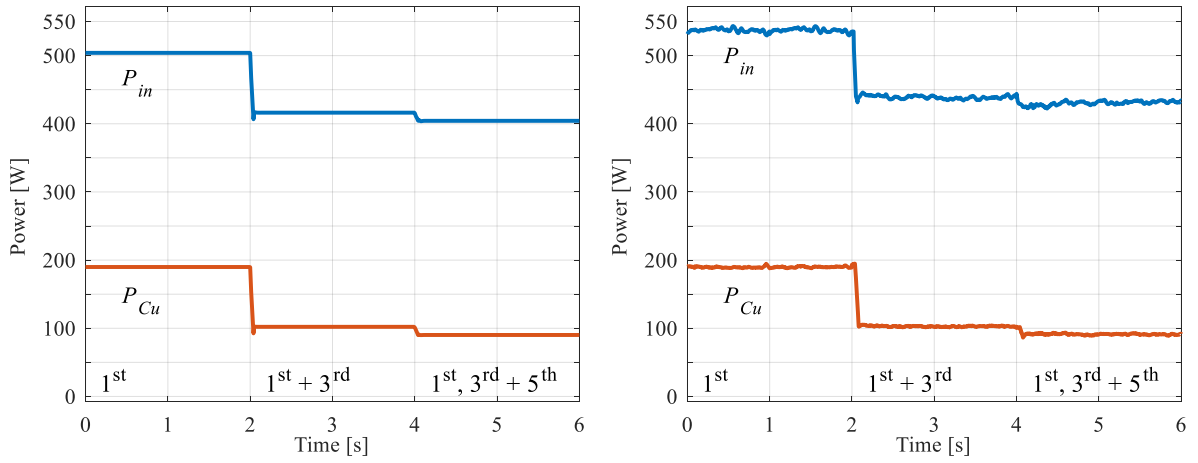

a) b)

Figure 6.13 – Power analysis based on results recorded in: (a) simulation, and (b) experiment.

production, which results in additional *x-y* current components in the x_3y_3 subspace (where the third harmonic maps). As x_3y_3 currents increase, peak values of α-β currents decreases. A similar response can be seen in the last region (4 - 6 s) where the fifth harmonic injection is performed. As new harmonic is added, already employed components decrease their peak values. If experimental results (Fig. 6.14b) are compared with the simulations (Fig. 6.14a), good agreement between results can be observed.

Flux- and torque-producing currents are related to currents in Fig. 6.14 through rotational transformations and are shown in Fig. 6.15. It can be seen that, by adding additional harmonics into the control, fundamental torque-producing current drops, while the third and the fifth harmonic components change their value in accordance with the optimal injection ratios k_{13} and k_{15}. Mean values of each torque producing current in different regions are summarised in Table 6.5. As already noted, the fifth harmonic rotates in the opposite direction, hence torque-producing current has negative values. Once again, very good agreement between simulation and experimental results can be seen. During the entire sequence, flux-producing currents (i_{d1}, i_{d3}, i_{d5}) are equal to zero as set by MTPA based current control strategy.

Table 6.5 – Torque-producing current components analysis.

Reg. / i_{qh} **[A]**		**Simulation**						**Experiment**					
		1st		**1st + 3rd**		**1st, 3rd + 5th**		**1st**		**1st + 3rd**		**1st, 3rd + 5th**	
i_{q1}	$I_{RMS}=\sqrt{\frac{\sum_1^3 i_{qh}^2}{2}}$	1.1519	0.8145	0.6186	0.5973	0.5458	0.5613	1.1549	0.8167	0.6207	0.5993	0.5484	0.5630
i_{q3}		0		0.5753		0.5076		0		0.5772		0.5086	
i_{q5}		0		0		-0.2729		0		0		-0.2743	

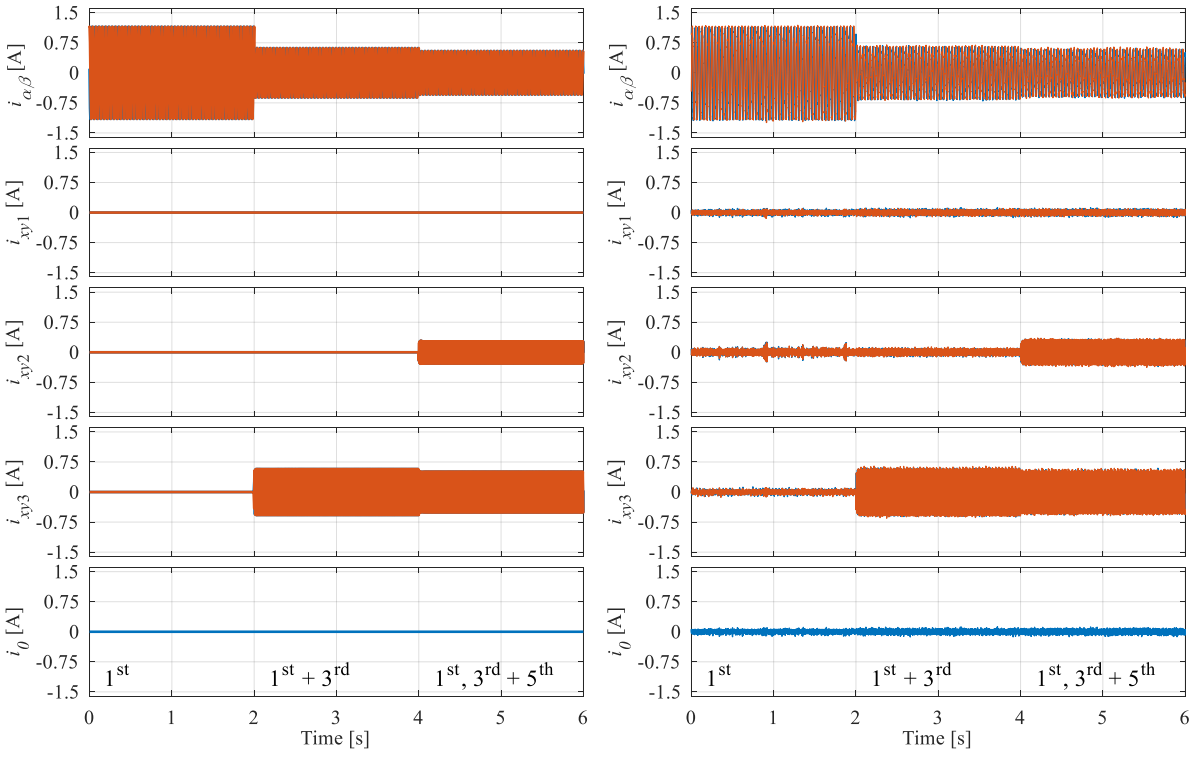

a) b)

Figure 6.14 – Current mapping after system decoupling for: (a) simulation, and (b) experiment.

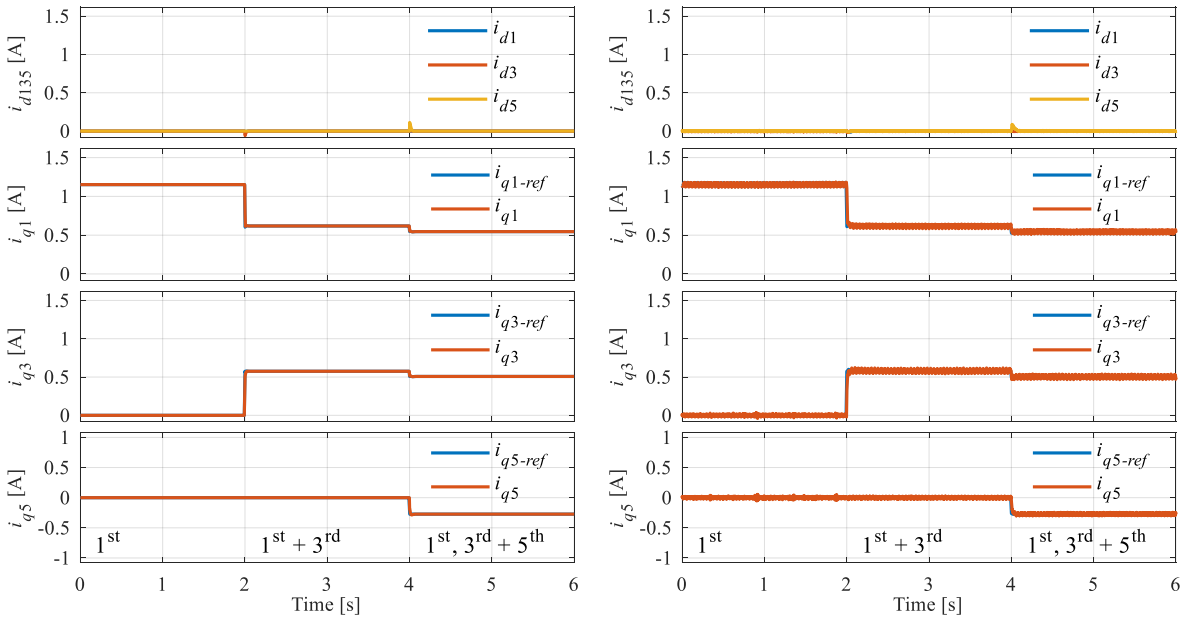

a) b)

Figure 6.15 – Flux- and torque-producing current results for: (a) simulation, and (b) experiment.

6.6 Summary

In this chapter, a general approach for injection of any number of desired harmonic currents (single or multiple) in a nine-phase surface PMSM was presented. This includes synchronous reference frame machine modelling equations and corresponding PI current control. Optimal harmonic current injection ratios were also investigated using different approaches. Calculated results were additionally compared with the ones previously recorded in finite element method software tool, and very good agreement was noted. Furthermore, it has been concluded that optimal ratio calculation of the single harmonic does not depend on the controlled harmonics in other subspaces. Hence, instead of complex multi-dimensional function solving (complexity of which increases by one dimension with each additional harmonic), optimal injection ratio between fundamental and any other harmonic can be calculated as a simple two-dimensional T_{em1h} / k_{1h} function. Although easier to perform, such optimisation does not contain information about the maximal reachable torque in multi-harmonic injection case, so that additional calculations are needed.

The seventh harmonic component was not included in the final control testing. This decision was made based on electromagnetic torque analysis, i.e. the fact that the seventh harmonic has negligible contribution to the final electromagnetic torque production (< 1% if compared with the contribution achieved using combination of the third and the fifth harmonics). Resonant controllers were therefore implemented to eliminate both seventh and eleventh (losses producing) harmonics which map into the same subspace.

Related to the phase current analysis, it has been shown that with each additionally injected harmonic, current RMS value decreases. This results in lower copper losses, so that the machine can produce more torque for the same RMS current. It should be noted however that, with each new injected harmonic, slight increase in phase current peak value occurs. Although this was not of interest in this chapter, it will be important in chapter 8 where machine's current and voltage limits (i.e. flux-weakening operation) are studied.

Finally, theoretical considerations were tested on the experimental setup using nine-phase surface PMSM prototype. As expected, lowest RMS current value was achieved in 1^{st}, 3^{rd} +5^{th} region, meaning that the value of the torque can be therefore increased for approximately 45% when compared with torque produced in 1^{st} region (thus confirming the validity of the derived advanced FOC algorithm). As already mentioned in previous chapters, recorded improvement is strictly related to the investigated machine configuration (back-EMF harmonic magnitudes and angles). By applying the control principles from this chapter in combination with the different machine configurations, a different torque improvement values might be obtained.

Chapter Seven

EMF-BASED SENSORLESS POSITION ESTIMATION

7.1 Introduction

It has been shown in the previous chapters that existing back-EMF harmonic spectrum can be used to significantly improve torque capability of the studied PMSM prototype. In this chapter, the same harmonic spectrum is again considered, this time to investigate control of the machine after a position sensor fault is detected. To measure the rotor's position and compute the speed, typically an encoder or resolver is mounted on rotor's shaft. As already explained in chapter 2, the position sensor incurs mounting and maintenance cost and reduces the reliability of the whole system. It is for these reasons that, in some applications, it is avoided and so called sensorless strategies are implemented. Even if the position sensor is not completely removed from the drive system, sensorless methods are sometimes still used as a backup to provide rotor position/speed information in case of a position sensor failure. This is of a major interest for safety critical applications such as electrical aircraft and electrical transportation applications in general. EMF based sensorless techniques have been implemented in three-phase drives for position estimation in the past. Here, the harmonics contained within the EMF are employed for the same purpose as well - hence extending previously derived advanced control algorithm with built-in position sensor fault-tolerant capability.

After introduction, machine model in α-β reference frame is given (section 7.2). As it will be shown, if harmonic current elimination is performed in a specific *x*-*y* subspace, angular position and speed information can be precisely extracted out of the remaining h^{th} harmonic order back-EMF. This is possible because, after VSD, the harmonics are uniquely mapped each in separate subspaces. To estimate angular position and speed, two approaches can be used: trigonometrical (which calculates required variables using the inverse of the trigonometrical sine, cosine and tangent functions), or phase-locked-loop (which calculates the same variables, but avoids computationally intensive trigonometrical inverse and derivative operation). Therefore, the phase-locked-loop (PLL) approach is investigated in subsection 7.2.1. Although work in [Stiscia et al (2019)] briefly showed how to employ the third EMF harmonic for this purpose, this harmonic was not used for the best possible outcome (torque boost). Consequently, a different control algorithm is here proposed, which combines control in two auxiliary subspaces with the control of the first plane. The third harmonic is, in combination with the fifth, used for the torque boost prior to the fault. Once a position sensor fault is detected, the fifth EMF harmonic is switched to enable position estimation for position-sensorless control, and is thus no longer boosting the torque. Hence, previously reported maximal torque improvement is preserved until a position sensor fault is detected; afterwards the machine continues to operate in position-sensorless mode while still partially enhancing the torque. Details of the developed control algorithm are provided in section 7.3 and its performance is verified using an experimental setup. Corresponding results are given in section 7.4, and are published in [Slunjski et al (2021)].

7.2 *α-β* Domain Machine Model and Phase-Locked-Loop Method

As mentioned in introduction, back-EMF based position/speed estimation is studied in the stationary *α-β* domain, after application of (3.20). Machine model (which takes into account harmonic components of the order 1 to 7) after vector space decomposition transformation can be written in the complex form as:

$$\begin{cases} \underline{v}_{\alpha\beta} = R_s \cdot \underline{i}_{\alpha\beta} + L_1 \cdot \dfrac{d\underline{i}_{\alpha\beta}}{dt} + j\omega\lambda_{m1} \cdot e^{-j(\theta_1)} \\ \underline{v}_{xy1} = R_s \cdot \underline{i}_{xy1} + L_7 \cdot \dfrac{d\underline{i}_{xy1}}{dt} - j7\omega\lambda_{m7} \cdot e^{-j(\theta_7)} \\ \underline{v}_{xy2} = R_s \cdot \underline{i}_{xy2} + L_5 \cdot \dfrac{d\underline{i}_{xy2}}{dt} - j5\omega\lambda_{m5} \cdot e^{-j(\theta_5)} \\ \underline{v}_{xy3} = R_s \cdot \underline{i}_{xy3} + L_3 \cdot \dfrac{d\underline{i}_{xy3}}{dt} + j3\omega\lambda_{m3} \cdot e^{-j(\theta_3)} \end{cases} \tag{7.1}$$

where

$$\begin{cases} \alpha\beta: \quad L_{\alpha\beta} = L_{ls} + L_{m1} \\ xy_1: \quad L_1 = L_{ls} + L_{m7} \\ xy_2: \quad L_2 = L_{ls} + L_{m5} \\ xy_3: \quad L_3 = L_{ls} + L_{m3} \end{cases} \tag{7.2}$$

In (7.1) and (7.2), $\underline{v}_{xy,i}$, $\underline{i}_{xy,i,}$ L_{ls}, L_{mh}, $\omega = \omega_{el}$ and θ_{el} denote voltages and currents in the i^{th} subspace (i = 1, 2, 3), stator leakage and mutual inductances due to the h^{th} order spatial harmonic, and electrical speed/angle, respectively. As before, $\theta_h = h \cdot \theta_{el} + \theta_{phsh}$, where θ_{phsh} is harmonic angular shift. To distinguish space vectors from other variables, underlining is used.

Regardless of the operating condition (healthy or post-fault), the third back-EMF harmonic is employed for torque enhancement because of its high magnitude. If the fifth (or any other low-order odd) back-EMF harmonic component is not controlled for the torque enhancement purpose, it will induce loss-producing stator current of the same order, which must be eliminated using VPI controllers. These controllers, as shown in chapter 5, keep the induced fifth harmonic stator current at zero. This leads to the conclusion that the voltage reference in the 5th harmonic subspace is actually equal to the back-EMF, that is:

$$\begin{aligned} &\underline{i}_{xy2} \approx 0; \;\; \theta_{phs5} \approx 0 \\ &\quad \rightarrow \underline{v}_{xy2} = \underline{\hat{e}}_{xy2} = -j5\omega \cdot \lambda_{m5} \cdot e^{-j5\theta_{el}} \end{aligned} \tag{7.3}$$

In (7.3) and further on, sign ^ over a symbol stands for an estimated value. It follows from the given equation that the argument of the back-EMF contains rotor position information. Hence, rotor position can be obtained after reconstruction of the phase voltage references generated at the output of the control system, using:

$$5\hat{\theta}_{el} = \arctan\left(\frac{\sin(5\cdot\hat{\theta}_{el})}{\cos(5\cdot\hat{\theta}_{el})}\right) = \arctan\left(\frac{-\hat{e}_{x5}}{-\hat{e}_{y5}}\right) \tag{7.4}$$

In (7.4), sine and cosine are calculated as:

$$\begin{aligned}\sin(5\cdot\hat{\theta}_{el}) &= \frac{-\hat{e}_{x5}}{\sqrt{\hat{e}_{x5}^2+\hat{e}_{y5}^2}}\\ \cos(5\cdot\hat{\theta}_{el}) &= \frac{-\hat{e}_{y5}}{\sqrt{\hat{e}_{x5}^2+\hat{e}_{y5}^2}}\end{aligned} \tag{7.5}$$

7.2.1 PLL Position Estimation using Fifth EMF Harmonic

Since finding the inverse of trigonometrical functions is computationally intensive, rotor position and speed information are in this work obtained using a phase-locked-loop (PLL) control. The PLL is a computational method which avoids derivative calculation. As shown in Fig. 7.1, it receives at the input voltage reference $\underline{v}_{xy2\text{-}ref}$, reconstructed from the FOC algorithm, while on its output it provides angle information θ_{PLL}, from which rotor position can be extracted. By applying (7.5) to the input voltages, corresponding sine and cosine values are calculated. Using these, PLL error ε_θ can be obtained. Any error (assuming that it is small), can be approximated with the following equation [Bolognani et al 2014]:

$$\begin{aligned}\varepsilon_\theta &\approx \sin(5\hat{\theta}_{el}-\theta_{PLL})\\ &\approx \sin(5\hat{\theta}_{el})\cdot\cos(\theta_{PLL})-\cos(5\hat{\theta}_{el})\cdot\sin(\theta_{PLL})\end{aligned} \tag{7.6}$$

The error is then forwarded to the input of the PLL PI controller, which gives at the output estimated speed ω_{PLL}. Since integral part $\omega_{PLL\text{-}I}$ is already filtered, this speed information can be used as a feedback of the speed loop regulation in sensorless control. To obtain feedback angle θ_{PLL}, an integrator is placed in cascade with the PI controller. Because of the harmonic gain in feedback loop (Fig. 7.1, red box), θ_{PLL} angle actually equals estimated rotor position (i.e. electrical angle $\hat{\theta}_{el}$).

To ensure the best possible harmonic PLL response, tuning of the parameters used in the PI controller must be performed. To briefly explain this, one can start from the closed-loop transfer function, which can be written as:

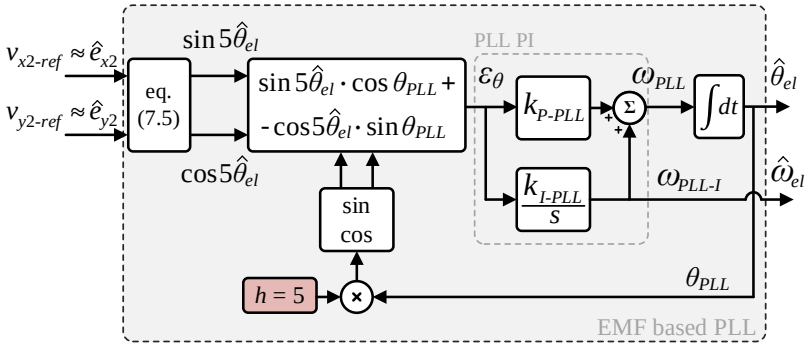

Figure 7.1 – Angular position and speed estimation using back-EMF based phase-locked-loop method.

$$G(s) = \frac{k_{P-PLL} \cdot s + k_{I-PLL}}{s^2 + 5 \cdot k_{P-PLL} \cdot s + 5 \cdot k_{I-PLL}} \tag{7.7}$$

where $k_{P\text{-}PLL}$ and $k_{I\text{-}PLL}$ are corresponding proportional and integral gains. These parameters can be tuned using [Bolognani et al 2014]:

$$\begin{aligned} k_{P-PLL} &= \frac{1}{5} \cdot \frac{\omega_{cr} \cdot \tan(\theta_{mar})}{\sqrt{1 + \tan(\theta_{mar})^2}} \\ k_{I-PLL} &= \frac{1}{5} \cdot \frac{\omega_{cr}^2}{\sqrt{1 + \tan(\theta_{mar})^2}} \end{aligned} \tag{7.8}$$

In (7.8), ω_{cr} is the angular crossover frequency and θ_{mar} is the phase margin. In order to ensure the control loop stability, the conditions

$$\begin{aligned} \frac{k_{I-PLL}}{k_{P-PLL}} &< \sqrt{2} \cdot 5 \cdot k_{P-PLL} \\ \theta_{mar} &> \frac{\pi}{4} \end{aligned} \tag{7.9}$$

must also be taken into account.

For the studied PM synchronous machine, phase margin and the angular crossover frequency are set to $\theta_{mar} = 60°$ and $\omega_{cr} = 188$ rad/s. The PLL proportional and integral gains were then calculated as $k_{P\text{-}PLL} = 32.6$ and $k_{I\text{-}PLL} = 3535$. Use of these parameters in the PLL controller will ensure sufficient margin of the error and robustness of the controlled system, i.e. significant improvement in estimated angular position/electrical speed quality (when compared with trigonometrical approach defined with (7.4)) can be achieved. It should be noted however, that in the ideal conditions (and by keeping the error ε_θ sufficiently close to zero), both trigonometrical and phase-locked-loop approaches should give approximately equal responses.

7.3 Current Harmonic Injection Control with Built-in Fault Tolerance

The generalised field-oriented control algorithm, originally derived in chapter 6, is further modified in the part associated with the 5th harmonic. The modified control scheme is illustrated in Fig. 7.2. The figure shows a particular case in which, in addition to the fundamental, the third and the fifth current harmonics are considered. Nevertheless, the same (back-EMF based sensorless) principles can be applied to the other multiphase PMSMs as long as at least one additional harmonic exists in the back-EMF spectrum. As detailed further on, depending on the scenario, switches are changed from position 1 (harmonic injection) to 2 (sensorless control).

There are two possible operating scenarios: in the first one a selected (x_2y_2) plane is not used for the torque enhancement at all and the position estimation is constantly performed, while in the second case the plane is used for torque enhancement as long as the position sensor is in healthy state. In both cases the sole purpose of the selected plane/harmonic is to enable rotor position estimation once when the position sensor failure is detected. The difference in the two scenarios stems from the fact that the back-EMF of any particular plane cannot be sensed and only *x-y* voltages, applied as references, are known. In the former case there is no current flow in the given plane prior to sensor fault and the back-EMF equals to the stator *x-y* voltages (regarded as equal to the reference values because dead time and on-state voltage drop are neglected). In the latter case, the applied *x-y* voltages differ from the back-EMF because of the harmonic current flow prior to the sensor failure. Both defined scenarios have their advantages and drawbacks, as discussed further on.

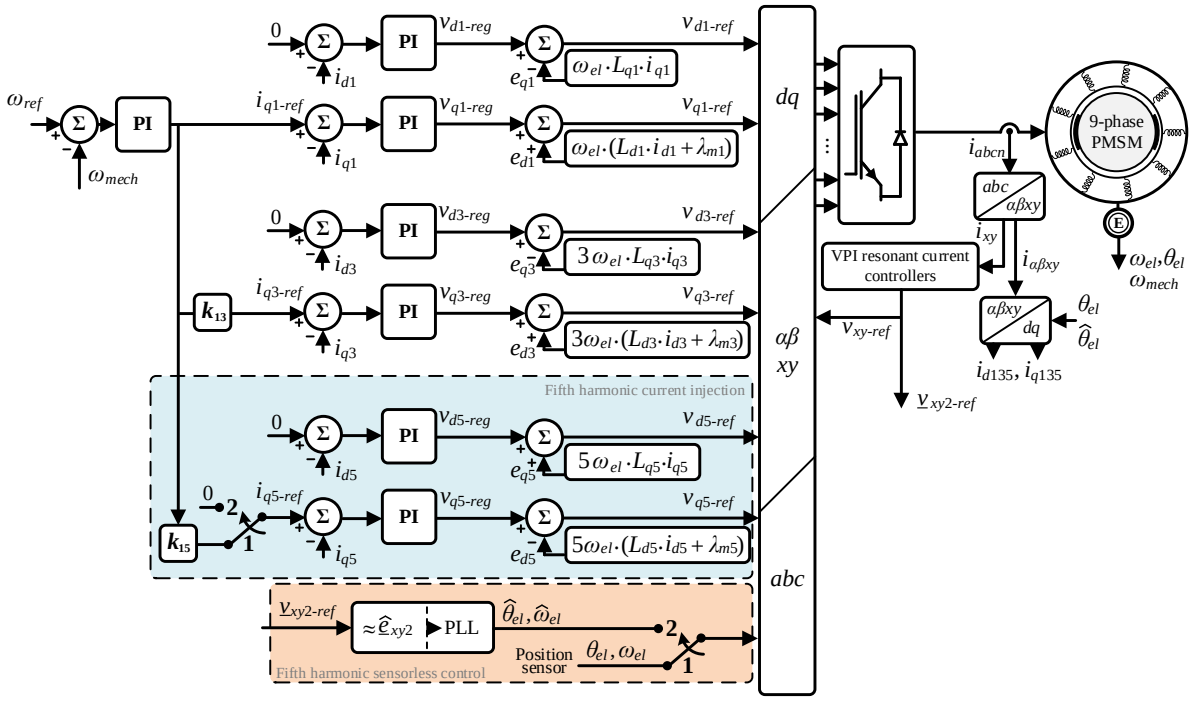

Figure 7.2 – Field-oriented control algorithm modified for harmonic current injection and low-order harmonic elimination with built-in fault-tolerant capability.

7.4 Experimental Verification

In what follows, each of the two previously defined scenarios is tested using the same experimental setup as in earlier chapters. The performance of the control algorithm is evaluated during steady state and speed transient. First, the scenario where the third harmonic is continuously used for harmonic injection (i.e. torque enhancement), while the fifth harmonic is continuously used for position estimation is analysed (Scenario 1). In this case the switches in Fig. 7.2 are constantly set to the position 2. The results are shown in Figs. 7.3 - 7.10. In the second scenario (Figs. 7.11 - 7.18; Scenario II), the third and the fifth harmonic are initially used for torque enhancement, while after a sensor fault occurs, the fifth harmonic current injection control is switched from position 1 to position 2 and position-sensorless control is performed. Consequently, the fifth harmonic current reference is stepped from its previous value to zero. It should be noted that the fault detection method is not considered in this work. Also, although not used in control, signals from position sensor are after fault instant also recorded, mainly for control validation and comparison purpose.

Results recorded in steady state for Scenario I are shown in Figs. 7.3 - 7.5. Speed at which steady state testing was performed is n_{ref} = 1000 rpm. The position sensor fault occurs at t = 0.2 s. As is visible in Fig. 7.3a, almost negligible speed oscillation occurs at the fault instant. Similar can be noted for Fig. 7.3b as well, where measured electromagnetic torque is given. The measured torque (from the torque meter) is filtered using a 2.90 kHz noise filter. The average value of the measured torque comes out as ≈0.86 Nm.

In steady state at 1000 rpm, the error (depicted in the middle plot of Fig. 7.4) between measured position sensor angle and estimated angle before sensor fault is equal to 0.1237 rad i.e. 7.09°, while after sensor fault occurs it is 0.1009 rad i.e. 5.78°. Both before and after sensor failure, mentioned angles are constant. Please note that error between real position sensor angle and estimated angle in a real scenario (where the fault does happen, rather than being emulated), of course, cannot be measured.

Fig. 7.5 shows measured phase currents (phases $a1$, $a2$, $a3$) in combination with the electromagnetic torque. Since the fundamental and the third harmonic currents are used for torque production, typical phase current shape (analysed in chapter 5) can be noted.

The transient performance of the drive can be seen in Figs. 7.6 - 7.10. Speed and angle traces recorded in healthy operation are given first (Fig. 7.6a and b, respectively) followed by the torque and phase currents in Fig. 7.7. Typical of EMF sensorless methods a poor speed estimation accuracy is visible at low speeds. Therefore, in order to avoid unwanted behaviour, the fault mitigation algorithm cannot be applied before the mechanical speed reaches ≈280 rpm (hence, a simple speed comparison is also implemented). As a consequence, in a parallel work strand to this thesis, a sensorless start-up technique for the prototype PMSM, termed *I*/*f* technique, was developed and implemented in

[Stiscia et al (2019)], and is not further discussed here. Corresponding phase currents and electromagnetic torque can be seen in Fig. 7.7. It should be noted that the speed reference is slowly ramped and so the torque is not hitting the limit.

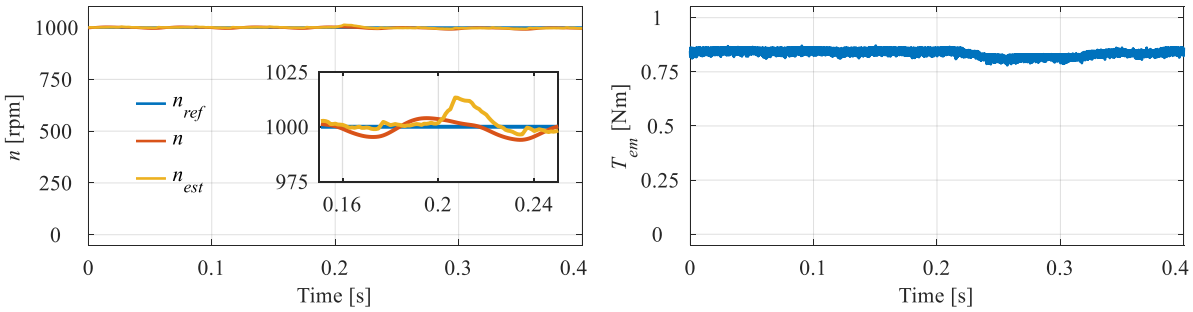

a) b)

Figure 7.3 – Experimentally recorded speed (a), and electromechanical torque (b) – Scenario I, steady state.

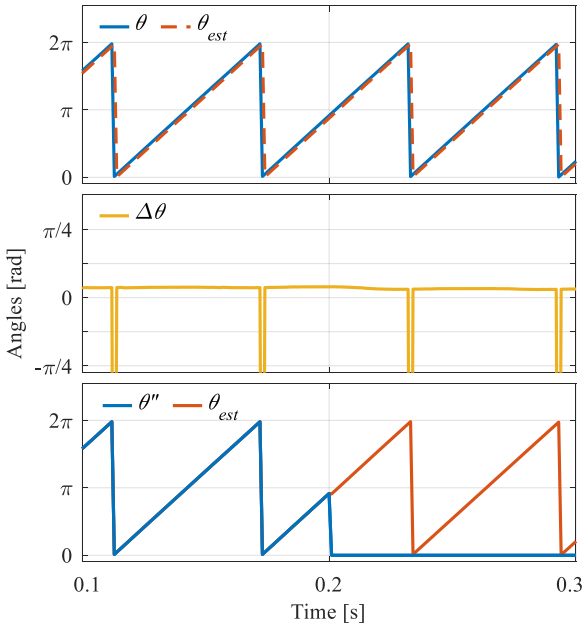

Figure 7.4 – Position angle analysis: actual θ and estimated θ_{est} angles and position estimation error $\Delta\theta$ (zoomed extracts around the instant of fault; θ'' stands for encoder position signal θ as seen by the control system) – Scenario I, steady state.

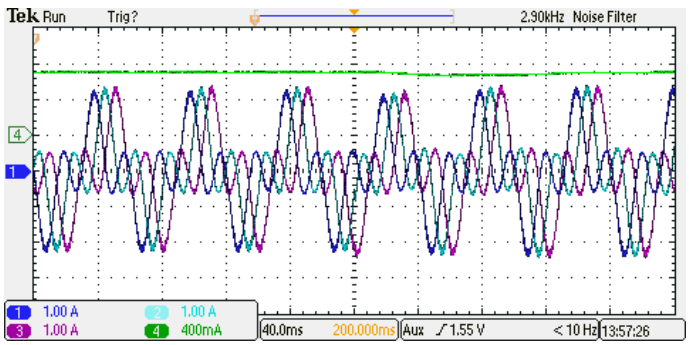

Figure 7.5 – Oscilloscope screenshot of phase currents (phases $a1$, $a2$, $a3$; 1 A on oscilloscope = 0.25 A of real current) and torque (400mA on oscilloscope = 0.5 Nm of real torque) – Scenario I, steady state.

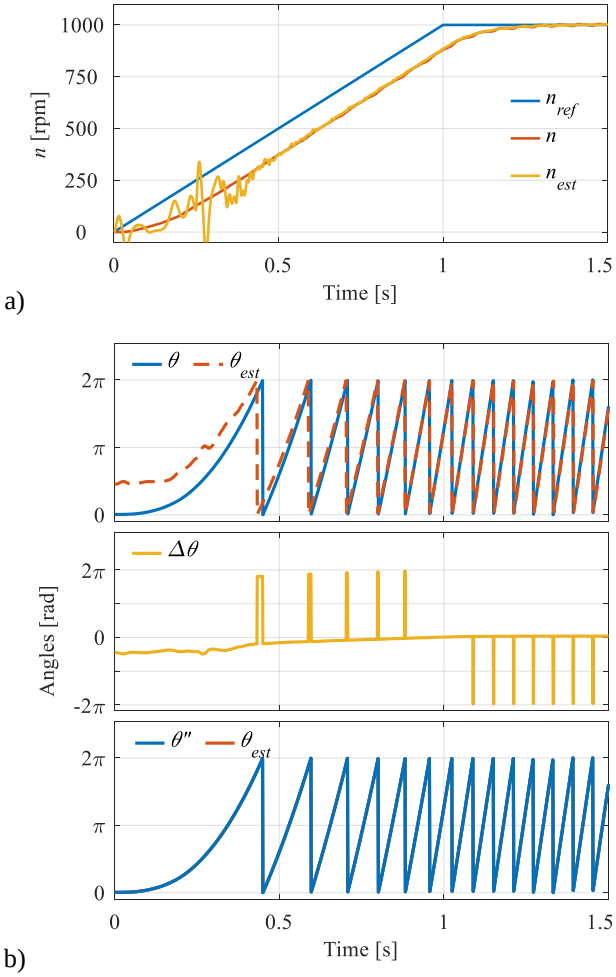

Figure 7.6 – Experimentally recorded speed (a), and position angle analysis (b) – Scenario I, speed transient, no fault.

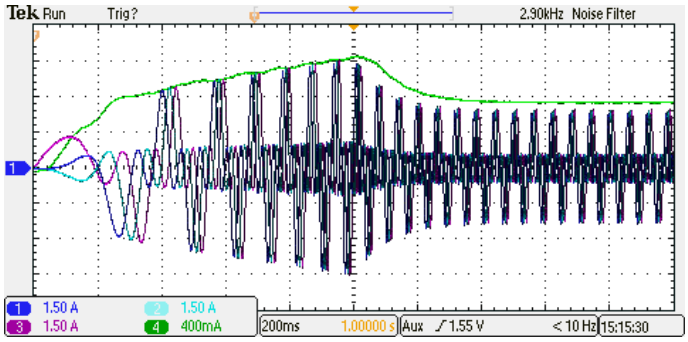

Figure 7.7 – Oscilloscope screenshot of phase currents (phases *a*1, *a*2, *a*3; 1 A on oscilloscope equals to 0.25 A of real current) and torque (400mA on oscilloscope = 0.5 Nm of real torque) – Scenario I, speed transient, no fault.

Next the fault mitigation strategy is tested for Scenario I. A small drop in estimated speed can be seen when the fault occurs at 500 rpm (Fig. 7.8a). This is entirely related to the high angular $\Delta\theta$ error between measured and estimated angles (Fig. 7.9a; middle and bottom plots). On the other hand, because angular error value is reduced as the speed increases (Fig. 7.9b), estimated speed drop recorded when

fault occurs at 800 rpm is negligible. Oscilloscope screenshots of the electromagnetic torque and phase current traces are given in Fig. 7.10 and show that there is no noticeable impact of the position/speed sensor fault.

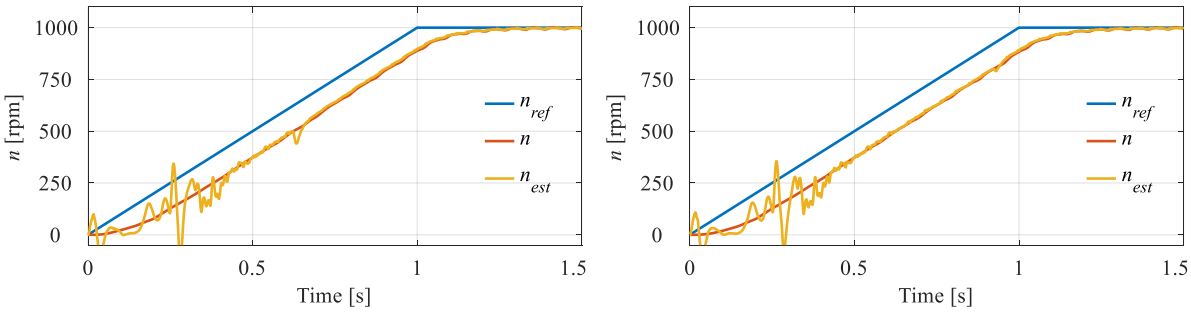

a) b)

Figure 7.8 – Experimentally recorded speed – Scenario I, speed transient, fault occurs at (a) 500 rpm, and (b) 800 rpm.

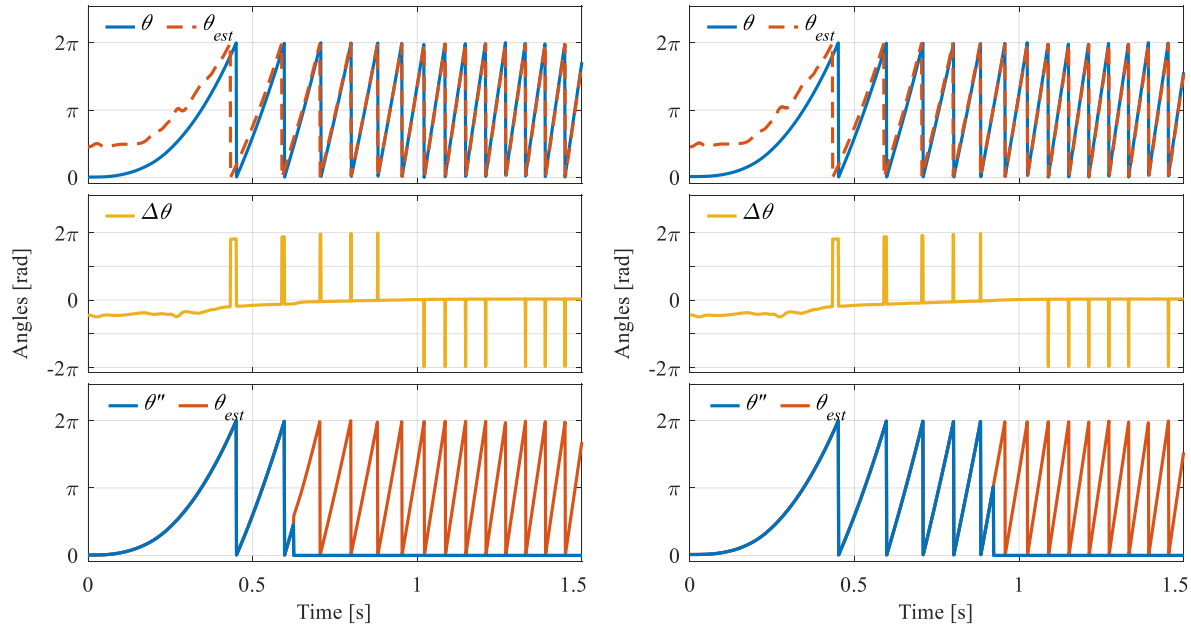

a) b)

Figure 7.9 – Angle analysis – Scenario I, speed transient, fault occurs at (a) 500 rpm, and (b) 800 rpm.

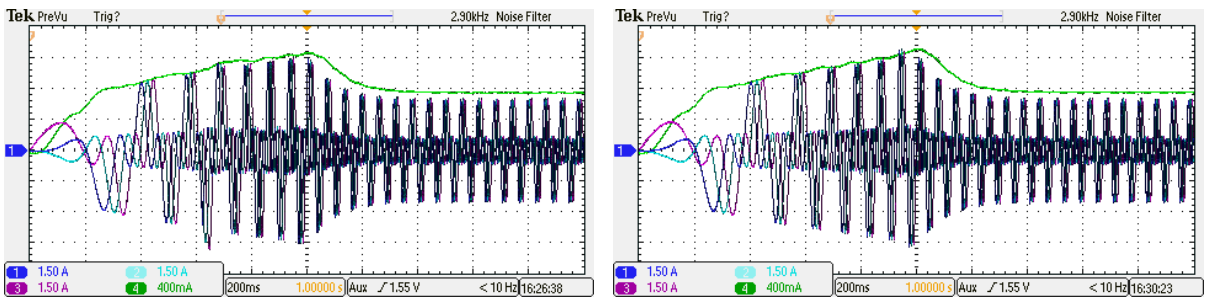

a) b)

Figure 7.10 – Oscilloscope screenshot of phase currents (phases *a*1, *a*2, *a*3; 1 A on oscilloscope = 0.25 A of real current) and torque (400mA on oscilloscope = 0.5 Nm of real torque) – Scenario I, speed transient, fault occurs at (a) 500 rpm, and (b) 800 rpm.

Next, analysis of the results recorded while testing the system under Scenario II is performed. Steady state speed is once again set to n_{ref} = 1000 rpm, but the fault now occurs at t = 0.08 s. Related to the speed (Fig. 7.11a), significantly larger speed drop can now be noted (if compared with the speed recorded in Fig. 7.3a). The same can be concluded for the electromagnetic torque (Fig. 7.11b). The average value of measured torque is once again ≈ 0.868 Nm. Angle signals (Fig. 7.12) are shown

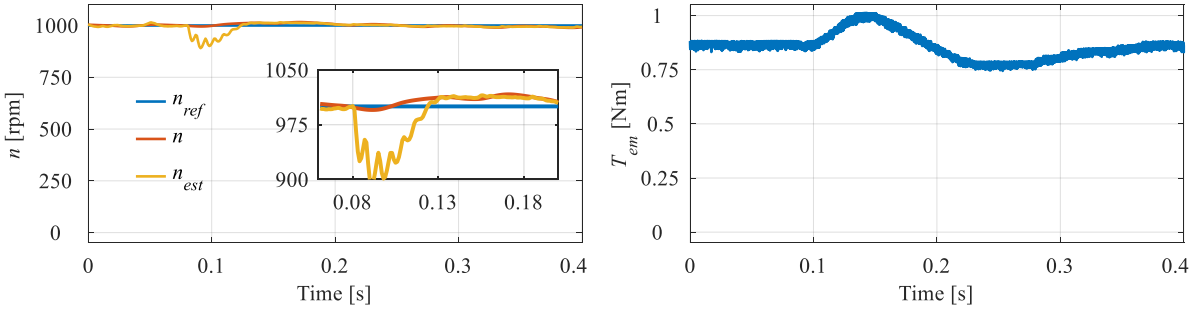

Figure 7.11 – Experimentally recorded speed (a), and electromechanical torque (b) – Scenario II, steady state.

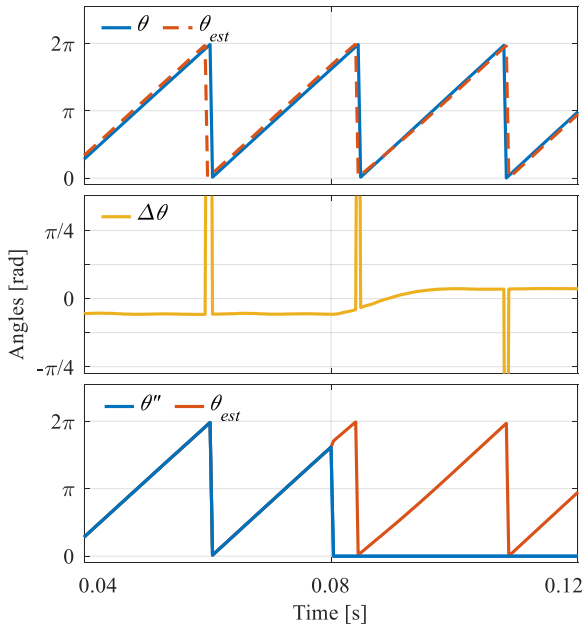

Figure 7.12 – Angle analysis – Scenario II, steady state.

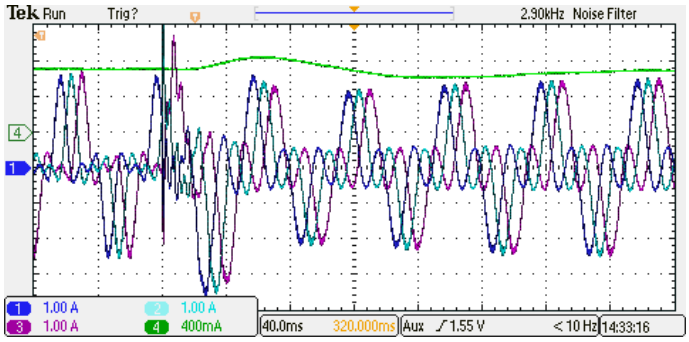

Figure 7.13 – Oscilloscope screenshot of phase currents (phases *a*1, *a*2, *a*3; 1 A on oscilloscope = 0.25 A of real current) and torque (400mA on oscilloscope = 0.5 Nm of real torque) – Scenario II, steady state.

(zoomed) for the time interval 0.04 - 0.12 s. Error between measured (position sensor) angle and the estimated angle before the fault (depicted in the middle plot of Fig. 7.12) equals -0.174 rad, i.e. 9.97°, while after the fault the position error is 0.1079 rad, i.e. 6.18°. Phase currents (and electromagnetic torque) are shown in Fig. 7.13. As expected, two different current shapes can be seen. Before the fault, the torque is produced by combining all three considered harmonics, while afterwards only the fundamental and the third harmonic currents are employed.

Finally, a set of Scenario II results during a speed transient is shown in Figs 7.14 - 7.18. Once again, speed transition without fault is given first in Figs. 7.14 – 7.15. After ≈280 rpm, estimated speed equals the measured, hence the sensorless control can be utilized. Different to Fig. 7.7, during healthy operation the torque is produced by the fundamental and two additionally injected current harmonic. As concluded in chapter 6, this consequentially causes higher current peak value, but with lower RMS. A position sensor fault was once again emulated at 500 rpm and 800 rpm (Figs. 7.16 - 7.18). Although in both cases estimated speed and phase current drops were significant, after short transient (≈0.1 s long), drive continues to maintain stable operation.

Taking into account all the above given results (Figs. 7.3 - 7.18), following conclusions can be given. In Scenario II, it is reasonable to expect a higher position error prior to the fault than in Scenario I ($\Delta\theta$ = - 9.97° and $\Delta\theta$ = - 7.09°, respectively). This is due to the control mode, which is before sensor failure using the fifth harmonic for torque enhancement and is at the same time extracting rotor position information out of it. Therefore, current is in this subspace not 0, i.e. reference voltage in this subspace does not correspond to the back-EMF. As a consequence, angle estimation is achieved with additional error; hence higher angular error between position sensor angle and estimation angle occurs. As shown, in the instant of switchover, this (higher) angular error causes more severe speed and torque transients. Thus, because of the bigger angular error during control with position sensor in Scenario II, transient is more pronounced with higher spikes in torque and speed. After the fault, the position error in Scenario II is $\Delta\theta$ = 6.18° (it was $\Delta\theta$ = 5.78° in Scenario I). Because the fifth harmonic is now used (only) for position estimation in the same way as in the earlier experiments, angular error value is similar to error recorded before (Scenario I).

It is important to note however that, regardless of the investigated scenario (which of course means higher or lower speed/torque transient oscillation and higher or lower fundamental torque production prior to the fault), after sensor fault occurs, drive continues to operate in the steady state or transient, as appropriate, i.e. sensorless control successfully provides the control system with the needed rotor position. Selection of the desired scenario simply comes down to the desired performance of the investigated application, but, as shown with Scenario II, one can have the highest torque production prior to the fault and position sensor fault tolerance after the fault detection.

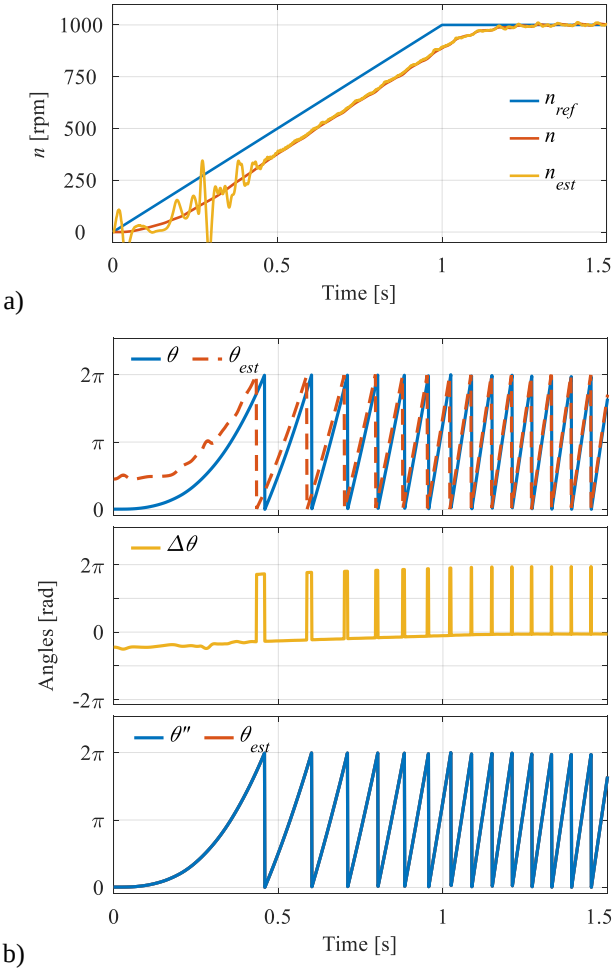

Figure 7.14 – Experimentally recorded speed (a), and angle analysis (b) – Scenario II, speed transient, no fault.

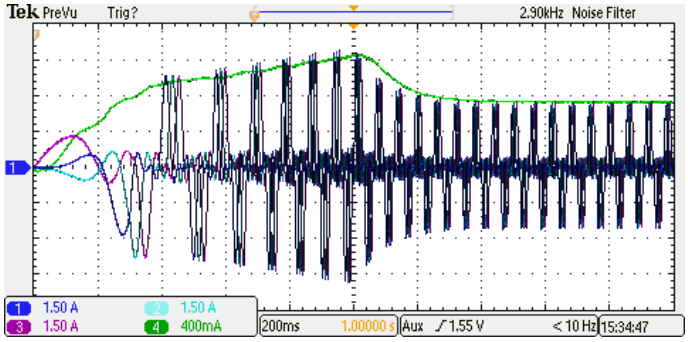

Figure 7.15 – Oscilloscope screenshot of phase currents (phases *a*1, *a*2, *a*3; 1 A on oscilloscope = 0.25 A of real current) and torque (400mA on oscilloscope = 0.5 Nm of real torque) – Scenario II, speed transient, no fault.

7.5 Summary

In this chapter, a back-EMF based rotor position estimation is introduced in order to achieve position sensor fault tolerance. For this purpose, *α*-*β* machine model is given first. As shown, in this domain, rotor position and speed can be precisely extracted. Although this can be achieved using either

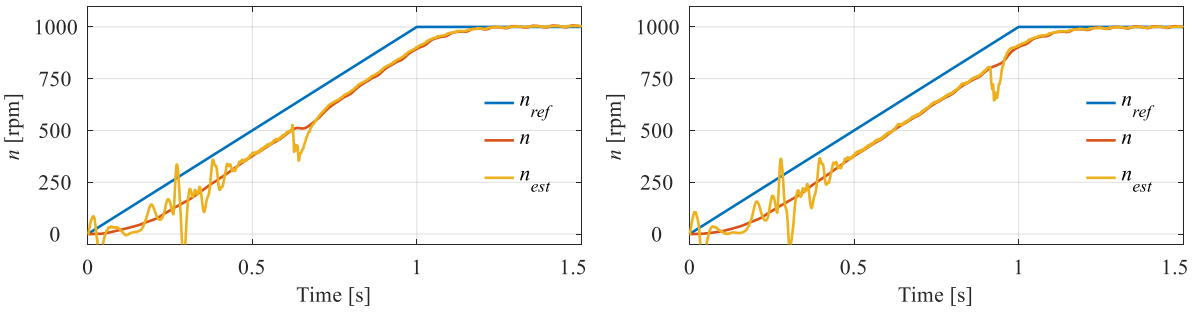

a) b)

Figure 7.16 – Experimentally recorded speed – Scenario II, speed transient, fault at (a) 500 rpm, and (b) 800 rpm.

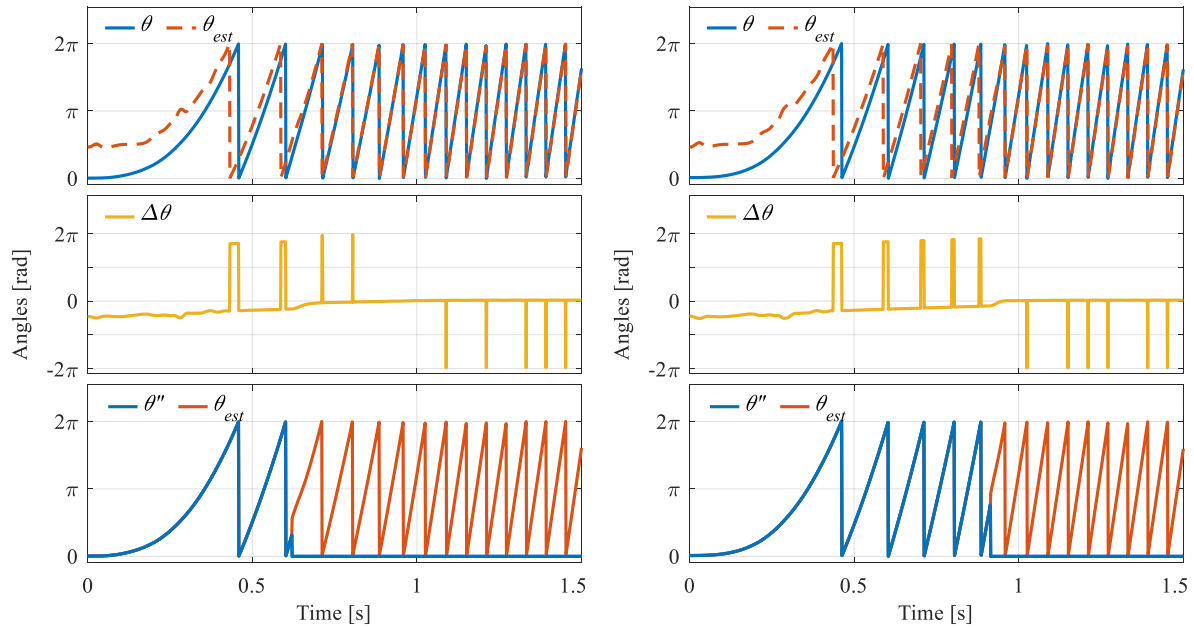

a) b)

Figure 7.17 – Angle analysis – Scenario II, speed transient, fault at (a) 500 rpm, and (b) 800 rpm.

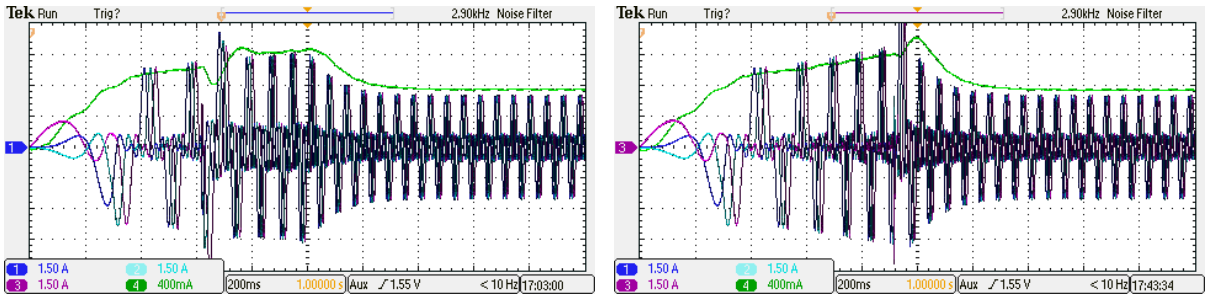

a) b)

Figure 7.18 – Oscilloscope screenshot of phase currents (phases *a*1, *a*2, *a*3; 1 A on oscilloscope = 0.25 A of real current) and torque (400mA on oscilloscope = 0.5 Nm of real torque) – Scenario II, speed transient, fault at (a) 500 rpm, and (b) 800 rpm.

a trigonometrical or PLL approach, here the latter is selected. Once when the control algorithm, derived in chapter 6, was extended with the fault-tolerant capability, experimental testing was performed, and two different scenarios were analysed. It is shown that when the third harmonic current injection is

employed in combination with continuous fifth harmonic angle estimation (Scenario I), transient behaviour caused by sensor fault is much smoother than that in the case when the fifth harmonic is used for torque enhancement prior to the fault (Scenario II). Nevertheless, in both cases the control algorithm manages to continuously provide sufficiently accurate position estimation to the drive system, thus ensuring continuation of stable operation after a sensor fault is detected. The control algorithm, introduced in chapter 6, therefore now incorporates a fault-tolerant capability, which makes it potentially very interesting for electric transportation applications.

Chapter Eight

EMF-BASED FLUX-WEAKENING PERFORMANCE IMPROVEMENT ANALYSIS

8.1 Introduction

In this chapter the flux-weakening capability of the studied nine-phase surface-mounted PMSM is investigated. When a permanent magnet motor is operated at a variable speed, the internal back-EMF fundamental, induced in the stator winding, increases linearly in proportion with the speed/frequency. Eventually, as the speed increases beyond the point at which constant rated torque can still be developed with the rated current (constant torque region), induced back-EMF in the machine becomes higher than the voltage available from the power source. Hence, the inverter is no longer capable of feeding currents into the motor [Hemmati and Lipo (2012)]. To operate above the base speed (in the constant power region), EMF must be counteracted with the component of a demagnetizing current which opposes flux created by the permanent magnets, so that the total stator flux is gradually reduced. This control is in the literature known as the flux weakening (FW). In relation to surface PMSMs, for maximal torque production in the constant torque region MTPA based control strategy is usually employed (chapters 5, 6), while to achieve maximal speed (with reduced output torque), flux-weakening control is employed above the base speed. The goal of this chapter is to combine both strategies and form the best control algorithm for the investigated nine-phase machine prototype over the entire speed region.

Multiphase machines are simultaneously controlled in several orthogonal *dq* subspaces. As shown previously in the thesis, this offers the opportunity to increase the torque density by exploiting the low-order high-magnitude odd spatial harmonics in the magnetic field. Although analytical computation of current references in the case of non-salient multiphase PM machines below the voltage and current limits is straightforward (chapters 5 and 6, MTPA strategy), this becomes difficult once the voltage limit has been reached. The problem is mostly related to the fact that when a voltage limit is reached in one *dq* subspace, it becomes difficult to know what the limit voltage/current references are in other subspaces (a multidimensional problem). As shown in the literature review (chapter 2), only a small number of research works has therefore addressed the field-/flux-weakening operation of multiphase motors when non-fundamental harmonics are considered for additional output torque production.

Finding a set of harmonic current references which maximise the torque by taking into account the voltage/current limits leads to a difficult problem to formulate and it is often impossible to solve it analytically - except if using very restrictive assumptions. In [Parsa et al (2005), Casadei et al (2010, Xuelei et al (2011)] the introduced simplifications considered only magnitudes of the different *dq* vectors as variables of the problem, disregarding their phase angles. This corresponds to the worst-case scenario that can be encountered, assuming that all harmonic components reach their peak values at the same time instant. Consequently, this causes maximal use of the dc-bus voltage, which in most cases does not guarantee the optimality of the developed solution [Lu et al (2012)]. In addition to the disregarded harmonic phase angles, stator resistance is usually also neglected (e.g. [Parsa et al (2005), Xuelei et al (2011)]). Recently, an alternative to the analytical approach was proposed, showing how

optimal *dq* current references can be calculated numerically using an offline optimisation procedure [Lu et al (2012), Bermudez et al (2019), Zhang et al (2019a)].

Because assumptions that are used in the analytical approach can lead to only a partial exploitation of full performance capabilities and to a costly oversizing of the power converter components, the work in this chapter builds on a technique to numerically compute optimal current references. Additional reasons to choose this approach are also related to a significant system complexity increase with inclusion of each additional harmonic, and to a non-negligible stator resistance value in the machine prototype (R_s = 31.3 Ω). In order to obtain the best performance (the highest torque and speed) under the given voltage and current limits, current harmonics up to (and including) the fifth are analysed and injected to couple with the corresponding back-EMF harmonics.

The chapter commences with the basic flux-weakening concepts (section 8.2) and introduction of the optimisation procedure (section 8.3), which is then followed by the explanation of the used current (both peak and RMS) and voltage limits, and validation of the optimisation tool (sections 8.3 and 8.4, respectively). The procedure uses classical optimization function (called *fmincon*) offered by the *Matlab* Toolbox. For validation of the procedure, combination of the fundamental and the third harmonic current is examined. The analysis is afterwards extended to the other combinations of previously considered harmonics. After optimal *dq* current references for each harmonic are obtained and saved in look-up tables (offline), previously derived MTPA based FOC strategy is further expanded with the FW capability (section 8.5). As it will be shown, if compared with the currently existing analytical approaches, fewer assumptions are made; it is therefore believed that better utilisation of the set limits is obtained. By considering more than one additional harmonic, higher maximal speed in the flux-weakening region is achieved, i.e. dc-bus voltage is better exploited. Multiple back-EMF harmonics have not been investigated for this purpose in the literature so far. Simulation validation and experimental verification of the proposed control scheme are given in sections 8.6 and 8.7, respectively.

8.2 Basic Concepts of Flux-Weakening in Surface-Mounted PMSMs

For motors such as an induction motor, separately excited dc motor, and a synchronous motor with a field winding on the rotor, the airgap flux can be reduced directly by controlling the field current (or a corresponding stator current component). For PMSMs (both internal and surface), the field flux cannot be controlled in the same way because it is generated by the permanent magnets. Therefore, to reduce stator flux linkage, flux in the direction opposite to the magnet flux must be produced, i.e. a negative *d*-axis stator current must be imposed, as shown in Fig. 8.1. This technique is referred to as flux-weakening control [Kim (2017)]. It is easy to conclude from the given figure that, for effective flux-weakening control, a large *d*-axis inductance is desirable. Please note that, for simplicity reasons, only one torque producing harmonic is considered further on in this section.

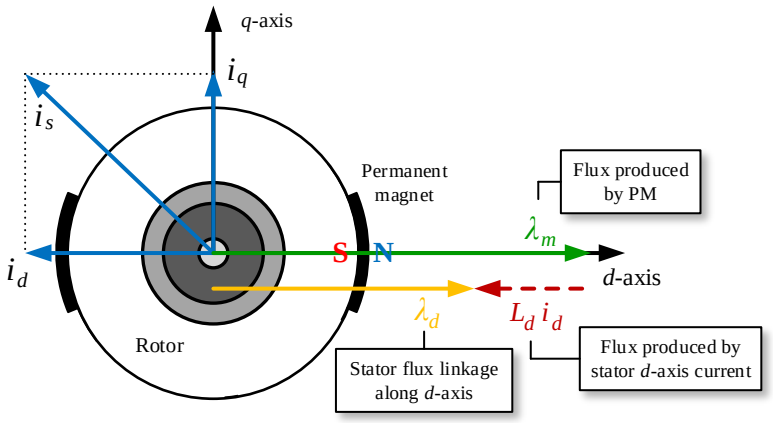

Figure 8.1 – Concept of flux-weakening technique in PMSMs.

As briefly mentioned in the introduction, the operating regions of the PMSMs can be normally divided into the following two speed regions (Fig. 8.2):

- speed range below the base speed (constant torque region), and
- speed range above the base speed (constant/reduced power region).

The second one is also known as the flux-weakening region. Constant torque region is similar to that of separately excited dc motors. However, PMSMs may have a different flux-weakening characteristic, which depends on their magnetic system design (Figs. 8.2a-c). This characteristic can be determined by comparing machine's characteristic current i_{ch} and machine's maximal current I_{max}. Characteristic current is defined as the ratio between the permanent magnet flux λ_m and the *d*-axis stator inductance L_d (i.e. $i_{ch} = \lambda_m / L_d$). If $i_{ch} = I_{max}$, the PMSM has in the flux-weakening region nearly ideal characteristic similar, to that of a dc motor (Fig. 8.2a). In the case of $i_{ch} > I_{max}$, there is a limitation on the operating speed at which the magnetic flux can be reduced by using the stator current, hence this type of motor has a finite maximum speed (Fig. 8.2b). Finally, in the case of $i_{ch} < I_{max}$, by using the right amount of stator current, magnetic flux can be fully reduced. This type of motor has therefore (theoretically) infinite maximum speed, which is limited only by the machine's mechanical strength (Fig. 8.2c). As it will be shown further on, defined current constraint for the studied prototype in combination with machine's electrical parameters results in $i_{ch} > I_{max}$ characteristic. Hence, other two cases will not be further discussed here (see e.g. [Kim (2017)] for more information).

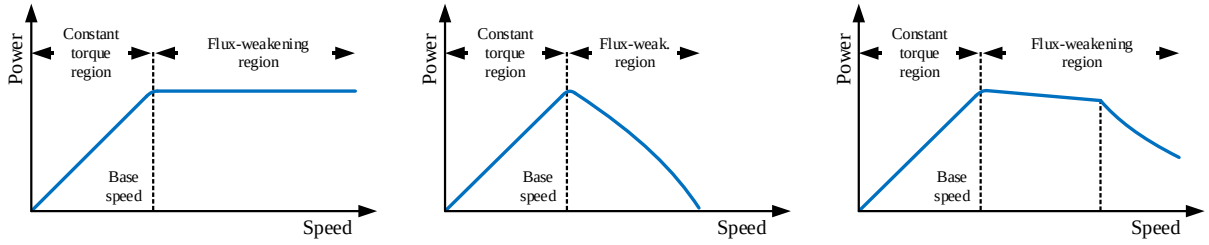

Figure 8.2 – Possible output power characteristics of PMSMs defined by magnetic design: (a) $i_{ch} = I_{max}$, (b) $i_{ch} > I_{max}$, (c) $i_{ch} < I_{max}$.

Regardless of the magnetic system design, in surface PMSMs current limit ($i_d^2 + i_q^2 \leq I_{max}^2$) and voltage limit ($v_d^2 + v_q^2 \leq V_{max}^2$) boundaries are defined as circles for which radii are the maximum stator current I_{max} (Fig. 8.3, red area) and maximum stator voltage V_{max} (Fig. 8.3, blue circles), respectively [Kim (2017), Vaez-Zadeh (2018)]. Current constraint circle always has the same radius, while voltage reserve circle decreases as the speed increases. By neglecting the voltage drop on the stator resistance in the *dq* machine model and after short mathematical manipulation, voltage limit centre can be obtained as ($(-\lambda_m/L_s, 0)$; $L_s = L_d = L_q$). As it can be seen from the figure and different to the PMSMs with internal magnets, voltage limit is here not an ellipse.

In the low- and mid-speed range, the voltage circle is large enough to encompass the current limit circle (Fig. 8.3, ω_1). Thus, the voltage reserve is sufficient, and the output torque depends only on the available current. In this case the optimal operating point is on the MTPA trajectory, according to the given torque command (Fig. 8.4, A→B). The nominal (maximal steady state) torque $T_{em\text{-}nom}$ is produced at the intersection B of the current limit circle and the MTPA (yellow) line. As the rotor speed increases, the voltage reserve circle is reduced. Once this circle encounters the MTPA line at operating point B, the flux-weakening control begins. This speed is also known as the base speed ω_{base}. If the operating speed is further increased above the base speed, the voltage reserve circle shrinks more, hence the operating point B is now outside the voltage circle and the voltage is not sufficient any more to regulate required currents. Thus, the current command should be moved to the controllable operating region (Fig. 8.4, grey area). Considering both voltage and current circles, the optimal point for producing the maximum output torque is the intersection (e.g. point C) of the two. The developed torque $T_{em\text{-}FW}$ is at this point lower than the nominal torque $T_{em\text{-}nom}$ in the constant torque region. In such operation, the *d*-axis stator current increases by absolute value in the negative direction while the *q*-axis stator current decreases. This operation continues until $i_d = I_{max}$ and $i_q = 0$, i.e. point D, at which the operating (finite) speed reaches its maximum (Fig. 8.3, ω_4). Corresponding illustrations of torque/speed and output power/speed plots can be seen in Fig. 8.5.

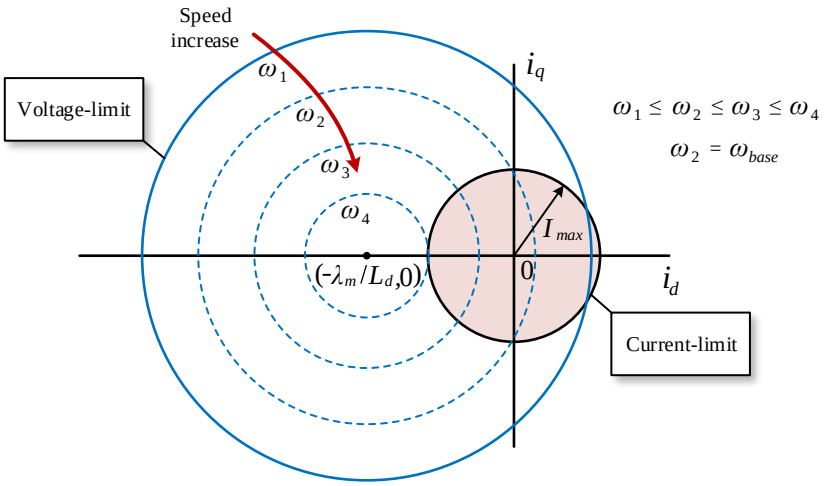

Figure 8.3 – Current limit (red) and voltage limit (blue) constraints in a surface PMSM.

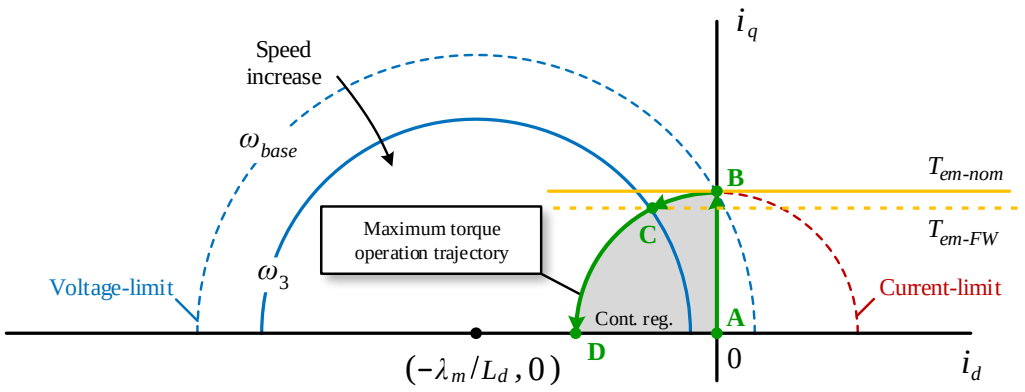

Figure 8.4 – Trajectory of the optimal current vector in finite maximal speed surface permanent magnet synchronous machine drive.

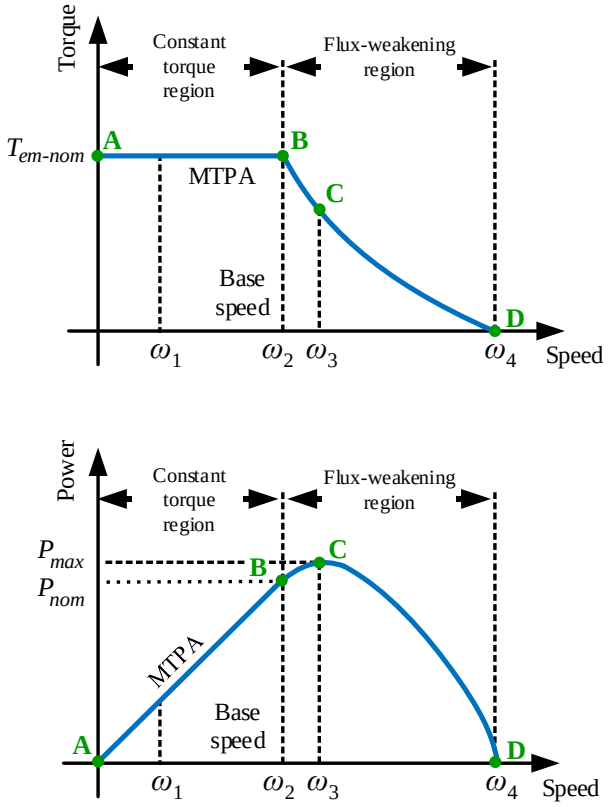

Figure 8.5 – Torque/speed characteristic (upper plot) and power/speed characteristic (bottom plot) in surface mounted PMSMs.

The flux-weakening control techniques for the high-speed operation of surface PMSMs can be classified into the three commonly applied methods: feedforward method, which determines the current commands from steady-state voltage equations, feedback method, which generates the current commands from the voltage feedback, and a method that combines these techniques [Vaez-Zadeh (2018)]. Depending on the type of the machine (internal or surface mounted magnets) and on the magnetic system design, a different flux-weakening control strategy may be needed. In what follows, a control strategy similar to the feedforward method is addressed and used.

8.3 Flux-weakening Control Applying Low-order Harmonics under Peak Current Limit

To commence with the multiple harmonic machine analysis, a nine-phase surface PMSM rotational reference frame machine model is first briefly discussed. This domain is chosen since i_{dqh} current references needed for the control algorithm look-up tables can be directly obtained during model optimisation steps. In the modelling process, the simplifying assumptions are the same as before, and are restricted to the following: i) effects such as hysteresis/eddy currents losses and magnetic saturation in the iron are not taken into account; ii) slot effects are neglected; and iii) the ninth, eleventh and thirteen back-EMF harmonics are not modelled. Electrical parameters changes due to, for example, temperature variation (as studied in [Li et al (2017), Shrestha and Seok (2011)] for internal-mounted PMSMs), as well as any other real-world uncertainties (which would require additional feedback in below proposed offline optimisation) are also not taken into account in this chapter (i.e. are proposed as potentially interesting topics for future work).

Contrary to the customary analytical approach (for example as in [Parsa et al (2005), Xuelei et al (2011)] for multiphase case, but also valid for most of the three-phase FW literature), stator resistance is in the following numerical optimisation steps not neglected. To briefly explain this, general harmonic *dq* machine model, provided already in chapter 6, is repeated here for convenience:

$$v_{dh} = R_s \cdot i_{dh} + L_{dh}\frac{di_{dh}}{dt} \mp h\omega_{el} \cdot \lambda_{qh}; \qquad v_{qh} = R_s \cdot i_{qh} + L_{qh}\frac{di_{qh}}{dt} \pm h\omega_{el} \cdot \lambda_{dh} \tag{8.1}$$

$$\lambda_{dh} = L_{dh} \cdot i_{dh} + \lambda_{mh}; \qquad \lambda_{qh} = L_{qh} \cdot i_{qh} \tag{8.2}$$

When a PMSM is operated in the flux-weakening region, product of the stator resistance and flux-/torque-producing currents $R_s \cdot i_{dq}$ is usually much smaller than the back-EMF ($\omega_{el} \cdot \lambda_{dq}$) part. This is mostly because of the negligible stator resistance value when compared with significantly larger electrical speed. Hence, $R_s \cdot i_{dq}$ part is usually neglected. Although this simplification would make analytical flux-weakening analysis of multiphase systems with more than two torque-producing harmonics an interesting research topic, this is not attempted in this work because of the stator resistance high value (R_s = 31.3 Ω). Please note that the *dq* models for the fundamental and the third harmonic are slightly different from the models for the fifth and the seventh harmonics. As explained in chapter 6, section 6.2, this is related to the rotation of these harmonics in the opposite direction (hence the opposite signs in front of the EMF parts).

Maximal physically achievable torque capability of the multiphase drive depends on the voltage and current constraints. Voltage limits are strictly related to the maximal dc-bus voltage (that is, maximal phase-to-phase voltage) that the voltage source inverter can supply to the machine. When the peak phase-to-phase voltage value $v_{ph\text{-}ph}$ is equal to the dc-link voltage, the machine enters constant/reduced

power region and with further speed increase flux-weakening begins. On the other hand, current limit can be imposed by the power converter and its electrical switches (i.e. maximum phase current peak value I_{VSI}; [Lu et al (2012), Bermudez et al (2019)]) or by the winding (copper) losses in the machine ([Parsa et al (2005), Xuelei et al (2011)]). Copper losses affect thermal performance and are usually limited by the maximum allowed phase current RMS value (I_{RMS}). This current limit value can be found on the machine's nameplate. Although most of the three-phase machines related literature (as well as majority of the existing multiphase machines literature) consider phase current RMS limit as the only one relevant in the FW region, when multiphase machines with more than one torque-producing harmonic are considered, this might not be the best limiting solution. To explain this point, the following example is given.

To start with, it must be noted that the case when the inverter's switching components are not oversized is considered. If for the single torque-producing harmonic RMS current constraint on the machine's nameplate is 10 A, this means that the switches of the inverter must be rated at $10\sqrt{2}$ A (≈14.1 A) peak value. If in the same machine two harmonics are used (fundamental and the third), one with 9.8 A RMS and other with 2 A RMS, this will still give $I_{RMS} = \sqrt{(i_{q1}^2 + i_{q3}^2)/2} = 10$ A RMS, and hence, machine's thermal limit will once again be respected. Peak values of the observed two harmonics are $i_{q1} = 9.8\sqrt{2}$ A (≈13.7 A) and $i_{q3} = 2\sqrt{2}$ A (≈2.8 A). By considering the scenario when fundamental harmonic is at 0° and the third harmonic is shifted by 180° (like in the studied machine prototype), after two harmonics sum, they produce the total phase current shape whose peak value exceeds the inverter's limit (14.1 A < 16.7 A).

As it will be shown in the following sections (and as illustrated in the example above), when the system is limited with RMS current, this does not guarantee that the peak is going to be inside the set boundaries. Also, when the current is limited by the peak value, the RMS value does not necessarily have to be below the set limit. The peak current might damage the converter, while the RMS value acts across a longer time span by increasing the working temperature of the machine. Even if inverter switches can withstand short over-the-limit operation, in the given example protection set to 10 A RMS will not be triggered, and therefore, switches will be working constantly with a current above the rated values, most likely leading to a failure in the converter. Based on these considerations, both the RMS and peak current limits in combination with phase-to-phase voltage limit are investigated here, the goal being to find the best possible limiting solution for the PMSM prototype. For the sake of simplicity, limits are first considered separately, i.e. when the current is limited by the peak, it is assumed that phase current RMS does not exceed the maximal value, and vice versa. The peak current limit approach is considered first and it is afterwards compared with the results obtained in the RMS current limit case.

The electrical constraints that will be considered in this chapter for peak current limit case can be summarised as follows:

$$i_{phase}(t) \le I_{VSI}; \qquad v_{ph-ph}(t) \le V_{dc} \tag{8.3}$$

Here, $i_{phase}(t)$ and $v_{ph\text{-}ph}(t)$ are instantaneous peak values. I_{VSI} and V_{dc} are maximal phase current peak value (inverter switches boundary) and maximal phase-to-phase peak voltage value (limited by dc-bus voltage), respectively.

To obtain the optimal *dq* current references, which are going to be implemented in the control algorithm using the look-up tables, the following two optimisation steps are considered. It is important to note that both steps are implemented using numerical optimisation approach available in the *Matlab* Optimisation Toolbox (that is, function *fmincon*). This procedure minimises (maximises) a given objective function under set constraints. The first step in the optimisation is to calculate the maximal torque-speed boundaries, i.e. the objective function to be maximized with the given constraints is:

$$\max(T_{em}) \; \frac{such}{that} \begin{cases} peak(i_{a1},...,i_{c1}) \le I_{VSI} \\ peak(v_{a1-a2},...,v_{a1-c3}) \le V_{dc} \\ \\ T_{em} = \dfrac{n \cdot P}{2} \cdot \left\{ \begin{array}{l} \left[\lambda_{d1} \cdot i_{q1} - \lambda_{q1} \cdot i_{d1}\right] + ... \\ \quad + 3 \cdot \left[\lambda_{d3} \cdot i_{q3} - \lambda_{q3} \cdot i_{d3}\right] + ... \\ \quad + 5 \cdot \left[\lambda_{q5} \cdot i_{d5} - \lambda_{d5} \cdot i_{q5}\right] \end{array} \right\} \end{cases} \tag{8.4}$$

The second step is to find several sets of optimal i_{dqh} current references for previously obtained torque/speed boundary, while minimizing the copper losses and respecting at the same time defined peak values of currents/voltages. The objective function to be minimised is:

$$\min(P_{Cu}) \; \frac{such}{that} \begin{cases} peak(i_{a1},...,i_{c1}) \le I_{VSI} \\ peak(v_{a1-a2},...,v_{a1-c3}) \le V_{dc} \\ T_{em} = (T_{em})_{ref} \\ \\ P_{Cu} = R_s(i_{d1}^2 + i_{q1}^2 + ...) \end{cases} \tag{8.5}$$

The schematic overview of the complete optimisation procedure, given with the equation (8.5) for the peak current limit case, can be seen in Fig. 8.6. Given procedure finds the best way to divide current references between *d* and *q* axes, while respecting at the same time given constraints. Initialization parameters and initial solver conditions are loaded and set first. The for-loop repeats the *fmincon* optimisation function for every speed value between 1 and ω_{max} with an arbitrary pre-set step (in this figure, 1). An additional (inner) for-loop to obtain current references for other non-maximal torque values in the interval [0-$T_{em\text{-}max}$] can be added to the procedure as well, but this is here not shown for simplicity reasons. The function solving is repeated until either an optimal solution is found, or the maximal number of iterations has been reached. For peak current limit evaluation (Fig. 8.6, red block), *dq* variables must be transformed to phase variable reference frame, where phase current and phase-to-

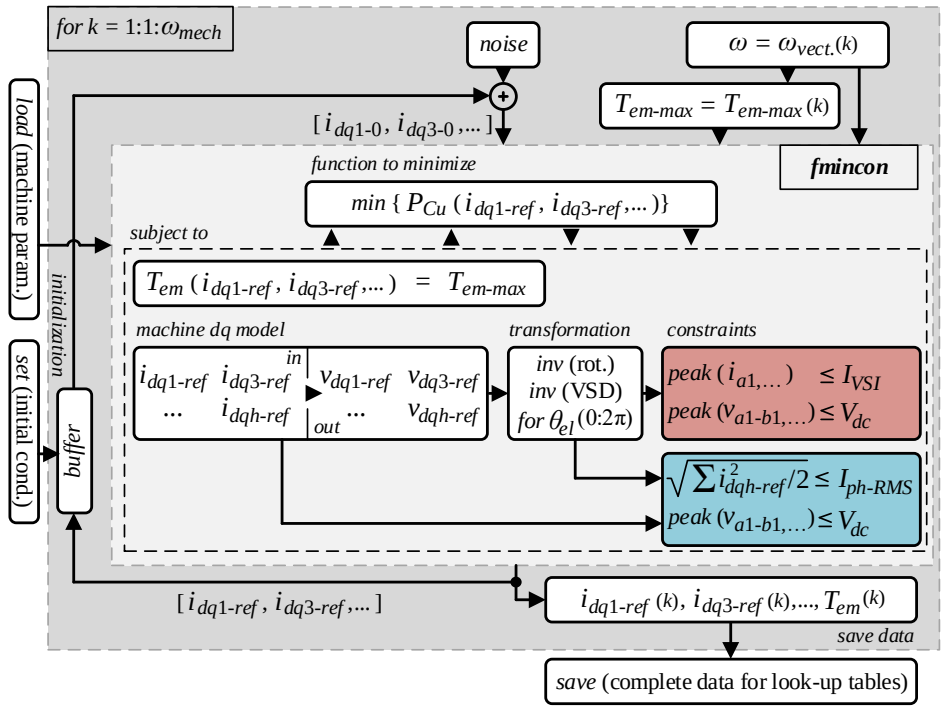

Figure 8.6 – Block diagram of the proposed optimisation procedure.

phase voltage peaks can be evaluated. Regarding RMS limitation (Fig. 8.6, blue block), this can be checked directly from *dq* current references by using well-known RMS value calculation equation. The vector containing current references from the completed step is saved in the buffer block. In this way, initial solver condition is changed, and solving can start for the following set speed, taking into account optimal solution from the previous one. At the end of the optimisation sequence, complete results are saved into the corresponding look-up tables.

Regarding the maximisation of the torque (defined with (8.4)), the optimisation principle is similar to the one presented for the minimisation of the copper losses. In this case, the objective function to be maximised in *fmincon* block is $max\{T_{em}(i_{dq1}, i_{dq3}, \ldots)\}$, and it is subject to the current and voltage constraints only. Because procedure is in this case evaluating maximal torque, $T_{em\text{-}max} = T_{em\text{-}max}(i)$ is not needed in the optimisation procedure shown in Fig. 8.6.

8.3.1 Optimisation Procedure Validation by Injecting the Third Harmonic Current

Peak current limited optimisation procedure is validated by injecting the third harmonic current. This harmonic is selected since expected results have been analysed and confirmed multiple times so far in the thesis. Phase current peak limit is set to I_{VSI} = 1.2 A. For this constraint, expected (maximal) torque in both fundamental only (k_{13} = 0) and fundamental plus third harmonic (k_{13} = optimal) cases is ≈2 Nm (chapters 5, 6, Method II). The optimal ratio between the two considered harmonics is here not

set, i.e., it is determined by the optimisation procedure. Phase-to-phase peak voltage limit (dc-link voltage) is set to V_{dc} = 450 V, the same value as in the previous chapters.

Figs. 8.7a-d show torque, phase currents, *dq* currents and phase voltages obtained using optimisation procedure, respectively. Because in the optimisation procedure torque is calculated in relation to the speed, given transition results were recorded once the system was in steady state. Steady state is in Fig. 8.7a shown with the red circle (2 Nm, 1500 rpm) and this is the point in the base speed region that was analysed in previous chapters as well. At this point, both speed and torque are constant, hence no further changes are visible in the plot. Results for *dq* currents were recorded separately, and afterwards merged. Based on the presented current/voltage results and comparative analysis of the results in chapter 5, it can be concluded that the procedure works correctly in the constant torque region. The obtained optimal ratio is once again k_{13} = 0.927. Small differences in phase voltages are caused by simplifying assumptions, i.e. the fact that in this chapter only 1st - 7th back-EMF harmonics are modelled.

From this point on, the single harmonic case (k_{13} = 0) is not discussed any more, i.e. all the results are given for the case when both the fundamental and the third harmonic are employed for the torque production. Fundamental only case will be again studied in the following subsection where different combinations of harmonics are analysed. V_{dc} value is also reduced to 190 V, for which the optimisation procedure returns the base speed as 750 rpm. This mostly relates to experimental validation; hence further explanations will be given at the end of the chapter, were the corresponding results are analysed.

By performing optimisation of the torque under the given constraints ((8.4) with the neglected fifth harmonic), results presented in Fig. 8.8a (blue trace) are obtained. As is visible, for 1.2 A current peak, maximum reachable torque in the constant torque region is 2.1 Nm (blue trace), rather than 2 Nm (red trace) as expected. The red trace was obtained after minimisation of winding losses under 2 Nm torque boundary, which will be addressed in more detail shortly. The difference between torques can be explained if Fig. 8.8b is examined, where the relationship between the ratio of currents i_{q3}/i_{q1} and torque T_{em13} is shown. The optimal ratio between the two harmonics for torque interval [0-2] Nm, is k_{13} = 0.927. By changing the ratio (i.e. reducing the magnitude and altering the angle of the third harmonic current in [2-2.1] Nm interval), optimisation procedure manages to increase torque by ≈0.1 Nm. Hence, the final value after maximisation is 2.1 Nm. Because the amount of the third harmonic is reduced almost to zero, current has a near-sinusoidal shape (Fig. 8.9b). It must be noted however that, although a slight increase in the torque was achieved, optimisation exploited current limit instead of minimising the losses. As a result, by increasing the torque from 2 Nm to the maximum possible value, copper losses were also increased. Based on the magnitudes of harmonics (Fig. 8.10) and shapes of currents (near- and non-sinusoidal; Fig. 8.9, top), it can be estimated that the increase in the copper losses is in the range of 30-36%, which corresponds to findings in chapters 4, 5.

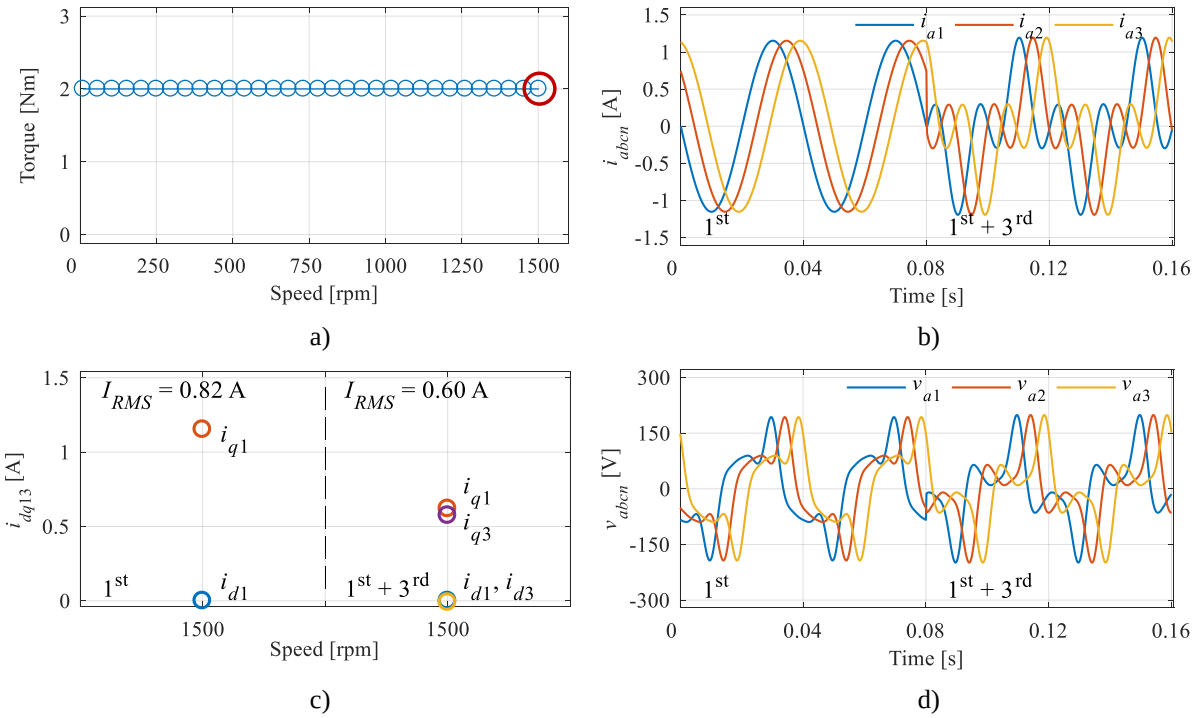

Figure 8.7 – Validation of the optimisation procedure in steady state for 2 Nm and 1500 rpm: torque/speed (a), phase current (b), *dq* currents (c), and phase voltages (d).

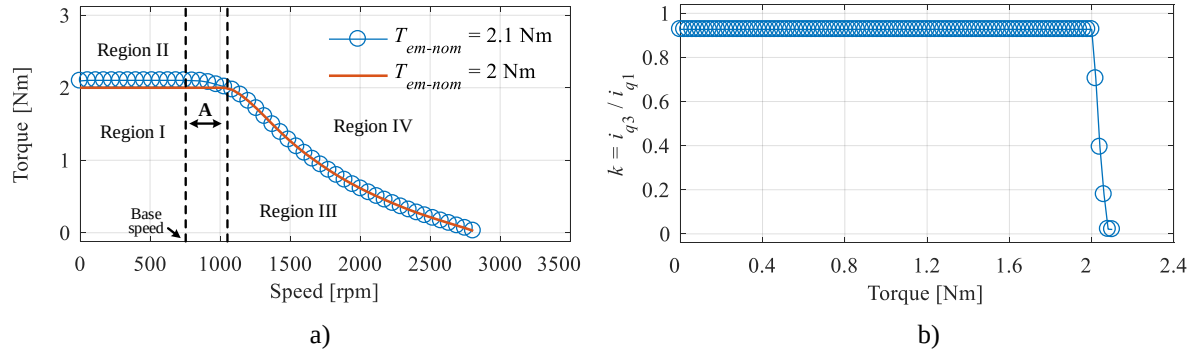

Figure 8.8 – Optimal electromagnetic torque (a), and i_{q3}/i_{q1} versus T_{em} relation (b).

On the basis of the given results in Fig. 8.8a, Regions I and II can be established. In both regions machine operates up to the base speed (≈750 rpm) and by applying MTPA control principles. Region I is defined with [0-2] Nm interval. Phase currents in this region have a shape which is similar to that of the back-EMF (Fig. 8.9a, top), and optimal ratio is calculated as EMF/PM flux ratio between two harmonics (chapter 5). Above Region I (i.e. red 2 Nm torque line in Fig. 8.8a; further on, Region II), corresponding ratio between harmonic components is changed (the third harmonic is reduced) and currents do not follow the shape of the back-EMF. At the maximum value (≈2.1 Nm), almost sinusoidal current shape can be noted (Fig. 8.9b, top). A small amount of the third harmonic, which is still present, under set angle causes flat current shape around the peak. Phase voltages are for the two discussed cases given in Figs. 8.9a and b, middle plots. Regarding phase-to-phase voltages (Figs. 8.9a and b, bottom plots), because machine works in the constant torque region, corresponding peaks are below the set constraints (blue dashed line). All analysed results in Fig. 8.9 were recorded at 500 rpm.

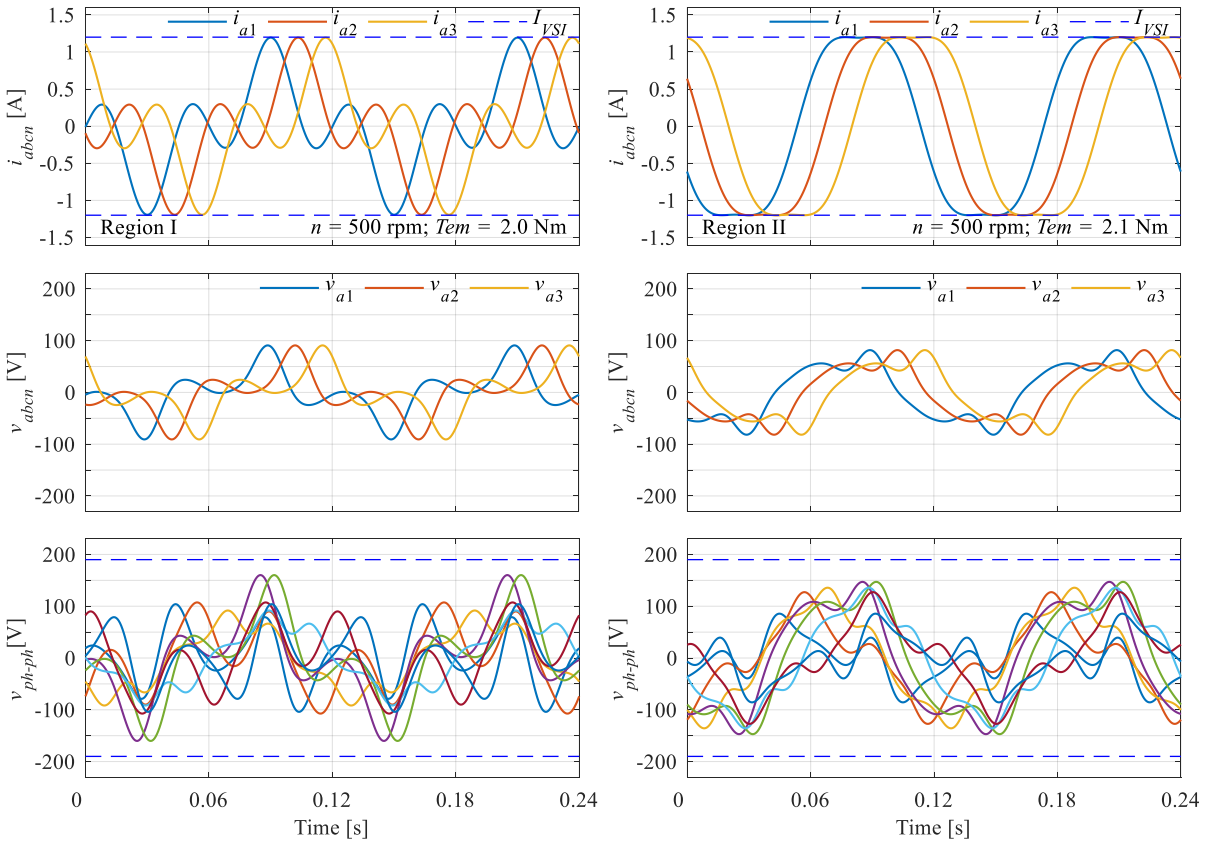

Figure 8.9 – Phase currents, phase voltages and phase-to-phase voltages for (a) 2 Nm, and (b) 2.1 Nm torque values recorded in the constant torque region at 500 rpm – simulation results.

Finally, in Figs. 8.10a and b torque- and flux-producing current references, recorded in Regions I and II, are given for the speed range up to 300 rpm. By observing Fig. 8.10a, one can easily conclude that under maximal torque-per-Ampere control and for 2 Nm, torque-producing (peak) currents for the two harmonics are i_{q1} = 0.622 A and i_{q3} = 0.577 A. These are the exact optimal values discussed numerous times in the previous chapters. On the other hand, for the near-sinusoidal case given in Fig. 8.10b, electromagnetic torque is almost entirely produced by the fundamental only (i_{q1} = 1.15 A). Since there is no need for weakening of the flux in this region, flux-producing currents i_{d1} and i_{d3} are in both cases equal to 0.

Above the base speed, the additional two regions (Region III and Region IV, Fig. 8.8a) can be established. Different from the previously defined regions, machine here works constantly in the voltage limit. This can be seen in Fig. 8.11a, where instantaneous phase-to-phase voltage peaks are plotted for each set speed. Speed interval defined with **A** [≈750 to ≈1100 rpm] is considered first. In this interval, the phase-to-phase voltage is already in the limit, but by rearranging the *dq* currents (Fig. 8.11b, 2 Nm case), optimisation procedure manages to keep output torque value approximately at its maximum. If maximum torque case is considered (Fig. 8.8a, blue line), output torque value is decreased by ≈0.1 Nm in this interval. On the other hand, if optimal (MTPA) torque from constant torque region is considered

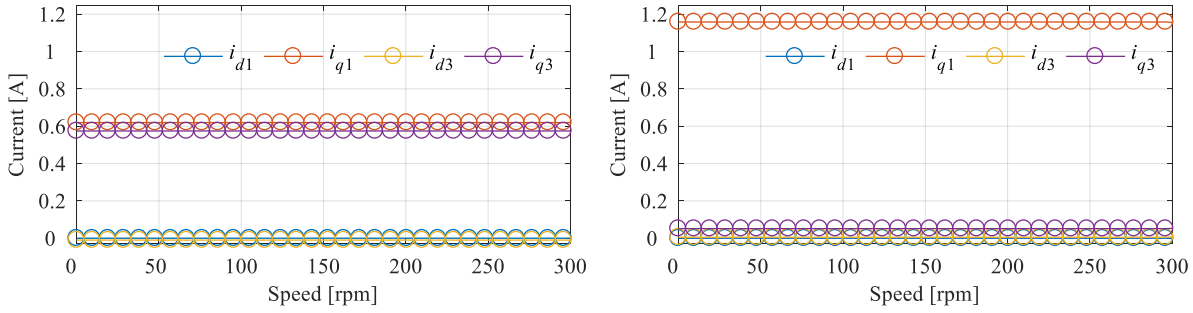

Figure 8.10 – Flux- and torque-producing currents for (a), 2 Nm, and (b) 2.1 Nm cases recorded below the base speed in constant torque region – simulation results.

(Fig. 8.8a, red line), up until the end of the **A** region, output torque is preserved. In relation to the rearrangement of the current components, as is visible in Fig. 8.11b, i_{d1} and i_{q3} currents start to drop, while i_{q1} and i_{d3} current components show slight increase.

Beyond the interval **A** the torque is reduced. Optimal and maximal torque values from the constant torque region analysis (Fig. 8.8a) are now equal. In Region III, machine operates in the voltage limit, but with a torque value which is lower than the maximal possible. Consequently, current peak value will not be in the limit. In Region IV, which corresponds to the maximal achievable torque, machine hits both limits. Corresponding phase currents/voltages and phase-to-phase voltages can be seen in Figs. 8.12a and b. The results were recorded at 1500 rpm, and with 0.5 Nm for Region III (Fig. 8.12a), that is, ≈1.26 Nm for Region IV (Fig. 8.12b). Maximal reachable speed is ≈2800 rpm. With completely analysed maximal and optimal output torques, optimisation of copper losses to obtain *dq* current references (eq. (8.5)) can now be performed. This is explained next. Before that, it is important to note that, because of the higher importance for this research and for easier tracking, 2 Nm is further considered as the maximal and optimal torque boundary below the base speed. This is justified because for 2.1 Nm case, the existence of the third harmonic is not exploited and therefore much higher input power is required for almost the same torque production.

Recorded synchronous reference frame current references, for 2 Nm case, obtained after copper loss minimisation are given in Fig. 8.13a. As expected, torque-producing currents i_{q1} and i_{q3} are decreasing, while i_{d3} increases by absolute value, in the negative direction. Because i_{d1} current reached its minimum in speed interval **A**, it is now increasing slightly. For the sake of completeness, corresponding power analysis is given in Fig. 8.13b. Because only winding losses are modelled, by adding output power, input power (and subsequentially efficiency η) can be calculated. As it can be seen, although copper losses were increased when the machine entered the FW region (higher RMS), efficiency is not dropping significantly until ≈1900 rpm, i.e. ≈2.5 times the base speed. As explained in section 8.2, shape of output power is a direct consequence of the magnetic system design, i.e. $i_{ch} > I_{max}$ characteristic of the PM synchronous machine prototype.

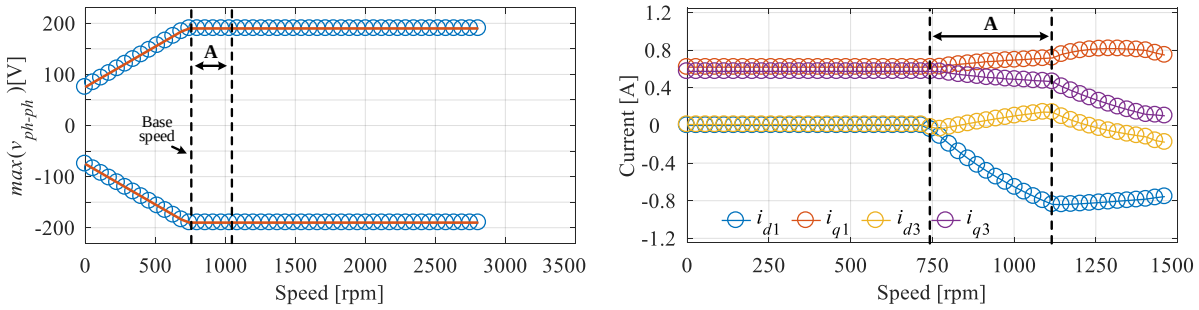

a) b)

Figure 8.11 – Dc-bus voltage utilisation (a), and *dq* current references for 2 Nm in speed interval **A** (b).

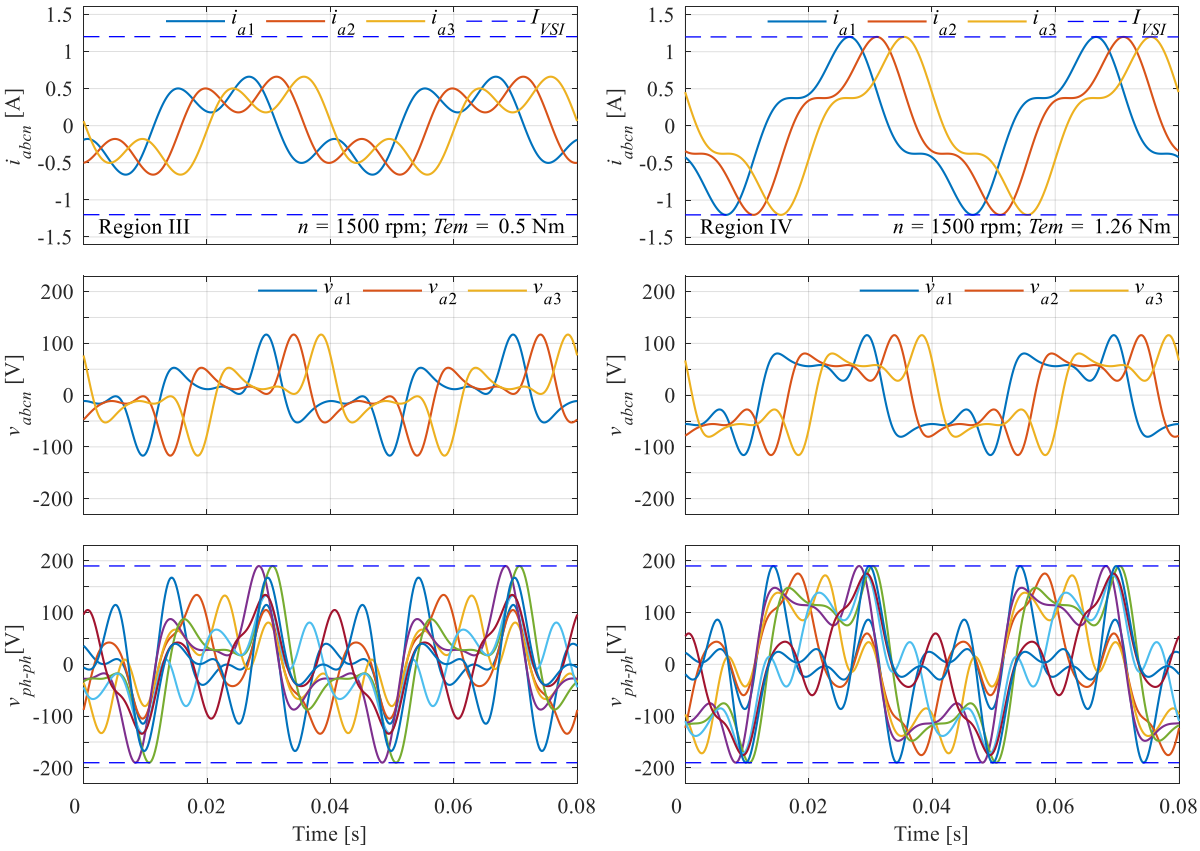

a) b)

Figure 8.12 – Phase currents, phase voltages and phase-to-phase voltages for (a) 0.5 Nm, and (b) maximum possible torque recorded in constant power region at 1500 rpm – simulation results.

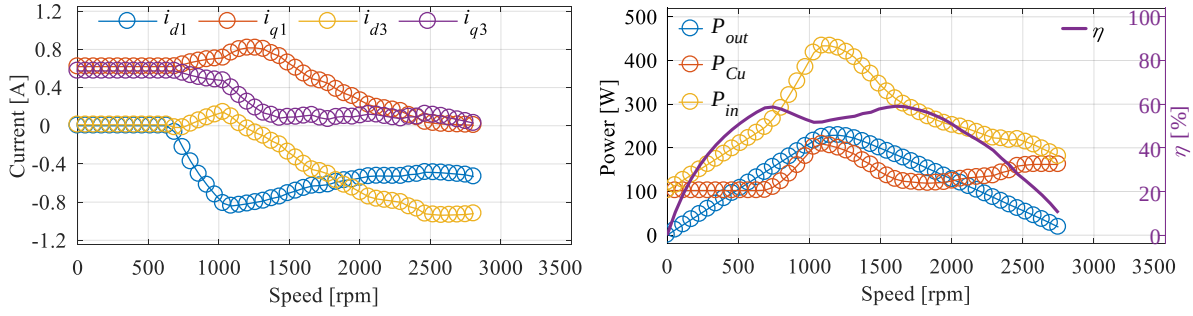

a) b)

Figure 8.13 – Optimally determined *dq* current references (a), and power analysis (b) recorded for the whole speed range – 2 Nm boundary case.

8.3.2 Comparative Analysis Including all High-Magnitude Odd Harmonics

Optimisation procedure is at this point extended further to the other torque producing harmonics. In addition to the already investigated fundamental and the third, this includes system optimisation for fundamental only, fundamental plus the fifth, and fundamental and the third plus the fifth harmonic as well. For all the listed combinations, optimisation procedures are simply formulated by expanding the one from the previous subsection. Optimisation results can be found in Fig. 8.14 and Table 8.1.

As it can be seen from Fig. 8.14a, under the MTPA control and for the set current peak limit, fundamental harmonic by itself produces the highest torque (T_{em1} = 2.08 Nm). Combination of the fundamental and third harmonic produces slightly lower torque value (T_{em13} = 2.01 Nm), while fundamental plus the fifth and combination of all harmonics produce lower output torque values (T_{em15} = 1.73 Nm and T_{em135} = 1.81 Nm, respectively). Although fundamental harmonic by itself produces the highest torque, copper losses (RMS current) are in this case the highest - meaning also the highest input power is needed. In Table 8.1, RMS current values for all analysed cases are summarised. Corresponding output power/efficiency plots are given in Fig. 8.14b. As expected, highest efficiency is achieved when in addition to the fundamental, the third and the fifth harmonics are used for torque production. As is visible from plots in Fig. 8.14, all harmonic combinations show characteristics of a finite maximal speed PMSM drive. Because the machine's mechanical limitations must also be taken into account during the FW analysis, the maximal achievable speed is set as 3500 rpm.

On the basis of the given results, it can be concluded that the highest output torque with the best (the lowest) RMS current is in the constant torque region produced by combining the fundamental and the third harmonic currents under the peak current limit constraint (combination of the first, the third and the fifth harmonic results in a higher peak current). Above the base speed, the best result (the highest speed) is achieved when combination of all harmonics is used. By observing the MTPA and flux-weakening regions separately, one concludes that the different combinations of harmonics will be required for the two regions, in order to achieve the best performance. The suggested torque/speed reference is given in Fig. 8.15a. The idea is to first use fundamental and the third harmonic in MTPA region and at the beginning of the FW, while afterwards, when this combination reaches torque produced by all harmonics, injection of the fifth harmonic for further operation in the constant power region commences. Corresponding *dq* current references, saved in look-up tables, are as shown in Fig. 8.15b.

Table 8.1 – Analysis of torque and corresponding *dq* current references for different combination of harmonics.

Peak Limit	**MTPA (n_{base} ≈ 750 rpm)**						**Flux-Weakening**
Harmonics	**$T_{em\text{-}max}$ [Nm]**	**I_{peak} [A]**	**I_{RMS} [A]**	**i_{qh} [A]**			**n_{max} [rpm]**
1st	2.08	1.20	0.85	i_{q1} = 1.20			≈1750
1st + 3rd	2.01	1.20	0.60	i_{q1} = 0.62	i_{q3} = 0.58		≈2800
1st + 5th	1.73	1.20	0.63	i_{q1} = 0.80	i_{q5} = 0.40		≈2250
1st, 3rd + 5th	1.81	1.20	0.51	i_{q1} = 0.49	i_{q3} = 0.46	i_{q5} = -0.25	> 3500

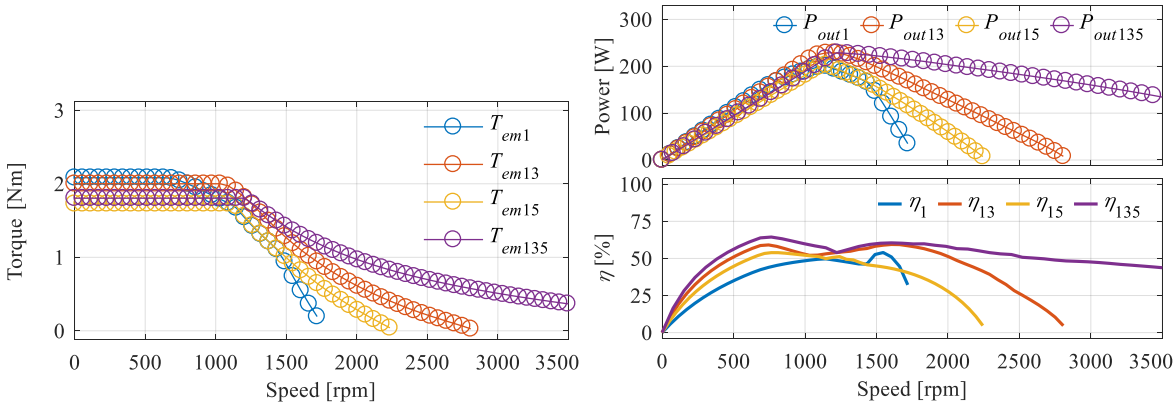

a) b)

Figure 8.14 – Optimisation of output torque/speed (a), and corresponding power/speed and efficiency/speed traces (b) for different harmonic combinations.

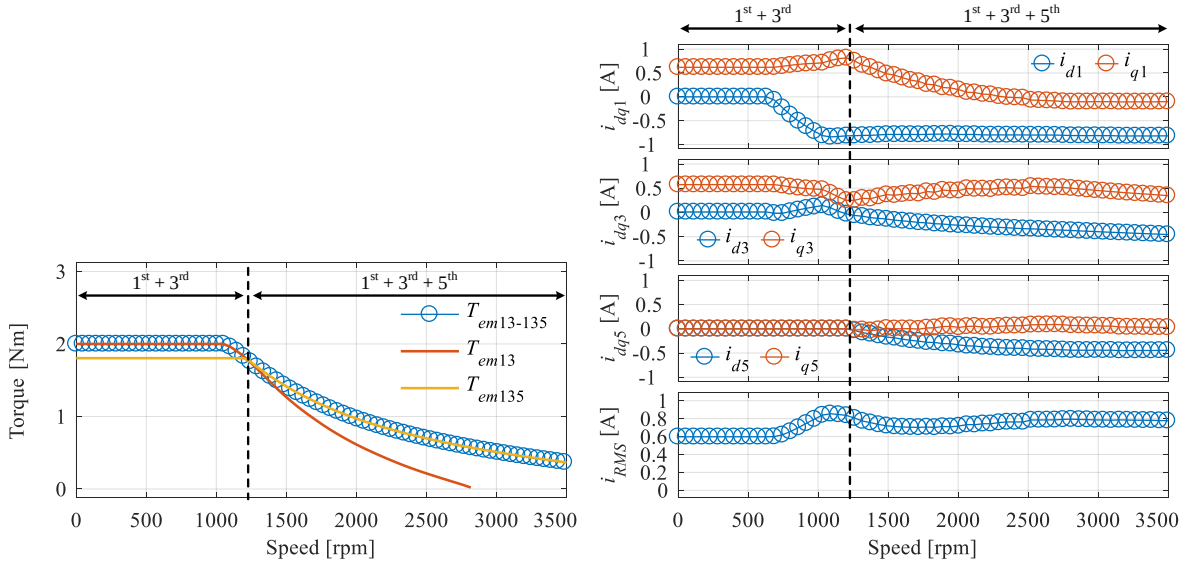

a) b)

Figure 8.15 – Optimal torque (a), and corresponding current references (b) for the combined control under peak current limitation.

8.4 Flux-weakening Control Applying Low-order Harmonics under RMS Current Limit

A similar analysis to the one in the previous section is performed next, this time considering system limited by the phase current RMS (i.e. thermal constraint of the machine). To start with, combination of the fundamental and the third harmonic is considered once again, the reason being validation simplicity. The new constraints can be written as:

$$\begin{aligned} & I_{RMS}(t) \le I_{ph-RMS} \\ & \rightarrow I_{RMS} = \sqrt{\frac{i_{d1}^2 + i_{q1}^2 + i_{d3}^2 + i_{q3}^2}{2}} \\ & v_{ph-ph}(t) \le V_{dc} \end{aligned} \tag{8.6}$$

It is important to note that, as explained already in the thesis, the studied prototype was manufactured abroad. Hence, not all machine parameters (including limits) are known. Phase current RMS limit is therefore chosen in the same way as the peak current limit, i.e. it is based on the calculated/measured values required to produce 2 Nm of torque when considered two harmonics are combined. As shown in chapters 5 and 6, this value corresponds to $I_{ph\text{-}RMS}$ = 0.6 A. By taking defined limit into account, torque related optimisation problem which needs to be solved can be defined as:

$$\max(T_{em})\ \frac{such}{that}\begin{cases} I_{RMS}=\sqrt{\dfrac{i_{d1}^2+i_{q1}^2+i_{d3}^2+i_{q3}^2}{2}}\le I_{ph-RMS} \\ peak(v_{a1-a2},...,v_{a1-c3})\le V_{dc} \\ T_{em}=\dfrac{n\cdot P}{2}\cdot\left\{\begin{matrix}\left[\lambda_{d1}\cdot i_{q1}-\lambda_{q1}\cdot i_{d1}\right]+... \\ +3\cdot\left[\lambda_{d3}\cdot i_{q3}-\lambda_{q3}\cdot i_{d3}\right]\end{matrix}\right\} \end{cases} \tag{8.7}$$

Optimisation results are shown in Fig. 8.16a. As it can be seen from the figure, maximal torque boundary (≈2.008 Nm), obtained from the optimisation procedure is almost the same as the expected (2 Nm), MTPA strategy calculated one. In relation to the speed, although base speed remains approximately the same as in the previous section, maximal reachable speed ($n_{max\text{-}RMS}$ ≈2400 rpm; Fig. 8.16a) is now lower than the value achievable under the peak current constraint ($n_{max\text{-}peak}$ ≈2800 rpm; Fig. 8.8a). As it will be shown in the following sections, this is a direct consequence of having lower FW RMS current value in the RMS limit case.

By performing the minimisation of the copper losses:

$$\min(P_{Cu})\ \frac{such}{that}\begin{cases} I_{RMS}=\sqrt{\dfrac{i_{d1}^2+i_{q1}^2+i_{d3}^2+i_{q3}^2}{2}}\le I_{ph-RMS} \\ peak(v_{a1-a2},...,v_{a1-c3})\le V_{dc} \\ T_{em}=(T_{em})_{ref} \\ P_{Cu}=R_s(i_{d1}^2+i_{q1}^2+i_{d3}^2+i_{q3}^2) \end{cases} \tag{8.8}$$

current references in the rotational reference frame, illustrated in Fig. 8.16b, are obtained. In the constant torque region recorded values are i_{q1} = 0.62 A and i_{q3} = 0.57 A (I_{RMS1} = 0.44 A, I_{RMS3} = 0.41 A). Torque in this region is entirely produced by the torque-producing currents (hence, i_{d13} = 0). As expected, above the base speed decrease in both direct and quadrature currents can be seen. Although all four currents are now changed with the speed increase, the total RMS value is always equal to the set limit (Fig. 8.16b, red and green traces, respectively).

It is to be noted that, because recorded results/conclusions for Regions I and III are almost identical to the ones previously given in relation to the peak current limit analysis, these regions are not addressed further here. As far as the phase currents and phase-to-phase voltages in operating Regions II and IV are

concerned, the following conclusions can be stated. When the system operates at the optimal torque value below the base speed (Region II), phase current has the shape which follows the shape of the back-EMF (Fig. 8.17a, top). It is important to note that the peak current limit of the previous section is still shown in the plots, for comparative purposes. New RMS limit and peak limit are related through the same torque value, hence maximal peak value is here 1.2 A. As before, phase-to-phase voltage peak (Fig. 8.17b, top) is in this region lower than the set limit. In Region IV, the system is analysed for 1500 rpm and maximal possible torque (≈1.07 Nm). Different from peak current limit analysis, phase current peak is now below the maximal possible peak value (Fig. 8.17a, bottom). On the other hand, phase-to-phase peak voltage is in the limit (Fig. 8.17b, bottom). Finally, to complete the study, power analysis is performed in Fig. 8.18a, where input/output powers, winding losses and efficiency are shown. A comparison with peak current limit result is illustrated in Fig. 8.18b and as expected, power losses are in RMS limit case lower (FW region). Because of this, efficiency of machine above base speed is therefore here slightly higher. Once again, at ≈1900 rpm, efficiency starts to drop.

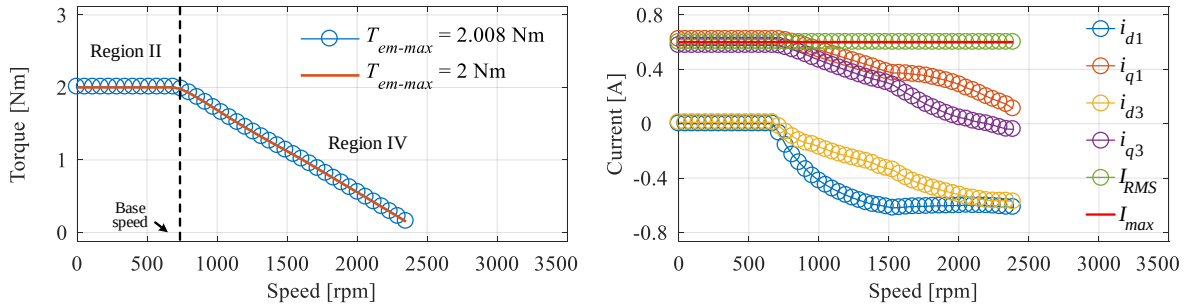

a) b)

Figure 8.16 – Optimal electromagnetic torque (a), and corresponding *dq* currents (b) recorded with combined fundamental and the third harmonic currents.

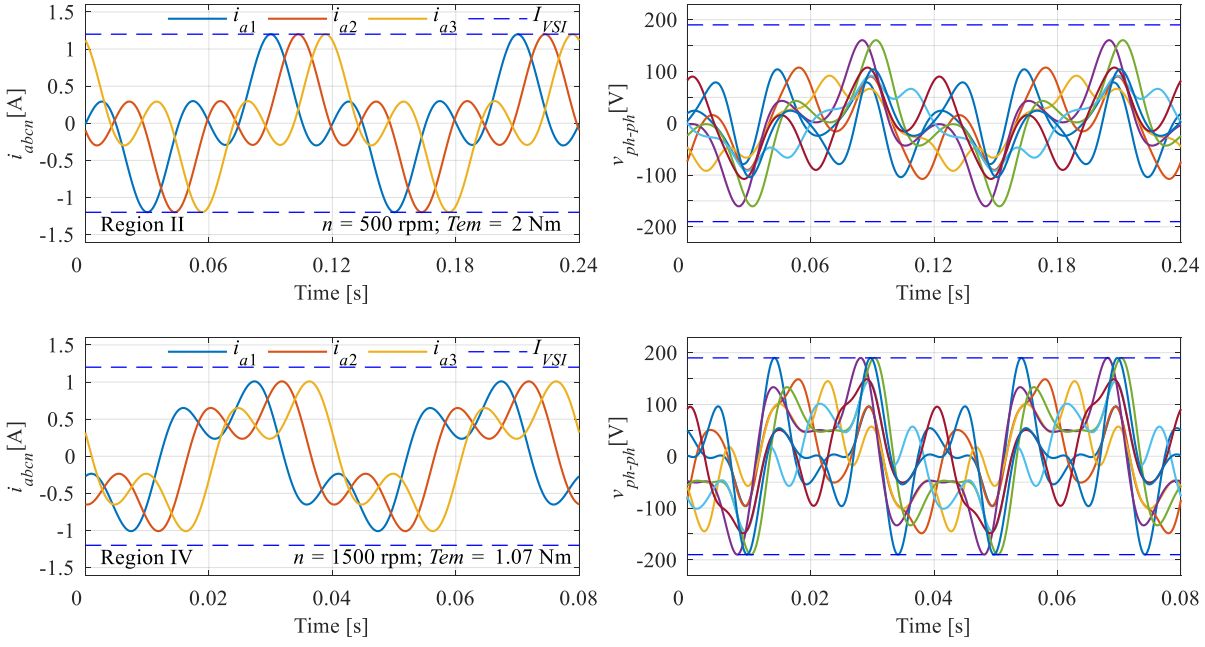

a) b)

Figure 8.17 – Phase currents (a) and phase-to-phase voltages (b) recorded for different operating regions.

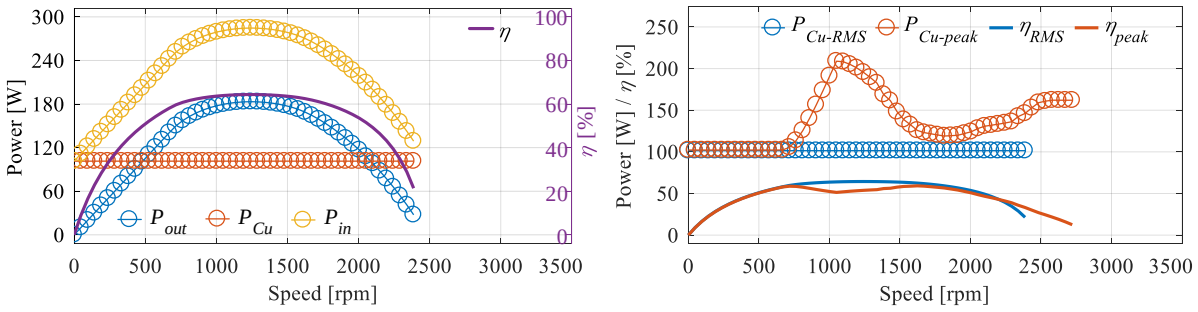

a) b)

Figure 8.18 – Power analysis in RMS limit case (a), and comparison of power losses/efficiency in both cases (b) recorded for the entire speed range.

8.4.1 Comparative Analysis Including all High-Magnitude odd Harmonics

The final step in separate consideration of current limits is to extend the studied concepts to the other combinations of harmonics under the RMS current constraint. The results are summarised in Fig. 8.19a and Table 8.2. As can be seen from the figure, in the MTPA region, combination of all harmonics produces the highest torque (T_{em135} = 2.13 Nm). This also means the highest phase current peak (i_{q1} = 0.58 A, i_{q3} = 0.54 A, i_{q5} = -0.29 A, $I_{peak135}$ = 1.42 A) among the analysed cases. Fundamental and the third harmonic produce a bit lower torque T_{em13} = 2 Nm with the current peak value of I_{peak13} = 1.20 A (i_{q1} = 0.62 A, i_{q3} = 0.58 A). For a similar phase current peak (I_{peak15} = 1.14 A, i_{q1} = 0.76 A, i_{q5} = 0.38 A), combination of the fundamental and the fifth harmonic produces a smaller torque, that is T_{em15} = 1.64 Nm. Finally, the lowest torque is produced by the fundamental only. In this case, achieved torque is T_{em1} = 1.47 Nm, while current peak is I_{peak1} = 0.85 A, i_{q1} = 0.85 A. It can be concluded from these results that, although RMS current value (winding loss) was in all the analysed cases the same, current peak is different for each combination of harmonics. One can thus conclude that, when the system is limited by the RMS constraint, peak value does not necessarily fall below the desired limiting value. For example, an inverter limited with the $0.6\sqrt{2}$ A = 0.85 A peak, can only work if the torque in the machine is produced by the fundamental harmonic only. In all other harmonic combination cases, the current peak value is above the inverters' limit; hence semiconductor components must be selected for higher peaks. Regarding the flux-weakening region, conclusions are similar to the ones previously given for the torque (Fig. 8.19a). The highest speed is produced by the combination of all harmonics (≈3000 rpm; ≈4 times higher than the base speed), while the lowest speed is achieved with the fundamental harmonic only (≈1700 rpm). Other two harmonic combinations lead to maximal speeds which are in between (Table 8.2). As the case was with the fundamental plus the third harmonic example, maximal achievable speed with any harmonic combination is in the RMS limit case lower than the one achievable in the peak current limit. Output power/efficiency plots are given in Fig. 8.20. Based on the presented results, it can be concluded that the best performance under the RMS limit is obtained by combining all harmonics; hence this case is chosen for further investigation in the following sections.

Table 8.2 – Analysis of torque and corresponding *dq* currents for different combinations of injected harmonics.

RMS Limit	**MTPA (n_{base} ≈ 750 rpm)**						**Flux-Weakening**
Harmonics	**$T_{em\text{-}max}$ [Nm]**	**I_{peak} [A]**	**I_{RMS} [A]**	**i_{qh} [A]**			**n_{max} [rpm]**
1st	1.47	0.85	0.60	i_{q1} = 0.85			≈1700
1st + 3rd	2.00	1.20	0.60	i_{q1} = 0.62	i_{q3} = 0.58		≈2400
1st + 5th	1.64	1.14	0.60	i_{q1} = 0.76	i_{q5} = 0.38		≈2150
1st, 3rd + 5th	2.13	1.42	0.60	i_{q1} = 0.58	i_{q3} = 0.54	i_{q5} = -0.29	≈3000

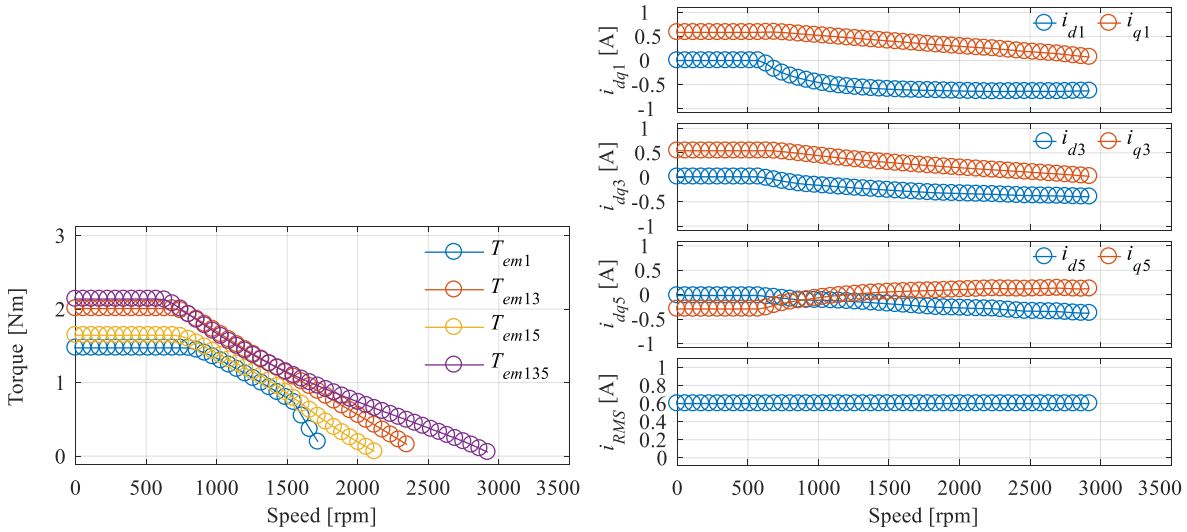

a) b)

Figure 8.19 – Torque for all harmonic combinations (a), and current references for T_{em135} case (b).

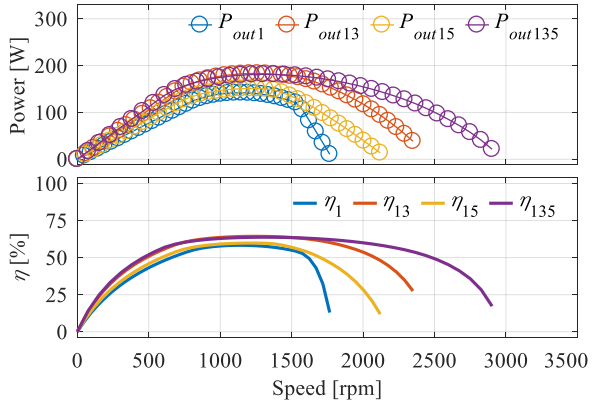

Figure 8.20 – Output power versus speed characteristic recorded for all considered harmonic combinations.

8.5 FOC Algorithm Based on the Look-Up Tables

The optimisation procedure saves current references and torque (both as functions of speed) in the look-up tables. Harmonic combinations which ensure the best performance (Fig. 8.15 and Fig. 8.19) can in this form be implemented in any digital control software. It is important to note that, although up to this point in time only the nominal torque cases were analysed, before saving data in the tables, results for lower torque values in the interval [0-$T_{em\text{-}nom}$] are also optimised (each for interval [0-ω_{max}]). If the system operates below the base speed, FOC which includes additional harmonics (derived in earlier

chapters) can be used for machine control. This is justified because the results obtained by the optimisation procedure are identical to the results obtained with FOC operating under MTPA control.

In the FW region, system operates using optimal references saved in the look-up tables. Transition from one control method to the other is achieved using combination of a simple speed switch and voltage limit detecting strategy (similar to the one proposed in [Xuelei et al (2011)]), with speed at switching condition equal to the base speed, and voltage limit equal to V_{dc} (Fig. 8.21a). Because look-up tables also contain optimised results for torque/speed characteristics which are below nominal reachable characteristic (e.g. Fig. 8.21b, where fundamental, the third and the fifth harmonics RMS current limited case is shown), in the FW the control can optimally operate even if the torque is not nominal. A complete schematic overview of the developed control can be seen in Fig. 8.22, where its generalised form is given. By using derived algorithm, machine can work by applying MTPA concepts below the base speed and with the optimal FW control above the base speed; hence optimal performance is ensured.

The control algorithm is implemented and validated in *Matlab*/*Simulink* environment. Although different harmonic scenarios and limiting cases were analysed in the previous sections, for validation purposes the focus is here put on the best performing combination under RMS current limit. This means

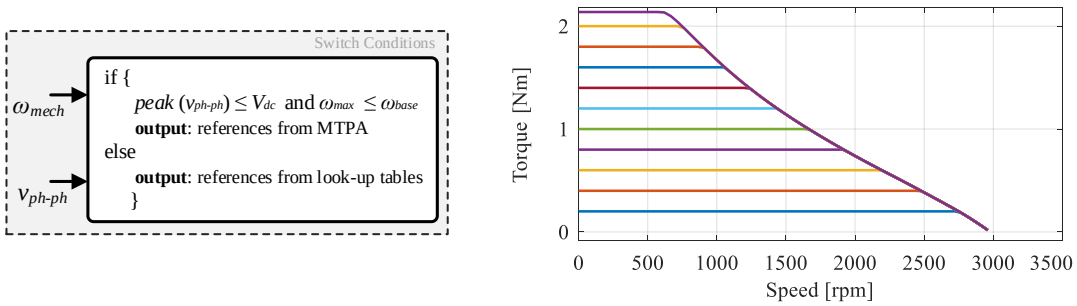

a) b)

Figure 8.21 – Switching conditions in the developed algorithm (a), and [0-$T_{em\text{-}max}$] interval under RMS limit (b).

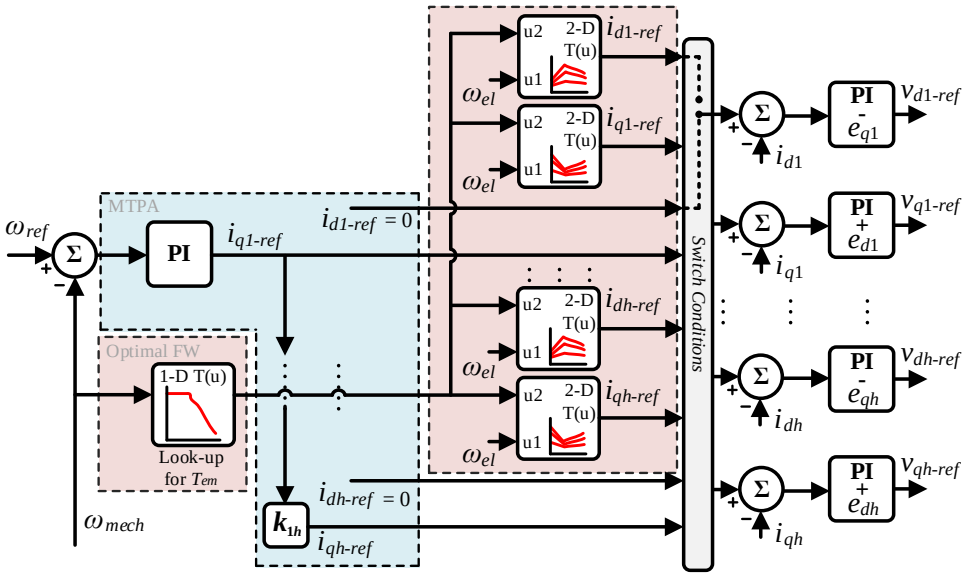

Figure 8.22 – Overview of the generalised MTPA FOC algorithm extended with flux-weakening capability.

combination of all possible harmonics in both constant torque and constant/reduced power regions (Fig. 8.19). Recorded results are given in Figs. 8.23 - 8.25. Due to the very good agreement between optimisation tool and *Matlab*/*Simulink* simulations, only a brief discussion of these figures is provided.

Electromagnetic torque and mechanical speed are given in Fig. 8.23a (top and bottom, respectively). Speed reference slope is set in such a way that the machine immediately goes into the torque limit. Reference speed increase commences at 0.2 s. Maximal reference value is limited to 3000 rpm. Both traces were recorded until the instant when measured speed and speed reference are approximately equal. In given plots, this is achieved at approximately t = 2.0 s. As it can be seen, for the time of simulation, electromagnetic torque follows precisely the corresponding reference.

Rotational reference frame currents are given in Fig. 8.23b. After the machine's speed surpasses the base speed, flux-producing currents start to increase their value in the negative direction, while fundamental and the third harmonic torque-producing currents start to reduce. Because i_{q5} current is in the MTPA region negative, injected reference of this current has in the FW a positive sign. As is visible from the bottom plot in the given figure, RMS current value never exceeds set limit (that is, 0.6 A).

Phase current results (phases $a1$, $a2$, $a3$) are given in Fig. 8.24. As it can be seen, maximal value of ≈1.4 A, is achieved in the MTPA region. Afterwards, this value slowly decreases. Cases for maximal torques and speeds below (500 rpm) and above (1500 rpm) the base speed are given in the bottom left and right plots, respectively. As it can be seen in the left plot, phase current shape is formed as a combination of all three torque producing currents. This directly follows from the already reported earlier analysis, regarding the best performing harmonic combinations in different regions.

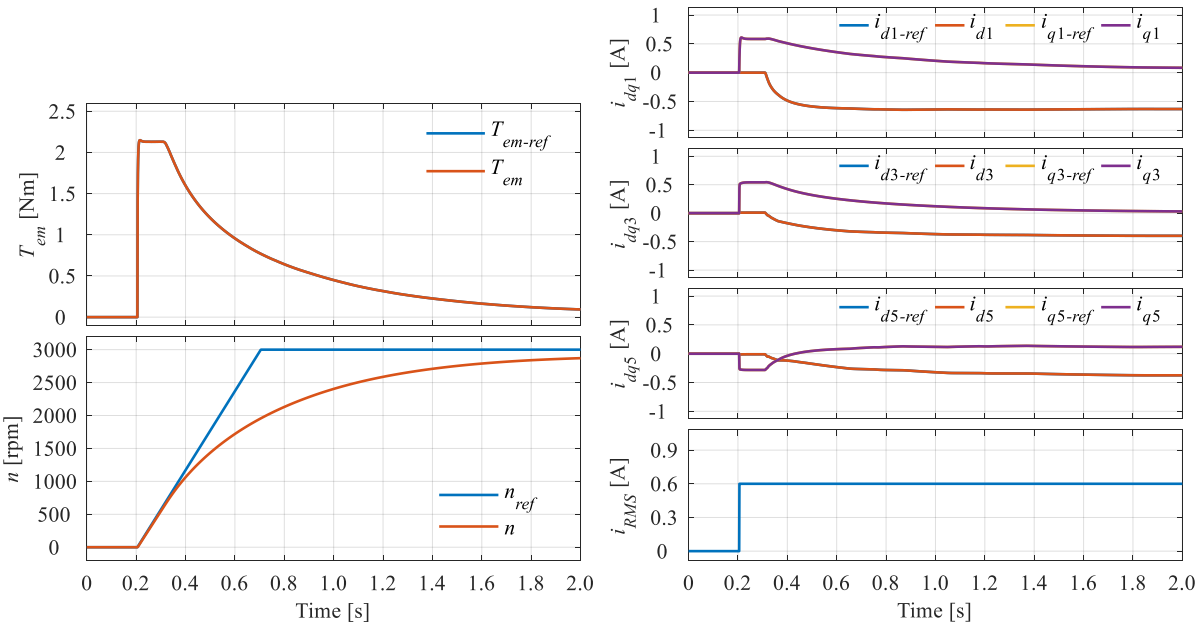

a) b)

Figure 8.23 – Electromagnetic torque and mechanical speed results (a), and rotational reference frame currents (b) under current RMS constraint.

Finally, phase-to-phase voltage results are given in Fig. 8.25. As it can be seen from the top plot, maximal instantaneous (peak) phase-to-phase voltage value never exceeds set voltage limit, that is, V_{dc} (blue dashed line). Depending on the considered speed, the maximal phase-to-phase voltage value is either below (e.g. 500 rpm) or in (e.g. 1500 rpm) the voltage limit. It should be noted that four groups of phase-to-phase voltages exist (four planes). As is visible from Fig. 8.25 top, the largest (instantaneous peak) ones are phase $a1$ to phases $b2/b3$, then $a1$ to $a3/c2$ and $a1$ to $a2/c3$, while the smallest are phase $a1$ to phases $b1$ and $c1$. A similar consideration is given in [Bermudez et al (2019)], where a similar optimisation approach was applied.

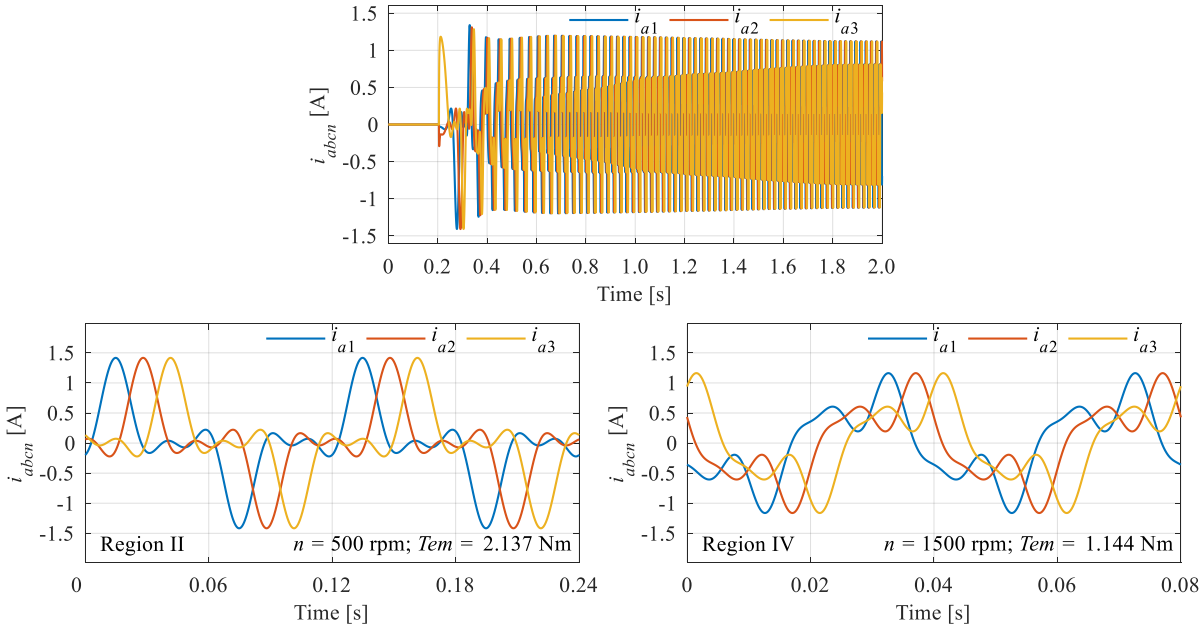

Figure 8.24 – Phase current results under the current RMS constraint: instantaneous peaks of phases $a1$, $a2$, $a3$ (top) and cases for nominal torques and speeds below (bottom-left) and above (bottom-right) the base speed.

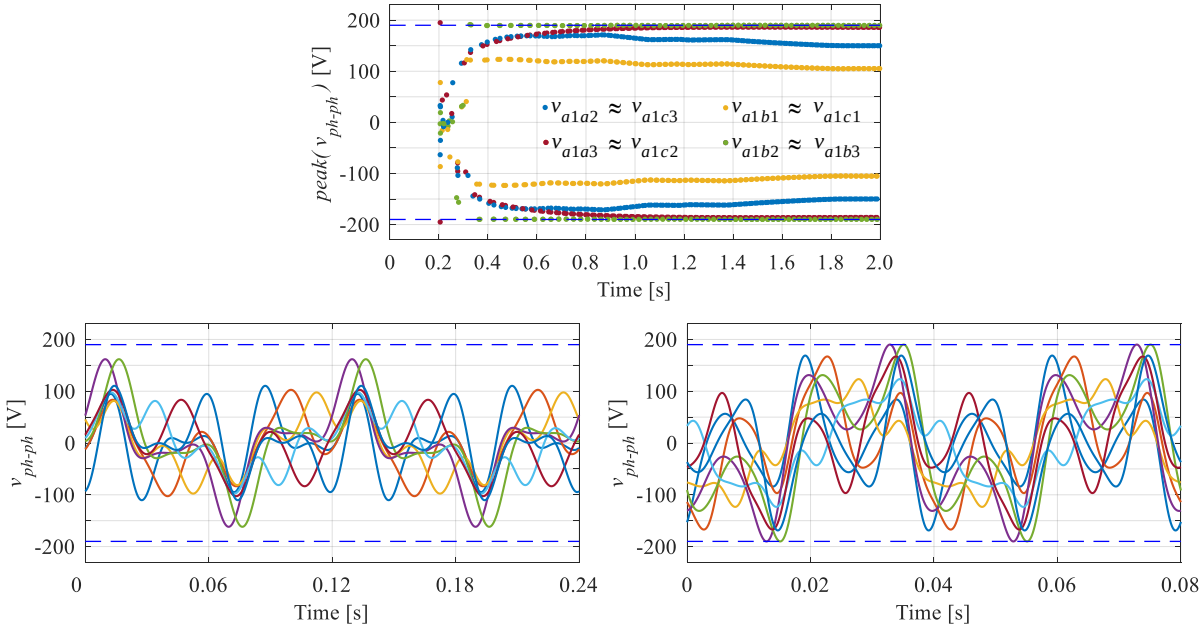

Figure 8.25 – Phase-to-phase voltage results under the current RMS constraint: maximal instantaneous peaks (top) and cases for nominal torques and speeds below (bottom-left) and above (bottom-right) the base speed.

8.6 Combined Peak and RMS Current Limit Analysis

It is easy to conclude from the subsection 8.3.2 and section 8.5 that, in the separately considered peak and RMS current limit cases, one of the two constraints is in the constant torque or constant power region not satisfied. For the RMS current limit case, this is visible from Fig. 8.24 where it can be seen that for given RMS limit, peak current value is in constant torque region above the 1.2 A peak limit. On the other hand, Fig. 8.15b (bottom plot) shows that, in the peak current limit case, although satisfied below the base speed, RMS value exceeds the desired machine's RMS limit (i.e. 0.6 A) in the FW region. To deal with this problem, multiphase PMSM system is once again optimised, this time considering both current limits at the same time. Recorded torque result is given in Fig. 8.26, where it is compared with the previously recorded best performing RMS/peak current limit output torque results.

As is visible from the figure, in the constant torque region the new recorded torque (T_{em}) is now equal to the torque previously recorded in the peak current limit case ($T_{em\text{-}peak}$), i.e. it is produced by the fundamental and the third harmonic currents. Above the base speed, recorded torque is produced by the combination of all harmonic currents and is equal to the torque recorded in the RMS current limit case ($T_{em\text{-}RMS}$). As it can be seen in Fig. 8.27, both peak and RMS boundaries are now respected (peak current is not at all times maximal allowed, because otherwise RMS limit would not be respected). In spite of respected constraints, it must be noted that maximal achievable torque in the constant torque region is now lower than the one achievable in the RMS current limit case only, that is, maximal achievable FW speed is now lower that the one achieved when system is limited by the peak current limit only.

To test the control scheme under both current limits, the following speed/torque sequence, shown in Fig. 8.28, is applied. As can be seen in Fig. 8.28a, speed sequence has three ramped increases. The first increase from 0 to 700 rpm starts at 0.2 s (below the base speed), hence the machine works under MTPA control. Because of the set speed slope, during this increase torque (Fig. 8.28b) is in the limit.

After speed reaches steady state, a load torque of 0.30 Nm is applied at 0.6 s. As can be seen, no visible change in speed occurs. Final load torque increase is performed at approximately 0.8 s (total load torque is now 1 Nm) together with the speed increase from 700 to 1100 rpm. The machine now works above the base speed ($n_{base} \approx 750$ rpm), hence flux-weakening control is active. As is visible from

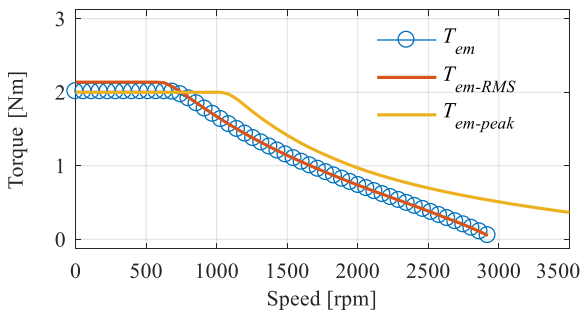

Figure 8.26 – Comparison of output torques recorded under different peak/RMS current limits.

Fig. 8.28b, torque during this speed increase decreases, i.e. the control is not capable of maintaining constant torque for the set constraints. Once speed reaches the steady state reference value, output torque reduces back to 1 Nm. At 1.2 s, load torque is reduced to 0.5 Nm, while at 1.4 s speed is further increased to 1500 rpm (twice the n_{base}). Similar speed and electromagnetic torque responses as during the second speed increase transient can once again be noted, but torque is now lower. As it can be concluded, both mechanical speed and output torque follow precisely the references.

Fig. 8.29 shows recorded *dq* currents. Fundamental and the third harmonic currents are used from the start of the sequence (as explained at the beginning of the section), while the fifth harmonic current injection is performed after flux-weakening control starts. Because up until ≈0.8 s MTPA control is applied, only quadrature current components can be seen in the given plots. After FW control commences, all three torque producing currents exhibit a decrease (i_{q5} is negative), but a change in flux-producing currents (to respect the voltage limit) can also be noted. This can be seen in the subsequent speed increase from 1100 to 1500 rpm. As is visible from the bottom plot, RMS current never exceeds the set current limit.

Finally, phase currents and phase-to-phase voltages are shown in Figs. 8.30a and b, respectively. Regarding phase currents (Fig. 8.30a), typical MTPA control strategy current shape, which follows the back-EMF shape, can be seen in the time interval between 0.2 - 0.8 s. After flux-weakening region is entered, shape of the current is changed in accordance with new current references, i.e. it now contains both flux- and torque-producing currents. Nevertheless, it never exceeds the set peak current limit (I_{VSI} = 1.2 A). The same can be concluded from the phase-to-phase voltage plot (Fig. 8.30b), for which maximal (peak) value never exceeds the maximal dc-bus voltage.

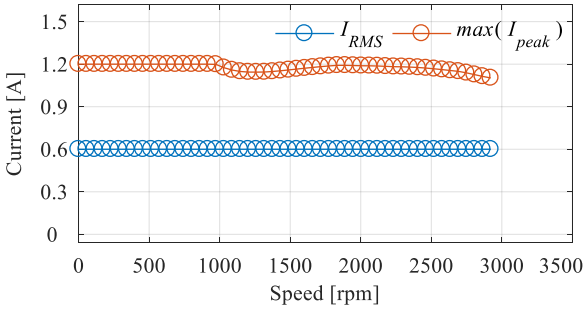

Figure 8.27 – Recorded RMS and peak current values under both current limits.

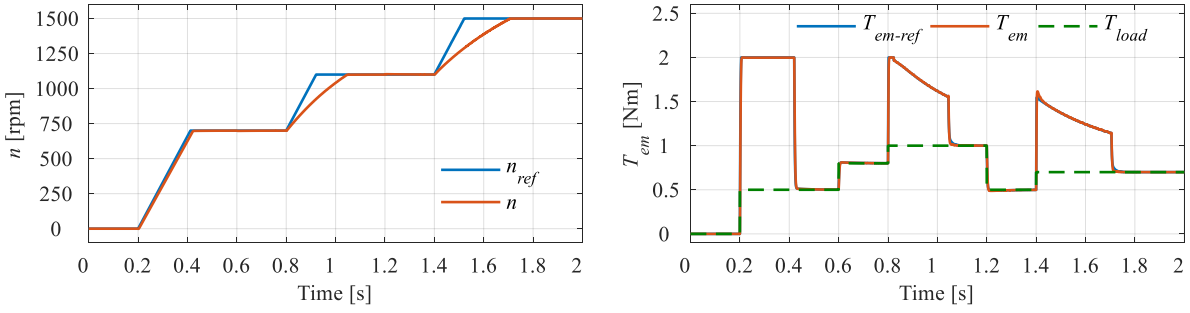

a) b)

Figure 8.28 – Speed (a) and load and electromagnetic torque (b) results recorded for the applied sequence.

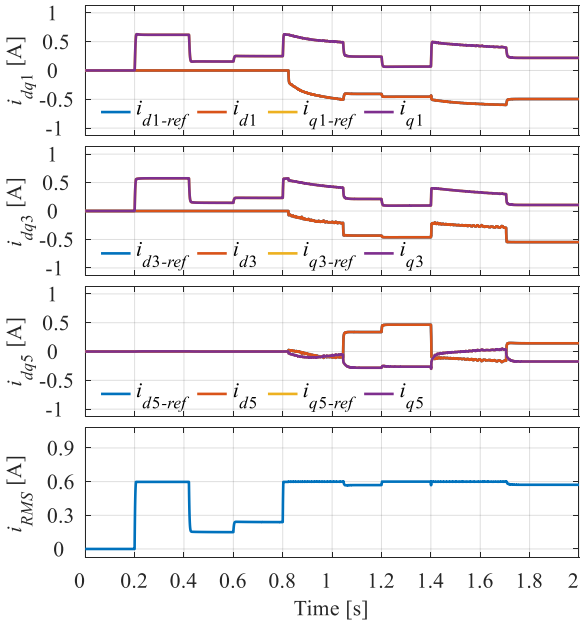

Figure 8.29 – Recorded *dq* currents for the applied speed reference/load torque sequence.

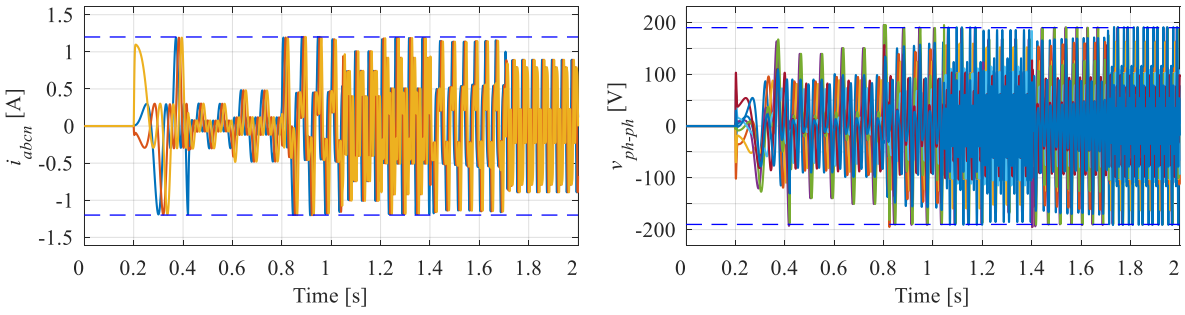

a) b)

Figure 8.30 – Simulation phase current (a) and phase-to-phase voltage (b) results recorded for the applied speed reference/load torque sequence.

8.7 Experimental Verification

Experimental verification is given next. For this purpose, look-up tables containing optimal current references obtained under both peak and RMS current limits are used/implemented in control algorithm. As mentioned earlier in the chapter, dc-link voltage is set to 190 V. With such a value of V_{dc}, base speed of PMSM is approximately 750 rpm. By taking into account the maximal speed that the loading dc machine can achieve (≈1800 rpm, Appendix A), permanent magnet synchronous machine flux-weakening operation can be tested up to two times the base speed. Experimental investigation (i.e. a study of the flux-weakening control performance) is first performed in steady state, and afterwards in transient operation. Regarding steady state, starting from 700 rpm (which is taken as the first value, and is below the base speed), speed is in each separate experiment increased by 150 rpm, while load is reduced adequately using resistors connected to the PM dc machine terminals. Final experimentally

tested speed is 1450 rpm, which is approximately twice the base speed. Torque values were set in accordance with expected values on the basis of simulations performed earlier in this chapter. Relationship between simulation torque/speed results and the ones used in experiments can be seen in Fig. 8.31.

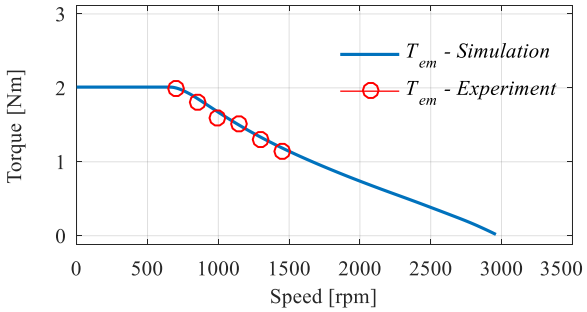

Figure 8.31 – Relationship between torque/speed characteristic recorded using simulations and actual steady state torque/speed values used in experiments.

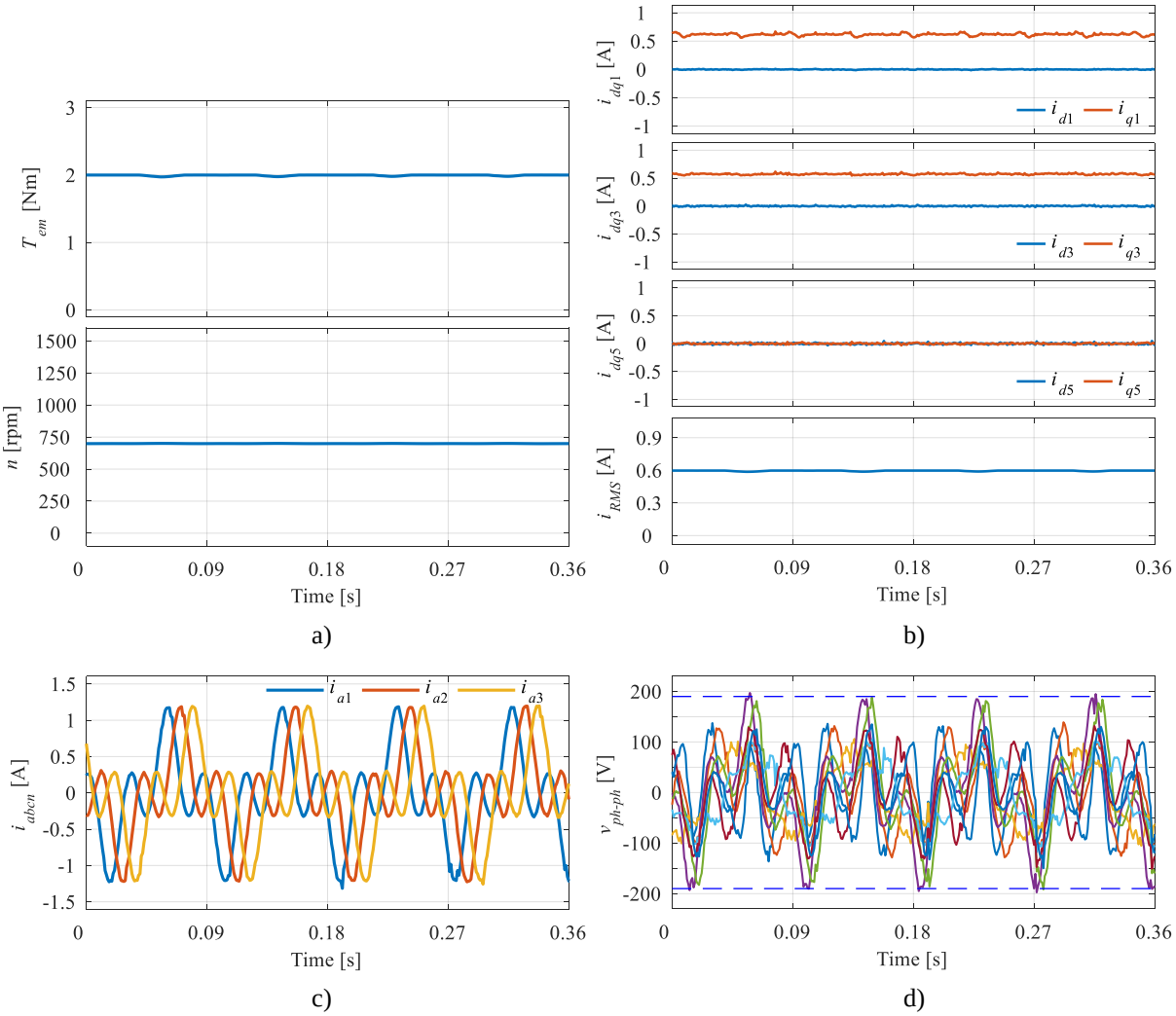

Figure 8.32 – Experimentally recorded electromagnetic torque and speed (a), *dq* currents (b), phase currents (phases *a*1, *a*2, *a*3) (c), and phase-to-phase voltages (d) – 700 rpm, ≈2 Nm.

Fig. 8.32 shows results for the case when speed is equal to 700 rpm. Since at this speed machine still operates according to the maximal torque-per-Ampere principles, torque is here equal to the maximal possible value, i.e. ≈2 Nm. Furthermore, such torque is produced only by the combined fundamental plus the third harmonic torque-producing currents, as is visible in Fig. 8.32b. As it can be seen from Fig. 8.32c, the peak of the phase current is therefore equal to ≈1.2 A, while RMS value equals ≈0.6 A, as expected because of the fundamental plus third harmonic control. The shape of phase currents similar to that of back-EMF can also be noted. Although it is expected that for such torque/speed values maximal instantaneous phase-to-phase voltage would be right below V_{dc} limit, it is here already hitting the dc-link voltage setting (Fig. 8.32d). This phenomenon (i.e. the cause of this difference between experiments/simulations) is assumed to be a consequence of neglected 11th and 13th harmonics, and is recommended as a potential topic for future work later on in the thesis.

In the next experiment, speed was increased to 850 rpm (Fig. 8.33a). Because the machine now operates above base speed, electromagnetic torque value must be reduced. New value is therefore

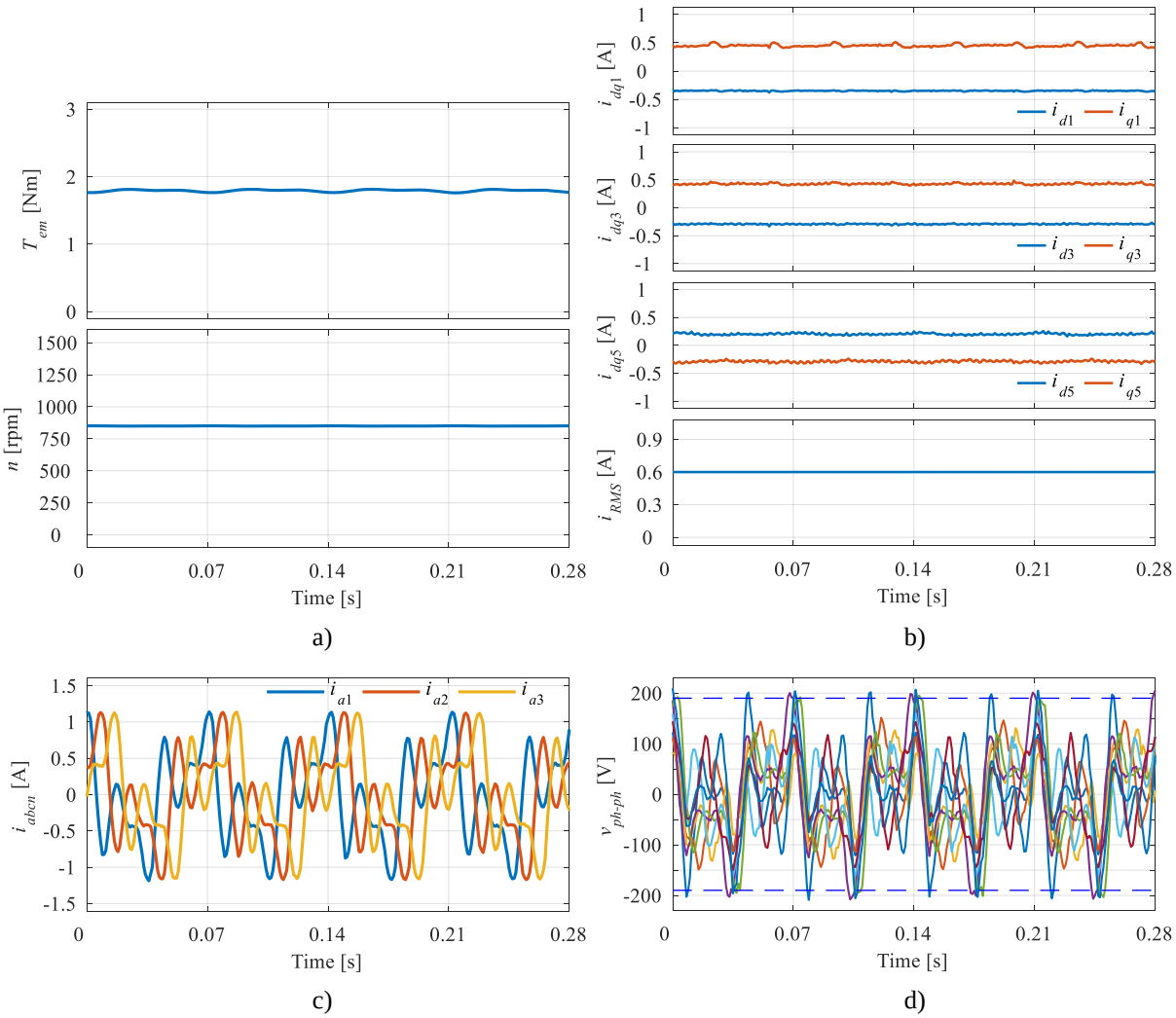

Figure 8.33 – Experimentally recorded electromagnetic torque and speed (a), *dq* currents (b), phase currents (phases *a*1, *a*2, *a*3) (c), and phase-to-phase voltages (d) – 850 rpm, ≈1.8 Nm.

≈1.8 Nm (Fig. 8.31). Because flux-producing (*d*-axes) currents are now different from zero (Fig. 8.33b), shape of the phase current is altered (Fig. 8.33c). Phase current RMS value is ≈0.602 A, while peak value is slightly reduced and is now ≈1.14 A. Phase-to-phase voltages (Fig. 8.33d) keep approximately the same maximal instantaneous value, which is again slightly higher than the set limit, very much the same as in Fig. 8.32d.

Figs. 8.34-37 show other experimentally recorded cases with speed/torque values equal to 1000 rpm/1.6 Nm (Fig. 8.34), 1150 rpm/1.5 Nm, (Fig. 8.35), 1300 rpm/1.3 Nm (Fig. 8.36), and 1450 rpm/1.15 Nm (Fig. 8.37). Note that, for the mentioned cases, only phase currents and phase-to-phase voltages are shown. As it can be seen from given plots, although speed is increased to approximately twice the base speed value, maximal instantaneous phase-to-phase voltage value is always around set V_{dc}. Regarding phase currents, in addition to the given plots, further analysis of the results can be found in Table 8.3. As it can be concluded based on the results in this table, phase current RMS value is in all cases ≈0.6 A (as per limit used in the optimisation strategy). Maximal instantaneous peak current value varies, but is always equal to, or slightly below set peak limit, i.e. 1.2 A.

Table 8.3. – Analysis of phase currents in different experimental scenarios.

***n* [rpm]**	700	850	1000	1150	1300	1450
***T*$_{em}$ [Nm]**	≈2.0	≈1.8	≈1.6	≈1.5	≈1.3	≈1.15
***I*$_{RMS}$ [A]**	≈0.60	≈0.60	≈0.60	≈0.60	≈0.60	≈0.60
***I*$_{peak}$ [A]**	≈1.20	≈1.14	≈1.08	≈1.1	≈1.08	≈1.14

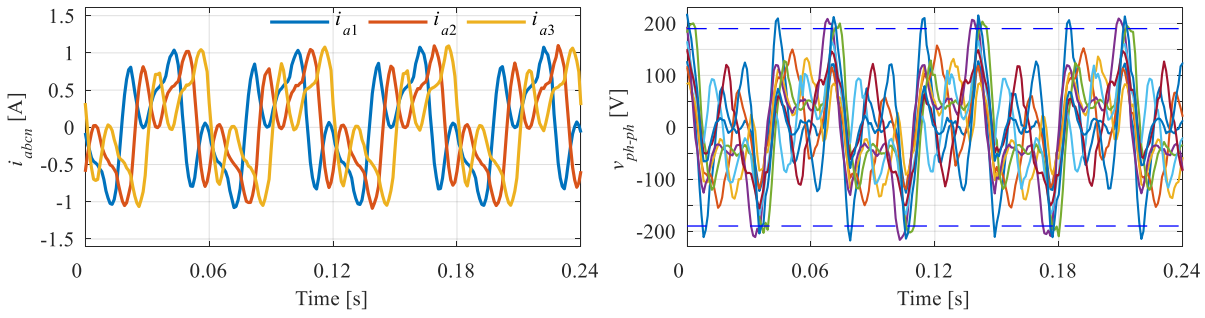

a) b)

Figure 8.34 – Experimentally recorded phase currents (phases *a*1, *a*2, *a*3) (a), and corresponding phase-to-phase voltages (b) – 1000 rpm, ≈1.6 Nm.

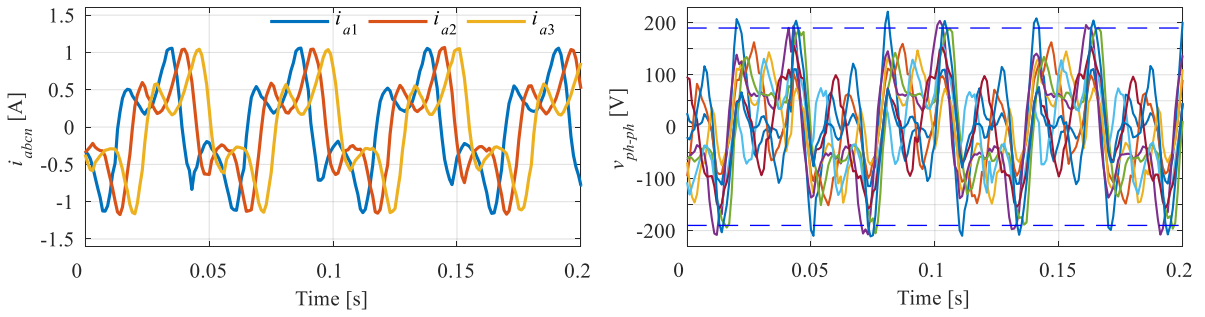

a) b)

Figure 8.35 – Experimentally recorded phase currents (phases *a*1, *a*2, *a*3) (a), and corresponding phase-to-phase voltages (b) – 1150 rpm, ≈1.5 Nm.

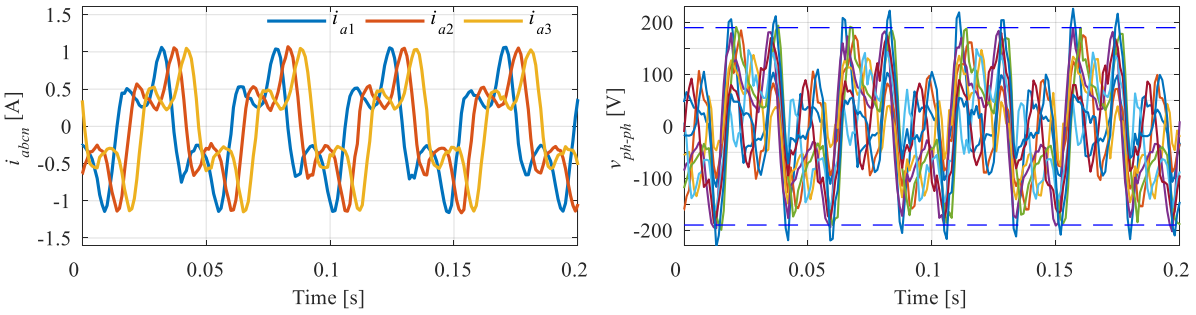

a) b)

Figure 8.36 – Experimentally recorded phase currents (phases *a*1, *a*2, *a*3) (a), and corresponding phase-to-phase voltages (b) – 1300 rpm, ≈1.3 Nm.

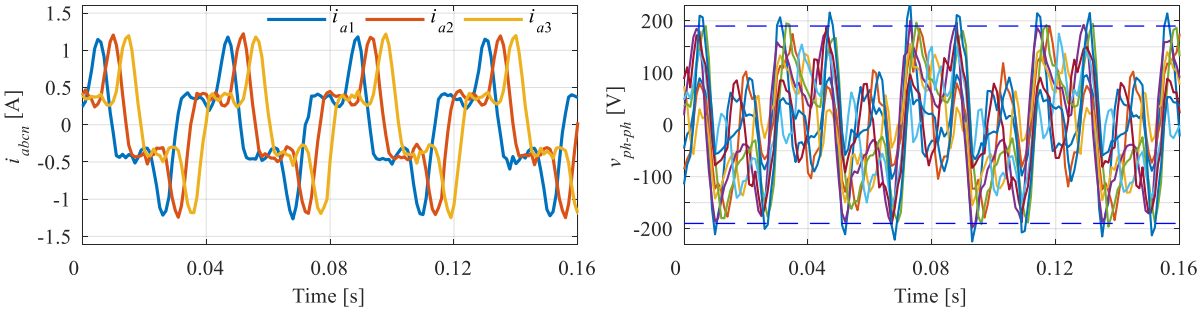

a) b)

Figure 8.37 – Experimentally recorded phase currents (phases *a*1, *a*2, *a*3) (a), and corresponding phase-to-phase voltages (b) – 1450 rpm, ≈1.15 Nm.

Finally, performance in transient operation is analysed. In Fig. 8.38, electromagnetic torque and speed sequences are shown. As it can be seen, the first speed increase from 0-700 rpm starts at t = 0.2 s. Because of the speed reference slope, electromagnetic torque is, during this increase, constantly in its limit (i.e. 2 Nm). Once steady state is reached ($t \approx 0.65$ s), electromagnetic torque drops to ≈0.6 Nm. A further speed increase (from 700-1450 rpm) starts at t = 1.4 s. Because the base speed (≈750 rpm) is quickly reached, for further speed increase, FW must be performed. This causes the electromagnetic torque to drop. At $t \approx 2.65$ s target speed of 1450 rpm is reached; hence the electromagnetic torque reduces to steady state value (i.e. 1 Nm). To achieve such a load torque in the experiment, a resistor connected to the PM dc machine terminals was used. It follows from Fig. 8.38 that there is a very good agreement between simulation results (Fig. 8.38a) and the experiment (Fig. 8.38b).

Fig. 8.39 shows the flux- and torque producing currents during explained speed/torque sequence. In MTPA control (i.e. before base speed is reached), only fundamental and the third torque-producing currents are used for torque production. Once the machine enters the FW region, the fifth harmonic *dq* currents are activated. During speed increase from 700-1450 rpm, all three flux-producing currents increase their values with negative sign. Torque-producing values are now (similar to the electromagnetic torque) reducing. Fundamental and the third harmonic currents have such (dropping) characteristics during entire speed increase, while after a short reduction at the beginning of the FW region, i_{q5} starts to increase. Once steady state is reached at 1450 rpm, both flux- and torque-producing

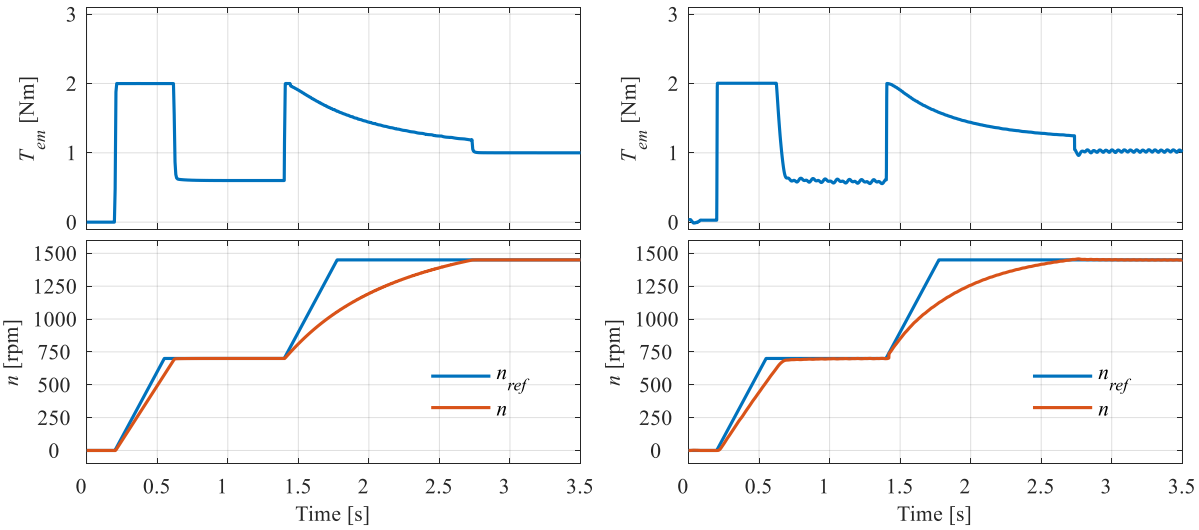

a) b)

Figure 8.38 – Electromagnetic torque and speed recorded in: (a) simulation, and (b) experiment.

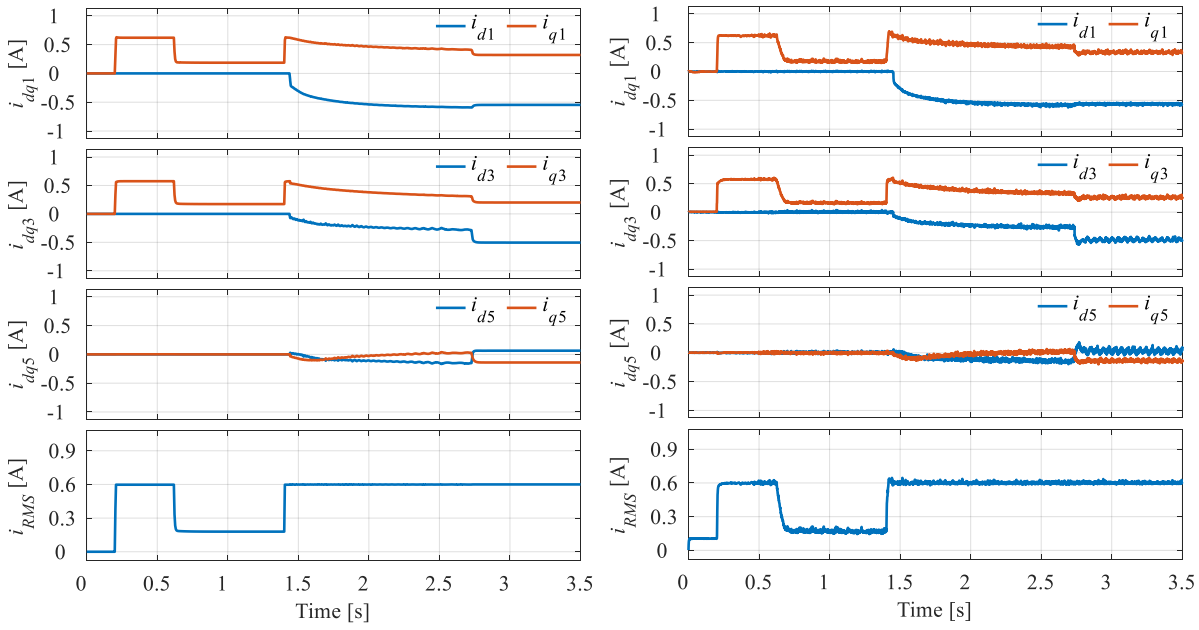

a) b)

Figure 8.39 – *dq* currents recorded in: (a) simulation, and (b) experiment.

currents become constant until the end of the recording. As it can be concluded from the bottom plots in Fig. 8.39, RMS value never exceeds the set limit, i.e. 0.6 A. Although experimental results are characterised with some ripples, excellent agreement between simulation (Fig. 8.39a) and experimental (Fig. 8.39b) results can be seen.

Phase current results (phases *a*1, *a*2, *a*3) are given in Figs. 8.40a and b (simulation and experiment, respectively). In the MTPA region, typical fundamental plus the third harmonic current shape, similar to that of back-EMF, can be seen. Once the system enters FW region, the shape (as well as the peak) of

the phase currents is changed. Regardless, in both simulation and experimental case, set peak limit of 1.2 A is respected for the entire duration of the sequence.

Finally, phase-to-phase voltages are shown in Fig. 8.41. While so far a very good agreement between simulation and experimental results was evidenced, here a small difference can be seen. In the simulation (Fig. 8.41a), maximal instantaneous phase-to-phase value never exceeds set V_{dc} limit. This is however not the case in the experimental verification (Fig. 8.41b), where the value exceeds the dc-link voltage setting. As mentioned before, reasons for this difference remain to be investigated in the future work.

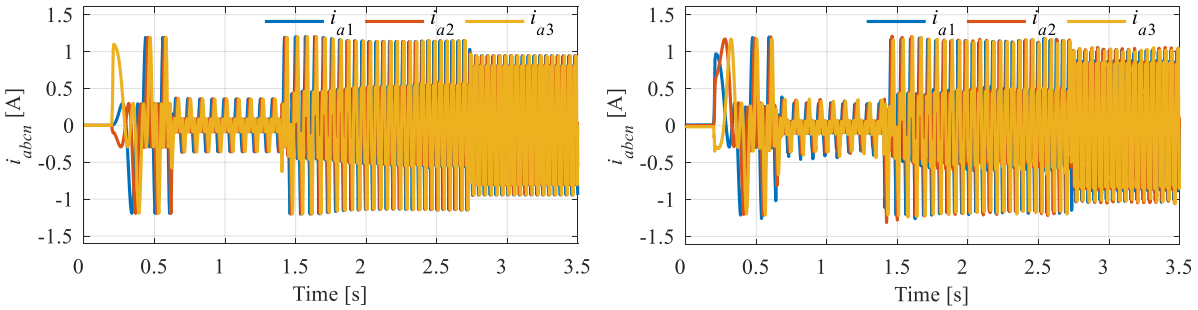

a) b)

Figure 8.40 – Phase currents (phases $a1$, $a2$, $a3$) recorded in: (a) simulation, and (b) experiment.

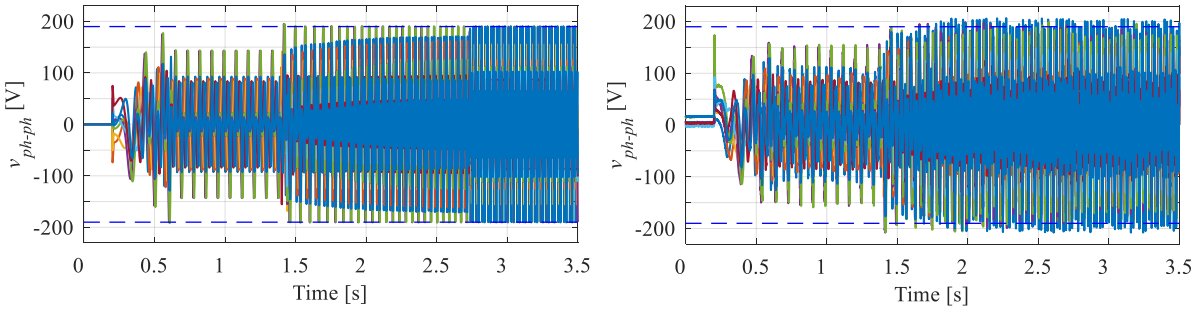

a) b)

Figure 8.41 – Phase-to-phase voltages recorded in: (a) simulation, and (b) experiment.

8.8 Summary

In this chapter, surface PMSM FW performance was studied by injecting different combinations of current harmonics to couple with the back-EMF. Harmonics up to the (and including) the fifth were analysed for this purpose. Limitation of voltage was achieved by comparing instantaneous phase-to-phase voltage value with the dc-link voltage of the inverter. Because current can be limited by thermal (RMS) constraint or by inverter switches (peak) constraint, both cases were here analysed with the intention to find the best possible *dq* current references for the highest torque/speed production in the investigated prototype. To analyse the system, a numerical optimisation procedure was used for offline data calculation. In this way, simplifying assumptions used in the analytical approaches, which usually

lead to non-optimal operation, were avoided. Recorded data were saved in look-up tables and implemented in a new control algorithm, which was afterwards validated using simulations/experiments.

As shown with the given results, for the peak current limit case the best performance is achieved when the fundamental and the third harmonic are employed for torque production in the constant torque region, and the fifth harmonic is additionally injected shortly after passing the base speed setting. Because current is here limited only by the peak, as shown, RMS current value does not necessarily stay below the set machine thermal limit. On the other hand, for the RMS current limit, the best performance is achieved when combination of all harmonics is used in both constant torque and constant/reduced power regions. The highest achievable speed is here ≈4 times the base speed. Although the current RMS value stays at all times in the limit, as concluded from the results, this does not guarantee that phase current peak value will not exceed the desired maximum value, set by the inverter limitations, since there can be a current with a small RMS but high peak.

Finally, it was shown that limiting the system with both constraints leads to a safe machine operation within the set boundaries, but neither the maximal torque nor the maximal speed, obtained when the analysis is done separately for the two cases, can be achieved. This led to the conclusion that limitations in the flux-weakening region (when using multiple current harmonic injections) must be carefully considered and precisely specified for the investigated drive. Otherwise the drive system will either not be optimally utilised, or, in the worst case scenario, inverter switches will be oversized (which means higher price) or damaged (if working above the specified limit), i.e. the machine can overheat and damage to the winding isolation may result, thus reducing its lifespan.

Please note that although conclusions given in this chapter are strictly related to the investigated machine prototype (back-EMF harmonic magnitudes and corresponding angles), presented methodology can be also applied to any other machine with a specific back-EMF. Conclusions about best performing harmonics combinations might not be the same.

Chapter Nine

CONCLUSION

9.1 Summary and Conclusions

In this thesis, a novel nine-phase surface permanent magnet synchronous machine was investigated. The stator of the machine is equipped with 36 slots inside which a single-layer (distributed) symmetrical winding is arranged, so that there are 18 slots per pole. Hence, a regular distributed winding is designed and mounted on the stator. However, the 2-pole rotor has been obtained by removing four from original six poles, so that the magnet span on rotor is shortened. This causes production of highly non-sinusoidal back-EMF force in the stator windings. Analysis of the back-EMF reveals a high third harmonic component, which is almost equal in magnitude to the fundamental. In addition to the approximately equal fundamental and the third, a significant fifth harmonic component with a magnitude equal to approximately half of the fundamental and some seventh harmonic component also exist. Utilizing this harmonic spectrum, suitable control algorithms were derived, which can significantly improve studied machine performances, as confirmed with simulations and experiments.

After the detailed literature survey in chapter 2, modelling of the machines with arbitrary number of stator phases was studied in chapter 3. Two different modelling approaches were considered, that is, machine models in terms of phase variables and in rotating reference frames were studied. Because analysis and modelling of the machine in phase-variable reference frame can be difficult to achieve, transformation matrices for decoupling were also presented. Specifically, vector space decomposition transformation was used for this purpose. Matrices were derived for both symmetrical and asymmetrical winding configurations (and with assumed single isolated neutral). After applying rotational transformation, machine model in rotating reference frame was further studied. This allowed for modelling to be performed using phase variables (which was more convenient because of the specific EMF) and for control to be implemented in a synchronous reference frame. Because machine investigated in this thesis can be placed into composite odd phase number category of machines, for which change of winding configuration can be easily achieved only by rearranging power supply leads in the machine's terminal box, this feature was also further investigated and generalised. Finally, by applying the derived modelling and control concepts, benchmark machine (with 180° magnet span) was defined. The chapter ended with *Matlab*/*Simulink* testing of the machine.

At the beginning of chapter 4, the real machine prototype (the one with 45° magnets) was introduced, and the back-EMF was recorded experimentally in no-load generation mode. Cross-section of the machine and the known electrical/design parameters were summarized at this stage as well. These parameters were necessary for FEM model construction, which was afterwards in the focus throughout the chapter. Both near- and non- sinusoidal machine models were first tested under the sinusoidal phase current, with the same current RMS value. The aim of this test was to determine the extent of the reduction in developed torque between the two machines. Although the torque produced with shortened magnets was, as expected, significantly lower, the rotor is having four times less magnet material. The

non-sinusoidal configuration was further tested under different combinations of injected current harmonics and a significant (up to 43%) torque improvement was reported. Even though significantly enhanced, the maximal torque in the machine with 45° magnets was still lower than the torque produced by the machine with 180° magnets. Therefore, an additional study was conducted and different (higher than 45°) magnet spans were tested. As it turns out, to produce torque equal to the one of the benchmark machine, rotor needs to be with ≈75° magnets if next to the fundamental, the third harmonic is considered, that is, ≈70° magnet span is required if all meaningful low order EMF harmonics are used for torque production. In the latter case, the machine is operating with ≈2.4 times less magnet material.

A suitable FOC algorithm was derived in chapter 5. The system was first analysed for the third harmonic current only because it was expected (and afterwards confirmed) that the highest torque improvement contribution will come by using this harmonic. The chapter started with the discussion related to the general modelling approach for non-standard back-EMF force in PMSMs. Once machine model was confirmed (by comparing simulation and experimental back-EMF), a control algorithm was derived. By performing the third harmonic current injection (under optimal injection ratio), the reported torque improvement was ≈36%. Optimal ratio between two harmonics was calculated/verified using MTPA and design approaches, respectively. Because other existing and for the time being non-torque producing back-EMF harmonics are, if left unattended, producing losses, their elimination was required. Vector proportional integral controllers in α-β reference frame were introduced for this purpose.

Current injection analysis of chapter 5 was in chapter 6 further generalised, and vector control algorithm which employs all possible (meaningful) high-magnitude low-order odd back-EMF harmonics for torque improvement was derived. To determine optimal current injection ratios between fundamental and all other considered harmonics, optimisation procedure and maximal torque-per-Ampere method were used. How various injection ratios interact mutually was also studied. As shown, with such an advanced control, torque can be increased by ≈45%, which is a significant improvement from the value produced using fundamental current only.

In chapter 7, position sensor fault tolerance was investigated. The derived estimation method is EMF based, i.e. it extracts rotor position out of the h^{th} harmonic machine model in x-y subspace. Corresponding reference frame machine model was therefore given as well. The control algorithm derived in chapter 6 is here further extended, so that in healthy mode both third and fifth harmonics are used for torque enhancement, while once when the sensor fault occurs, the fifth harmonic instantaneously switches for position estimation (reference current for this harmonic is set to zero). In this way, two non-fundamental harmonics in two different subspaces are used for two different control purposes simultaneously, which has not been done before. Different switching scenarios at various fault occurring speeds were studied, and it was concluded that although transients can have oscillations in both torque and speed, the system successfully continues to operate without the position sensor.

Finally, the flux-weakening performance of the studied nine-phase surface PMSM was investigated in chapter 8. The work presented in this chapter uses numerical approach to compute the optimal current references needed in above-nominal speed region. Additional reasons to choose this approach were related to a significant system complexity increase with each additionally considered harmonic, and to a significant stator resistance value in the machine prototype. The chapter started with the basic flux-weakening concepts and introduction of the optimisation (*fmincon*) procedure. In order to obtain best performance under the given voltage and current limits, current harmonics up to (and including) the fifth were analysed and injected to couple with the back-EMF. Limitation of voltage was achieved by comparing measured phase-to-phase voltage value with the maximal dc-link voltage which the inverter can provide. Because current can be limited by thermal (RMS) constraint or by the inverter switch (peak) constraint, both cases were analysed with the intention to find the best possible *dq* current references for highest torque/speed production in the investigated prototype. After optimal *dq* current references for each harmonic were obtained and saved in look-up tables (offline), MTPA based field-oriented control from chapters 5, 6, 7 was further extended with the flux-weakening capability. By employing derived control algorithm, theoretical results were successfully confirmed.

It is important to note that above given conclusions regarding torque improvement, sensorless control and above nominal speed operations are strictly related to the investigated machine prototype. Although the same principles can be applied to the other multiphase surface-mounted PMSMs with non-sinusoidal back-EMF as well, the results and corresponding conclusions (obtained torque improvements and advanced control performances) might not be the same. In another words, above given conclusions for this thesis are directly related to the specific back-EMF harmonic magnitudes and corresponding angles, and therefore can be different in other machines with different back-EMF harmonic spectra.

9.2 Future Work

As already highlighted several times in different chapters, investigated PMSM prototype was made by stator rewinding (from the three-phase to the nine-phase), and by removing four out of the originally mounted six magnet poles from the rotor. This, on one hand gave an interesting machine prototype with multiple (EMF harmonics based) research possibilities (torque enhancement, sensorless control, flux-weakening improvement), but on the other hand brought some non-optimality. For example, 45° span of magnets is not optimal, hence studied machine with shortened magnet span is not capable of producing the same torque as the one with the full (180° long) magnet length. As concluded in chapter 4, an increase of the magnet span to approximately 70° would result in the same torque production in both machines, while the reduction of the magnet material in the new prototype would still be significant. Hence, multiple tasks in the future should be related to design and testing of 70° magnet span PMSM prototype. In the same process, benchmark machine should also be built, allowing better experimental

comparison of two configurations. While researching the optimal magnet span, magnet segmentation should also be investigated for the reasons explained next.

Another interesting issue that could be further examined is how to create the back-EMF with the magnitudes as in the existing machine, but with the different harmonic angular shifts. The fundamental and the third harmonic are shifted by 180°; hence phase-to-phase voltage peak hits the voltage limit constraint at much lower speed than would be the case if these two harmonics were to be with the same angular position. It has been already shown in the literature how to create different back-EMF shapes and spectra by adding the small magnets inside the rotor and by performing magnet segmentation, hence by adopting the similar principles, an investigation in this direction could also be made. In the worst-case scenario, even if the amount of the magnet material is increased back to the original, that would still most likely give the new prototype machine a significant advantage in the flux-weakening region.

Investigation of the back-EMF based (sensorless) position estimation could be further progressed. Although the proposed algorithm manages to continuously provide sufficiently accurate position estimation to the drive system controller and thus ensure continuation of stable operation after a sensor fault is detected, actual algorithm, which would detect position sensor fault, was in this thesis not implemented. Furthermore, in the first testing scenario, the fifth harmonic was continuously (both prior and after sensor fault) used for sensorless position estimation. Regardless, there were unwanted speed and torque disturbances at the instant of switchover. Hence, an additional angular error compensating algorithm could be developed and implemented, by comparing the estimated and real angle values prior to the fault. In this way, torque and speed transients, which occur immediately after the fault, could be mitigated. A similar investigation, which is likely to be more complicated, could be performed for the second scenario as well, where disturbances in the motor speed and torque are more severe and a compensation algorithm could have significant impact on improvement of the transient behaviour. Finally, a study of the relationship between the harmonic order of the harmonic used for position estimation and corresponding estimation error could also be performed. If the increase in the error is not significant, estimation could be performed using the seventh harmonic, while the third and the fifth could then be continuously used for the torque production. In other words, torque production by the fifth harmonic could be then maintained after the fault.

With respect to the flux-weakening, the cause of difference between simulation and experimental phase-to-phase voltage results needs to be addressed in future. Although it is believed that this difference is related to the unavoidable existence of the 11th and 13th harmonics (which were in simulations not modelled, but are in the experiment adequately controlled), this needs to be confirmed. Analytical approach for optimal current reference calculation could also be further investigated. Although this was not the case in this thesis because of the high value, stator resistance could be neglected in high-power machines, allowing investigation of a new analytical approach which considers multiple current

harmonics for control above the base speed. This could result in a new approach for multiple "on-line" optimal harmonic reference calculation, which has not been reported in the literature so far. Another potentially interesting topic for future investigations is related to the offline optimisation procedure adjustments, in which stator resistance (as well as some other electrical parameters) variation caused by the temperature would also be taken into account during the optimisation process. This could result in even more precise current/voltage references optimisations.

With all above mentioned topics in mind, it could be concluded that the future work should be mainly oriented toward the new rotor design investigation. By applying the same control principles derived in this thesis, it is assumed that this could give an interesting new (but also cheaper) motor solution for electric transportation applications. Furthermore, how new machine configuration can be beneficial in faulty condition (e.g. open phase) could also be investigated. Finally, possible benefits of specific machine configurations in combination with the other control techniques (such as for example direct torque control and model predictive control) could also be investigated in the future.

Chapter Ten

REFERENCES

Abdel-Khalik A. S., Masoud M. I., Wiliams B. W., (2010), "Eleven-phase induction machine: steady-state analysis and performance evaluation with harmonic injection," *in IET Electric Power Applications*, vol. 4, no. 8, pp. 670-685.

Abdel-Khalik A. S., Mostafa G. S., Masoud M. I., Wiliams B. W., (2011), "Optimum flux distribution with harmonic injection for a multiphase induction machine using genetic algorithms," *in IEEE Transactions on Energy Conversion*, vol. 26, no. 2, pp. 501-512.

Acarnley P. P., Watson J. F., (2006), "Review of position-sensorless operation of brushless permanent-magnet machines," *IEEE Transactions on Industrial Electronics*, vol. 53, no. 2, pp. 352-362.

Alberti L., Bianchi N., (2013), "Theory and design of fractional-slot multilayer windings," *in IEEE Transactions on Industry Applications*, vol. 49, no. 2, pp. 841-849.

Apsley J. M., Williamson S., Smith A. C., Barnes M., (2006), "Induction motor performance as a function of phase number," *IEEE Proceedings - Electric Power Applications*, vol. 153, no. 6, pp. 898-904.

Arahal M. R., Duran M. J., Barrero F., Toral S., (2009), "Analysis of variable third harmonic injection for five-phase induction machine," *European Control Conference*, pp. 4350-4355.

Arahal M. R., Duran M. J., (2009), "PI tuning of five-phase drives with third harmonic injection," *in Control Engineering Practice*, vol. 17, no. 7, pp. 787-797.

Arkkio A., Bianchi N., Bolognani S., Jokinen T., Luise F., Rosu M., (2002), "Design of synchronous PM motor for submersed marine propulsion systems," *15th International Conference on Electrical Machines*, paper 523.

Aslan B., Korecki J., Vigier T., Semail E., (2012), "Influence of rotor structure and number of phases on torque and flux weakening characteristics of V-shape interior PM electrical machine," *Journal of Energy Power Engineering*, vol. 6, pp. 1461.

Aslan B., Semail E., (2014), "New 5-phase concentrated winding machine with bi-harmonic rotor for automotive application," *International Conference on Electrical Machines*, pp. 2114-2119.

Aslan B., Semail E., Legranger J., (2014), "General analytical model of magnet average eddy-current volume losses for comparison of multiphase PM machines with concentrated winding," *in IEEE Transactions on Energy Conversion*, vol. 29, no. 1, pp. 72-83.

Aström K. J., Hägglund T., (1995), "*PID Controllers: Theory, Design, and Tuning*," 2nd edition, Research Triangle Park, NC: Instrument Society of America.

Barrero F., Arahal M. R., Gregor R., Toral S., Duran M. J., (2009), "A proof of concept study of predictive current control for VSI-driven asymmetrical dual three-phase AC machines," *IEEE Transactions on Industrial Electronics*, vol. 56, no. 6, pp. 1937-1954.

Barrero F., Duran M. J., (2016), "Recent advances in the design, modelling, and control of multiphase machines: Part I.," *IEEE Transactions on Industrial Electronics*, vol. 63, no. 1, pp. 449-458.

Bastos R. R., Valle R. M., Nau S. L., Filho B. J. C., (2015), "Modelling and analysis of a nine-phase induction motor with third harmonic current injection," *9th International Conference on Power Electronics and ECCE Asia*, pp. 688-694.

Batzel T. D., Lee Y. E., (2000), "Slotless permanent magnet synchronous motor operation without a high resolution rotor angle sensor," *in IEEE Transactions on Energy Conversion*, vol. 15, no. 4, pp. 366-371.

Benecki W. T., Claggett T. K., Trout S. R., (2010), "*Permanent magnets 2010-2020: A comprehensive overview of the global permanent magnet industry*," Walter T. Benecki LLC, Highland, FL.

Bermudez M., Gomozov O., Kestelyn X., Barrero F., Nguyen N. K., Semail E., (2019), "Model predictive optimal control considering current and voltage limitations: Real-time validation using OPAL-RT technologies and five-phase permanent magnet synchronous machines," *Mathematics and Computers in Simulation*, vol. 158, pp. 148-161.

Betin F., Capolino G. A., Casadei D., Kawkabani B., Bojoi R., Harnefors L., Levi E., Parsa L., Fahimi B., (2014), "Trends in electrical machines control: samples for classical, sensorless, and fault-tolerant techniques," *in IEEE Industrial Electronics Magazine*, vol. 8, no. 2, pp. 43-55.

Bianchi N., Pre M. D., (2006), "Use of star of slots in designing fractional-slot single-layer synchronous motors," *IEEE Proceedings - Electric Power Applications*, vol. 153, no. 3, pp. 459-466.

Bierhoff M. H., (2017), "A general PLL-type algorithm for speed sensorless control of electrical drives," *IEEE Transactions on Industrial Electronics*, vol. 64, no. 12, pp. 9253-9260.

Boglietti A., El-Refaie A. M., Drubel O., Omekanda A. M., Bianchi N., Agamloh E. B., Popescu M., Gerlando A. D., Bartolo J. B., (2014), "Electrical machine topologies: hottest topics in the electrical machines research community," *in IEEE Industrial Electronics Magazine*, vol. 8, no. 2, pp. 18-30.

Bojoi R., Cavagnino A., Tenconi A., Vaschetto S., (2012), "Multiphase PM machine for more electric aircraft applications: Prototype for design validation," *38th Annual Conference on IEEE Industrial Electronics Society*, pp. 3628-3634.

Bojoi R., Cavagnino A., Tenconi A., Vaschetto S., (2016), "Control of shaft-line-embedded multiphase starter/generator for aero-engine," *IEEE Transactions on Industrial Electronics*, vol. 63, no. 1, pp. 641-652.

Boldea I., (2008), "Control issues in adjustable speed drives," *in IEEE Industrial Electronics Magazine*, vol. 2, no. 3, pp. 32-50.

Bolognani S., Calligaro S., Petrella R., (2014), "Design issues and estimation errors analysis of back-EMF-based position and speed observer for SPM synchronous motors," *in IEEE Journal of Emerging and Selected Topics in Power Electronics*, vol. 2, no. 2, pp. 159-170.

Briz F., Degner M. W., (2011), "Rotor position estimation - A review of high-frequency methods," *in IEEE Industrial Electronics Magazine*, pp. 24-36.

Camillis De L., Matuonto M., Monti M., Vignati A., (2001), "Optimizing current control performance in double winding asynchronous motors in large power inverter drives," *IEEE Transaction of Power Electronics*, vol. 16, no. 5, pp. 676-685.

Cao W., Mecrow B. C., Atkinson G. J., Bennett J. W., Atkinson D. J., (2012), "Overview of electric motor technologies used for more electric aircraft (MEA)," *IEEE Transactions on Industrial Electronics*, vol. 59, no. 9, pp. 3523-3531.

Casadei D., Dujic D., Levi E., Serra G., Tani A., Zarri L., (2008), "General modulation strategy for seven-phase inverters with independent control of multiple voltage space vectors," *IEEE Transactions on Industrial Electronics*, vol. 55, no. 5, pp. 1921-1932.

Casadei D., Mengoni M., Serra G., Tani A., Zarri L., Parsa L., (2010), "Control of a high torque density seven-phase induction motor with field-weakening capability," *IEEE International Symposium on Industrial Electronics*, pp. 2147-2152.

Cavagnino A., Li Z., Tenconi A., Vaschetto S., (2013), "Integrated generator for more electric engine: design and testing of a scaled-size prototype," *in IEEE Transactions on Industry Applications*, vol. 49, no. 5, pp. 2034-2043.

Che H. S., Duran M. J., Hew P. J., Rahim N. A., Levi E., Jones M., (2012), "Dc-link voltage balancing of six-phase wind energy sys. with series-connected machine side converters and NPC grid-side converter," *38th Annual Conference on IEEE Industrial Electronics Society*, pp. 3541-3546.

Che H. S., Levi E., Jones M., Duran M. J., Hew W. P., Rahim N. A., (2014), "Operation of a six-phase induction machine using series-connected machine-side converters," *IEEE Transaction of Industrial Electronics*, vol. 61, no. 1, pp. 164-176.

Coates C. E., Platt D., Gosbell V. J., (2001), "Performance evaluation of a nine-phase synchronous reluctance drive," *in Proceeding of IEEE Industry Applications Conference, Annual Meeting*, vol. 3, pp. 2041-2047.

Cervone A., Slunjski M., Levi E., Brando G., (2019), "Optimal third-harmonic current injection for an asymmetrical nine-phase PMSM with non-sinusoidal back-EMF," *45th Annual Conference on IEEE Industrial Electronics Society*, pp. 6223-6228.

Cervone A., Slunjski M., Levi E., Brando G., (2020), "Optimal multi-harmonic current injection strategy for an asymmetrical nine-phase PMSM," *International Symposium on Power Electronics, Electrical Drives, Automation and Motion*, pp. 796-801.

Cervone A., Slunjski M., Levi E., Brando G., (2021), "Optimal third-harmonic current injection for asymmetrical multiphase PMSMs," *IEEE Transactions on Industrial Electronics*, vol. 68.

De Belie F., Kestelyn X., Nguyen N. K., (2014), "Fault-tolerant optimal-current torque-controlled five-phase PMSMs with open-circuited phases: position self-sensing operation," *IEEE Vehicle Power and Propulsion Conference*, pp. 1-6.

Duran M. J., Salas F., Arahal M. J., (2008), "Bifurcation analysis of five-phase induction motor drives with third harmonic injection," *IEEE Transactions on Industrial Electronics*, vol. 55, no. 5, pp. 2006-2014.

Duran M. J., Barrero F., (2016), "Recent advances in the design, modelling, and control of multiphase machines: Part II.," *IEEE Transactions on Industrial Electronics*, vol. 63, no. 1, pp. 459-468.

Đorđević O., Bodo N., Jones M., (2010), "Model of an induction machine with an arbitrary phase number in Matlab/Simulink for educational use," *45th International Universities Power Engineering Conference*, pp. 1-6.

El-Refaie A. M., Jahns T. M., Novotny D. W., (2006), "Analysis of surface permanent magnet machines with fractional-slot concentrated windings," *IEEE Transactions on Energy Conversion*, vol. 21, no. 1, pp. 34-43.

El-Refaie A. M., Shah M. R., Qu R., Kern J. M., (2008a), "Effect of number of phases on losses in conducting sleeves of surface PM machine rotors equipped with fractional-slot concentrated windings," *IEEE Transactions on Industry Applications*, vol. 44, no. 5, pp. 1522-1532.

El-Refaie A. M., Zhu Z. Q., Jahns T. M., Howe D., (2008b), "Winding inductances of fractional slot surface-mounted permanent magnet brushless machines," *IEEE Industry Applications Society Annual Meeting*, pp. 1-8.

El-Refaie A. M., (2010), "Fractional-slot concentrated-windings synchronous permanent magnet machines: Opportunities and challenges," *IEEE Transactions on Industrial Electronics*, vol. 57, no. 1, pp. 107-121.

El-Refaie A. M., (2011), "Fault-tolerant permanent magnet machines: a review," *in IET Electric Power Applications*, vol. 5, no. 1, pp. 59-74.

Farshadnia M., Cheema M. A. M., Pouramin A., Dutta R., Fletcher J. E., (2018), "Design of optimal winding configurations for symmetrical multiphase concentrated-wound surface-mount PMSMs to achieve maximum torque density under current harmonic injection," *IEEE Transactions on Industrial Electronics*, vol. 65, no. 2, pp. 1751-1761.

Fatu M., Teodorescu R., Boldea I., Andreescu G., Blaabjerg F., (2008), "I-F starting method with smooth transition to EMF based motion-sensorless vector control of PM synchronous motor/generator," *IEEE Power Electronics Specialists Conference*, pp. 1481-1487.

Fei M., Zanasi R., (2011), "Control of a five-phase synchronous motors with third harmonic constrained injection," *9th IEEE International Conference on Control and Automation*, pp. 957-962.

Ferraris P., Lazzari M., (1983), "Phase numbers and their related effects on the characteristic of inverter fed induction motor drives," *in Proceeding of IEEE Industry Applications Society Annual Meeting*, pp. 494-502.

Figueroa J., Cros J., Viarouge P., (2006), "Generalized transformations for polyphase phase-modulation motors," *IEEE Transaction on Energy Conversion*, vol. 21, no. 2, pp. 332-341.

Fornasiero E., Bianchi N., Bolognani S., (2012), "Slot harmonic impact on rotor losses in fractional-slot permanent-magnet machines," *IEEE Transactions on Industrial Electronics*, vol. 59, no. 6, pp. 2557-2564.

Fortescue C. L., (1918), "Method of symmetrical co-ordinates applied to the solution of polyphase networks," *in Proceedings of American Institute of Electrical Engineers*, vol. 37, no. 6, pp. 629-716.

Garcia P., Briz F., Degner M. W., Diaz-Reigosa D., (2007), "Accuracy, bandwidth, and stability limits of carrier-signal-injection-based sensorless control methods," *in IEEE Transactions on Industry Applications*, vol. 43, no. 4, pp. 990-1000.

Garcia-Entrambasaguas P., Zoric I., González-Prieto I., Duran M. J., Levi E., (2019), "Direct torque and predictive control strategies in nine-phase electric drives using virtual voltage vectors," *in IEEE Transactions on Power Electronics*, vol. 34, no. 12, pp. 12106-12119.

Gautam A., Karugaba S., Ojo J., (2011), "Modeling of nine-phase interior permanent magnet machines (IPM) including harmonic effects," *IEEE International Electric Machines & Drives Conference*, pp. 681-686.

Gong J., Zahr H., Semail E., Trabelsi M., Aslan B., Scuiller F., (2019), "Design considerations of five-phase machine with double p/3p polarity," *in IEEE Transactions on Energy Conversion*, vol. 34, no. 1, pp. 12-24.

Gonzalez-Prieto I., Duran M. J., Che H. S., Levi E., Bermúdez M., Barrero F., (2016), "Fault-tolerant operation of six-phase energy conversion systems with parallel machine-side converters," *in IEEE Transactions on Power Electronics*, vol. 31, no. 4, pp. 3068-3079.

Gu Z. Y., Wang K., Zhu Z. Q., Wu Z. Z., Liu C., Cao R. W., (2018), "Torque improvement in five-phase unequal tooth SPM machine by injecting third harmonic current," *IEEE Transaction in Vehicular Technology*, vol. 67, no. 1, pp. 206-215.

Hassan W. J., (2018), "Design, analysis and control of a 5-phase fractional slot surface mounted PM machine for applications with a wide speed range," *University of Leicester,* Thesis.

Hemmati S., Lipo T. A., (2012), "Field weakening of a surface mounted permanent magnet motor by winding switching," *International Symposium on Power Electronics, Electrical Drives, Automation and Motion*, pp. 736-740.

Hu Y., Zhu Z. Q., Liu K., (2014), "Current control for dual three-phase permanent magnet synchronous motors accounting for current unbalance and harmonics," *in IEEE Journal of Emerging and Selected Topics in Power Electronics*, vol. 2, no. 2, pp. 272-284.

Hu Y., Zhu Z. Q., Odavic M., (2017), "Torque capability enhancement of dual three-phase PMSM drive with fifth and seventh current harmonics injection," *in IEEE Transactions on Industry Applications*, vol. 53, no. 5, pp. 4526-4535.

Ilioudis V. C., (2017), "PLL type estimator applied in PMSM sensorless control for speed and position," *12th International Conference on Ecological Vehicles and Renewable Energies*, pp. 1-8.

Jones M., Dujic D., Levi E., Vukosavic S. N., (2009), "Dead-time effects in voltage source inverter fed multi-phase ac motor drives and their compensation," *in Proceedings of 13th European Conference on Power Electronics and Applications*, pp. 1-10.

Jung E., Yoo H., Sul S. K., Choi H. S., Choi Y. Y., (2012), "A nine-phase permanent-magnet motor drive system for an ultrahigh-speed elevator," *in IEEE Transactions on Industry Applications*, vol. 48, no. 3, pp. 987-995.

Kang H., Zhou L., Wang J., (2013), "Harmonic winding factors and MMF analysis for five-phase fractional-slot concentrated winding PMSM," *International Conference on Electrical Machines and Systems*, pp. 1236-1241.

Karampuri R., Prieto J., Barrero F., Jain S., (2014), "Extension of the DTC technique to multiphase induction motor drives using any odd number of phases," *IEEE Vehicle Power and Propulsion Conference*, pp. 1-6.

Kim S. H., (2017), "*Electric Motor Control: DC, AC, and BLDC Motors*," Elsevier, 1st edition.

Klingshirn E. A., (1983), "High phase order induction motors - Part I - description and theoretical considerations," *IEEE Transactions on Power Apparatus and Systems*, vol. PAS-102, no. 1, pp. 47-53.

Krause P. C., Wasynczuk O., Sudhoff S. D., (2002), "Chapters 1-5 and 14-15 in *Analysis of electric machinery and drive systems*," IEEE Press, Piscataway, New Jersey, ISBN-10: 111802429X, ISBN-13: 978-1118024294.

Levi E., Bojoi R., Profumo F., Toliyat H. A., Williamson S., (2007), "Multiphase induction motor drives - a technology status review," *IET Electric Power Applications*, vol. 1, no. 4, pp. 489-516.

Levi E., (2008), "Multiphase electric machines for variable-speed applications," *IEEE Transactions on Industrial Electronics*, vol. 55, no. 5, pp. 1893-1909.

Levi E., Dujic D., Jones M., Grandi G., (2008), "Analytical determination of dc-bus utilization limits in multiphase VSI supplied ac drives," *IEEE Transaction on Energy Conversion*, vol. 23, no. 2, pp. 433-443.

Levi E., (2011), "Multiphase AC machines, "Chapters 3 and 24," in "*The Industrial Electronics Handbook, Power Electronics and Motor Drives*, edited by B. M. Wilamowski, J. D. Irwin, 2nd edition, CRC Press, pp. 3.1-3.31 and pp. 24.1-24.32.

Levi E., (2016), "Advances in converter control and innovative exploitation of additional degrees of freedom for multiphase machines," *IEEE Transactions on Industrial Electronics*, vol. 63, no. 1, pp. 433-448.

Li F., Hua W., Cheng M., (2014), "Design and optimization of a nine-phase flux-switching PM generator for wind power systems," *17th International Conference on Electrical Machines and Systems*, pp. 471-477.

Li G. J., Ren B., Zhu Z. Q., (2017), "Design guidelines for fractional slot multi-phase modular permanent magnet machines," *IET Electric Power Applications*, vol. 11, no. 6, pp. 1023-1031.

Li S., Han D., Sarlioglu B., (2017), "Compensation control algorithm for IPM machines considering temperature effects based on online multi-parameter estimation," *IEEE Applied Power Electronics Conference and Exposition*, pp. 1188-1195.

Li Y., Zou J. B., Lu Y. P., (2003), "Optimum design of magnet shape in permanent-magnet synchronous motors," *IEEE Transaction on Magnetics*, vol. 39, pp. 3523-3526.

Lidozzi A., Solero L., Crescimbini F., Di Napoli A., (2007), "SVM PMSM drive with low resolution hall-effect sensors," *IEEE Transactions on Power Electronics*, vol. 22, no. 1, pp. 282-290.

Lim C. S., Levi E., Jones M., Rahim N. A., Hew W. P., (2014), "FCS-MPC-based current control of a five-phase induction motor and its comparison with PI-PWM control," *IEEE Transactions on Industrial Electronics*, vol. 61, no. 1, pp. 149-163.

Lipo T. A., Wang F. X., (1984), "Design and performance of a converter optimized AC machine," *IEEE Transactions on Industry Applications*, vol. IA-20, no. 4, pp. 834-844.

Liu G., Lin Z., Zhao W., Chen Q., Xu G., (2018), "Third harmonic current injection in fault-tolerant five-phase permanent-magnet motor drive," *IEEE Transactions on Power Electronics*, vol. 33, no. 8, pp. 6970-6979.

Lu L., Aslan B., Kobylanski L., Sandulescu P., Meinguet F., Kestelyn X., Semail E., (2012), "Computation of optimal current references for flux-weakening of multi-phase synchronous machines," *38th Annual Conference on IEEE Industrial Electronics Society*, pp. 3610-3615.

Lyra R. O. C., Lipo T. A., (2001), "Torque density improvement in a six-phase induction motor with third harmonic current injection," *in Proceeding of IEEE Industry Applications Conference, Annual Meeting*, vol. 3, pp. 1779-1786.

Lyra R. O. C., Lipo T. A., (2002), "Torque density improvement in a six-phase induction motor with third harmonic current injection," *IEEE Transactions on Industry Applications*, vol. 38, no. 5, pp. 1351-1360.

Ma Z., Zhang X., (2018), "FPGA implementation of sensorless sliding mode observer with a novel rotation direction detection for PMSM drives," *IEEE Access*, vol. 6, pp. 55528-55536.

Magnussen F., Thelin P., Sadarangani C., (2004), "Performance evaluation of permanent magnet synchronous machines with concentrated and distributed windings including the effect of field-weakening," *Second International Conference on Power Electronics, Machines and Drives*, vol. 2, pp. 679-685.

McCleer P. J., Bailey J. M., Lawler J. S., (1991), "Five phase trapezoidal back EMF PM synchronous machines and drives," *in Proceeding on PE'91*, pp. 4.128-4.133.

Mengoni M., Tani A., Zarri L., Serra G., Casadei D., (2012), "Position control of a multi-motor drive based on series-connected five-phase tubular PM actuators," *IEEE Transactions on Industrial Applications*, vol. 48, no. 6, pp. 2048-2058.

Mengoni M., Zarri L., Tani A., Parsa L., Serra G., Casadei D., (2015), "High-torque-density control of multiphase induction motor drives operating over a wide speed range," *IEEE Transactions on Industrial Electronics*, vol. 62, no. 2, pp. 814-825.

Miller J. F., Howell D., (2013), "The EV everywhere grand challenge," *World Electric Vehicle Symposium and Exhibition*, pp. 1-6.

Nanoty A. S., Chudasama A. R., (2011), "Design of multiphase induction motor for electric ship propulsion," *IEEE Electric Ship Technologies Symposium*, pp. 283-287.

Nelson R. H., Krause P. C., (1974), "Induction machine analysis for arbitrary displacement between multiple winding sets," *IEEE Transactions on Power Apparatus and Systems*, vol. PAS-93, no. 3, pp. 841-848.

O'Dwater A., (2003), "*Handbook of PI and PID controller tuning rules*," Imperial College Press, London.

Olivieri C., (2013), "A fault-adaptive and observer-based sensorless strategy for a fault-tolerant five-phase BLDC motor," *IEEE International Symposium on Sensorless Control for Electrical Drives and Predictive Control of Electrical Drives and Power Electronics*, pp. 1-8.

Parsa L., Toliyat H., (2003), "Multi-phase permanent magnet motor drives," *38th IAS Annual Meeting on Conference Record of the Industry Applications Conference*, vol. 1, pp. 401-408.

Parsa L., Toliyat H. A., (2004), "Fault-tolerant five-phase permanent magnet motor drives," *IEEE Industry Applications Conference, Annual Meeting*, vol. 2, pp. 1048-1054.

Parsa L., (2005), "On advantages of multi-phase machines," *31st Annual Conference on IEEE Industrial Electronics Society*, pp. 1574-1579.

Parsa L., Toliyat H. A., (2005a), "Five-phase permanent-magnet motor drives," *IEEE Transactions on Industry Applications*, vol. 41, no. 1, pp. 30-37.

Parsa L., Toliyat H. A., (2005b), "Five-phase permanent magnet motor drives for ship propulsion applications," *IEEE Electric Ship Technologies Symposium*, pp. 371-378.

Parsa L., Kim N., Toliyat H. A., (2005), "Field weakening operation of high torque density five-phase PM drives," *IEEE International Conference on Electric Machines and Drives*, pp. 1507-1512.

Parsa L., Toliyat H. A., (2007a), "Fault-tolerant interior PM machines for hybrid electric vehicle applications," *IEEE Transactions on Vehicular Technology*, vol. 56, no. 4, pp. 1546-1552.

Parsa L., Toliyat H. A., (2007b), "Sensorless direct torque control of five-phase interior permanent-magnet motor drives," *IEEE Transactions on Industry Applications*, vol. 43, no. 4, pp. 952-959.

Patkar F., Jidin A., Levi E., Jones M., (2017), "Performance comparison of symmetrical and asymmetrical six-phase open-end winding drives with carrier-based PWM," *6th International Conference on Electrical Engineering and Informatics*, pp. 1-6.

Peng Y., Vrancic D., Hanus R., (1996), "Anti-windup, bumpless, and conditioned transfer techniques for PID controllers," *IEEE Transactions on Control Systems Technology*, vol. 16, pp. 48-57.

Pouramin A., Dutta R., Rahman F. M., (2017), "Preliminary study on differences in the performance characteristics of concentrated and distributed winding IPM machines with different rotor topologies," *IEEE Energy Conversion Congress and Exposition*, pp. 3565-3570.

Pillay P., Krishnan R., (1989a), "Modeling, simulation, and analysis of permanent-magnet motor drives: Part I - The permanent-magnet synchronous motor drive," *IEEE Transactions on Industry Applications*, vol. 25, no. 2, pp. 265-273.

Pillay P., Krishnan R., (1989b), "Modeling, simulation, and analysis of PM motor drives: Part II - The brushless DC motor," *IEEE Transactions on Industry Applications*, vol. 25, no. 2, pp. 274-279.

Pyrhonen J., Jokinen T., Hrabovcova V., (2008), "Chapter 2 in *Design of rotating electrical machines*," John Wiley and Sons, ISBN: 978-0-470-69516-6.

Rahman M. A., (2013), "History of interior permanent magnet motors," *IEEE Industry Applications Magazine*, vol. 19, no. 1, pp. 10-15.

Reddy P. B., El-Refaie A. M., Huh K. K., (2015), "Effect of number of layers on performance of fractional-slot concentrated-windings interior permanent magnet machines," *IEEE Transactions on Power Electronics*, vol. 30, no. 4, pp. 2205-2218.

Rezazadeh G., Vaschetto S., Tahami F., Capolino G. A., Henao H., Nasiri-Gheidari Z., (2018), "Analysis of six-phase induction motor with distributed and concentrated windings by using the winding function method," *XIII International Conf. on Electrical Machines*, pp. 2423-2429.

Rockhill A. A., Lipo T. A., (2009), "A simplified model of a nine-phase synchronous machine using vector space decomposition," *in Proceedings of IEEE Power Electronics and Machines in Wind Applications*, pp. 1-5.

Rockhill A. A., Lipo T. A., (2015), "A generalized transformation methodology for polyphase electric machines and networks," *in Proceedings of IEEE International Electric Machines and Drives Conference*, pp. 27-34.

Rubino S., Bojoi R., Cittanti D., Zarri L., (2020), "Decoupled and modular torque control of multi-three-phase induction motor drives," *in IEEE Transactions on Industry Applications*, vol. 56, no. 4, pp. 3831-3845.

Ryu H.-M., Kim J.-W., Sul S.-K., (2004), "Synchronous frame current control of multi-phase synchronous motor: Part I - Modeling and current control based on multiple *d-q* spaces concept under balanced condition," *Conference Record of the 2004 IEEE Industry Applications Conference, Annual Meeting*, pp. 63.

Sadeghi S., Mohammadpour A., Parsa L., (2014), "Design optimization of a high performance five-phase slot-less PMSM," *International Symposium on Power Electronics, Electrical Drives, Automation and Motion*, pp. 6-11.

Schiferl R., Lipo T. A., (1988), "Power capability of salient pole permanent magnet synchronous motors in variable speed drive applications," *Conference Record of the 1988 IEEE Industry Applications Society, Annual Meeting*, vol. 1, pp. 23-31.

Scuiller F., Semail E., Charpentier J. F., Letellier P., (2009), "Multi-criteria-based design approach of multi-phase permanent magnet low-speed synchronous machines," *IET Electric Power Applications*, vol. 3, no. 2, pp. 102-110.

Scuiller F., Semail E., Charpentier J. F., (2010), "General modelling of the windings for multi-phase machines - application for the analytical estimation of mutual stator inductance for smooth air gap machines," *The European Physical Journal Applied Physics*, vol. 5, no. 3, pp. 135-151.

Scuiller F., Semail E., (2014), "Inductances and back-EMF harmonics influence on the torque/speed characteristic of 5-ph SPM machine," *IEEE Vehicle Power and Propulsion Conference* pp. 1-6.

Scuiller F., Zahr H., Semail E., (2016), "Maximum reachable torque, power and speed for five-phase SPM machine with low armature reaction," *IEEE Transactions on Energy Conversion*, vol. 31, no. 3, pp. 959-969.

Scuiller F., Zahr H., Semail E., (2017), "A bi-harmonic five-phase SPM machine with low ripple torque for marine propulsion," *IEEE International Electric Machines and Drives Conference*, pp. 1-7.

Semail E., Bouscayrol A., Hautier J.-P., (2003), "Vectorial formalism for analysis and design of polyphase synchronous machines," *European Physical Journal*, vol. AP 22, pp. 207-220.

Semail E., Kestelyn X., Bouscayrol A., (2004), "Right harmonic spectrum for the back-electromotive force of an *n*-phase synchronous motor," *IEEE Industry Applications Conference, Annual Meeting*, pp. 71-78.

Shi R., Toliyat H. A., El-Antably A., (2001), "Field oriented control of five-phase synchronous reluctance motor drive with flexible 3rd harmonic current injection for high specific torque," *in Proceeding of IEEE Industry Applications Conference, Annual Meeting*, vol. 3, pp. 2097-2103.

Shrestha R. L., Seok J-K., (2011), "Online compensation of parameter variation effects for robust interior PM synchronous motor drives," *Journal of Power Electronics*, vol. 11, no. 5 pp. 713-718.

Slunjski M., Jones M., Levi E., (2018), "Analysis of a symmetrical nine-phase machine with highly non-sinusoidal back-EMF force," *44th Annual Conference on IEEE Industrial Electronics Society*, pp. 6229-6234.

Slunjski M., Jones M., Levi E., (2019), "Control of a symmetrical nine-phase PMSM with highly non-sinusoidal back-electromotive force using third harmonic current injection," *45th Annual Conference on IEEE Industrial Electronics Society*, pp. 969-974.

Slunjski M., Dordevic O., Jones M., Levi E., (2020), "Symmetrical/asymmetrical winding reconfiguration in multiphase machines," *IEEE Access*, vol. 8, pp. 12835-12844.

Slunjski M., Stiscia O., Jones M., Levi E., (2021), "General torque enhancement approach for a nine-phase surface PMSM with built-in fault tolerance," *IEEE Transactions on Industrial Electronics*, vol. 68.

Stiscia O., Slunjski M., Levi E., Cavagnino A., (2019), "Sensorless control of a nine-phase surface mounted permanent magnet synchronous machine with highly non-sinusoidal back-EMF," *45th Annual Conference on IEEE Industrial Electronics Society*, pp. 1327-1332.

Stiscia O., (2019), "*Position sensorless control of multiphase PMSMs*," Master degree Thesis, Politecnico di Torino.

Stumberger B., Stumberger G., Hamler A., Trlep M., Jesenik M., Gorican V., (2003), "Increasing of output power capability in a six-phase flux-weakened PM synchronous motor with a third harmonic current injection," *IEEE Transactions on Magnetics*, vol. 39, no. 5, pp. 3343-3345.

Subotic I., Bodo N., Levi E., Jones M., (2015), "Onboard integrated battery charger for EVs using an asymmetrical nine-phase machine," *IEEE Transactions on Industrial Electronics*, vol. 62, no. 5, pp. 3285-3295.

Subotic I., Bodo N., Levi E., Jones M., Levi V., (2016), "Isolated chargers for EVs incorporating six-phase machines," *IEEE Transactions on Industrial Electronics*, vol. 63, no. 1, pp. 653-664.

Sui Y., Zheng P., Wu F., Yu B., Wang P., Zhang J., (2014), "Research on a 20-slot/22-pole five-phase fault-tolerant PMSM used for four-wheel-drive electric vehicles," *Energies 2014*, vol. 7, no. 3, pp. 1265-1287.

Sui Y., Zheng P., Fan Y., Zhao J., (2017), "Research on the vector control strategy of five-phase permanent-magnet synchronous machine based on third-harmonic current injection," *IEEE International Electric Machines and Drives Conference*, pp. 1-8.

Sui Y., Yin Z., Cheng L., Zheng P., Tang D., Chen C., (2019), "Multiphase modular fault-tolerant permanent-magnet machine with hybrid single/double-layer fractional-slot concentrated winding," *in IEEE Transactions on Magnetics*, vol. 55, no. 9, pp. 1-6.

Tessarolo A., (2009), "On the modeling of poly-phase electric machines through vector-space decomposition: theoretical considerations," *in Proceeding of IEEE International Conference of Power Engineering, Energy and Electrical Drives*, pp. 519-523.

Tessarolo A., (2010), "Benefits of increasing the number of stator phases in terms of winding construction technology in high-power electric machines," *5th IET International Conference on Power Electronics, Machines and Drives*, pp. 1-6.

Thongam J. S., Tarbouchi M., Okou A. K., Bouchard D., Beguenane R., (2013), "Trends in naval ship propulsion drive motor technology," *IEEE Electrical Power & Energy Conference*, pp. 1-5.

Toliyat H. A., Xu L., Lipo T. A., (1990), "A five phase reluctance motor, with high specific torque," *in Proceedings of IEEE Industry Applications Society, Annual Meeting*, vol. 1, pp. 207-213.

Toliyat H. A., Rahimian M. M., Lipo T. A., (1991a), "*dq* modeling of five phase synchronous reluctance machines including third harmonic of air-gap MMF," *in Proceedings of IEEE Industry Applications Society, Annual Meeting*, vol. 1, pp. 231-237.

Toliyat H. A., Lipo T. A., White C. J., (1991b), "Analysis of a concentrated winding induction machine for adjustable speed drive applications, Part I - Motor analysis," *IEEE Transaction of Energy Conversion*, vol. 6, pp. 679-683.

Toliyat H. A., Lipo T. A., White C. J., (1991c), "Analysis of a concentrated winding induction machine for adjustable speed drive applications, Part II - Motor design and performance," *IEEE Transaction of Energy Conversion*, vol. 6, pp. 684-692.

Toliyat H. A., Xu L., Lipo T. A., (1992), "A five-phase reluctance motor with high specific torque," *IEEE Transaction on Industrial Application*, vol. 28, no. 3, pp. 659-667.

Toliyat H. A., Lipo T. A., (1994), "Analysis of concentrated winding induction machines for adjustable speed drive applications - experimental results," *IEEE Transactions on Energy Conversion*, vol. 9, no. 4, pp. 695-700.

Toliyat H. A., Shi R., Xu H., (2000), "A DSP-based vector control of five-phase synchronous reluctance motor," *in Proceedings of IEEE Industry Applications Society, Annual Meeting*, CD-ROM Paper No. 40_05.

Toliyat H. A., Waikar S. P., Lipo T. A., (1998), "Analysis and simulation of five-phase synchronous reluctance machines including third harmonic of airgap MMF," *IEEE Transaction on Industrial Applications*, vol. 34, no. 2, pp. 332-339.

Vaez-Zadeh S., (2018), "*Control of permanent magnet synchronous motors*," 1st edition, Oxford University Press, ISBN: 9780198742968, Great Clarendon Street, Oxford, United Kingdom.

Varatharajan A., Pescetto P., Pellegrino G., (2018), "Injectionless sensorless control of synchronous reluctance machine for zero to low speeds region," *9th International Symposium on Sensorless Control for Electrical Drives*, pp. 72-77.

Villani M., Tursini M., Fabri G., Castellini L., (2011), "Multi-phase permanent magnet motor drives for fault-tolerant applications," *IEEE International Electric Machines & Drives Conference*, pp. 1351-1356.

Visioli A., (2003), "Modified anti-windup scheme for PID controllers," *IEEE Control Theory and Applications*, vol. 150, no. 1, pp. 49-54.

Wang K., Zhu Z. Q., Ombach G., Chlebosz W., (2012), "Optimal rotor shape with third harmonic for maximizing torque and minimizing torque ripple in IPM motors," *in Proceeding of 20th International Conference on Electrical Machines*, pp. 397-403.

Wang K., Zhu Z. Q., Ombach G., (2014), "Torque enhancement of surface-mounted PM machine using third-order harmonic," *IEEE Transactions on Magnetics*, vol. 50, no. 3, pp. 104-113.

Wang K., Lin D. S., Zhou P., Zhu Z. Q., Zhang S., (2015), "Analytical determination of 3rd order harmonic current into five phase PM machine for maximum torque," *IEEE International Electric Machines & Drives Conference*, pp. 630-636.

Wang K., Gu Z. Y., Zhu Z. Q., Wu Z. Z., (2017a), "Optimum injected harmonics into magnet shape in multiphase surface-mounted PM machine for maximum output torque," *IEEE Transaction on Industrial Electronics*, vol. 64, no. 6, pp. 4434-4443.

Wang K., Zhang J. Y., Gu Z. Y., Sun H. Y., Zhu Z. Q., (2017b), "Torque improvement of dual three-phase permanent magnet machine using zero sequence components," *IEEE Transactions on Magnetics*, vol. 53, no. 11, pp. 1-4.

Wang K., Gu Z. Y., Liu C., Zhu Z. Q., (2018), "Design and analysis of a five-phase SPM machine considering third harmonic current injection," *IEEE Transactions on Energy Conversion*, vol. 33, no. 3, pp. 1108-1117.

Ward E. E., Härer H., (1969), "Preliminary investigation of an inverter-fed 5-phase induction motor," *in Proceedings of the Institution of Electrical Engineers*, vol. 116, no. 6, pp. 980-984.

Weh H., Schroder U., (1985), "Static inverter concepts for multiphase machines with square-wave current-field distribution," *in Proceedings of European Power Electronics and Drives Association*, pp. 1.147-1.152.

White D. C., Woodson H. H., (1959), "*Electromechanical energy conversion*," John Wiley and Sons, New York, NY.

Widmer J. D., Martin R., Kimiabeigi M., (2015), "Electric vehicle traction motors without rare earth magnets," *Sustainable Materials and Technologies*, vol. 3, pp. 7-13.

Xu H., Toliyat H. A., Petersen L. J., (2001), "Rotor field oriented control of five-phase induction motor with the combined fundamental and third harmonic currents," *in Proceeding of IEEE Applied Power Electronics Conference and Exposition*, vol. 1, pp. 392-398.

Xu H., Toliyat H. A., Petersen L. J., (2002), "Five-phase induction motor drives with DSP-based control system," *IEEE Transactions on Power Electronics*, vol. 17, no. 4, pp. 524-533.

Xuelei S., Xuhui W., Wei C., (2011), "Research on field-weakening control of multiphase permanent magnet synchronous motor," *International Conference on Electrical Machines and Systems*, pp. 1-5.

Yepes A. G., Malvar J., Vidal A., López O., Doval-Gandoy J., (2015), "Current harmonics compensation based on multi-resonant control in synchronous frames for symmetrical *n*-phase machines," *IEEE Transaction of Industrial Electronics*, vol. 62, no. 5, pp. 2708-2720.

Yepes A. G., Doval-Gandoy J., Baneira F., Pérez-Estévez D., López O., (2016), "Current harmonic compensation for *n*-phase machines with asymmetrical winding arrangement," *in Proceedings of IEEE Energy Conversion Congress and Exposition*, pp. 1-8.

Yepes A. G., Doval-Gandoy J., Baneira F., Pérez-Estévez D., López O., (2017), "Current harmonic compensation for *n*-phase machines with asymmetrical winding arrangement and different neutral config.," *IEEE Transactions on Industry Applications*, vol. 53, no. 6, pp. 5426-5439.

Yu F., Cheng M., Li F., Chau K. T., Huang J., Hua W., (2014), "Fault tolerant control of harmonic injected nine-phase flux switching permanent magnet motor drive system," *17th International Conference on Electrical Machines and Systems*, pp. 3117-3122.

Zabaleta M., Levi E., Jones M., (2016a), "Modelling approaches for triple three-phase permanent magnet machines," *XXII International Conference on Electrical Machines*, pp. 466-472.

Zabaleta M., Levi E., Jones M., (2016b), "Modelling approaches for an asymmetrical six-phase machine," *IEEE 25th International Symposium on Industrial Electronics*, pp. 173-178.

Zahr H., Gong J., Semail E., Scuiller F., (2016a), "Comparison of optimized control strategies of a high-speed traction machine with five phases and bi-harmonic electromotive force," *Energies 2016*, vol. 9, no. 12, pp. 1-19.

Zahr H., Semail E., Aslan B., Scuiller F., (2016b), "Maximum torque per ampere strategy for a biharmonic five-phase synchronous machine," *International Symposium on Power Electronics, Electrical Drives, Automation and Motion*, pp. 91-97.

Zahr H., Trabelsi M., Semail E., Nquyen N. K., (2017), "Five-phase bi-harmonic PMSM control under voltage and currents limits," *43rd Annual Conference on IEEE Industrial Electronics Society*, pp. 7995-8000.

Zhao Y., Lipo T. A., (1994), "Space vector PWM control of dual three phase induction machine using vector space decomposition," *IEEE Transactions on Industry Applications*, vol. 31, no. 5, pp. 1100-1109.

Zhao P., Yang G., (2011), "Torque density improvement of five-phase PMSM drive for electric vehicles applications," *Journal of Power Electronics*, vol. 11, pp. 401-407.

Zhang G., Wang G., Xu D., Zhao N., (2016), "ADALINE-network-based PLL for position sensorless interior permanent magnet synchronous motor drives," *IEEE Transactions on Power Electronics*, vol. 31, no. 2, pp. 1450-1460.

Zhang H., Zhao B., Gong J., Xu Y., Vu T. D., Nguyen N. K., Semail E., Moraes T. J. S., (2019a), "Torque optimization of a seven-phase bi-harmonic PMSM in healthy and degraded mode," *International Conference on Electrical Machines and Systems*, pp. 1-6.

Zhang L. F., Wang K., Sun H. Y., Zhu S. S., (2019b), "Multiphase PM machines with Halbach array considering third harmonic flux density," *IEEE Transactions on Industrial Electronics*, vol. 66, no. 12, pp. 9184-9193.

Zheng L., Fletcher J. E., Williams B. W., He X., (2008), "Dual-plane vector control of a five-phase induction machine for an improved flux pattern," *IEEE Transaction on Industrial Electronics*, vol. 55, no. 5, pp. 1996-2005.

Zheng P., Sui Y., Zhao J., Tong C., Lipo T. A., Wang A., (2011), "Investigation of a novel five-phase modular permanent-magnet in-wheel motor," *IEEE Transactions on Magnetics*, vol. 47, no. 10, pp. 4084-4087.

Zheng P., Wu F., Lei Y., Sui Y., Yu B., (2013), "Investigation of a novel 24-slot/14-pole six-phase fault-tolerant modular permanent-magnet in-wheel motor for electric vehicles," *Energies 2013*, vol. 6, no. 10, pp. 4980-5002.

Zhu Z. Q., Wang K., Ombach G., (2012), "Optimal magnet shaping with third order harmonic for maximum torque in SPM machines," *in Proceeding of 6th IET Conference on Power Electronics, Machines and Drives*, pp. 1-6.

Zoric I., Jones M., Levi E., (2017a), "Arbitrary power sharing among three-phase winding sets of multiphase machines," *IEEE Transactions on Industrial Electronics*, vol. 65, no. 2, pp.1128-1139.

Zoric I., Jones M., Levi E., (2017b), "Vector space decomposition algorithm for asymmetrical multiphase machines," *International Symposium on Power Electronics (Ee)*, pp. 1-6.

Appendix A

DESCRIPTION OF THE EXPERIMENTAL SETUP

A.1 Hardware Description

Experimental setup used to test different control algorithms and record corresponding experimental results is described next. Hardware components are presented in this section, while software components needed for successful machine control implementation can be found in the following section. List of used hardware components is given below. Images of the corresponding components can be seen in Fig. A1. Fig. A2 shows scaled down drawing of the experimental setup.

The list of hardware components is as follows:

- Symmetrical/asymmetrical nine-phase permanent magnet synchronous machine,
- PM dc machine shaft-coupled to the nine-phase PM synchronous machine,
- Datum Electronics M425 S1 0-50 Nm torque meter,
- two custom made two-level eight-phase voltage source inverters,
- dSPACE rapid prototyping system,
- two Tektronix oscilloscopes with active high voltage differential and current probes,
- current and voltage measurement sensors adapted to work with dSPACE,
- Sorensen SGI600/25 single quadrant dc-voltage source,
- resistor box used to load the dc machine,
- encoders OMRON E6B2-6WZ1X and RS 2048, and
- Windows PC with Control Desk used for machine control.

The key component in the experimental setup (as well as in the entire thesis) is the symmetrical/asymmetrical nine-phase permanent magnet synchronous machine. Because prototype machine configuration was presented in detail in chapter 4 (including design and electrical parameters, and corresponding cross-section), it will not be further discussed here (please see section 4.2). Nevertheless, for the completeness reason, it should be noted that the original machine was a three-phase brushless servomotor produced by MOOG. Original machine's serial number is T-2-M2-030 (rated voltage 180 V, rated current 8.5 A, rated power 1.73 kW, rated speed 3000 rpm, rated frequency 150 Hz, and rated torque 7.5 Nm).

Coupled to the PMSM is a PM dc machine, which can rotate in positive or negative direction, that is, can produce positive or negative torque depending on the winding currents. Used PM dc machine is Leeson 108371, rated at 1.1/1.5 kW, 180 V, 7/9 A and 1800 rpm. Because field in this machine is produced by the permanent magnets, machine does not have the ability to operate above rated speed. Consequently, operational speed of both machines is therefore limited to 1800 rpm, i.e. to the rated speed of the PM dc machine. During the different experimental tests and testing scenarios, PM dc machine has been connected to the dc power source (Sorensen SGI600/25) and to variable resistive load (resistor bank), as appropriate:

- PM dc machine operates in generating mode: stator current and torque are governed by machine speed and chosen resistive load.
- PM dc machine operates in motoring mode: stator current and torque are set by dc power source which operates in constant current mode (torque is unrelated to the rotational speed).

In between two machines, Datum Electronics M425 S1 0-50 Nm torque meter is installed. Torque meter is connected to the companion signal processing unit Datum Universal Interface, which on its display shows measured electromagnetic torque, mechanical speed and corresponding output power. On the analogue output terminals of the processing unit, the same signals can be measured in the range between 0-15 V, hence oscilloscope probes are connected to these ports so that torque value is available on the oscilloscope as well.

Two (custom made) eight-phase two-level voltage source inverters (VSI) are used to supply the nine-phase permanent magnet synchronous machine. Outputs in each are provided by three Infineon FS50R12KE3 EUPEC IGBT 6-pack power modules. Eight legs are used as output, while the remaining one drives the braking resistor to protect dc-link capacitors in the case of the power reversal. Dc link can be supplied directly by dc-voltage source or by 3-phase grid (if dc link is supplied from the 3-phase grid, grid voltage is rectified by three Semikron SKKD 46 rectifier modules). In all experimental tests conducted in this work, dc link was supplied by dc-voltage source Sorensen SGI600/25. To measure the phase current, VSI is equipped with current measurement based on Honeywell CSNE151-100 current sensors. Each phase current is measured and made available to dSPACE DS2004 ADC board over DB50 connector. Gating signals to the VSI are provided by dSPACE DS5101 digital waveform output (DWO) board over DB37 connector. In order to control both VSIs with a single 16 channel DWO board, only seven channels are available per VSI while remaining two channels are used as enable signals, i.e. one for each VSI. Machine is connected in such a way that the first two winding sets are supplied by one VSI and the remaining winding set by the second inverter.

Control and measurements in all experiments are achieved using dSPACE rapid prototyping system. It consists of main processor board DS1006 and multiple peripheral boards which are:

- DS5101, digital waveform output board, used for gating signal generation.
- DS2004, analogue to digital (A/D) converter board, used for current/voltage measurements.
- DS3002, encoder board, used for capturing encoder pulses and finding position and speed.
- DS2101, D/A converter board, used to provide synchronisation with oscilloscopes.

More details regarding the control system are provided in the following section where software parts of the experimental setup are explained.

dSPACE system can only collect measurements at the control loop frequency. Therefore, two Tektronix oscilloscopes (Tektronix DPO2014b and MSO2014b) are used for more precise

measurements. Both are 100 MHz, four channel, deep memory scopes with 1 GS/s sampling frequency and 1.25 million points memory depth. Measurement of the phase currents and phase voltages is organised in such a way that one oscilloscope is used to capture three voltages and speed (or power) from torque meter, while the other captures three currents and the torque. Voltages are measured using high voltage active differential probes Tektronix P5205A, while currents are measured by current clamps Pico Technology TA189. When current was measured, additional four wire turns for more precise measurement were also used. To synchronise both oscilloscopes, the same triggering signal is used and provided to the oscilloscopes through auxiliary channels.

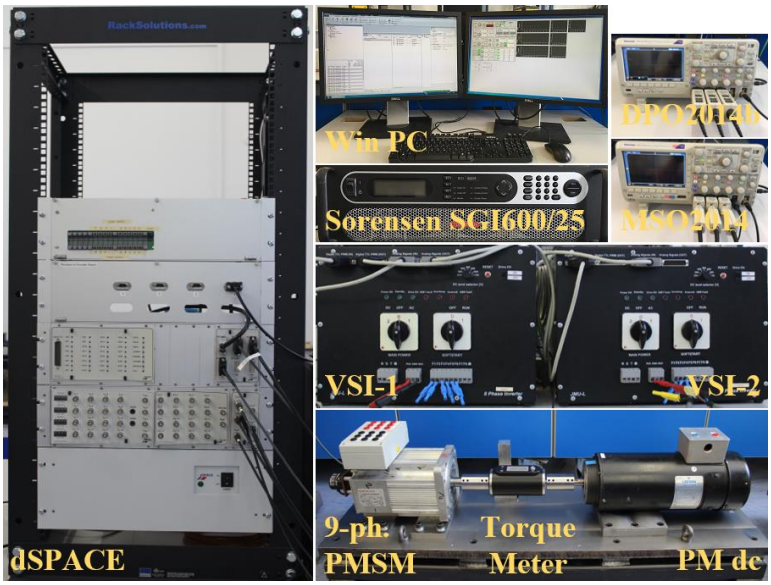

Figure A1 – Experimental setup.

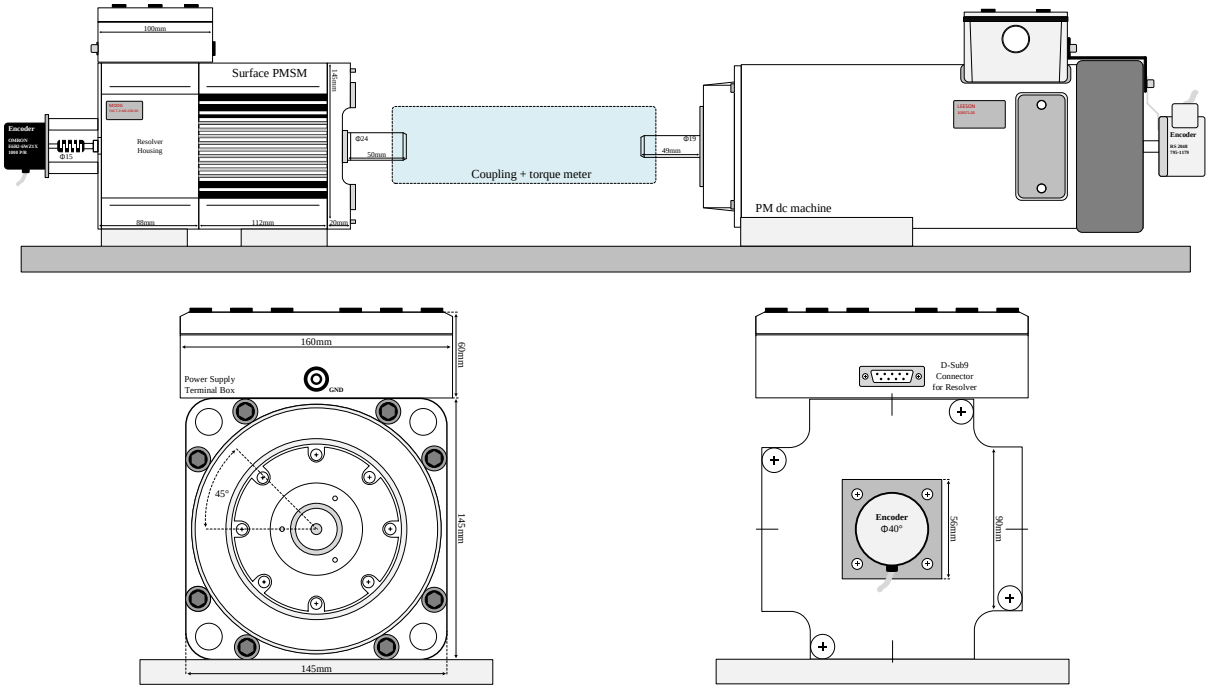

Figure A2 – Scaled drawing of the experimental setup (top) and PMSM cross-section: front (bottom, left), and back (bottom, right).

A.2 Software Description

As explained throughout chapters, before conducting any experiments in the thesis, simulation tests in *Matlab*/*Simulink* environment were performed first. *Matlab*/*Simulink* software tool was chosen because of highly advanced modelling and computation possibilities and because dSPACE workflow is capable of using Simulink files by means of Simulink Coder. This essentially means that initial Simulink file used in simulation can easily be adapted for experiments by removing blocks that simulate hardware components physically available in the laboratory and adding dSPACE specific blocks to create an interface to the dSPACE peripheral boards. This enables execution of the developed control on dSPACE processor board DS1006, while all user inputs are provided by graphical user interface developed in Control Desk.

Firstly, from simulation machine model (Fig. A3; the third harmonic injection case), VSI model, machine model and mechanical system are removed. Instead, dwell times are calculated and provided as variables to the DWO board (DS5101) by use of DS5101DWO block from the dSPACE specific Real-Time Interface (RTI) library. DS5101 board uses custom written code to create gating signals based on calculated dwell time. Triangular carrier is assumed. DWO board uses high precision counter (250 ns ticks), and it is used to generate an interrupt over PHS bus to the main processor board. DWO board interrupt is enabled and acknowledged by System Start and System Outputs blocks from the Simulink Coder library, respectively. Generated interrupt triggers the timer task and whole control code is executed. Furthermore, interrupt is synchronised with PWM signals so that control code is executed exactly at the beginning and in the middle of the switching period. PWM switching frequency is set to 5 kHz, while control loop is executed at 10 kHz in all experiments. Since DWO board has 16 channels, one board is enough for producing gating signals for both two-level inverters.

Besides gating signal generation, phase current and rotor position value measurements are also required, in order to implement FOC strategy. In order to capture encoder pulses, encoder board DS3002 is used. Position measurement is realised by counting the number of encoder pulses between two sample intervals. This behaviour is embedded in the DS3002POS_B1_C1 Simulink block which provides position and speed. Since this type of measurement is intended for high speed measurement and only few pulses were generated in one sampling interval when machine operates at 1500 rpm, error in measured position and speed could not be neglected. Therefore, position and speed measurement is started every 10 samples and additional filtering is implemented by use of the 2^{nd} order low-pass filter. Current measurements are provided by current sensors, while values are obtained by ADC board DS2004. Acquisition is started at each execution step by use of DS2004ADC_BLi block. Acquired current values are multiplied by predefined current sensor gains and offset is removed. Since acquisition is happening in the beginning and in the middle of the switching period, where current has an average value over switching period when triangular carrier is used, no additional filtering was needed.

As mentioned in previous section, all experimental measurements are captured by dSPACE and oscilloscopes. However, these measurements need to be synchronised, so that both devices capture the same data. dSPACE and oscilloscopes are synchronised by use of DAC board DS2101, i.e. signal used to start the measurements over the dSPACE platform is used as a trigger signal for both oscilloscopes. Control Desk Recorder is used to capture data by the dSPACE, while custom Matlab functions were created to access oscilloscopes and transfer captured data using VISA protocol. Communication between Matlab and oscilloscopes is made possible by use of Instrument Control Toolbox.

Graphic user interface to the dSPACE platform is created using Control Desk software. This software allows real time access to the control variables. An example of the developed graphic user interface can be seen in the Fig. A4, where all basic drive controls are shown.

Finally, it should be noted that although most of the simulations were conducted using *Matlab*/*Simulink*, brief experimental setup validation in PLECS was also made (Fig. A5).

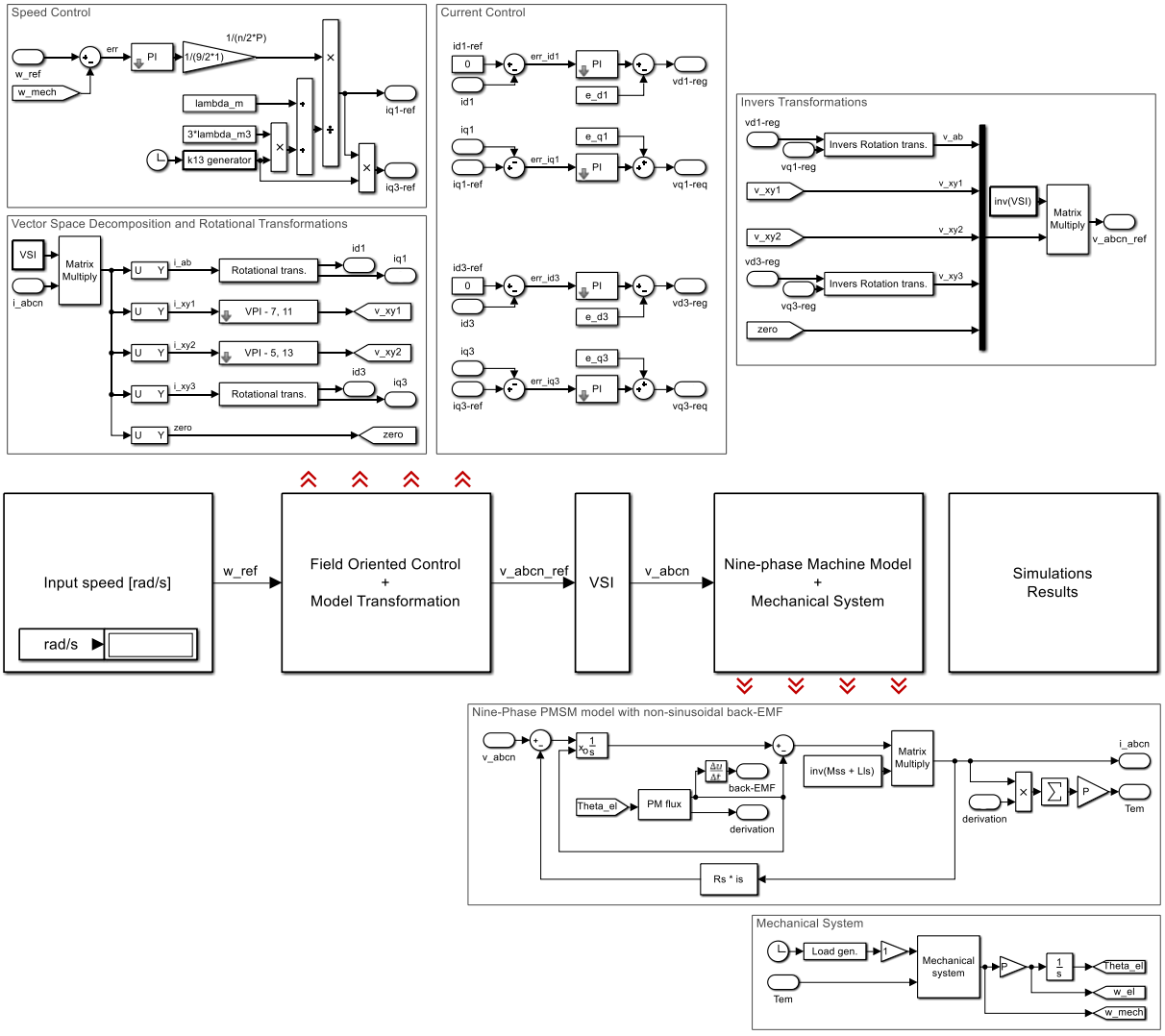

Figure A3 – *Matlab*/*Simulink* simulation model – third harmonic current injection case.

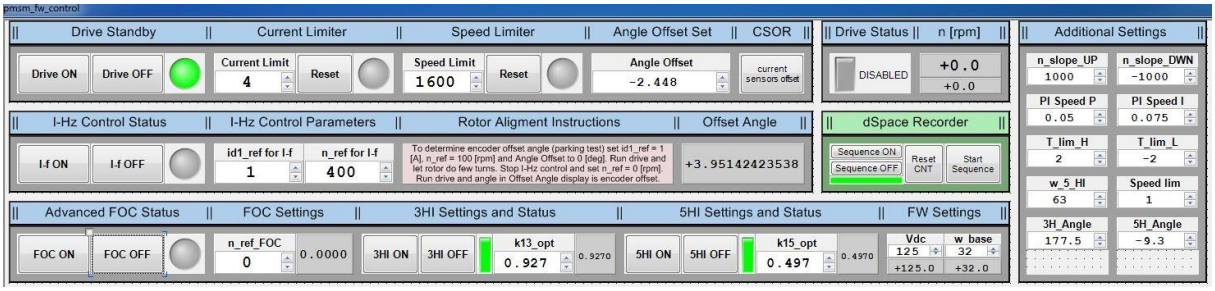

Figure A4 – Example of the graphic user interface developed in Control Desk and used to interact with dSpace.

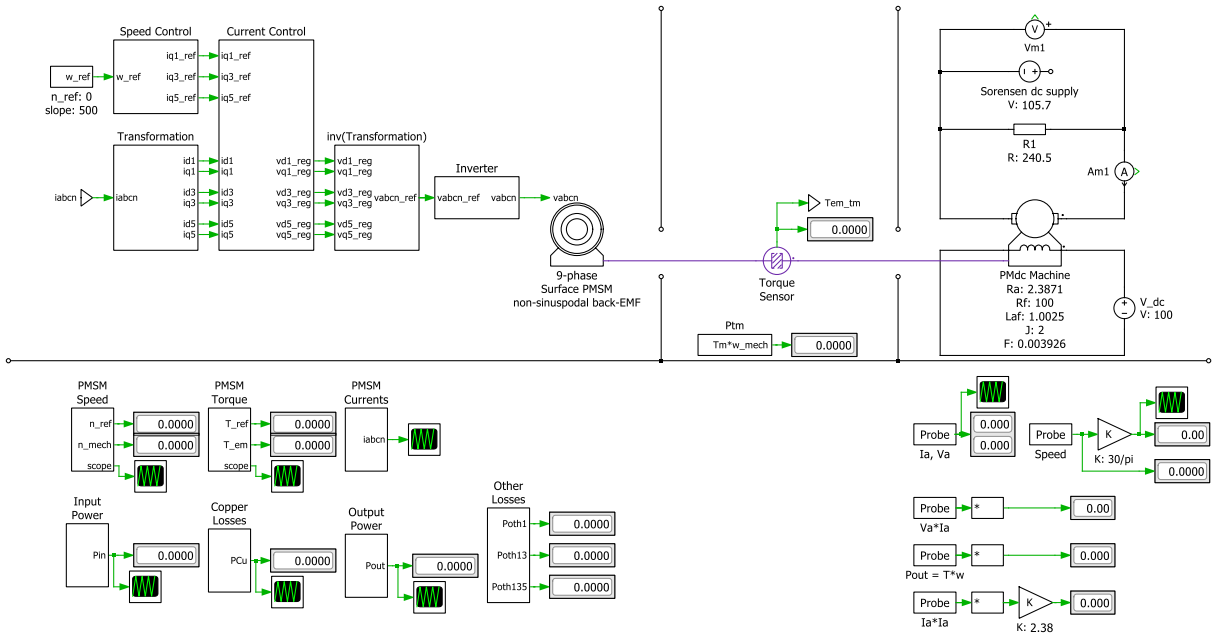

Figure A5 – Experimental setup modelled in PLECS.

Appendix B

PUBLICATIONS RESULTING FROM THE THESIS

B.1 Journal Publications

Slunjski M., Stiscia O., Jones M., Levi E., (2021), "General torque enhancement approach for a nine-phase surface PMSM with built-in fault tolerance," *IEEE Transactions on Industrial Electronics*, vol. 68.

Slunjski M., Dordevic O., Jones M., Levi E., (2020), "Symmetrical/asymmetrical winding reconfiguration in multiphase machines," *IEEE Access*, vol. 8, pp. 12835-12844.

B.2 Conference Publications

Slunjski M., Jones M., Levi E., (2018), "Analysis of a symmetrical nine-phase machine with highly non-sinusoidal back-EMF force," 44*th Annual Conference on IEEE Industrial Electronics Society*, pp. 6229-6234.

Slunjski M., Jones M., Levi E., (2019), "Control of a symmetrical nine-phase PMSM with highly non-sinusoidal back-electromotive force using third harmonic current injection," 45*th Annual Conference on IEEE Industrial Electronics Society*, pp. 969-974.

B.3 Co-Authored Publications

Cervone A., Slunjski M., Levi E., Brando G., (2021), "Optimal third-harmonic current injection for asymmetrical multiphase PMSMs," *IEEE Transactions on Industrial Electronics*, vol. 68.

Cervone A., Slunjski M., Levi E., Brando G., (2019), "Optimal third-harmonic current injection for an asymmetrical nine-phase PMSM with non-sinusoidal back-EMF," 45*th Annual Conference on IEEE Industrial Electronics Society*, pp. 6223-6228.

Cervone A., Slunjski M., Levi E., Brando G., (2020), "Optimal multi-harmonic current injection strategy for an asymmetrical nine-phase PMSM," *International Symposium on Power Electronics, Electrical Drives, Automation and Motion*, pp. 796-801.

Stiscia O., Slunjski M., Levi E., Cavagnino A., (2019), "Sensorless control of a nine-phase surface mounted permanent magnet synchronous machine with highly non-sinusoidal back-EMF," 45*th Annual Conference on IEEE Industrial Electronics Society*, pp. 1327-1332.